EXPERIMENTAL AND NUMERICAL INVESTIGATION OF MOLTEN SALT NANOMATERIALS FOR ENHANCED THERMAL ENERGY STORAGE (TES) AND HEAT TRANSFER FLUID (HTF)

A Dissertation

by

BINJIAN MA

Submitted to the Office of Graduate and Professional Studies of
Texas A&M University
in partial fulfillment of the requirements for the degree of

DOCTOR OF PHILOSOPHY

Chair of Committee,	Debjyoti Banerjee
Committee Members,	Partha Mukherjee
	Hong Liang
	Zhengdong Cheng
Head of Department,	Andreas A. Polycarpou

August 2017

Major Subject: Mechanical Engineering

ABSTRACT

Concentrating solar power (CSP) plants have been widely commercialized internationally for generating electricity from solar energy. Thermal energy storage (TES) systems are typically used in CSP plants to balance the fluctuations in demand with the intermittency of supply. In various CSP plants, molten salts are used as both the primary heat transfer fluid (HTF) and as TES medium. However, molten salts suffer from poor thermo-physical properties, e.g., specific heat capacity is typically less than 2 J/(g·K) and thermal conductivity is typically less than ~1 W/(m·K). Doping molten salts with minute quantities of nanoparticles has been shown to enhance their thermo-physical properties (also known as molten salt nanofluids). Stable dispersion of nanoparticles realized in different solvents (i.e., nanofluids) has been demonstrated to cause anomalous enhancement in the resulting thermo-physical property values. Traditional approaches employed for mixing nanoparticles in solvents often results in agglomeration and precipitation (fouling). This results in compromised reliability and not being cost-effective for industrial applications, such as in CSP plants.

In this study, an innovative one-step synthesis protocol was developed and the techno-economic feasibility of using the molten salt nanofluids was explored for CSP applications. Modulated Differential Scanning Calorimetry (MDSC) and Temperature-History (T-History) method were used to measure the specific heat capacity of the nanomaterial samples at high temperatures (~500 °C). In addition, the thermal conductivity of the nanofluid samples were also measured using a customized concentric

cylinder test apparatus. Solar salt ($NaNO_3$-KNO_3) was used as the neat solvent (base fluid) material. Various nanoparticles (SiO_2, Al_2O_3, MgO, ZnO) were either procured directly from commercial suppliers or generated in-situ from chemical reactions. Different parameters were explored in the synthesis: nanoparticle type, concentration, synthesis temperature, synthesis time, dispersing agents, etc.

Numerical models were developed to elucidate the mechanism of specific heat capacity enhancement of the synthesized nanomaterials and to explore the thermal-hydraulic performance of molten salt nanofluid samples in a flow loop. Molecular dynamics (MD) simulations were performed to elucidate the morphology of the compressed layer formed due to adsorption of the solvent molecules on the surface of a nanoparticle surface. Chemical kinetics simulations were performed to predict the nucleation and growth rate of ensembles of nanoparticles during one-step synthesis. CFD simulations were performed to predict the heat transfer coefficient of the molten salt nanofluids in a flow loop. The results from the experimental and numerical investigation demonstrated that the one-step synthesis protocol for nanofluids involving generation of nanoparticles in-situ from cheap additives is a cheap and cost-effective approach for industrial applications (e.g., CSP) for enhancing the energy storage capacity and power rating as well as for extending the life-cycle of equipment (e.g., heat exchangers).

DEDICATION

To my beloved family and friends for their sincere support and inspiration.

ACKNOWLEDGEMENTS

I would like to express my sincere gratitude to my advisor, Dr. Debjyoti Banerjee for his patient guidance and support. I would also like to thank my committee members, Dr. Partha Mukherjee, Dr. Hong Liang and Dr. Zhengdong Cheng for their invaluable advice for my research.

Special thanks to Dr. Donghyun Shin at UT Arlington who shared me with his experience on nano-synthesis and characterization, to Dr. Tom Stephens at MIC and Dr. Yordanos Bisrat at MCF for their support and help on SEM imaging, to Mr. Joohyun Seo at UT Arlington for the collaboration on the research project, to Mr. Navin Kumar, Mr. Aditya Kuchibhotla, Mr. Nicholas Niedbalski, Mr. Farzam Mortazavi and Mr. Harsh Tamakuwala for all the discussion and assistance. I would also like to extend my gratitude to Mr. Ryan Von Ness and Ms. Ronita Roy for your support and encouragement.

I would like to thank Alstom and General Electric (GE) for sponsoring the research tasks for my Ph.D. thesis.

Thanks also go to my friends and colleagues and the department faculty and staff for making my time at Texas A&M University a wonderful experience. Finally, thanks to my mother and father for their encouragement and to Yan (Vivien) Zhou for her patience and love.

CONTRIBUTORS AND FUNDING SOURCES

Contributors

Part 1, faculty committee recognition

This work was supervised by a dissertation committee consisting of Professor Debjyoti Banerjee (advisor), Professor Partha Mukherjee, Professor Hong Liang of the Department of Mechanical Engineering and Professor Zhengdong Cheng of the Department of Chemical Engineering.

Part 2, student/collaborator contributions

The corrosion experiment and data analyzed for Chapter 6 was conducted by Mr. Harsh Tamakuwala of the Department of Mechanical Engineering. The MDSC experiment and data depicted in Chapter 2 was provided by Professor Donghyun Shin from University of Texas Arlington.

All other work conducted for the dissertation was completed by the student independently.

Funding Sources

This work was made possible in part by the sponsorship from Alstom and General Electric (GE). Its contents are solely the responsibility of the authors and do not necessarily represent the official views of the industrial sponsors.

TABLE OF CONTENTS

Page

LIST OF FIGURES

Page

LIST OF TABLES

1. INTRODUCTION

1.1 From Renewable Energy to Solar Power

1.1.1 Global Energy Scenario

Human population is increasing rapidly worldwide with concomitant expansion in water, food and energy consumption. Hence, energy harvesting, especially for electricity generation, has become a crucial concern for supporting modern society while attempting to reduce their environmental footprint (e.g., by leveraging sustainable resources, development of cost-effective water desalination/ purification technologies, sustainable agricultural practices, etc.). The bulk of electrical power production currently relies on non-renewable sources such as fossil fuels (e.g., coal and natural gas) which in turn necessitate effective management of their environmental footprint (e.g., carbon capture/ sequestration, pollution mitigation, etc.). The development of cost-effective sustainable energy technologies provides a holistic approach to mitigating these issues by reducing the emissions of pollutants, carbon dioxide and other greenhouse gases. According to the World Energy Statistics from International Energy Agency (IEA) [1], more than 80% of contemporary energy supply comes from fossil fuels (coal, oil and natural gas) which is responsible for 99.4% of the total CO_2 emission. Figure 1 shows the total amount CO_2 emission from various sources within the last 40 years. It is worth noticing that the increasing contribution of the energy production (primarily from fossil fuels) has led to the total amount of CO_2 emission. Consensus among majority of meteorological experts allude to the definitive correlation between increase in average temperature of the earth in

the last century (i.e., global warming) with enhanced emission of CO_2 from anthropomorphic sources during the same geologic time period.

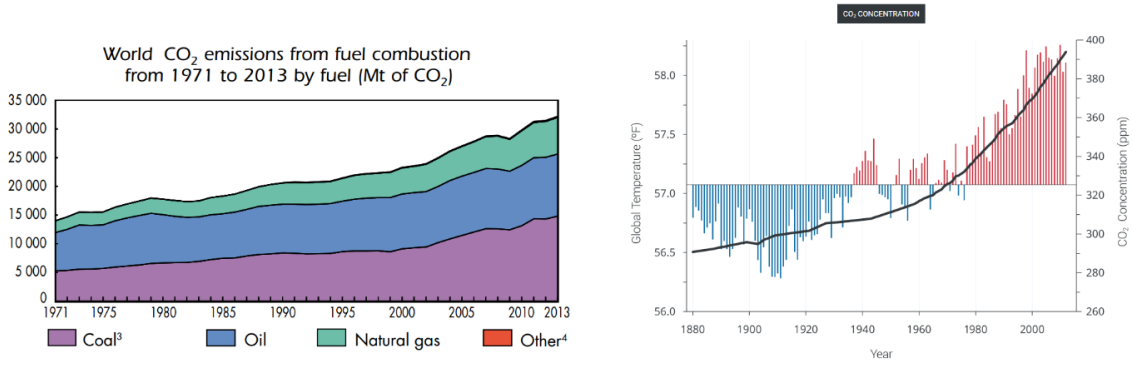

Figure 1. Global CO_2 emission and temperature change in past years [1] [2]

Different technological solutions are available to reduce greenhouse gas emissions. Novel approaches have been proposed in the literature in an effort to limit the long-term effects of global warming and for facilitating the switch from fossil fuels to renewable energy resources. Public policy in China, for example, promoted increasing use of green energy and have led to numerous installations for harvesting renewable energy. Such public policy decisions are estimated to result in the reduction in cumulative emission of CO_2 in China by 1.8% (when compared to the baseline emission estimates prior to the implementation of this public policy) [3].

Volatility in oil prices in contemporary energy markets have highlighted the inherent weaknesses in contemporary national security infrastructure and policies. This has generated awareness that the global security needs should be met by a more balanced

and diversified approach to power production (water-energy-food/WEF nexus), and development of renewable energy resources as well as sustainability practices. A balanced approach is considered to be an effective strategy for mitigating these concerns. Figure 2 shows the variation in the average price of crude oil and natural gas for the past 25 years. Although there was a deep drop for both oil and natural gas prices in 2009 as a result of global economic crisis, it is still evident that there is an overall trend of increase in the prices of oil and natural gas in the longer term. This trend is consistent with the rapid depletion of hydrocarbon fuels. For example, the production of oil was predicted to increase at roughly at 6% rate annually as forecast by several studies in the literature [4] [5]. Hence, to keep up the with the increasing energy demand, a substantial amount of alternative energy resources is needed to feed into the global energy demand.

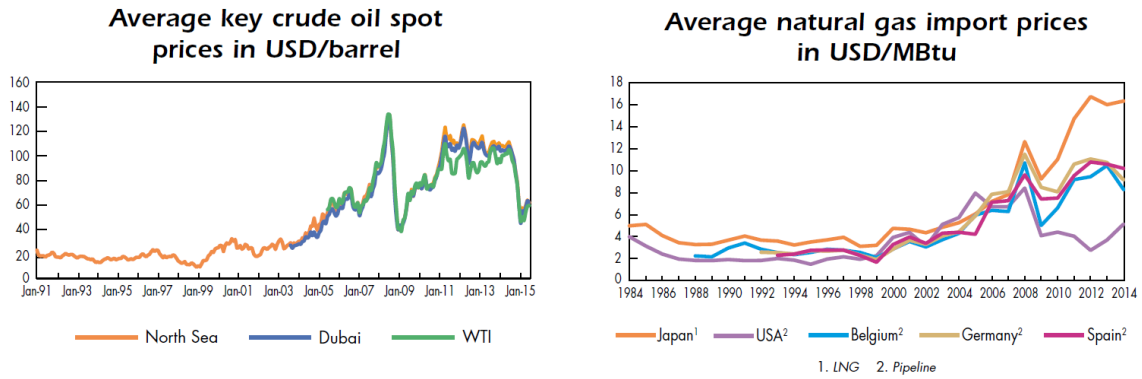

Figure 2. Trends in global average crude oil price [1]

1.1.2 Renewable energy sources overview

Sayigh [6] classified renewable energy sources into eight categories as: photo-voltaic, wind, solar thermal, fuel cell, biomass, hydro, geothermal and oceanic power. The use of wind energy dates back to 3000 years ago when windmills were employed to pump water. In contemporary applications, the key role of wind energy is to drive wind turbines for producing electrical power. The technique of wind power generation is quite mature and has been widely employed in large-scale electricity generation, such as, in wind farms [7]. Although wind power is regarded as environmentally benign, its application is restricted to geographical regions that have adequate wind resources. The noise and visual impact of large wind turbine blades can negatively impact their widespread deployment [8].

Hydropower is another renewable energy source that can be harnessed to generate electricity by leveraging the gravitational potential of falling water (or the inertia of flowing water). It is currently the largest source of renewable power that constitutes 16.3% of world electricity generation [1]. One of the common forms of hydropower generation involves the construction of a dam on a river that is typically fed by a large reservoir of water. Electricity is generated when water is channeled into the rotating blades of turbines. Hydropower does not produce any pollutant, but the need for large land resources (for reservoir catchment) as well as the displacement or destruction of habitats (human, flora and fauna) has significant negative impact on the local ecosystem and is an impediment to the wide scale deployment of this renewable energy platform. Soil erosion / sedimentation, destruction of wildlife habitats and relocation of local residents causes a

series of issues that need to be resolved when assessing and installing hydropower resources [9].

A fuel cell generates electricity from combustible fuels by harnessing their chemical potential by means of electrical charge transfer at the molecular scale. A fuel cell is comprised of a fuel electrode, an oxidant electrode and an electrolyte in between. This is an electrochemical device that converts the chemical energy of a fuel directly into electrical energy. In a typical hydrogen fuel cell, hydrogen reacts electrochemically at the fuel electrode. The ions migrate through the electrolyte towards oxidant electrode while the electrons pass through an external circuit which produces current. Considering that hydrogen is abundantly available and its use as a fuel only produces water as an emission product, fuel cells appear to be a clean and efficient renewable energy source. However, the high cost and low durability issues are an impediment to their commercialization. It is estimated that the cost of fuel cell has to drop by a factor of 10 and the durability has to increase by a factor of five - in order for fuel cells to be competitive with other alternative energy options currently available in the market [10].

Energy is derived from biomass by combustion, pyrolysis, gasification and other approaches for generating heat; which in turn can be used for process heating or generation of electrical power by driving steam turbines. These fuels are obtained either directly or indirectly from varied sources of biomass such as trees, crops, agricultural waste products, etc. Since living plants regenerate cyclically, the sources for biomass products are abundant and renewable. However, some big challenges associated with biomass include their high ash content (which is also associated with significant percentage of alkali metal

halides) as well as issues involving ash deposition, sintering, agglomeration, fouling, and corrosion [11]. The low energy content of the biomass derived fuels and the significant air pollution generated by the combustion of these fuels derived from biomass (with effluents containing CO_2, CO, NO_x, CH_4, volatile organic compounds and other particulates) are significant impediments to their largescale deployment and are often restricted to geographical regions in the vicinity of biomass production (as the transportation of biomass derived fuels is an expensive proposition owing to their low calorific values) [12].

Geothermal energy harnesses the heat from the deeper parts of the earth's crust. Geothermal sources are utilized for generation of steam for process heating and generating electrical power. The total amount of available geothermal energy available globally is estimated to be about 42×10^6 EJ with an average heat flow on the surface is estimated to be about 65 MW/m^2 globally [13]. Such a large source of energy is deemed to be adequate to supply the total global energy demand. However, only fraction of the available thermal power has been utilized due to technical limitations. Geothermal energy can only be exploited in areas where the thermal reservoirs exist at a depth less than 3 km and the temperature gradient is in excess of 25-30°C/km [14]. The need for such geological features severely restricts the large-scale use of geothermal energy sources and are therefore located in only a few regions in the world. However, geothermal energy has significant potential for deployment and scale-up in the future.

Among all sources of renewable energy, solar energy is considered to be the most promising and suitable alternative for supplementing current energy consumption profiles. Solar energy is an attractive option due to potential for almost zero pollution, cheap cost

of deployment and operation [15]. The theoretical limit for solar power on the surface of the earth is 89,300 TW [16] which suggests that there is more energy received by earth in one and a half hour than the world energy consumption in a year, say in 2013 (i.e.,108,170 TWh equivalent) [1]. With global energy demand progressively increasing at around 5% each year[1], solar energy may be the only long-term option which can satisfy the huge energy demand for supporting the progress of modern society.

1.1.3 Solar energy and Concentrated Solar Power (CSP) plants

There are several different techniques for harnessing solar energy as shown in Figure 3 [17]. Each of them is based on different scientific principal with its own advantage and drawback.

Among all available options, photovoltaic (PV) solar panels and concentrated solar power (CSP) are currently the most widely used as well as successfully deployed commercialized technologies for converting sunlight into electricity. PV panels use semiconductor materials to convert sunlight directly into electricity. The electrons in the semiconductor materials are excited to higher energy state upon exposure to frequencies higher than a critical value in the insolation (solar radiation). These excited electrons are then harnessed to generate electricity. The advantage of solar PV panels is that they afford

[1] Enerdata Global Energy Intelligence, *World Energy Use in 2010: Over 5% Growth*, May, 2011. Accessible at http://www.enerdata.net/enerdatauk/press-and-publication/publications/g-20-2010-strongly-energy-demand-increase.php

fast response, are compact and portable while providing ease of deployment, operation and maintenance.

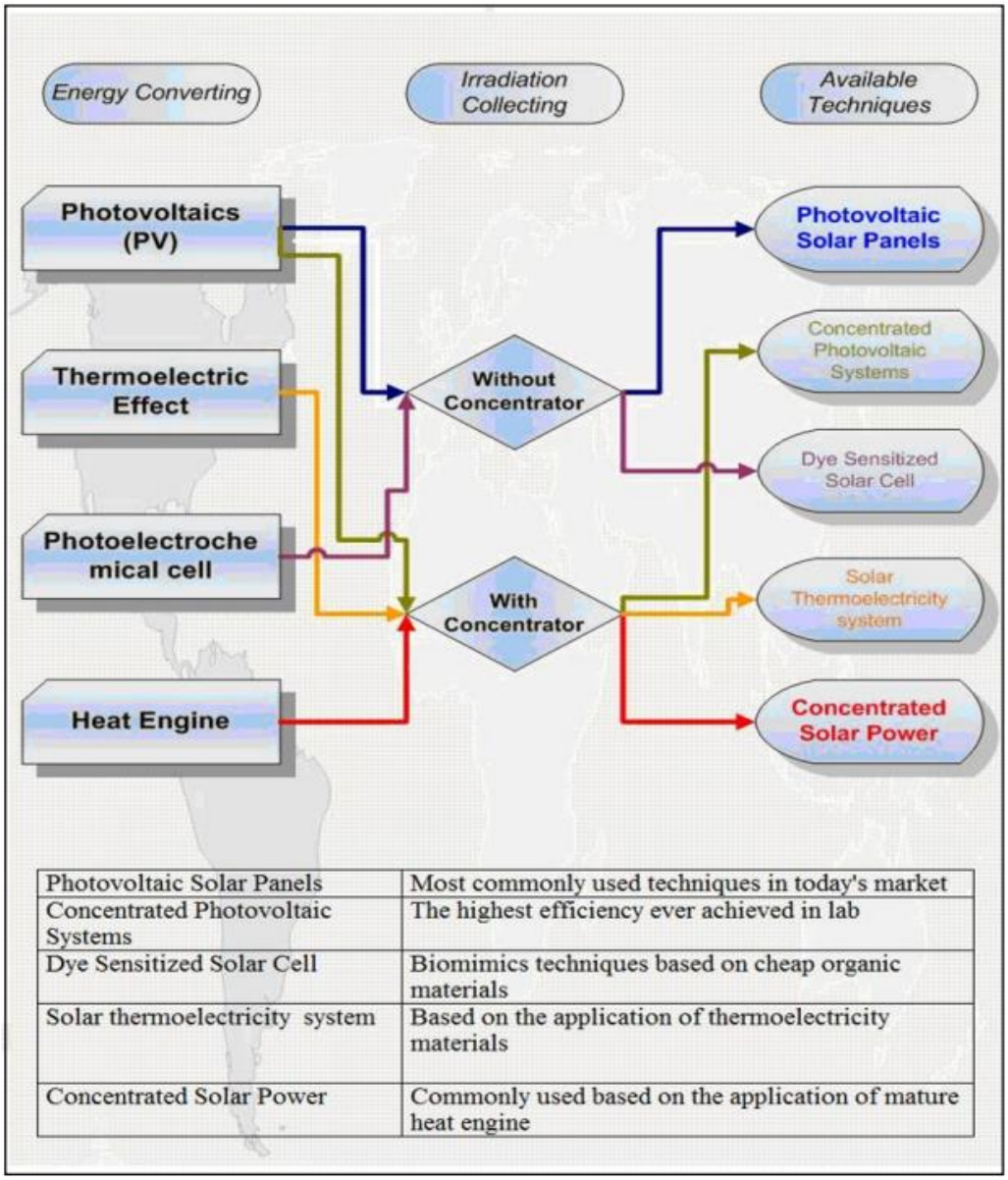

Photovoltaic Solar Panels	Most commonly used techniques in today's market
Concentrated Photovoltaic Systems	The highest efficiency ever achieved in lab
Dye Sensitized Solar Cell	Biomimics techniques based on cheap organic materials
Solar thermoelectricity system	Based on the application of thermoelectricity materials
Concentrated Solar Power	Commonly used based on the application of mature heat engine

Figure 3. Overview of different solar techniques [17]

PV panels can take advantage of either direct or indirect insolation which makes them applicable to a broad range of geographical regions. However, they usually have

very low energy conversion efficiencies (14% ~ 25%) due to their inherent physical limitations [18]. The inefficiencies and challenges / complexities associated with conversion from DC to AC when dispatching PV electricity to the grid system and the need for expensive electrical-storage (for ensuring reliability of this fluctuating power source as well as balancing fluctuating demand/ loads) are the two other major impediments for the large-scale deployment and installation of PV.

In CSP (solar thermal power plants), the thermal component of the solar spectrum is harnessed by concentrating the sun light by using an array of mirrors to focus the incident solar radiation into a narrow region (which raises the temperature significantly). Heat Transfer Fluids (HTF) are pumped for forced convection heat transfer of the thermal energy harnessed at a higher temperature from the incident solar radiation. The harvested thermal energy at elevated levels of thermodynamic quality (exergy) is then used as a heat source to produce electricity using the traditional heat engine (e.g., Rankine cycle) as well as esoteric thermodynamic cycles (e.g., supercritical Rankine, Brayton or Stirling cycles). Power cycles employed in CSP typically yield much higher levels of thermal efficiency (30% or higher) compared to that of PV. This is enabled by the high temperatures achieved in CSP power plants (ranging from 200 °C ~ 600 °C and envisioned to reach 1000 °C in a decade). In contemporary utility markets, the global deployment of CSP has grown rapidly to reach a total installed capacitance of 4.5GW (as shown in Figure 4). In the US, new CSP plants with a production capacity in excess of 200 MW have been established in different geographical regions in past three years (Figure 5).

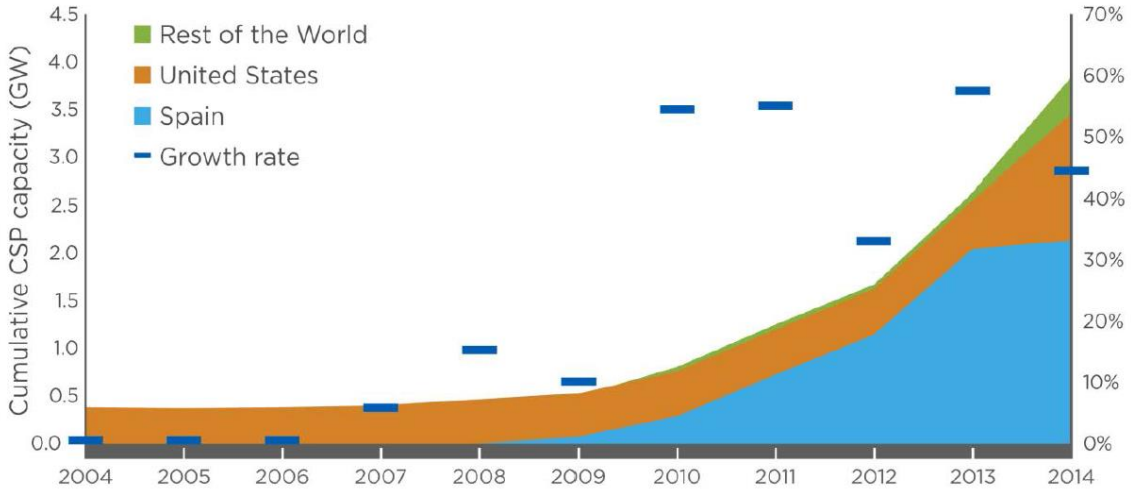

Figure 4. Global cumulative growth of CSP[2]

Project	Solana	Ivanpah	Genesis	Crescent Dunes	Mojave
Utility	APS	SCE + PG&E	PG&E	NVE	PG&E
State	Arizona	California	California	Nevada	California
Size	280 MW	392 MW	250 MW	110 MW	280 MW
Technology	Trough/Storage	Tower	Trough	Tower/Storage	Trough
COD	October 2013	February 2014	March 2014	March 2015	Late 2014
DOE Loan	$1.45 B	$1.63 B	$0.85 B	$.74 B	$1.2 B
Company	Abengoa	BrightSource	NextEra	SolarReserve	Abengoa

Total New CSP in US: 1,312 MW

Figure 5. Newly built CSP in US in past few years[3]

[2] Mark Mehos, Craig Turchi, Jennie Jorgenson, Paul Denholm, Clifford Ho, and Kenneth Armijo, "On the Path to SunShot: Advancing Concentrating Solar Power Technology, Performance, and Dispatchability", NREL & Sandia Natioanl Lab, from SunShot program.

[3] Ranga Pitchumani, "SunShot Concentrating Solar Power Program", Department of Energy, US

One particular advantage of CSP over PV panels is the possibility of integrating cheap thermal energy storage (TES) into the electricity generation system. The hybridization of these CSP plants with fossil-fuel (e.g., natural gas fired gas turbines) power plants is also an attractive commercial option as a source of cheap power with lower environmental footprint than conventional power generation approaches. The performance of solar power platforms is strongly sensitive to the local climate condition. Usually there is a significant difference in time between the peak in solar power generation and the peak in demand for electricity [19]. Hence, cheap thermal energy storage (TES) has become an important and indispensable part of CSP plants. TES platforms are used to store excess solar energy at any instant for subsequent electricity generation during peak energy demand. Figure 6 shows that insertion of a TES platform enables the extension of the operating time of solar power plants and thus delivers adequate power during the periods of peak demand for electricity (thus enhancing the reliability and improving the cost-effectiveness of power generation). The usage of the thermal energy storage (TES) systems enables the power plants to be operated during night time (after sunset) or during periods of disruption in solar energy input (e.g., during cloudy conditions). Hence cheap TES confers a competitive advantage of CSP over PV in commercial and utility scale power generation since electric energy storage is prohibitively expensive (especially compared to TES).

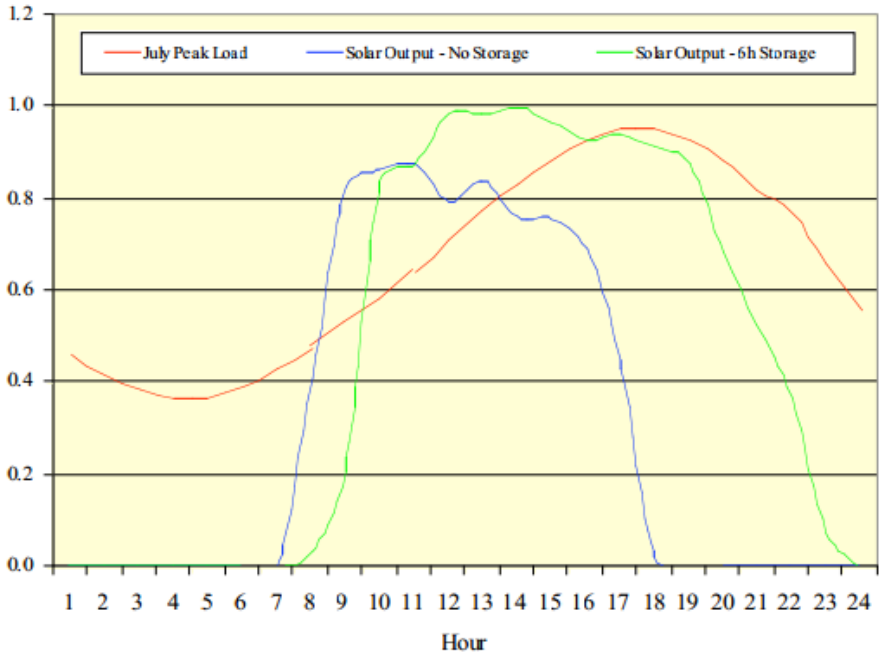

Figure 6. Solar power out vs. Electricity load of one day in July in California

1.2 Thermal Energy Storage (TES) Material

Numerous studies are available in the literature on commercially viable options for thermal energy storage systems. Some of these studies are concerned with augmenting the architecture and structure of thermal storage systems [20], while others are concerned with developing new mediums that store thermal energy either in the form of latent heat (phase changing materials/ "PCM") or in the form of sensible heat (thermal oil, ionic liquids and molten salts) [21]. Phase change materials (PCM) can store a much larger amount of heat per unit volume since the phase-transition enthalpy change of PCMs are substantially larger (100~1000 times) than that of the sensible heat for the same quantity of materials used. However, PCMs suffer from the drawbacks of low thermal conductivity (0.2~0.5 for

paraffin and inorganic salts) and thus enhanced heat transfer techniques are required to improve the power rating of these platforms [22]. Also, PCMs themselves usually cannot be used as heat transfer fluid (HTF) directly which means additional heat exchangers are required in the power cycles. This in turn reduces the overall system efficiency. From a more practical point of view, PCMs are generally more expensive (ranging from 4.28 US$/kg to 334.00 US$/kg) than the sensible heat storage media (ranging from 0.05 US$/kg to 5.00 US$/kg) [23]. Also, introducing PCMs as HTF confounds the risk of the HTF in the piping systems as they have a propensity for freezing at night time and clogging the flow conduits. As a consequence, additional complications arise in the efforts to melt the HTF in the daytime in order to resume the power cycle and have the CSP plant operational again. These factors make PCM unfavorable for industrial CSP application.

Among the commonly-used sensible heat storage materials, oils have a relatively low density, low heat capacity and lower limits for the maximum operating temperature (typically ~ 300 °C) which makes the cost of power generation to be quite expensive due to lower thermal efficiencies arising from lower operating temperatures [21]. Ionic liquids have good thermo-physical properties but can be highly unstable (chemical reactivity and corrosive to the containers) which also adds up to the overall cost – since they require extra safety measures [24]. Molten salts, have higher density, lower vapor pressure, higher operating temperature, lower chemical reactivity and moderate cost (compared to oils and ionic liquids). Hence molten salts have been explored for TES applications, especially for higher operating temperatures [25]. Pure salts suffer from the disadvantage of high melting point. However, a homogenous mixture of different salts, known as salt eutectic, can

decrease melting point significantly and further increases the range of working temperature. Hence, molten salt eutectics are considered to be an attractive option for reducing the cost of electricity generation.

1.2.1 Molten salt eutectic

A eutectic system is a homogeneous mixture of more than one species in which a joint super-lattice is formed between different components. This results in a system with a single melting point. This is also known as eutectic temperature and is the lowest possible melting temperature over all of the mixtures with different ratios. That is to say, the melting of a mixture of any atomic ratio will always start at the eutectic point with the eutectic ratio. A binary eutectic is made up from two compounds and has only one eutectic point with one specific eutectic ratio. The phase diagram below demonstrates the melting process of a non-eutectic binary mixture system [26]. Molten salt eutectic can be comprised of more than two compounds. These eutectics usually have more than one eutectic point and eutectic ratio. This means that all components of such eutectic could melt or freeze together at two or more different temperatures with different compositions (i.e., molar ratios).

A significant number of studies have explored the thermo-physical properties of molten salt mixtures. Most of these studies have concentrated on three major groups of salt eutectics: nitrate/nitrite salt, carbonate salt and chloride/fluoride salts, and their mixtures. By varying the composition of the salt mixtures, different melting points and material properties can be obtained. Table 1 provides a comparison of the lowest melting

point of several common salt eutectics with different cations and anions (all units in degree Celsius) [27] [28]. For selecting appropriate composition of molten salts in a chosen commercial application (such as in CSP plants), the design considerations typically require low melting point, commercial suppliers of the salts in large quantities at low cost and safety (minimal environmental and occupational hazards as well as low environmental footprint) [29]. For salts with high melting points, precautionary measures are needed to prevent the salts from freezing in the piping system (as this is a catastrophic failure condition for the CSP plants).

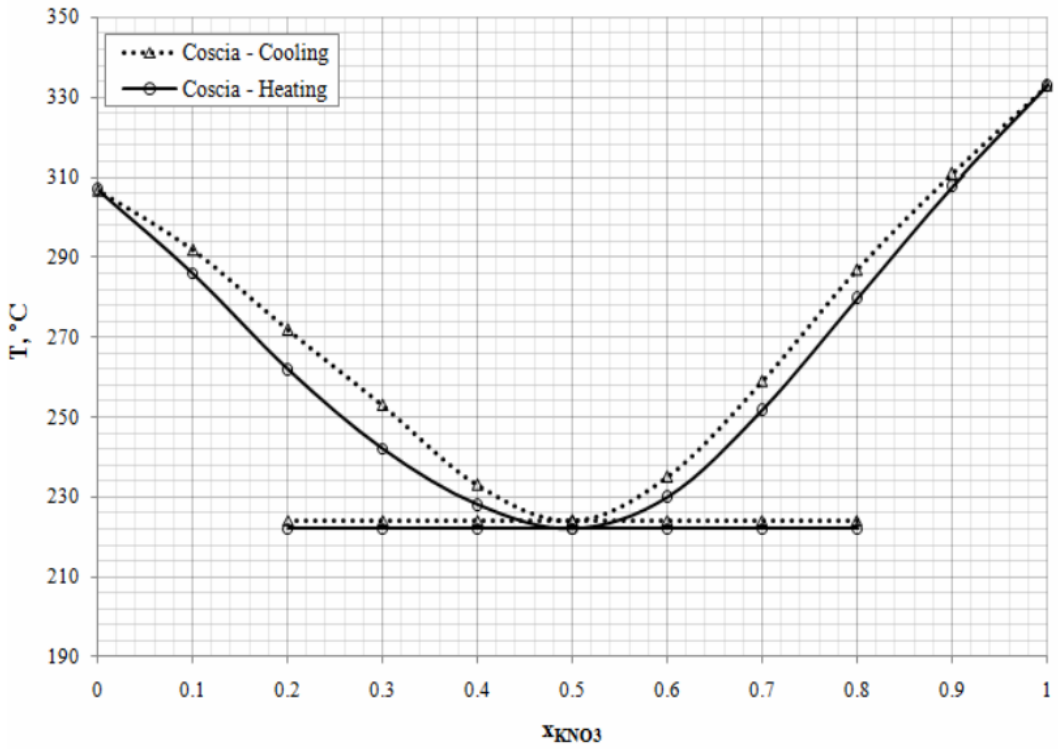

Figure 7. Phase diagram of binary eutectic system (example of $NaNO_3$-KNO_3 system) [30]

Table 1. Melting points for different salt systems (all units in degree Celsius) [27] [28]

Single salt

	NO_3	NO_2	CO_3	Cl	F
Na	307	282	858	800	995
K	337	440	898	770	856
Li	253	220	723	610	848
Ca	561	398	825	775	1418
Mg	325	350	990	714	1263

Multi-component eutectic

	NO_3	NO_2	CO_3	Cl	F
Na-K	220	228	710	685	710
Na-Li	192	150	496	557	649
Li-K	133	98	488	355	492
Na-K-Li	120		397	348	454
Na-K-Ca	133				

It is evident that nitrate/nitrite salts generally have a much lower melting point than the other groups. Hence, nitrate mixtures have gained popularity for solar energy applications [31]. Currently the $NaNO_3$-KNO_3 binary mixture (which is also known as solar salt) has been most widely used as the TES and HTF medium in commercial solar power plants since sodium nitrate and potassium nitrate are two of the cheapest salt materials compared to the other nitrate/nitrite salts. However, with the goal of attaining even lower melting points for offsetting operating risks of power plants, innovative nitrate/nitrite salt systems have also been proposed as TES material candidates. Reddy [32] summarized these low-melting salt eutectic systems as shown in Table 2. These salt systems generally have a melting point less than 120ºC and typically involve ternary or quaternary salt eutectic compositions.

Table 2. Low-melting point nitrate/nitrite salt eutectic candidates

Nitrate/nitrite molten salt eutectic system	**Melting Point [°C]**	**Density (ρ) [g/cm^3]**	**Specific Heat Capacity (C_p) [J/(g·K)]**	**Energy Density [MJ/m^3·K]**
$LiNO_3$-$LiNO_2$-$NaNO_3$-KNO_3-KNO_2	70.7	1.68	1.58	1141
$LiNO_3$-$NaNO_3$-KNO_3-$LiNO_2$	77	1.68	1.61	1146
$LiNO_2$-$NaNO_3$-KNO_3-KNO_2	79	1.69	1.50	1073
$LiNO_2$-$LiNO_3$-KNO_2-KNO_3	90.7	1.67	1.57	1070
$LiNO_2$-$NaNO_3$-KNO_3	92.7	1.68	1.57	1075
$LiNO_3$-$NaNO_2$-$NaNO_3$-KNO_2-KNO_3	95.7	1.78	1.54	1110
$LiNO_2$-$LiNO_3$ -KNO_3	98.4	1.67	1.61	1076
$LiNO_3$-$NaNO_3$-$NaNO_2$-KNO_3	99	1.78	1.56	1114
$LiNO_3$-$NaNO_3$-KNO_3-$AgNO_3$	107	2.79	1.08	1192
$LiNO_2$-$LiNO_3$-$NaNO_3$	108.4	1.66	1.73	1125
$LiNO_3$-$NaNO_3$-KNO_3	117	1.72	2.32	1524
$LiNO_3$-$NaNO_3$-KNO_3-$Ca(NO_3)_2$	109	1.73	1.58	1055
$LiNO_3$-$NaNO_3$-KNO_3-$Mg(NO_3)_2$	111.6	1.73	1.61	1081
KNO_3-$NaNO_3$-$NaNO_2$	123	1.84	1.46	1080

1.2.2 Thermal stability

Ideally, the desirable medium for thermal energy storage should provide the capability to sustain high temperature in the storage tank without any chemical degradation or decomposition. The fundamental reaction for the thermal decomposition in nitrate salts have been studied thoroughly by researchers [33, 34, 35] as:

$$NO_3^- \leftrightarrow NO_2^- + 1/2O_2 \quad (1)$$

The forward reaction is an endothermic process limited by the partial pressure of oxygen in the system. However, since the oxygen gas typically escapes from the molten salt into the environment, the reaction is irreversible at elevated temperatures. Further decomposition of the nitrite ions can be of the following forms:

$$2NO_2^- = O_2^- + 3/2O_2 + N_2 \quad (2)$$

$$2NO_2^- = O_2^- + NO_2 + NO \quad (3)$$

Thus, the use of nitrate salt for heat transfer and thermal storage medium at high temperature will be limited by the decomposition reaction (1) ~ (3). The decomposition temperature has been defined conventionally as the temperature at which oxygen gas or nitrous oxide are detected to be emitted from the salt samples [33, 34]. Depending on the type of metal cation, the nitrate salts possess different decomposition temperatures as listed below [36]:

Metal nitrate	$NaNO_3$	KNO_3	$Ba(NO_3)_2$	$Ca(NO_3)_2$	$Mg(NO_3)_2$	$Fe(NO_3)_3$
Decomposition temperature (K)	1013	1113	960	875	723	440

Such variations in decomposition temperatures is ascribed to the polarization effect induced by the higher charge density of the cations on the nitrate anions [36]. As shown in the image below, when the positive metal ion is close to the nitrate ion, it attracts the electrons in the nitrate ion towards itself during which the nitrate ion becomes polarized. As a consequence, less energy is needed to break the N-O bond which in turn lowers the decomposition temperature.

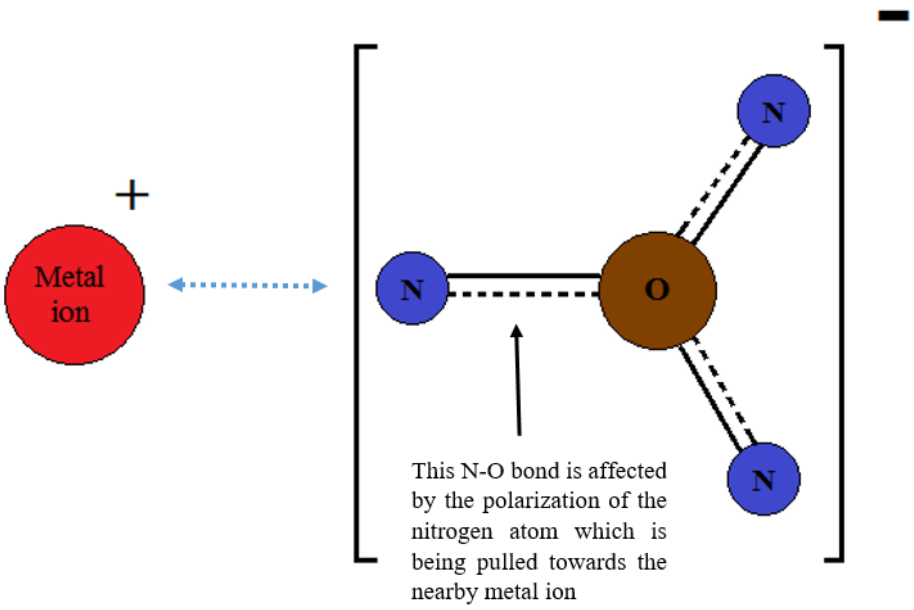

Figure 8. Intermolecular interaction in metal nitrate

For salt eutectics in which multiple metal nitrates are mixed, the decomposition temperature could vary significantly from the decomposition temperature of its individual components. Most multi-component nitrate molten salts have demonstrated chemical stability up to 500°C [31]. Higher operating temperatures are desired to enhance the thermal efficiency in the power generation cycles.

1.2.3 Corrosivity

When high temperature molten salts come in contact with the containment materials, corrosion of the metal is accelerated. In actual CSP plants, the corrosion involves both the dissolution and oxidation reaction of metal alloy in piping and tank which would trigger severe fouling and plugging issues in the system. The dissolution would result in excessive mass loss over time, but only few metals were found to be appreciably soluble in molten salt of their kind [37]. The corrosion process involves both the reduction and oxidation reactions, as listed below:

$$NO_3^- + 2e^- = NO_2^- + O^{2-} \quad (4)$$

$$Fe + O^{2-} = FeO + 2e^- \quad (5)$$

$$3FeO + O^{2-} = Fe_3O_4 + 2e^- \quad (6)$$

At elevated temperatures (e.g., above 600ºC), the decomposition of nitrate and nitrite ions yield significant concentration of oxide ions in the liquid salt which aggravate the rate of corrosion. At lower temperatures however, molten nitrates were shown to display behavior similar to weak bases due to absorption of moisture [38]. . Such effects, arising from the environmental conditions, promotes additional pathways for reaction with

the metals - which in turn increases the corrosive nature of these molten salts, as shown below:

$$H_2O + NO_3^- + 2e^- = NO_2^- + 2OH^- \quad (7)$$

Certain metal oxides could form a protective passivation layers which effectively isolates the metal from contacting the molten salt, thus decreasing the degree of corrosivity of the molten salt. However, some metal elements (particularly chromium, molybdenum and manganese) can produce soluble anions which makes them susceptible for easy removal from their oxide layers [39]. The corrosion of metals in molten salts is also modulated by nature of the imposed duty cycles (e.g., thermal cycling protocols) and the presence of impurities. Thermal cycling tends to exacerbate corrosion as the thermal expansion coefficient varies between the crust formed on the surface and the interior of the metal alloys (which in turn induces mechanical stresses that accelerate the rates of corrosion). Low grade nitrate salts usually contain impurities at significant concentration levels (such as NaCl, Na_2SO_4, $KClO_4$, etc.). The presence of such impurities could drastically accelerate the corrosion in high temperature oxidizing environments [40, 41, 42]. In general, corrosion has a direct bearing on component life cycle and it is necessary to quantify the corrosion caused by the molten salt samples before utilizing them for TES.

1.3 Nanofluid

Nanofluids are stable colloidal suspensions of nanoparticles (1~100 nm) in solvents. Since nanoparticles have a very large surface-area-to-volume ratio, the surface charges of the nanoparticles enable them to be dispersed in the liquid with relatively good

stability. Also, their unique surface properties have been proven to bring significant changes to various thermo-physical properties of the base fluid. It should be noted that although a large number of peer reviewed journal publications on nanofluids have been published, researchers have not reached a consensus on the characteristics of nanofluids (for both testing procedure and results). A fundamental physical explanation of the mechanism behind the anomalous change of thermophysical properties is also lacking. Nevertheless, majority of the studies have generated a consensus that well-dispersed nanoparticles can cause significant enhancement of the thermal conductivity of the base fluid (at the expense of enhanced viscosity). The effect of nanoparticle morphology (size, shape, material, concentration, synthesis protocol, etc.) on the specific heat capacity of the nanofluids has been shown to also depend on the properties of the solvent phase (base fluid). Significant degradation in the specific heat capacity values of nanofluids was observed for aqueous solvents while radical enhancement was observed for non-aqueous solvents [43]. This conundrum will be discussed in the following subsections.

1.3.1 Nanofluid synthesis

Nanofluids are typically synthesized by either two-step method or one-step method. The two-step method, as the name suggests, consists of two separate processes for synthesizing nanoparticles (or commercially procured) and dispersing the procured nanoparticles into base fluid. Such methods are being extensively used in nanofluid research due to their inherent simplicity. Proper choice of synthesis protocol can enable better stability as well as control over precision and size of nanoparticles in the suspension.

Nanomaterials used in this method are usually procured commercially, typically in the form of dry powders. With advances in synthesis techniques for nanoparticles, large-scale production of nanoparticles with good precision in size and shape have been achieved by commercial vendors (e.g., using combustion synthesis techniques). The techniques used for making nanoparticles include: mechanical methods (milling, grinding, etc.), physical methods (physical vapor deposition, inert gas condensation, etc.) and chemical synthesis (sol-gel process, solution combustion, electrolysis, combustion synthesis, etc.). Depending on the requirements of the chosen applications, different synthesis protocols can be selected to deliver the specification for nanomaterials with the desired constraints for size and shape. This review will be limited to discussion of dispersion protocols rather than the synthesis of nanoparticles in the form of dry powders. Excellent reviews are available in the literature on the topic of nanoparticle synthesis (e.g., by C. N. R. Rao [44]). These synthesis protocols for nanoparticles in the form of dry powders are categorized into: (a) top-down, and (b) bottom-up techniques. The reader interested in this topic can consult this reference (and similar reviews available in the literature).

For a majority of nanofluid samples synthesized via two-step method, nanoparticles were procured from commercial suppliers. The synthesis protocol is rather straight forward: the nanoparticles are first dispersed in the base fluid and then stabilized by different approaches. However, depending on the material of the nanoparticle and base fluid, the dispersion process could be either “spontaneous” or “non-spontaneous”. In the former case, the nanoparticles would readily spread out in the base fluid and remain in stable suspension state, while in the latter case, the nanoparticles tend to stay together

unless external forces are applied. Such variation give rise to the difference on the nanofluid preparation procedure. If the mixture is inherently unstable, additional stabilization approaches are typically implemented for enhancing the dispersion of the nanoparticles in the neat solvent (base fluid).

The one-step method relies on generation of nanoparticles in-situ in the solvent phase from precursors. In other words, the synthesis and dispersion of nanoparticles happen simultaneously in the solvent phase. As a result, the propensity for agglomeration of the nanoparticles (generated in-situ) is minimized. The one-step method can be implemented by either a physical technique (e.g., direct evaporation and condensation) or chemical technique (e.g., chemical decomposition). However, it is more difficult to control the morphology of the particles precisely as small variations in the designed synthesis conditions (temperature, time, feeding rate, etc.) can drastically alter the properties of the synthesized nanofluids due to variation in nanoparticle size distribution and stability. Thus, it is very important to understand, model and optimize the synthesis conditions to enable better control over the transport mechanisms (e.g., homogeneous or heterogeneous nucleation of the nanoparticles from the precursors as well as growth and subsequent agglomeration of the nanoparticles generated in-situ). It should be noted that if the generation of nanoparticle is a distinctly separate process from the dispersion step, such methods are categorized as a two-step process.

1.3.2 Thermal conductivity

The first scientific study on nanofluid thermal conductivity was reported in 1993 when a group of Japanese scientists from Tohoku University experimentally studied the possibility of increasing the thermal conductivity of a liquid by dispersing a small amount of ultra–fine particles. They found that by mixing 4% by volume of Al_2O_3 nanoparticles in water, the thermal conductivity was enhanced by 30% and the measured enhancement increases with increasing particle volume concentration [45]. Later in 1995, Choi and Eastman from Argonne National Lab studied the thermal characteristics of aqueous suspensions of copper nanoparticles and termed these class of colloids as "nanofluids". The authors reported that the addition of minute quantities of Cu or CuO nanoparticles could yield 60% enhancement in thermal conductivity of deionized water [46]. Since then, numerous studies were performed and reported - focusing on the anomalous enhancement of thermal conductivity for different categories of nanofluids. It was found that particle size, concentration, and material could have significant impact on the thermal conductivity of nanofluids. However, the effect of synthesis conditions on the resulting properties of nanofluids have been ignored in a significant number of these studies.

The effect of nanoparticle concentration has been studied by various research groups. Xuan studied the properties of the aqueous suspensions of copper nanoparticles in which the thermal conductivity ratio increases from 1.1 to 1.6 as the concentration of nanoparticles are increased from 1% to 5% [47]. Xie reported that the thermal conductivity enhancement of alumina-EG (ethylene glycol) nanofluid increased from 5% to 30% as the alumina volume fraction was increased from 1.8% to 5% [48]. A number of other studies

explored the dispersion of MWCNT (multi-walled carbon nanotubes) in solvents and reported that the thermal conductivity of nanofluid samples increased significantly with increasing MWCNT volume fraction [49, 50, 51, 52, 53, 54]. Regarding the effect of particle size, an increase in thermal conductivity with increasing nanoparticle size was reported for Al_2O_3-EG [55], gold-water [56] and Fe_3O_4-kerosene [57] nanofluids while opposite trends were reported for TiO2-water [58], Al_2O_3-water [59] and ZnO-water/EG [60] nanofluids. With these contradictory observations no clear consensus has emerged regarding the effect of nanoparticle size. The effect of nanoparticle material on thermal conductivity is also unclear since experiments involving different nanoparticle compositions were performed by different research groups for different experimental conditions with the results reported to show a wide variability. The study by Masuda [45] which compared the properties of Al_2O_3/SiO_2/TiO_2-water mixtures suggests that different nanoparticle materials cause significantly different levels of thermal conductivity enhancements. On the contrary, the study by Kim [60] showed that Al_2O_3/ZnO/TiO_2 – water/EG mixtures shared similar degree of thermal conductivity enhancement regardless of the nanoparticle material.

Part of the reason for such large discrepancies in the literature for the thermal conductivity values of nanofluids potentially arises from the different techniques used for measurement. Thermal conductivity measurement techniques can be categorized as either transient techniques or steady state techniques. One typical example of the transient technique is the transient how wire method [61]. Such method uses a long thin platinum wire as both heat source and temperature sensor. The hot wire is immersed in the center

of a cylindrical vessel with test liquid inside and the temperature change of the hot wire is recorded once a constant heating power is supplied. The thermal conductivity of the liquid is then obtained by solving the transient radial conduction equation using Fourier's law.

$$T(t) - T_{cell} = \Delta T = \frac{q}{4\pi k} \ln\left(\frac{4\alpha}{r^2 C} t\right) \tag{8}$$

where, $\boldsymbol{q}$ is the applied power, $\boldsymbol{k}$ is the thermal conductivity of the liquid, $\boldsymbol{\alpha}$ is the thermal diffusivity of the liquid, $\boldsymbol{r}$ is the radius of the hot wire and $\boldsymbol{\ln(C)}$ is Euler's constant. Such method is favored by many researchers for the low-cost and the ease of implementation. However, one disadvantage of this method is that the nanoparticles tend to precipitate and cause fouling on the hot wire due to the induced polarity within the particles if the heating wire is not insulated properly [62]. Such precipitation of nanoparticles on the hot wire surfaces results in scatter in the measurement data for nanofluid thermal conductivity and therefore is an unreliable technique when used for nanofluids samples.

In a typical steady state measurement method, the test samples are heated in one direction (i.e., in either a parallel plate configuration or concentric cylindrical cell geometry configuration [63, 64]). Once steady state conditions are reached, the thermal conductivity of the liquid is derived using 1-D conduction equation with heat flux and temperature information obtained from the experiments, as shown below:

Parallel plate:
$$\Delta T = \frac{qx}{kA} \tag{9}$$

Concentric cylinder:
$$\Delta T = \frac{q}{2\pi L k} \ln\left(\frac{r_2}{r_1}\right) \tag{10}$$

where, q is the applied power, k is the thermal conductivity of the liquid, x is the distance between two parallel plates, r_1 and r_2 are the inner and outer radius of the concentric cylinder, respectively.

This method provides more reliable result for thermal conductivity measurements since the steady state calculation obviates the uncertainty caused by thermal diffusion terms that typically exist in transient testing protocols. However, steady state measurements usually require much longer time for testing than the transient methods. Nevertheless, it is important to notice that in both methods, the heat transfer is assumed to be only through conduction. This requires a relatively small heat input or temperature gradient during actual test in which the natural convection of liquid is negligible. This is only valid for small values of Rayleigh number in the test configurations (i.e., in the absence of free convection within the test samples).

1.3.3 Specific heat capacity

Compared to the large number of studies on nanofluid thermal conductivity, the literature reports involving the specific heat capacity of nanofluids is significantly lower. Consistently for almost all molten salt based nanofluids that have been studied extensively by many researchers - anomalous enhancement in specific heat capacity was observed (as shown in Table 3). Different mechanisms were proposed to explain such drastic enhancements - which includes: higher surface energy of nanoparticles, interaction potentials at the solid-fluid interface and the semi-solid solvent phase formed due to adsorption on the surface of the nanoparticles.

Table 3. Studies in the literature on the specific heat capacity of nanofluids

Author	*Nanofluid*	*Mass fraction of nanoparticle*	*Particle size*	*Enhancement (%)*
Nelson (2009) [65]	Graphite *in* polyalfaolefin	0.6%	20 μm(D) × 100 nm(L)	50%
Shin (2010) [66]	CNT *in* Li_2CO_3-K_2CO_3	0.5%	30 nm(D) × 1.5 μm(L)	18%
Shin(2011) [66]	SiO_2 *in* Li_2CO_3-K_2CO_3	1.0%	30 nm	26%
Chieruzzi(2013) [67]	SiO_2/Al_2O_3/TiO_2 *in* $NaNO_3$-KNO_3	1.0%	7 nm/13 nm/ 20 nm	22.5%
Shin(2014) [68]	Al_2O_3 *in* Li_2CO_3-K_2CO_3	1.0%	10 nm	32%
Andreu-Cabedo (2014) [69]	SiO_2 *in* $NaNO_3$-KNO_3	1.0%	12 nm	25.03%
Schuller(2015) [70]	Al_2O_3 *in* $NaNO_3$-KNO_3	0.78%	40 nm	30.6%

For water-based nanofluids, it was reported that addition of nanoparticles at minute concentrations caused significant decrease in the overall specific heat capacity [71, 72, 73, 74, 75]. Since nanoparticles (being solid) have typically lower specific heat capacity than the solvents, reports involving degradation of specific heat capacity of aqueous nanofluids is in agreement with the conventional mixing rule for calculating properties of mixtures [76]. For non-aqueous nanofluid (e.g., ionic liquids and oils) however, numerous studies have shown that the addition of small amount of nanoparticles can increase the specific heat capacity by significant margins (even though nanoparticles typically possess lower specific heat capacity values than that of the base fluids or solvents [65, 77, 68, 78]).

1.3.4 Flow behavior

The nanofluid thermal properties have all been measured in static configuration and at perceived steady-state conditions. However, the actual heat transfer and flow behavior of nanofluids in a conduit may exhibit different rheological and thermophysical characteristics (compared to predictions obtained using conventional correlations) due to the nonlinear nature of the transport phenomena which can often be counter-intuitive. This is also affected by nanoparticle agglomeration (e.g., due to aggregation and coagulation), precipitation and deposition on conduit walls (i.e., caused by fouling or corrosion or formation of "nano-fins"). He and Jin [79] in 2006 investigated the flow behavior of TiO_2-DIW nanofluid in a vertical pipe and reported that the addition of nanoparticles resulted in more than 40% enhancement in the convective heat transfer while the enhancement in nanofluid thermal conductivity was observed to be less than 10%. Nelson et al. [65] performed flow loop experiment using polyalphaolefin nanofluids (using organic nanoparticles, such as exfoliated graphite nanoparticles) in 2009. Their result showed more than 4 times enhancement in thermal diffusivity while the enhancement in convective heat transfer was only 10%. Yu and Banerjee [80] in 2012 reported results from microchannel flow experiments using SiO_2-DIW (de-ionized water) nanofluids in which they observed anomalous and contradictory behavior for thermal properties of nanofluids (e.g., lower specific heat capacity of aqueous nanofluids) and the enhancement in the convective heat transfer. The authors theorized that the "nanoFin Effect (nFE)" could lead to an anomalous enhancement in forced convective heat flux. The formation of nanofins on the heat exchanging surfaces from precipitated nanoparticles could lead to

enhanced surface area that could in turn modulate the transport phenomena in the nanoscale. Such phenomenon is termed as the “nanoFin Effect (nFE)” [81] [82]. Gupta [83] performed a comprehensive review in 2014 for literature reports on the experimental investigation of forced convective heat transfer involving various nanofluids. The author concluded that most of the experimental studies demonstrated improved heat transfer coefficient for nanofluid which increases with increasing nanoparticle concentration as well as Reynolds number. However, no general correlation or equations have been developed for accurately predicting convective heat transfer coefficient for all classes of nanofluids.

1.4 Objective of this study

The aim of this study is to explore the role of additives for the realization of molten salts nanomaterials (e.g., nanofluids), as well as their effects on the thermophysical properties of the nanofluids. It is expected that these thermophysical properties would also impact the thermal-hydraulic performance of nanofluids in flow systems.

1.5 Hypothesis

A significant number of reports in the literature have demonstrated enhancements in the thermo-physical properties of nanofluid. However, different levels of enhancement have been reported in literature with same nanofluid samples, and the fundamental mechanisms responsible for such variations in enhancement have not been understood thoroughly. In practice, it was observed that the material properties of the nanofluids are

highly sensitive to small variations in the synthesis protocols. The properties of nanofluids can be tuned by varying the size, shape, morphology (surface functionalization), material composition, structure and mass concentration of nanoparticles as well as a variety of techniques for dispersing the chosen nanoparticles in the liquid solvents (which is often overlooked as an important variable in the nanofluids literature). In depth study of nanofluid morphologies have also revealed the potentially dominant role of a "compressed liquid layer" formed by the solvent phase on the surface of the nanoparticles (due to surface adsorption), in contributing to the overall property change.

Therefore, the hypothesis developed in this study is that the material properties of molten salt nanofluid (specifically, the specific heat capacity) is dependent on the synthesis protocol of nanofluid (i.e., particle type, concentration, dispersion method), and in particular dependent on the formation of the induced secondary nanostructure. Such phenomenon is more apparent, since the volume ratio of the compressed phase (secondary structure) can effectively amplify the mass fraction of the nanoparticle, which give rise to larger proportion of the contributions to the resultant material properties of the nanomaterial samples.

1.6 Motivation of the study

Studies involving molten salt nanofluids for thermal energy applications (particularly on the anomalous enhancement of thermophysical properties) are gaining popularity in the literature. However, critical issues and challenges are an impediment to their implementation in CSP. These include synthesis cost, long-term stability and

ambiguities in flow behavior (in realistic situations representative of practical engineering applications). For many of these studies the nanoparticles cost significantly more than the salt itself (which makes it unsuitable for cost-effective deployment in industrial applications). Also, only a few studies have explored the actual heat transfer behavior of the nanomaterials in a flow system. Therefore, novel approaches for synthesizing stable nanofluid with suitable thermophysical properties are desired that can enable simple operation and enhanced thermal-hydraulic performance. Various classes of molten salt nanofluids that address these concerns and challenges are therefore explored in this study.

1.7 Significance of this study

This study has contributed to both the fundamental understanding of transport phenomena at the nano-scale as well as the design and synthesis of novel molten salt nano-materials for solar thermal energy storage applications. The unique contributions enabled by this study are listed, as follows:

- Novel and convenient synthesis approaches for molten salts nanomaterials were explored that can enable rapid scale-up for manufacturing applications.
- Quantitative analysis of thermophysical properties of molten salt nanomaterials was performed (e.g., specific heat capacity, thermal conductivity, viscosity, etc.)
- Materials characterization and analyses of molten salts nanomaterials was performed (e.g., effect of nanoparticle shape, size, distribution, etc.)

- Parametric studies on the effect of operational parameters on the material properties of these nanomaterials were also explored (e.g., synthesis temperature, duration, additive concentration, etc.)

The results from this study are also applicable to related technologies. The significant enhancement in the thermo-physical properties of nanofluids, such as specific heat capacity and thermal conductivity (compared to that of the pure molten salts) can enable their use as materials for thermal energy storage (TES) and as heat transfer fluids (HTF), respectively. Hence, the solar salt nanofluids developed in this study can enable the applications in large-scale industrial plants for generating Concentrated Solar Power (CSP). Alternate applications include TES for load balancing in conventional power generation (coal fired and gas fired power plants), nuclear power generation, geothermal power generation, etc. TES applications of these solar salt nanofluids (and allied molten salt nanofluids) include industrial process heating, desalination, etc. Other conventional and unconventional applications include molten salt batteries (for mart grids and grid-scale power distribution/ electrical energy storage), chemicals processing, metallurgical operations (refining of metals and alloys from ores), synthesis of ceramic micro/ nano-particles, life-sciences/ medical applications, enhanced oil recovery (EOR) from tar-sands as well as in conventional and unconventional oil fields (e.g., hydraulic fracturing for recovery of hydrocarbons trapped in shale rocks), etc. Molten salts with enhanced thermo-physical properties could enable better system efficiencies as well as economies of scale.

1.8 Summary

Experimental and computational studies were performed to explore a variety of innovative synthesis protocol and their effect of the variations in the thermo-physical properties of molten salt nanomaterials. The ultimate goal of the study was to provide a pathway for translating the concepts of one-step synthesis protocols for molten salt nanofluids (e.g., ability for volume scale-up for manufacturing and provide economies of scale) into engineering practical applications – including for thermal energy storage and concentrating solar power (but may be applied in other power generation and energy conversion technologies as well as related applications such as EOR). A variety of parameters were examined in this study.

Chapter 2 provides the detailed information about the experimental procedures used in this study, which includes sample preparation (development of synthesis protocols), materials characterization and evaluation of materials compatibility (corrosion, chemical stability). Chapter 3 provides experimental results for thermophysical property measurements and materials characterization/compatibility. Chapter 4 gives analytical discussion on the enhancement of thermophysical properties observed in the experiments. . Chapter 5 provides experimental results for the effect of precursor concentration, material type and stabilizer on the material properties of the molten salt nanomaterial samples. Chapter 6 provides the experimental results for the corrosion and thermal stability of different molten salt nanomaterial samples. Chapter 7 provides the results obtained from computational modeling, and their implication of these numerical predictions for evaluating the thermal-hydraulic performance of molten salt nanofluid samples during

flow in a test section as a part of a flow-loop. Chapter 8 presents the computational approaches and the predicted results for determining particle size distributions in molten salt nanomaterials. This is vital for evaluating and predicting the thermo-physical properties of molten salt nanofluids. Chapter 9 summarizes the results from this study, provides conclusive remarks and identifies a few directions for future studies.

2. EXPERIMENTAL STUDY

The design of the experimental study of the molten salt nanofluids can be categorized in the following chart where different types of molten salt nanofluids were synthesized using several approaches and were evaluated for their efficacy based on their thermophysical properties.

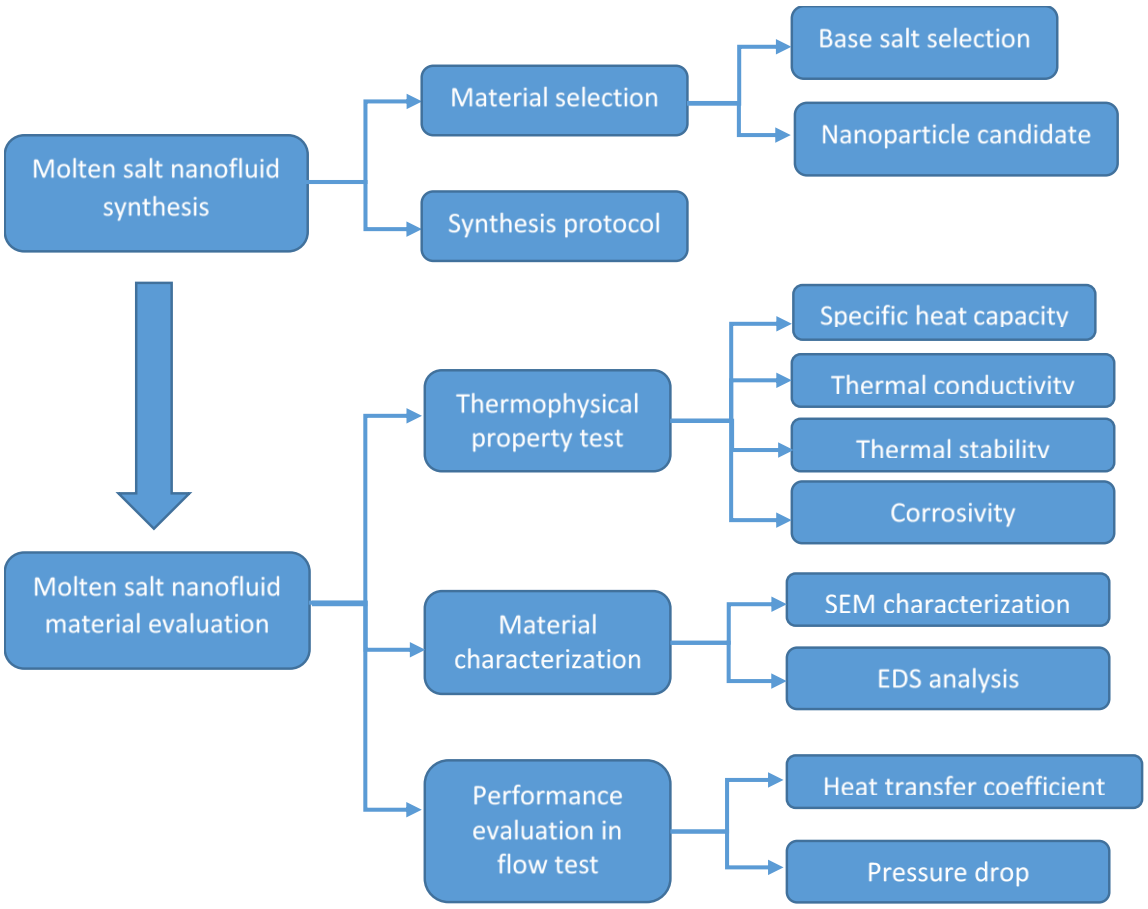

Figure 9. Overview of experimental tasks performed in this study

2.1 Material synthesis

In this study, the pure mixture of $NaNO_3$-KNO_3 binary nitrate salt eutectic (also known as solar salt) was used as the solvent. Molten salt nanofluids were synthesized using both a conventional two-step method and innovative one-step method. The samples were typically synthesized in 50g batches (which is the minimum amount required in the experimental protocols for chemical stability tests). The pure salts were purchased directly from Sigma-Aldrich (with a reagent grade ~ 99% purity). The salts were used directly without further purification to mimic the condition in actual CSP operations. The phase diagram of the binary salt mixture is shown in the figure below.

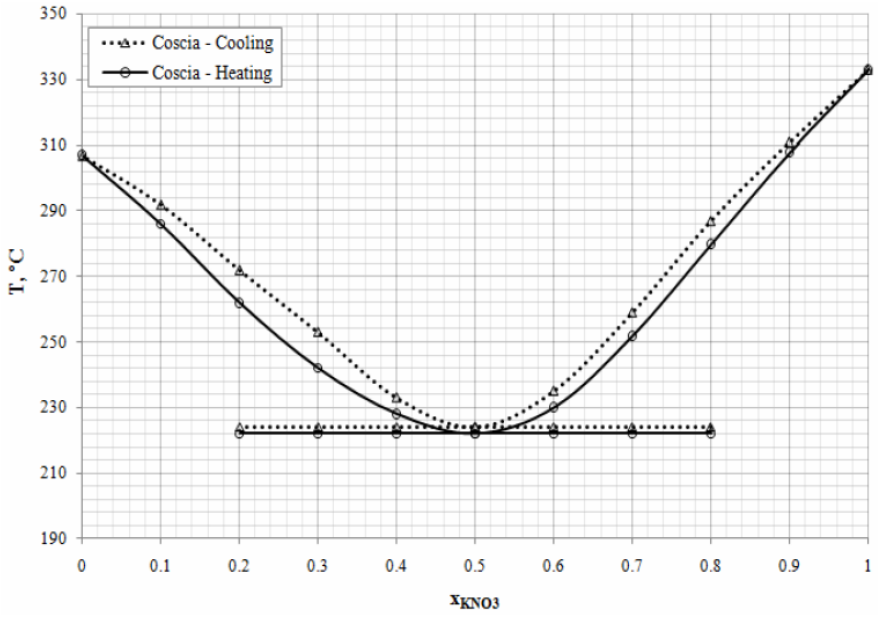

Figure 10. Phase diagram for the $NaNO_3$-KNO_3 system [30]

The phase diagram shows that the mixture has a eutectic point where the molar ratio of the two salts is 50:50 ($NaNO_3$:KNO_3) which is equivalent to a mass ratio of 60:40

for the two salts. The melting point is ~220°C. Such binary salt eutectic is also the most widely used material for TES in commercial solar power plants. The details of the synthesis protocols are discussed next.

2.1.1 Traditional two-step method

The two-step method employed in this study is similar to the approaches reported in previous studies in the literature [84] [85] [86]. These studies demonstrated that the dispersion of nanoparticles at small concentrations (e.g., at mass fractions of ~1.0 %) can significantly enhance the specific heat capacity values of molten salts. For the sake of validating such reports, only one kind of nanoparticle – SiO_2 was chosen for use in the two-step method. The nanoparticle samples were purchased from Sigma Aldrich with a nominal size of 5~15 nm. The actual size of the nanoparticles was measured from SEM images. A few of the nanoparticles in the SEM images were observed to be ~100 nm in diameter - which may be caused by the agglomeration of the smaller nanoparticles.

For the nanofluid synthesis experiments, initially sodium nitrate and potassium nitrate mixture (60:40 weight ratio) and SiO_2 nanoparticles were weighed using a microbalance and poured into a glass container. The total mass of the nitrate salt mixture with SiO_2 nanoparticles was 50g. The container was then filled with 150 ml of distilled water (DIW) for dissolving the salt completely. To attain uniform and homogeneous dispersion of SiO_2 nanoparticles in the system, the colloidal mixture was placed in an ultrasonication bath for 3 hours. Subsequently the container was transferred to a hot plate (set at 120°C) for evaporating the water from the mixture. The complete dehydration

required heating for 10 hours. Finally, the dry crystals of the salt-nanoparticle mixture was heated in a furnace at 250°C for melting and the samples were subsequently used for materials characterization studies (Figure 11). The synthesis protocol is shown in the schematic of Figure 12. The schematic lists the steps in the synthesis protocols for the solar salt nanofluids (SiO_2) samples.

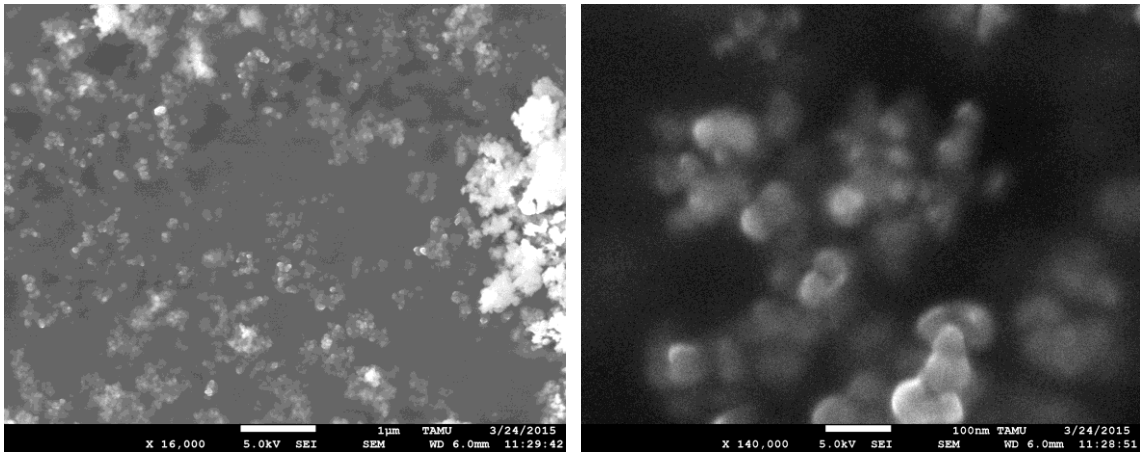

Figure 11. SEM images of the pure silica nanoparticles (before used in the two-step synthesis)

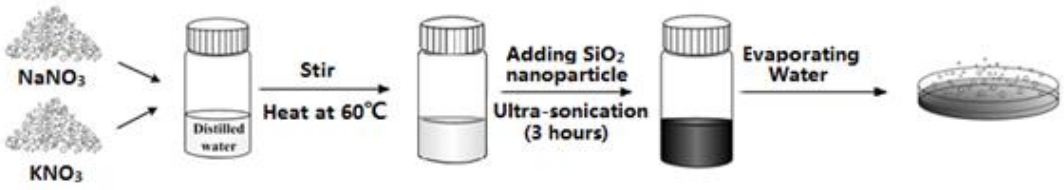

Figure 12. Schematic diagram of two-step synthesis procedure [84] [85] [86]

2.1.2 Innovative one-step method

The one-step method combines the nanoparticle generation and dispersion into one single step in which nanoparticles are synthesized in the base fluid in-situ. This can be achieved by either a physical approach or a chemical approach. One typical physical approach is vapor condensation in which metal vapor is directly condensed to form nanoparticles inside the base fluid by contacting the flowing vapor (at low pressures) within the liquid [46]. Other innovative physical methods include submerged arc spray synthesis [87] and laser ablation [88]. These methods produce well-dispersed nanofluids but requires complex set up which makes it impossible for scale-up and large-scale deployment in industrial applications [89].

In the wet chemical approach pioneered in this study, chosen additives are mixed with the base fluid and subsequently stimulated to yield nanoparticles. Such reactions could be either a direct precipitation from multiple additives [90] or thermal decomposition of certain precursors used as additives in the solvent [91]. These methods have also been proven to produce well-dispersed nanofluids with controllable particle size and shape. However, the wet chemistry method usually requires a different base fluid from that of the target nanofluid. Also, the introduction of additives risks the inadvertent contamination by impurities. Thus, it turns out, that most nanofluids synthesized by wet chemistry approach still falls into a two-step category, in which the filtered nano-precipitates are cleaned and re-dispersed into a new base fluid.

In this study, metal oxide nanoparticles were synthesized in-situ due to thermal decomposition of precursors (e.g., unstable salts) mixed a priori with the molten salt. Five

metal nitrate precursors were explored which include aluminum nitrate, magnesium nitrate, zinc nitrate, nickel nitrate and cobalt nitrate. These precursors share the same anions as the neat solvent. Hence when they decompose, no exterior contaminations (e.g., chloride ions) are explicitly introduced into the molten nitrate salt system. The following chart summarizes the mass fraction of the different precursors that are needed in order to generate corresponding metal oxide nanoparticles in the molten salt at a target mass fraction of 1%.

Table 4. Mass fraction of precursors needed for synthesis of nanoparticles of a target mass fraction (1%)

6.9 % $Al(NO_3)_3 \cdot 9H_2O$	**6.0 % $Mg(NO_3)_2 \cdot 6H_2O$**	**3.5 % $Zn(NO_3)_2 \cdot 6H_2O$**
⇩	⇩	⇩
1.0 % Al_2O_3	**1.0 % MgO**	**1.0 % ZnO**

To find the optimum synthesis temperature, thermogravimetric analysis (TGA) was performed (using SDT Q600 TA instrument) to help determine the final decomposition temperature of the additives (as precursors for nanoparticles). Figure 13 summarizes the decomposition reaction temperatures for each candidate precursor that were measured using a ramping rate of 5 °C / minute in a TGA apparatus.

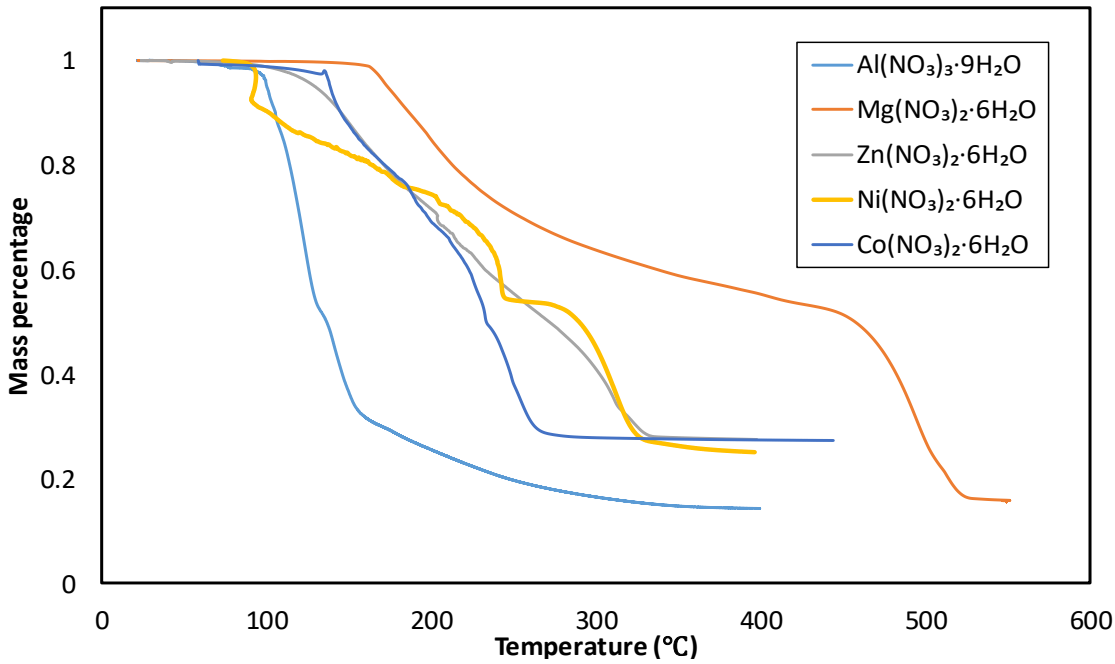

Figure 13. TGA curves for various additives (metal nitrates) as precursors for nanoparticles in the one-step synthesis protocol.

From the TGA results it was observed that these precursors decomposed into the corresponding metal oxides at a temperature below 400 °C except for magnesium nitrate (which was observed to decompose at a temperature of ~530 °C). To accomplish complete decomposition for all the precursors, the final synthesis temperature for attaining complete decomposition was set to 550°C. Both wet-mixing and dry-mixing approaches have been investigated in this study for mixing the powders of the precursors with that of the molten salt samples.

2.1.2.1 Water-assisted one-step method (wet mixing)

In wet mixing approach, all salt components are first mixed with the precursor according to the desired weight ratio and dissolved in DIW completely. After that, the solution is heated on hot plate at 120°C for about 10 hours until water is evaporated out from the mixture. Finally, the solid mixture in heated in furnace at 550°C for metal oxide nanoparticles to be synthesized in-situ in the salt samples by thermo-chemical decomposition of the precursors. The TGA tests suggest that a complete decomposition takes less than 1 hour but the sample is kept in furnace at 550°C for 10 hours for ensuring complete decompositions of the chosen precursors. Figure 14 shows the schematic of the procedure for wet-mixing synthesis approach.

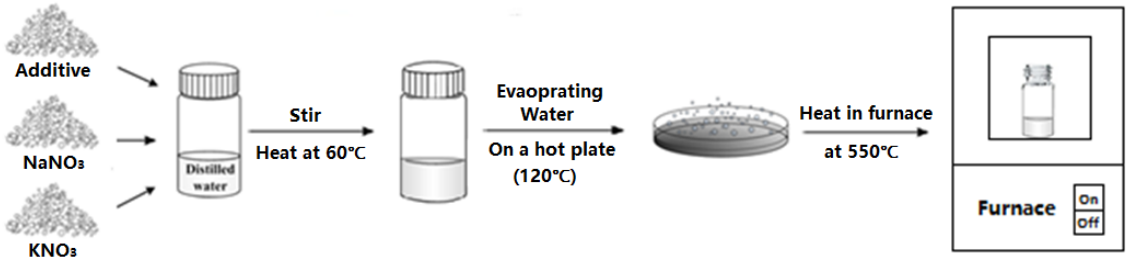

Figure 14. Schematic diagram of one-step nanofluid synthesis procedure using wet mixing approach.

2.1.2.2 Direct one-step method (dry mixing)

In dry mixing approach, all salt components are mixed with the precursors in solid powder form in the container. The mixture was stirred for around 1 minute and baked in furnace at 550°C directly for 10 hours. During the ramping and heating process the salt mixture crystal becomes liquid and the precursors possibly decompose in the liquid phase.

The procedure is illustrated in Figure 15 and Figure 16 where these schematics show the morphology change before and after heating.

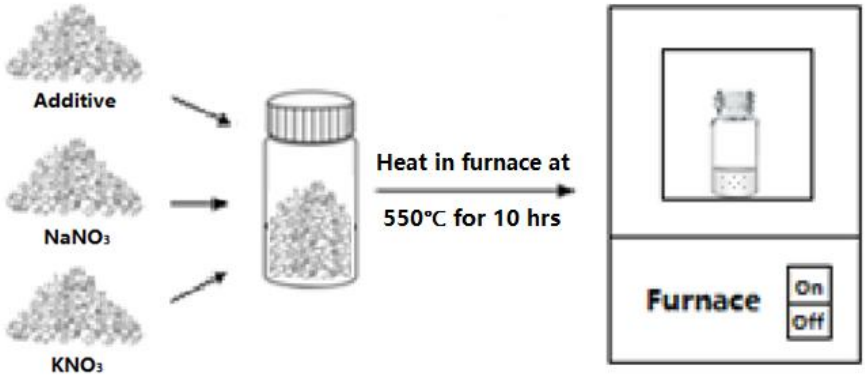

Figure 15. Schematic diagram of direct one-step synthesis procedure (dry mixing)

Figure 16. Images of solar salt samples. (LEFT) Additives mixed with pure solar salt before melting. (RIGHT) After melting and baking the mixture.

2.2 Material characterization

Scanning electron microscopy (SEM) coupled with Energy Dispersive X-Ray Spectroscopy (EDS) techniques were used for materials characterization of the nanofluids samples. For SEM, two scanning electron microscopes (FEI QUANTA 600 FE-SEM and JOEL JSM-7500F) were used to analyze the microstructure of the samples. The comparison of the images ontained from SEM for pure salt samples and additive-doped samples enable the visualization of the dispersion and morphological characteristics of nanoparticles generated in these samples. The procedure for sample preparation for SEM is listed below:

- Heat the vial with sample on hot plate at 400°C
- Once the sample melt, remove them from hot plate and keep stirring/scratching the sample using the spatula to prevent them agglomerating on the glass vial
- Load ~20 mg of sample in the aluminum pan.
- Heat the pan on hot plate at 400°C for few seconds until the sample melt, then quickly seal the pan with lid.
- Put the newly-prepared sample pan in furnace and heat at 550°C for half hour
- Remove the pan from furnace. Wait it cool down and take to SEM room
- When examining sample in SEM facility, remove the lid and place the sample pan in SEM chamber quickly to avoid absorption of moisture from the ambient.

EDS was performed to identify the elemental composition for different regions of the pure molten salts and molten salt nanofluid samples. To be more specific, regional EDS scan is employed to obtain elemental mapping. In order to highlight nano-cluster areas - point EDS analysis is employed to differentiate between the chemical composition in the nano-cluster areas and the bulk salt areas.

2.3 Thermophysical properties measurement

2.3.1 Specific Heat Capacity

The specific heat capacity of the different samples has been measured using both Modulated Differential Scanning Calorimetry (MDSC) and lumped capacitance (T-History) method. The details of the two methods are discussed below.

2.3.1.1 Modulated Differential Scanning Calorimetry (MDSC)

The MDSC tests were performed (suing DSC Q6000 TA Instrument) to measure the specific heat capacity of both neat molten salt samples and the molten salt nanofluid samples. The measurements were performed from 80°C to 550°C. The advantage of MDSC is that by applying a sinusoidal modulated heating rate in addition to a constant heating rate, the temperature response of the samples is obtained and recorded by the MDSC instrument; which enables the separation of the total heat flow into a reversible part and a non-reversible part (based on the temperature response for the varying heating rate). By analyzing the reversible heat flow signals - the specific heat capacity values can then be obtained directly for each cycle as follows:

$$\frac{\mathrm{dH}}{\mathrm{dt}} = \mathrm{Cp}\frac{\mathrm{dT}}{\mathrm{dt}} + f(\mathrm{T},\mathrm{t}) \tag{11}$$

$$\mathrm{Total} = \mathrm{Reversing} + \mathrm{Nonreversing}$$

where, ***H*** is the total heat flow and ***T*** is the instantaneous temperature of the sample

Tzero™ hermetic pans and lids (manufacturer: TA Instruments) were used to store the nanomaterial samples. To prepare for MDSC testing pan, the target testing sample vial (large quantity) was first heated on hot plate at 400°C for roughly 10 minutes until the salt

sample melted completely. Then the vial was removed from furnace and a small amount (~15 mg) of sample was scooped out using a spatula while the sample was in semi-molten state. An empty pan and lid was weighed and filled with the testing sample. The testing pan was heated on hot plate at 400°C again and sealed with the lid once the sample was observed to melt in the pan. The sealed pan and lid were re-weighed for determining the testing sample mass and used for subsequent MDSC tests. A custom protocol was programmed and implemented in the equipment for measuring the specific heat capacity of the samples as shown below:

MDSC test protocol (for solar salt nanofluids samples, 150°C - 565°C)

- Data storage Off
- Equilibrate at 300.00 °C
- Equilibrate at 150.00 °C
- Isothermal for 5.00 min
- Modulate ± 0.48 °C every 60 s
- Data storage On
- Ramp 5.00 °C/min to 565.00 °C
- Isothermal for 5.00 min

It should be noted that in order to prevent extraneous influence of the adsorbed moisture, the sealed hermetic pans containing the test samples, were heated in the furnace at 300 °C for 30 minutes. The total mass of the samples was then recorded and used for specific heat capacity calculation.

2.3.1.2 Lumped capacitance method (T-History method)

The setup of the T-History test is shown in Figure 17. One test vial is filled with solar salt nanofluid (sample mass: 30 g) and an identical reference vial is filled with pure solar salt (also using a sample mass: 30 g). The mass of each vial is measured carefully both before and after the filling step using microbalance (Sartorius ELT-130). Both testing and reference vials are first preheated in the furnace at 275ºC for 1 hour until steady state conditions are achieved. The temperature change of the test sample and the reference sample are monitored using two thermocouples inserted in the middle of each vial. The furnace air temperature close to both vials are monitored using three thermocouples installed at different locations.

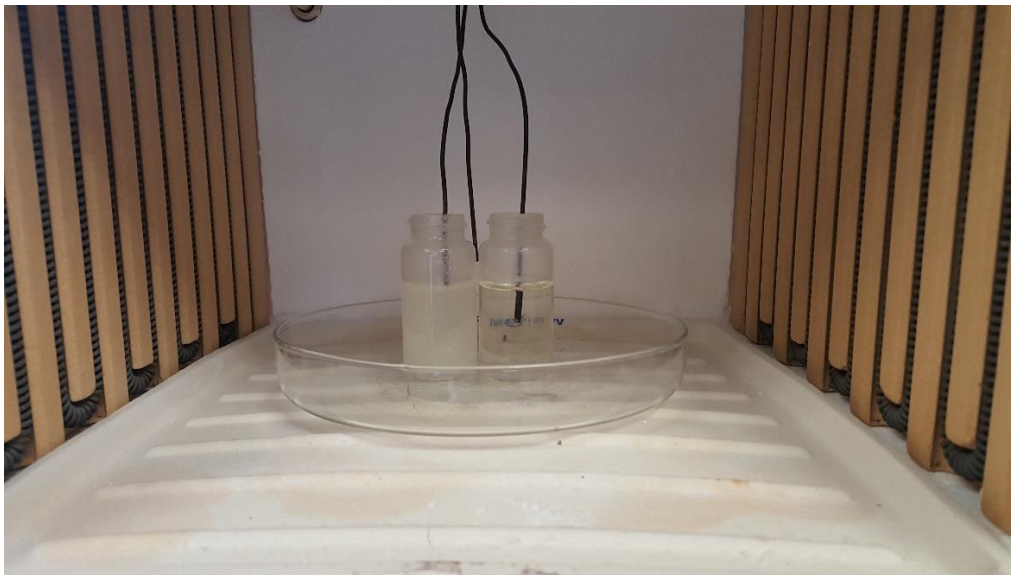

Figure 17. Experimental apparatus for T-History Measurements

For performing the T-History measurements, the furnace temperature was ramped up from 275 ºC to 650 ºC with a ramp rate of 20 ºC/ minute. The temperature change

(history) of both test sample and reference sample are recorded in the heating cycle, starting from the initial equilibration temperature (~275 ºC) to an upper temperature limit of 550 ºC. When both salt sample temperatures are close to 550ºC, the temperature history recording is cut off for specific heat capacity analysis. Furnace is then re-set to 275ºC and the testing cycle is repeated following the same sequence. The specific heat capacity ratio between molten salt nanofluids and pure molten salt is calculated by comparing the temperature history curve (*T* versus *t*.) of both nanofluid sample and the reference salt sample.

It is essential to validate that the Biot number is less than 0.1 for testing protocols that used the lumped capacitance approach (e.g., the T-History method). The Biot number of the pure solar salt in the reference vial is expressed as:

$$\mathrm{Bi} = \frac{h_{\mathrm{air}} L_C}{k} = \frac{h_{\mathrm{air}} V_{\mathrm{sample}}}{A_{\mathrm{surface}} k} \tag{12}$$

where, $\boldsymbol{h_{air}}$ is the natural convection coefficient for air, $\boldsymbol{k}$ is the thermal conductivity of the testing sample, $\boldsymbol{L_C}$ is the characteristic length of the testing sample, $\boldsymbol{V_{sample}}$ is the volume of the testing sample and $\boldsymbol{A_{surface}}$ is the surface area of the testing vial.

The volume and height of the samples in the vial are determined by the mass of test samples. In our setup, 1.0-inch diameter vial was used to contain the salt samples and have a nominal height of 1.25 inch. The characteristic length is calculated, i.e., Volume/Area = 0.178 in = 4.5 mm. Assuming the natural convection heat transfer coefficient to be 5 W/(m^2·K) and thermal conductivity to be 0.5 W/(m^2·K), the Biot number is calculated to be 0.045 which ensures the validity of employing the lumped

capacitance method in this study. Hence, the temperature distribution within the sample placed inside the vial could be treated to be uniform. Thus, the temperature ramping rate of both samples could be explicitly expressed by

$$T_s' = \frac{\mathrm{d}T_\mathrm{s}}{\mathrm{d}t} = \frac{h_\mathrm{air} A_\mathrm{surface}(T_\mathrm{air} - T_\mathrm{s})}{m_\mathrm{s} c_{p,\mathrm{s}}} \tag{13}$$

where, $\boldsymbol{T_{air}}$ and $\boldsymbol{T_s}$ are the instantaneous temperature of furnace air and testing sample, $\boldsymbol{m_s}$ is the mass of the testing sample and $\boldsymbol{c_{p,s}}$ is the specific heat capacity of the sample.

Both vials have the same heating surface area with same amount of mass inside. As the variation of natural convective heat transfer coefficient between two samples is negligible at the same sample temperature, the ratio of specific heat capacity of two samples at any temperature can be expressed by

$$\frac{c_{p,\mathrm{nano}}}{c_{p,\mathrm{ref}}} = \frac{m_\mathrm{ref}}{m_\mathrm{nano}} \cdot \frac{(\mathrm{d}T_\mathrm{s}/\mathrm{d}t)_\mathrm{ref}}{(\mathrm{d}T_\mathrm{s}/\mathrm{d}t)_\mathrm{nano}} \cdot \frac{(T_\mathrm{air} - T_\mathrm{s})_\mathrm{nano}}{(T_\mathrm{air} - T_\mathrm{s})_\mathrm{ref}} \qquad \text{at any fixed } T_\mathrm{s} \tag{14}$$

where, $\boldsymbol{m_{ref}}$ and $\boldsymbol{m_{nano}}$ are the mass of the reference sample (pure molten salt) and nanofluid sample.

The time derivative of the temperature is obtained by using an 8^{th} order polynomial fit to the temperature history curve. Figure 18 shows an example comparing the temperature ramping rate (time derivative of temperature) calculated using polynomial fitting and two-point finite difference method. The overall trends match for both calculations, but the curve fitting removes the random fluctuations. This enables smoother profiles in the results when compared with that of the two-point finite difference method.

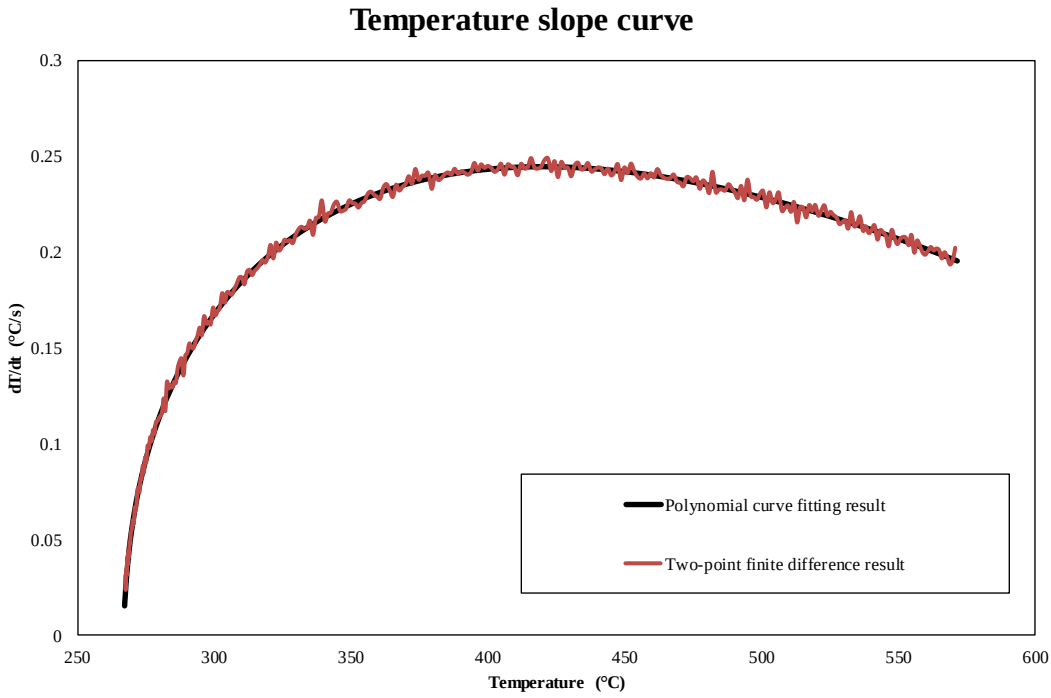

Figure 18. Comparison of temperature ramping rate using two methods

2.3.1.3 Discussion

MDSC is a well-established method for measuring specific heat capacity of various materials with high precision. However, it should be noted that the quantity of sample (sample mass) used in MDSC test is usually very small (~15 mg) and hence the measured values are more representative of the material property for small sample volumes. Normally specific heat capacity is an intensive property which is independent of the sample mass. However, since nanofluids are colloidal mixtures of nanoparticles (which are not ideally of homogeneous composition) property measurements performed for small quantities of sample mass may diverge significantly when these measurements

are performed for significantly larger sample sizes. (especially considering the boundary effect in MDSC test). T-History test on the contrary is less precise than MDSC techniques but provides for values of specific heat capacity that are more representative of the actual engineering applications since larger quantities of samples are used (~30 g). The main error of T-History method comes from the environment temperature measurement which could vary by ~10°C within the testing furnace. The T-History measurement results can be used to validate the MDSC measurements and provide a more realistic estimate of the thermal storage capacity values for the materials used in these testing protocols. In the actual experiments, MDSC tests were used to identify preferable candidate materials and T-History tests were performed subsequently to find optimum synthesis condition for these candidate materials.

2.3.2 Thermal conductivity test

After reviewing several different configurations of thermal conductivity measurement devices, a customized concentric cylinder testing chamber is constructed for measuring the thermal conductivity values using steady state techniques. The basic requirement of the testing chamber is to obtain 1-D steady state heat transfer in the radial direction from the coil heater at the center. The entire chamber is placed inside a furnace to maintain a constant temperature and the coil heater at the center supplies heat to the samples that is lost by conduction heat transfer in the radial direction. Figure 19 illustrates the design of the testing chamber.

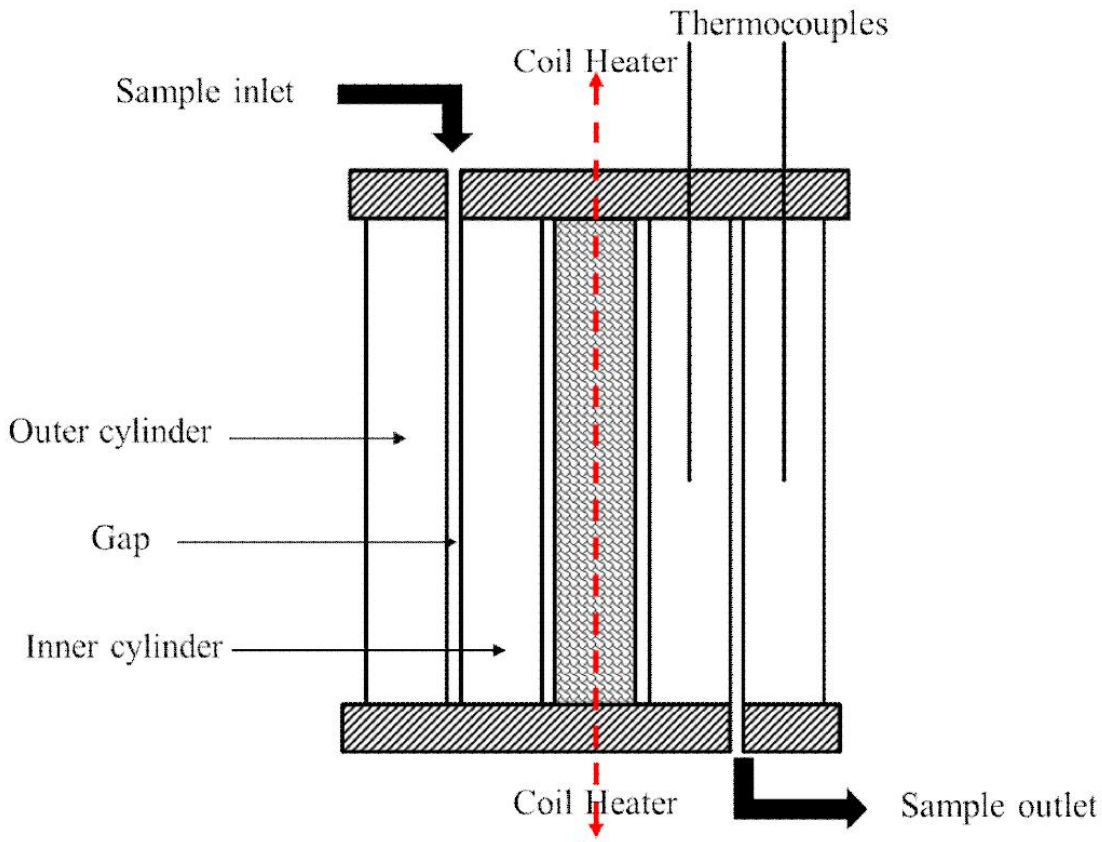

Figure 19. Design of thermal conductivity testing chamber

2.3.2.1 Concentric cylindrical testing chamber

After considering the interior space of the furnace available, a final design of testing chamber was made with dimensions are listed in Figure 20. The chamber consists for an inner cylinder and an outer cylinder shown in Figure 21. The inner cylinder sits on the top of the outer cylinder leaving a small gap in between for filling the test liquid. A high temperature cartridge heater would be located in the center of inner cylinder providing constant radial heat flux. Four pairs of thermocouples are mounted in four directions with the same radial distances. With one thermocouple located in the inner

cylinder and another one in the outer cylinder, the temperature drop across the thin layer of testing liquid is then represented by the difference between each pair of thermocouples. The thermal conductivity of the testing liquid could then be calculated with known heating power input and temperature drop across the thin liquid layer using steady state1-D radial conduction equation

$$\mathrm{k} = \frac{\dot{q} \cdot \ln(r_2/r_1)}{2\pi L \Delta T} \tag{15}$$

where, $\dot{q}$ is the applied power, L is the height of the testing chamber, r_1 and r_2 are the inner and outer radius of the concentric cylinder, respectively.

By equilibrating the system temperature in the furnace at different target values, the thermal conductivity of the testing liquid could be measured at different temperature points. The arrangement and setup of the testing chamber for high temperature molten salt measurement is illustrated in Figure 22.

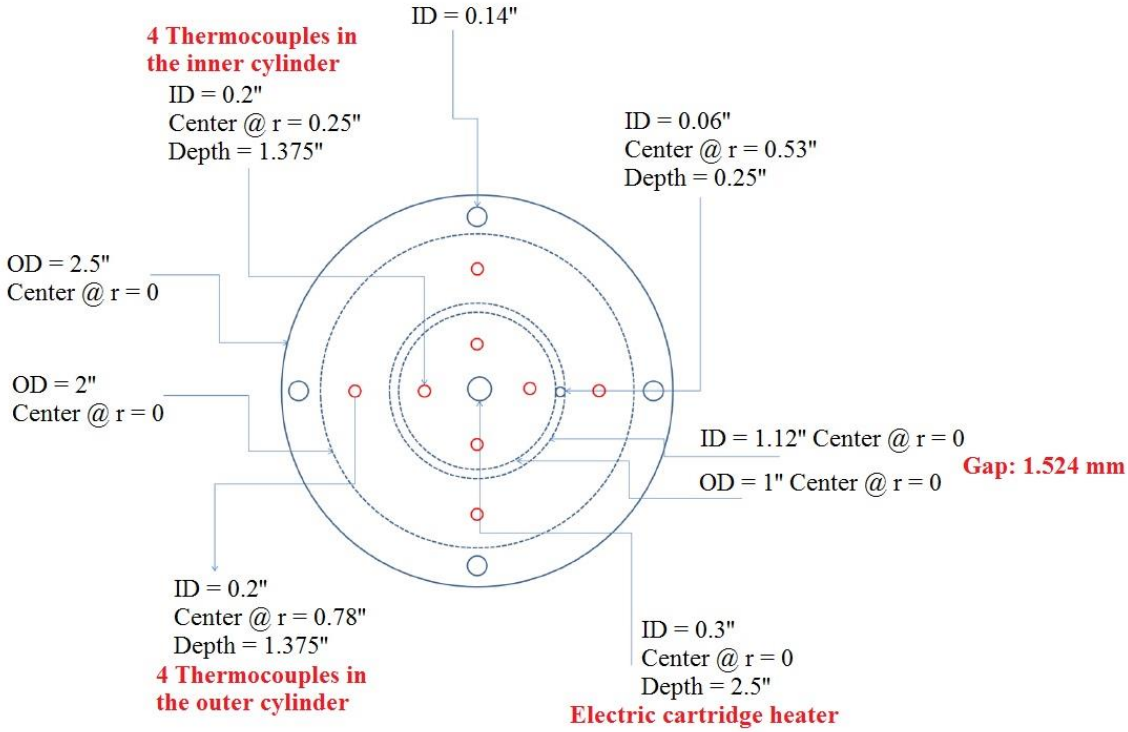

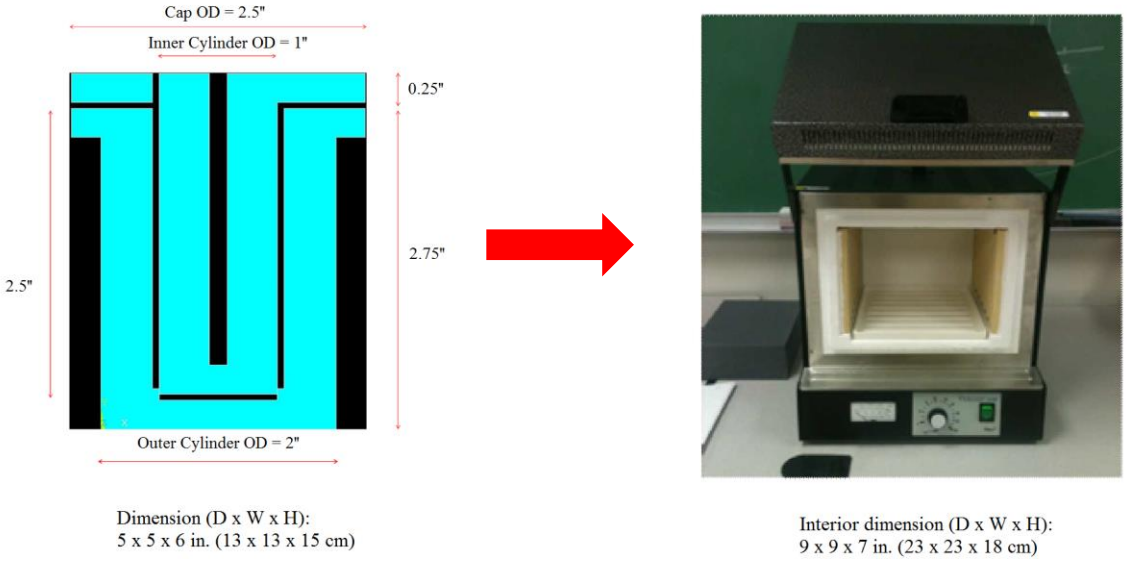

Figure 20. Design and dimensions of the concentric cylinder test apparatus for measuring thermal conductivity

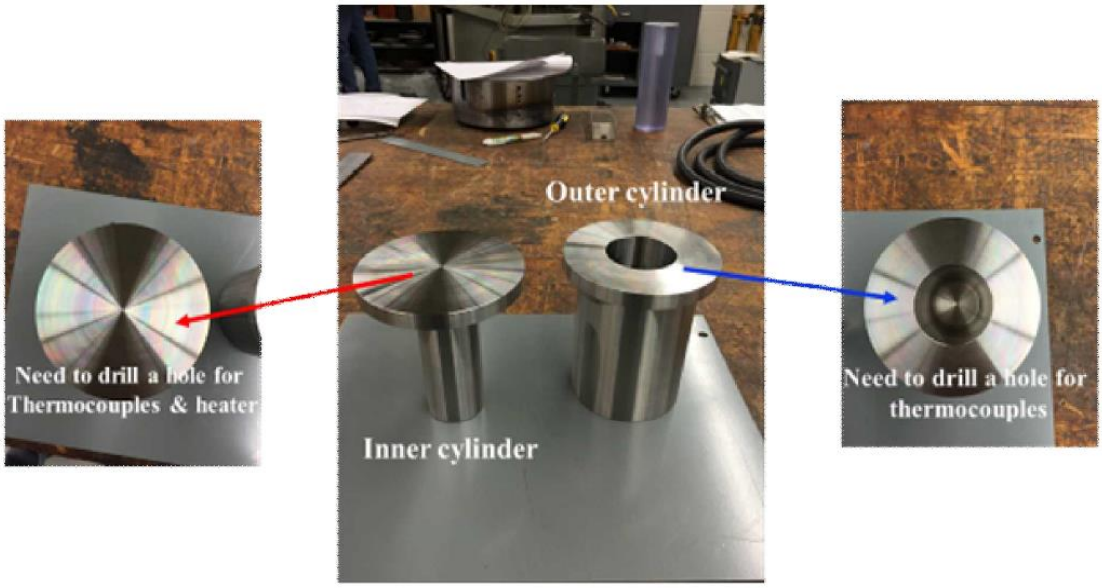

Figure 21. Design and assembly of the concentric cylinder test apparatus for measuring thermal conductivity

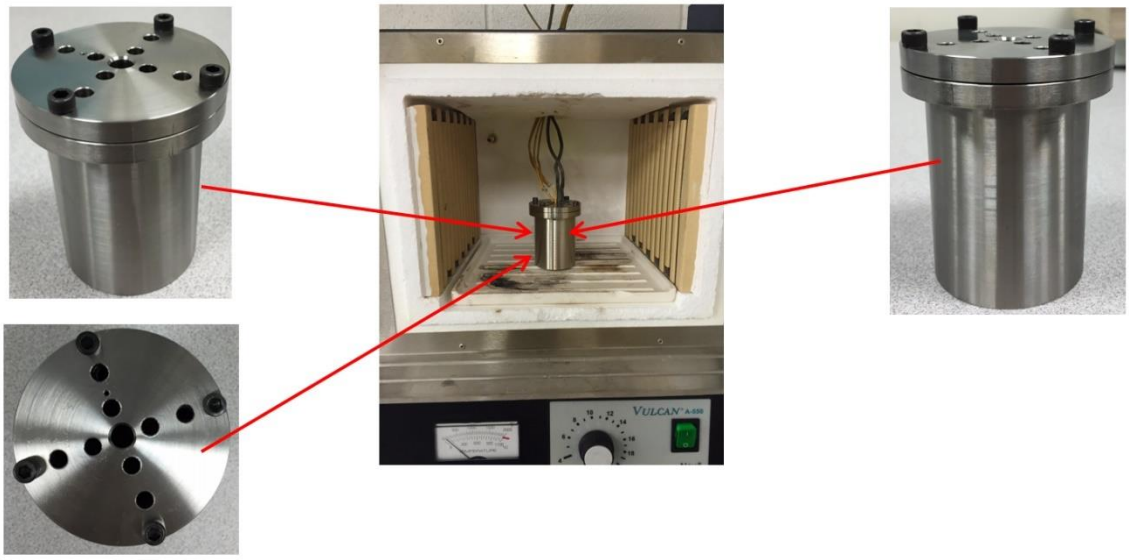

Figure 22. Assembly and implementation of the concentric cylinder test apparatus for measuring thermal conductivity

2.3.2.2 Validation of thermal conductivity testing chamber

To ascertain that the results obtained from the concentric cylinder test apparatus for measuring thermal conductivity is reliable, a few preliminary tests were performed using water as the test fluid. The measurements performed using water as the test fluid help to determine if the experimental setup was able to provide accurate data for thermal conductivity (and compared to that of the literature data for thermal conductivity of water). In these tests, the chamber is filled with water and the system is immersed in a constant-temperature water bath at 10ºC (as shown in Figure 23) for 12 hours before the steady state temperature data were recorded.

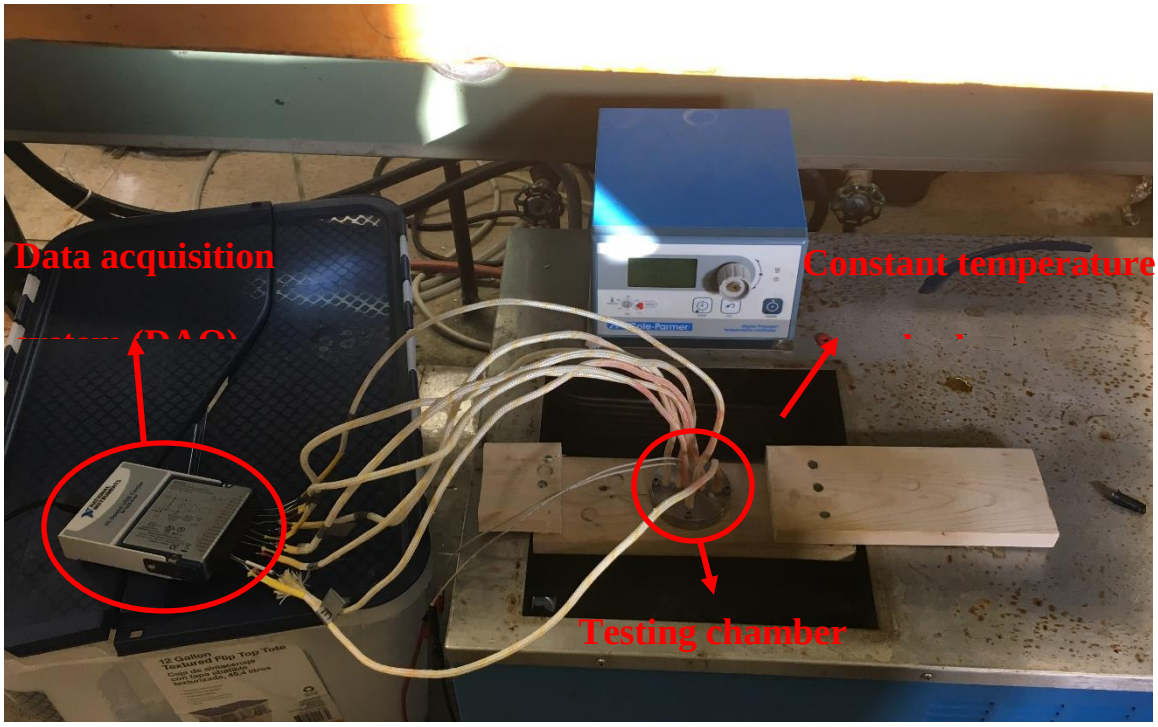

Figure 23. Image of experimental apparatus for measuring thermal conductivity of water (for validating the performance of the apparatus)

For thermal conductivity measurements performed using water as the test fluid, four different heating powers were used to record the temperature gradients in the thin liquid layer (water) under steady state conditions for measuring the thermal conductivity values. The steady state measurements of temperature differences between each pair of thermocouples are summarized in Figure 24. The results show a large variation of temperature difference between different pairs of thermocouples. This suggests that the conduction heat transfer is not quite uniform along the circumferential direction. An average temperature drop from the four pairs of thermocouples were used to calculated the thermal conductivity of water using Equation 6 and the result is shown in Figure 25 and Table 5. Despite the relatively large measurement uncertainty, the measurement of thermal conductivity for water at different temperatures is consistent with the literature data [92]. Hence, this shows that the thermal conductivity measurements performed using this apparatus is reliable.

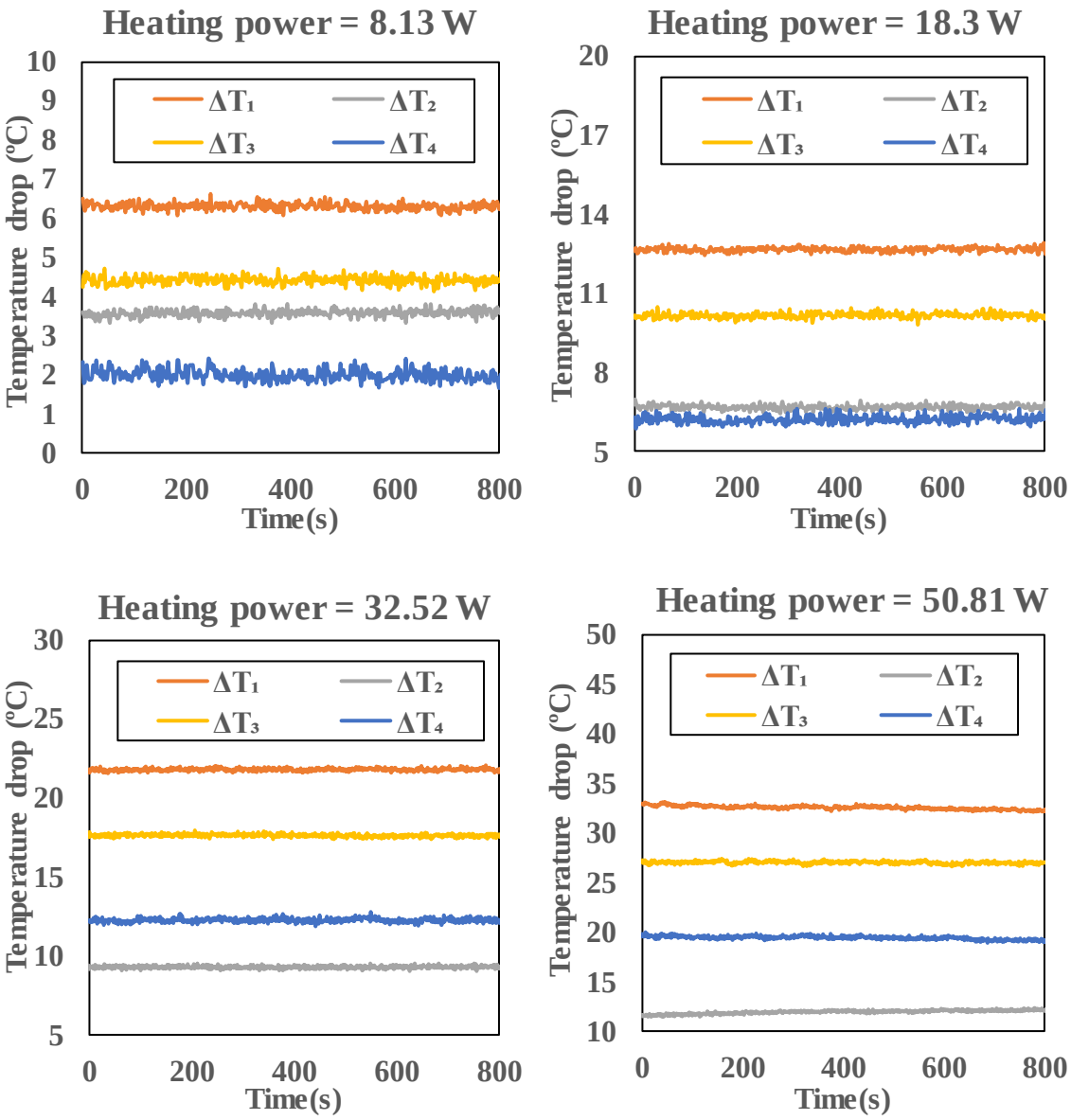

Figure 24. Steady state temperature difference measurements for water thermal conductivity test with four heating powers

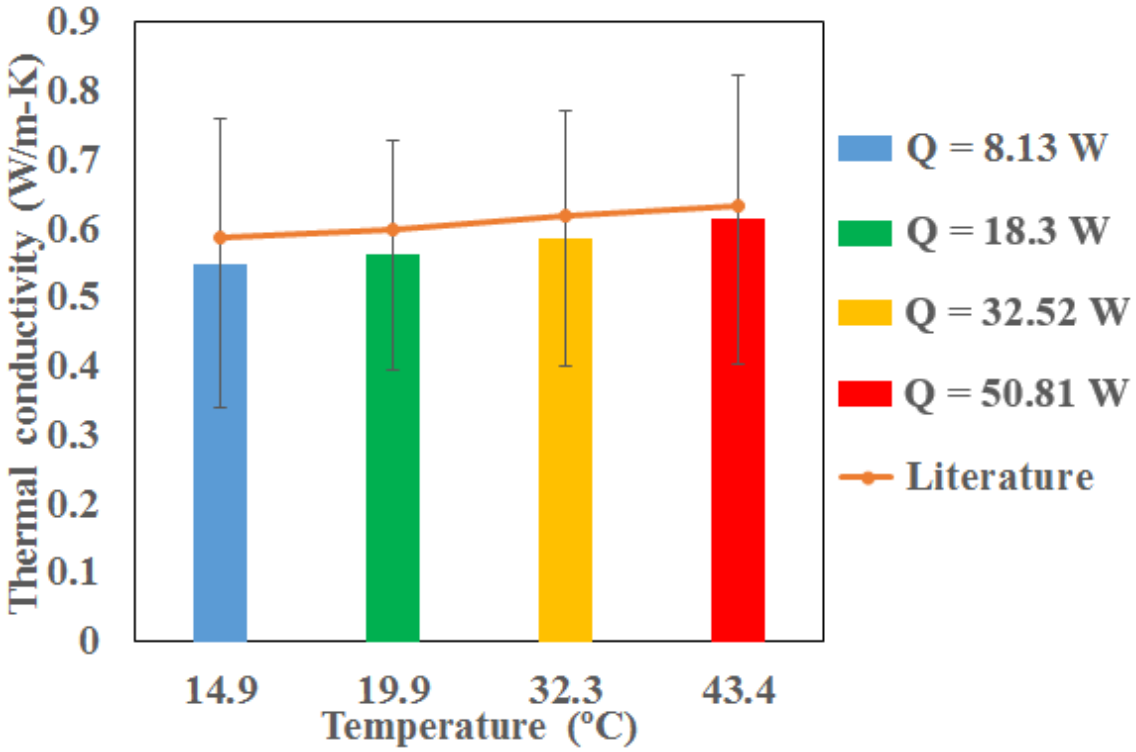

Figure 25. Measurement of thermal conductivity of water at different temperatures

Table 5. Comparison of thermal conductivity of water between experimental measurements and literature values

	Temperature [°C]	Thermal conductivity [W/(m·K)]	Standard Deviation	Literature value [W/(m·K)]
Test 1	14.9	0.549	38%	0.588
Test 2	19.9	0.561	29%	0.597
Test 3	32.3	0.585	32%	0.618
Test 4	43.4	0.614	34%	0.634

2.4 Thermal stability test

The stability of molten nitrate salt is usually studied by thermogravimetric analysis (TGA) and differential scanning calorimetry (DSC). These methods are fast and accurate but suffer from the drawbacks of short time frame in which the chemical equilibria are not reached. In order to investigate the lone-term chemical stability of large amount of salt samples, an alternative method is used. An array of samples of solar salt (with and without additives or nanoparticles) of a mass of 27.5 g were held at 565°C for 67.5 hours inside a furnace. Considering the high corrosivity of nitrate salt in metal containers at elevated temperature, Erlenmeyer flasks were used to hold the salt in the thermal cycling tests and the total mass change were recorded before and after each testing cycle. By calculating the mass change before and after the heating cycle, the thermal stability of the candidate molten salt was determined.

In early tests, open containers were used to hold the molten salt during the isothermal heating cycle. Table 6 shows the mass loss (in percentage) of pure solar salt samples, solar salt nanofluid samples (containing SiO_2 nanoparticles at mass fraction of 1%) and solar salt nanofluid samples (containing aluminum nitrate additives as precursors for alumina nanoparticles at mass fraction of 1%) from the stability tests performed at different temperatures.

Table 6. Mass loss over 67.5 hours of heating cycle at different temperatures

	% weight loss		
	350°C	400°C	550°C
Solar salt (binary nitrate salt)	0.04%	0.10%	60.53%
Solar salt nanofluid (two step) (containing SiO2 nanoparticles at mass fraction of 1%)	0.27%	0.45%	66.96%
Solar salt nanofluid (one step) (containing aluminum nitrate additives as precursors for alumina nanoparticles at mass fraction of 1%)	0.11%	0.16%	59.12%

The table shows that for operating temperatures less than 400°C, the mass loss of molten salt nanofluids is negligible. At 565°C however, all samples displayed abnormally high rates of mass loss (> 60%). Such result is inconsistent with the literature study in which the thermal decomposition of solar salt is typicaly initiated at a rapid rate at 600°C [93]. Since lots of white salt powders were identified near the container, it was inferred that such high mass loss was caused by the rapid evaporation of the nitrate salt at elevated temperatures. In order to minimize the evaporative mass loss, the containers for the molten salt samples (pure samples and nanofluids samples) were closed and sealed during the isothermal heating period (and the decomposed gases were only allowed to escape after the heating cycle was finished). The detailed procedure for performing the thermal stability test is shown below which consists of three parts:

Step I. *Preparation of 27.5 g molten salt nanofluid*

1.1 Carefully weigh the following amount of salt and additives for different salt nanofluid samples

	$NaNO_3$	KNO_3	Precursor
Base solar salt	16.335 g	10.89 g	N/A
Soalr salt - Al_2O_3 nanofluid			2.023 g $Al(NO_3)_3 \cdot 9H_2O$
Solar salt – MgO nanofluid			1.749 g $Mg(NO_3)_2 \cdot 6H_2O$
Solar salt – ZnO nanofluid			1.005 g $Zn(NO_3)_2 \cdot 6H_2O$

1.2 Mix the salt and additive powder in a glass container (beaker), stir the mixture to attain better dispersion of powder

1.3 Bake the mixture in furnace at 550°C overnight (around 8 hours)

1.4 Weigh the mixture after baking to assure that the additives have fully decomposed

Step II. *Stability test cycle*

2.1 Carefully weigh a glass flask and a stopper

2.2 Add 27.5g molten salt sample (pure salt or salt nanofluid) into the flask, put on stopper

2.3 Reweigh to access starting weight M_0 (with flask and stopper)

2.4 Soak the sample in furnace at target temperature (565°C) for exactly 67.5 hours

2.5 Bring sample out from furnace, reweigh immediately to get total sample mass M_1 (with flask and stopper)[4]

2.6 Open stopper and reweigh to get total sample mass M_2 (with flaks and without stopper)

[4] Usually the sample appears green color at this step

2.7 heat the sample and flask on hot plate at 250°C for 1 hour[5]
2.8 Reweigh to get total sample mass M_3 (with flask and without stopper)

Step III. *Repeating cycle and data-analysis*

3.1 Repeat step 2.3 to 2.8 with the same sample for two more cycles (three cycles in all)
3.2 For each cycle, $M_0 - M_1$ gives total mass loss with trapped/dissolved gas, $M_2 - M_3$ give the actual total mass loss (without trapped gas)

Figure 26 shows the experimental apparatus for measuring the thermal stability.

Figure 26. High temperature thermal stability testing setup

[5] After 1 hour baking with stopper open, the sample should appear transparent with no color

2.5 Corrosion test

2.5.1 Sample preparation

The corrosions tests were performed using the "coupon bomb" design proposed by Iyer [94]. This test protocol mimics the walls of the storage tank used in CSP plants. As shown in Figure 27, stainless steel coupons were immersed in the molten salt samples inside the stainless steel bomb.

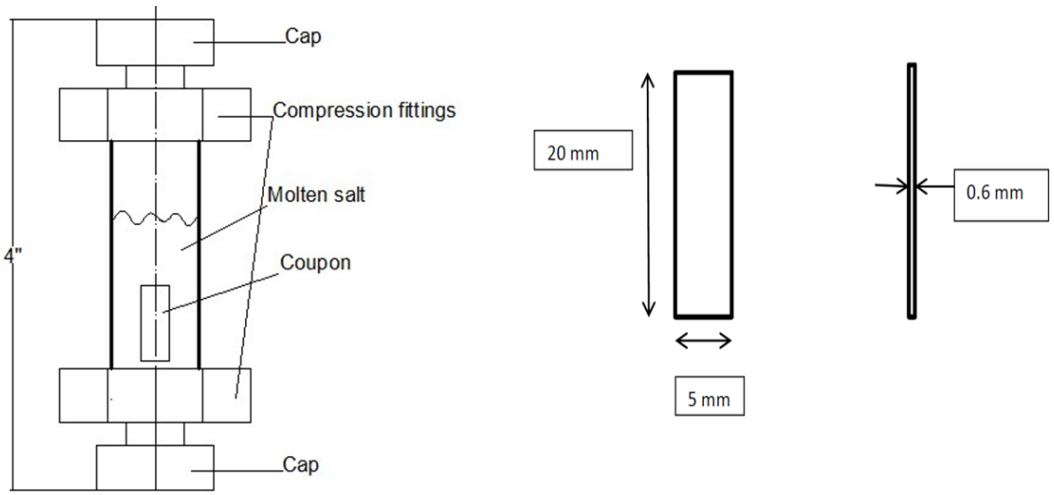

Figure 27. Design of corrosion test apparatus

The coupons used for conducting the corrosion test are made from SS304L and the specified dimensions are 20 mm x 5 mm x 0.6 mm. The bomb is made from SS316 tube with 2 in length and 3/8 in diameter. Each coupon is stamped with a unique number on the surface which helps to distinguish them after the corrosion tests. To assemble the stainless steel bomb, the SS316 tube was deburred properly and sealed on one end with compression fitting. After filling the bomb with molten salt sample and test coupons the test bomb was sealed on the other end with same type of compression fitting. The

isothermal corrosion tests were performed at 550 ºC which mimics the operating temperature of solar salts in commercial CSP plants. In the test, eight coupon bombs were placed inside the furnace with each bomb carrying one or two coupons. Figure 28 shows the corrosion test apparatus.

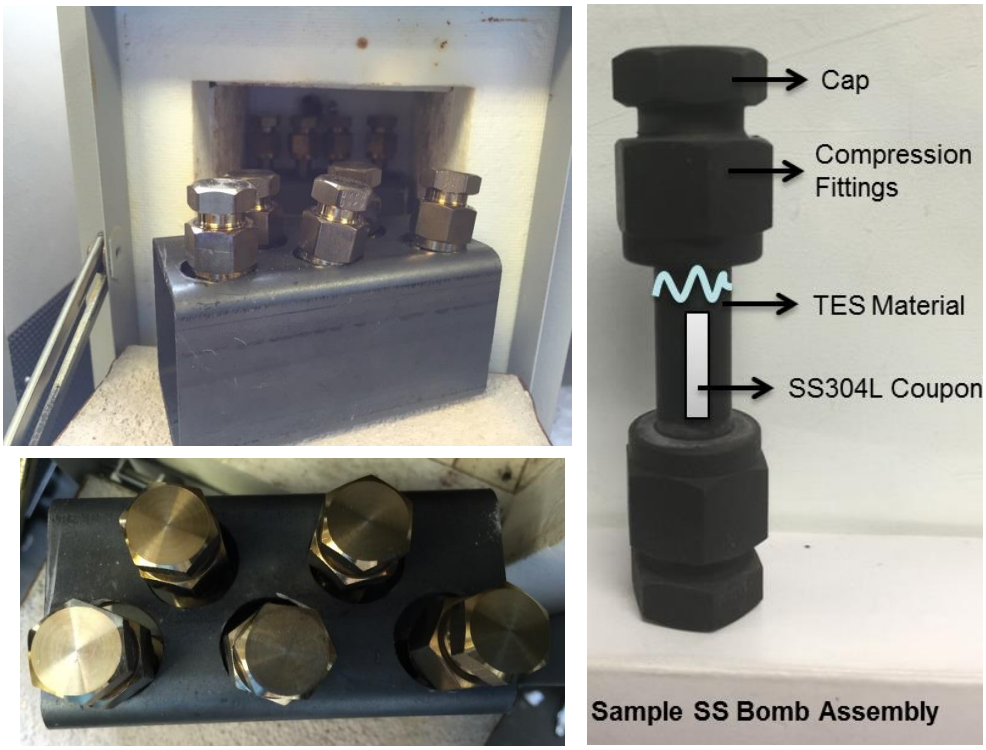

Figure 28. High temperature corrosion test apparatus indicating the level of the molten salt in the bomb.

Among the eight bombs, two were left empty (but with coupon inside), two were filled with pure solar salt, two were filled with solar salt nanofluid sample (one-step synthesis protocol) and the rest two were filled with solar salt nanofluid sample (one-step synthsis protocol). All coupons were wrapped with ceramic wire as shown in Figure 29 for electrical isolation (to ensure that they do not get in contact with each other or the

container wall in each test bomb). Such contact could result in potential galvanic corrosion which increases the magnitude of corrosion of metal in molten salt.

Figure 29. Separation of coupons by ceramic wire for electrical isolation.

The initial mass was recorded for each coupon and the level of corrosion was checked after 120 hours of heating in a furnace. Once the test was completed, one end of the compression fitting was opened and the coupons were removed from the bomb by melting the salt in a furnace at 300ºC. The molten salt along with the coupons was poured out in a glass tray. The coupons were descaled using different descaling protocols as discussed in the following chapter. The final mass of the coupon was recorded for determining the corrosivity of different molten salt samples.

2.5.2 Descaling protocol

Prior to the actual corrosion test, a customized descaling protocol (for removing corroded metal) was developed and optimized. The ultimate requirement for an "appropriate" descaling protocol is that it should be able to remove just the oxide layer

completely. However, in practice this may be impossible since some amount of corrosion (mass loss) of the metal by the descaling agent is unavoidable. However, appropriate choice of descaling agent can help alleviate the corrosion of the metal by the descaling agent (or can be designed to minimize he corrosion of the bare metal by the descaling agent). Iyer [94], Bradshaw [95] and Cabeza [96] adopted the decaling protocol mentioned in ASTM G4-84 in which 30% by weight of concentrated HCl solution was used for removing the corrosive products. In actual experiment, it was found that 30% HCl solution is too concentrated for descaling such that the metal was being attacked by the acid (this was apparent from the observation of bubbles forming on the surface of the coupons when immersed in concentrated HCl solution). Hence 10% HCl solution was not used for descaling in experiments performed later in this study.

A standard protocol for carrying out descaling specifying the time needed for dipping the sample in the HCl solution was not available in the literature. To determine the appropriate time needed for descaling, a preliminary corrosion test was performed with different descaling time intervals. Three coupons were immersed in pure molten solar salt and heated in furnace at 272 ºC for two weeks. Figure 30 and Table 7 shows the mass loss rate for each coupon using 10% HCl solution with descaling time of 1, 3, 5, 30 and 120 minutes. The mass loss rate was measured between each descaling interval (i.e., from 5 mins to 30 mins). The results show that within the first 30 minutes interval, all the test coupons showed significant mass loss in the descaling process (as the corroded parts were dissolved by the descaling solution). After 30 minutes of descaling, however, only marginal mass loss of mass was observed for the test coupons. Hence it was decided that

the coupons should be descaled by immersing in 10% HCl solution for at least 30 minutes.

The cumulative mass losses of corrosion coupons are shown in Figure 31 and Table 8.

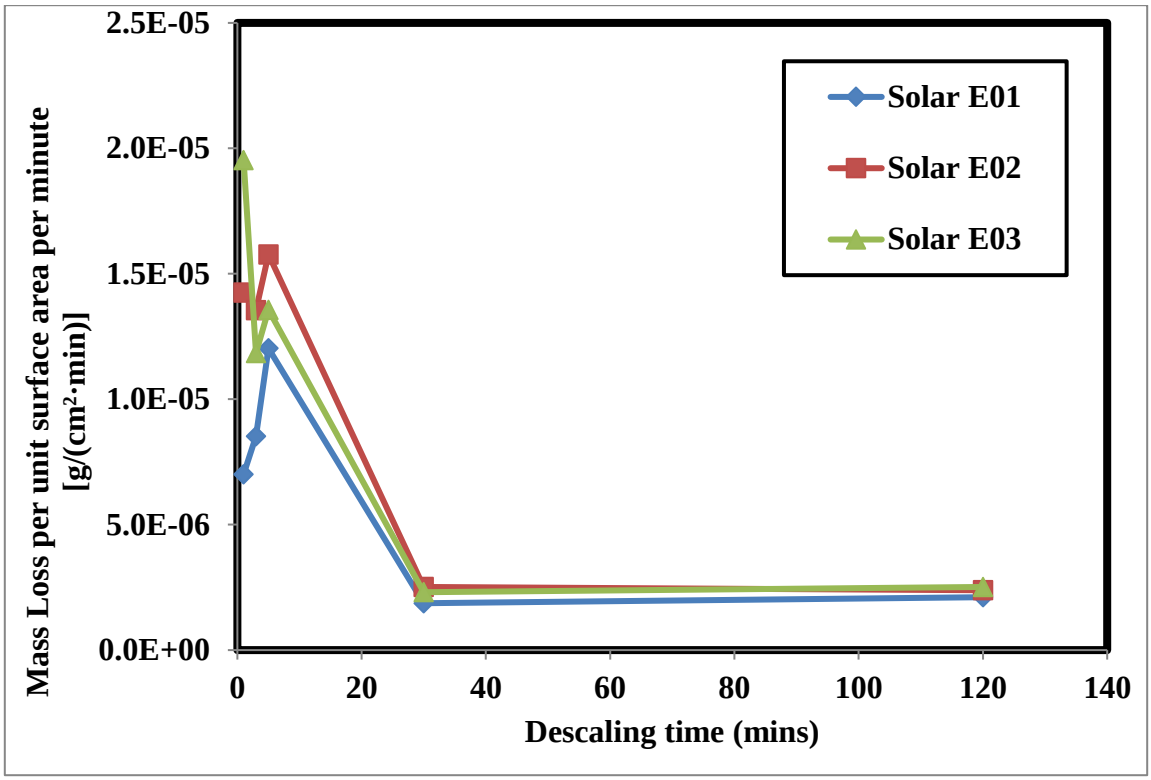

Figure 30. Mass loss rate per unit surface area of corrosion coupons with different descaling time (measured during each descaling time interval)

Table 7. Mass loss rate per unit surface area of corrosion coupons with different descaling time (measured during each descaling time interval) [g/(cm²·min)]

	1 min	3 min	5 min	30 min	120 min
E01	7.01×10^{-6}	8.52×10^{-6}	1.20×10^{-5}	1.87×10^{-6}	2.10×10^{-6}
E02	1.43×10^{-5}	1.36×10^{-5}	1.58×10^{-5}	2.51×10^{-6}	2.39×10^{-6}
E03	1.95×10^{-5}	1.18×10^{-5}	1.36×10^{-5}	2.31×10^{-6}	2.52×10^{-6}

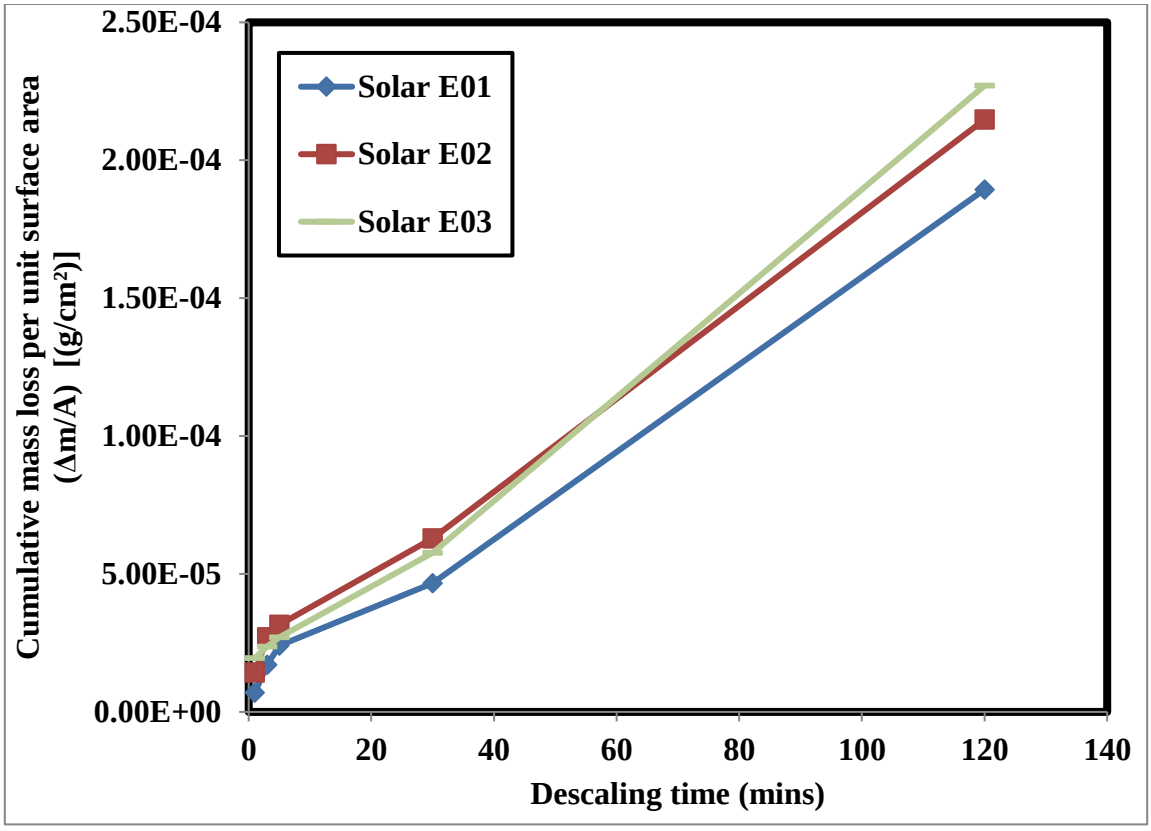

Figure 31. Cumulative mass loss per unit surface area of corrosion coupons with different descaling time (measured with respect to the initial sample mass)

Table 8. Cumulative mass loss per unit surface area of corrosion coupons with different descaling time (measured during each descaling time interval) [(g/cm²)]

	1 min	3 min	5 min	30 min	120 min
E01	7.01×10^{-6}	1.70×10^{-5}	2.41×10^{-5}	4.67×10^{-5}	1.89×10^{-4}
E02	1.43×10^{-5}	2.71×10^{-5}	3.15×10^{-5}	6.29×10^{-5}	2.15×10^{-4}
E03	1.95×10^{-5}	2.37×10^{-5}	2.71×10^{-5}	5.77×10^{-5}	2.27×10^{-4}

It should also be pointed out that the descaling time is also dependent on the degree of corrosion. If testing coupons are heavily corroded (which is usually not the case for molten salt corrosion test), extended descaling time is needed for removing the corroded parts completely. Also, there are several other procedures for removal of corrosion products with iron and steel according to ASTM protocol G1 [97]. Those include the use of nitrate acid solution, sodium hydroxide solution, boiling diammonium citrate, etc. However, there is no conclusive suggestion on the preferred implementation of the descaling protocols. The choice of the most appropriate protocol for descaling involving solar salt samples has not been examined thoroughly in the literature. Hence, a control study on the effect of different descaling protocols involving different samples is needed to elucidate and resolve this enigma.

2.6 Flow Loop Apparatus

A high temperature flow loop apparatus was designed, constructed and assembled for performing measurements of the heat transfer coefficient of molten salts nanofluids in a specified temperature range for a chosen test section. Pressure head and heat flux correlations for different solar salt nanofluid samples need to be measured and compared in a straight cylindrical channel. Other criteria for the evaluation of the thermal performance (i.e., Reynolds number versus Nusselt number correlation) were also investigated.

Figure 32 and Figure 33 shows examples of flow loop test facilities at other institutions. These designs were critically examined in order to develop the flow loop test facility in this investigation.

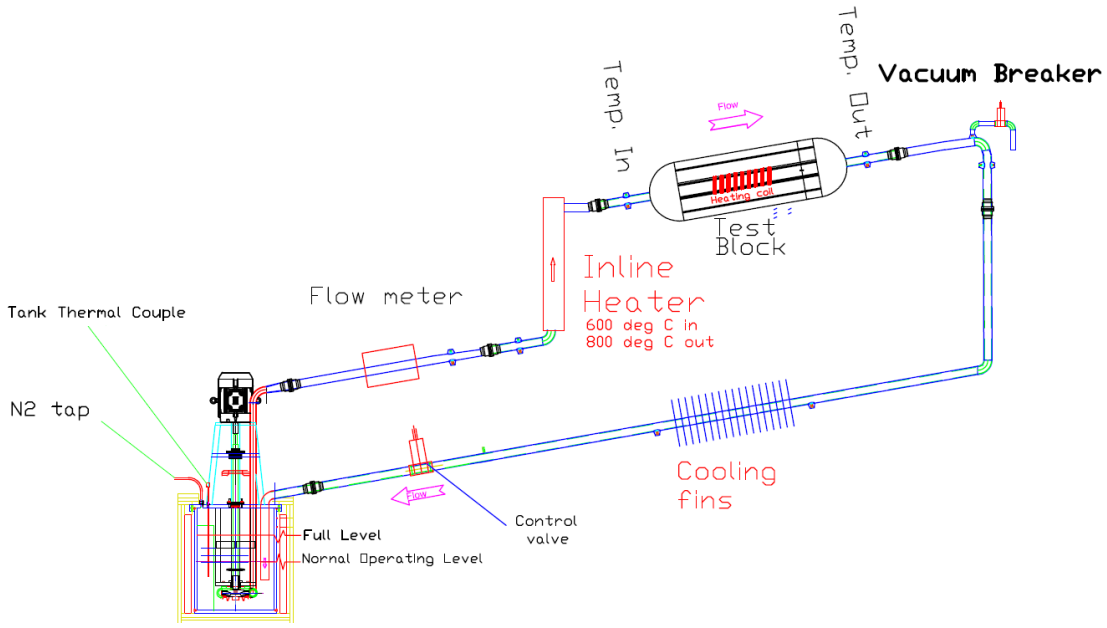

Figure 32. Molten Salts Test Loop at University of Arizona[6]

[6] Schematic diagram provided by project collaborator

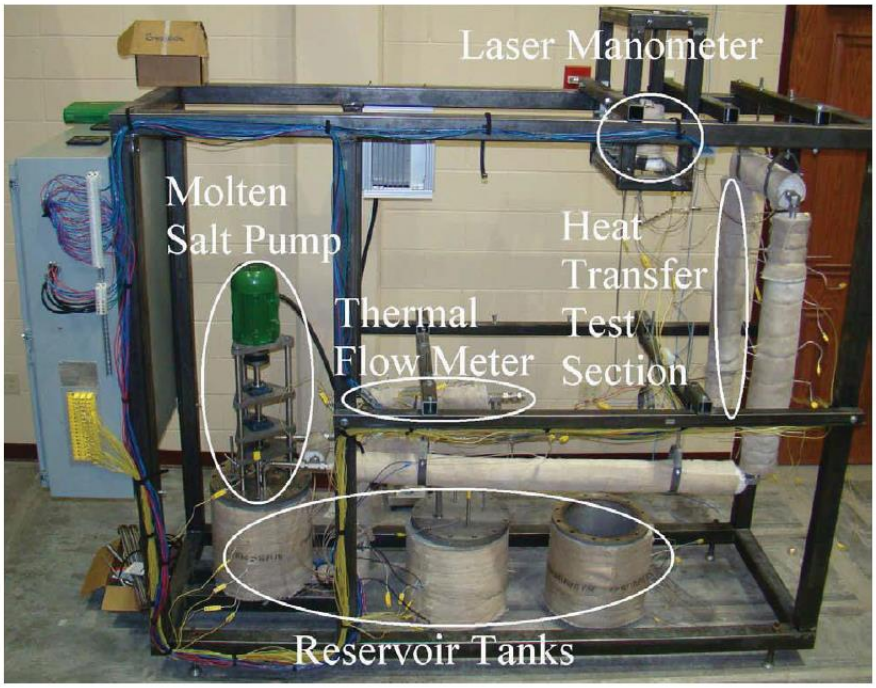

Figure 33. Molten Salts Test Loop at University of Wisconsin-Madison [98]

Some important characteristics of high temperature flow loop test facilities, derived from these designs include:

i) All pumps utilized in the molten salts system are vertical immersion pump. Such configuration guarantees a safe transfer and circulation of corrosive liquids

ii) The flow loops are constructed at a higher elevation from the storage tank. This ensures that in the event of pump failure, the liquid can still drain back to the tank by gravity.

iii) All lines are heat traced to prevent molten salts from solidifying and clogging in the flow loop. All lines are well insulated for minimizing heat loss and ensuring safety.

iv) The properties measured include: (1) temperature at the inlet and outlet of the test section; (2) pressure drop across test section; (3) flow rate.

The objective of developing the flow loop apparatus is for evaluating the thermal-hydraulic performance of the synthesized molten salt nanofluids. The flow loop is designed to sustain a maximum temperature of 600 °C (for a certain level of tensile stress and moderately corrosive environment). The details of the design and construction of the flow loop apparatus is listed in Appendix A.

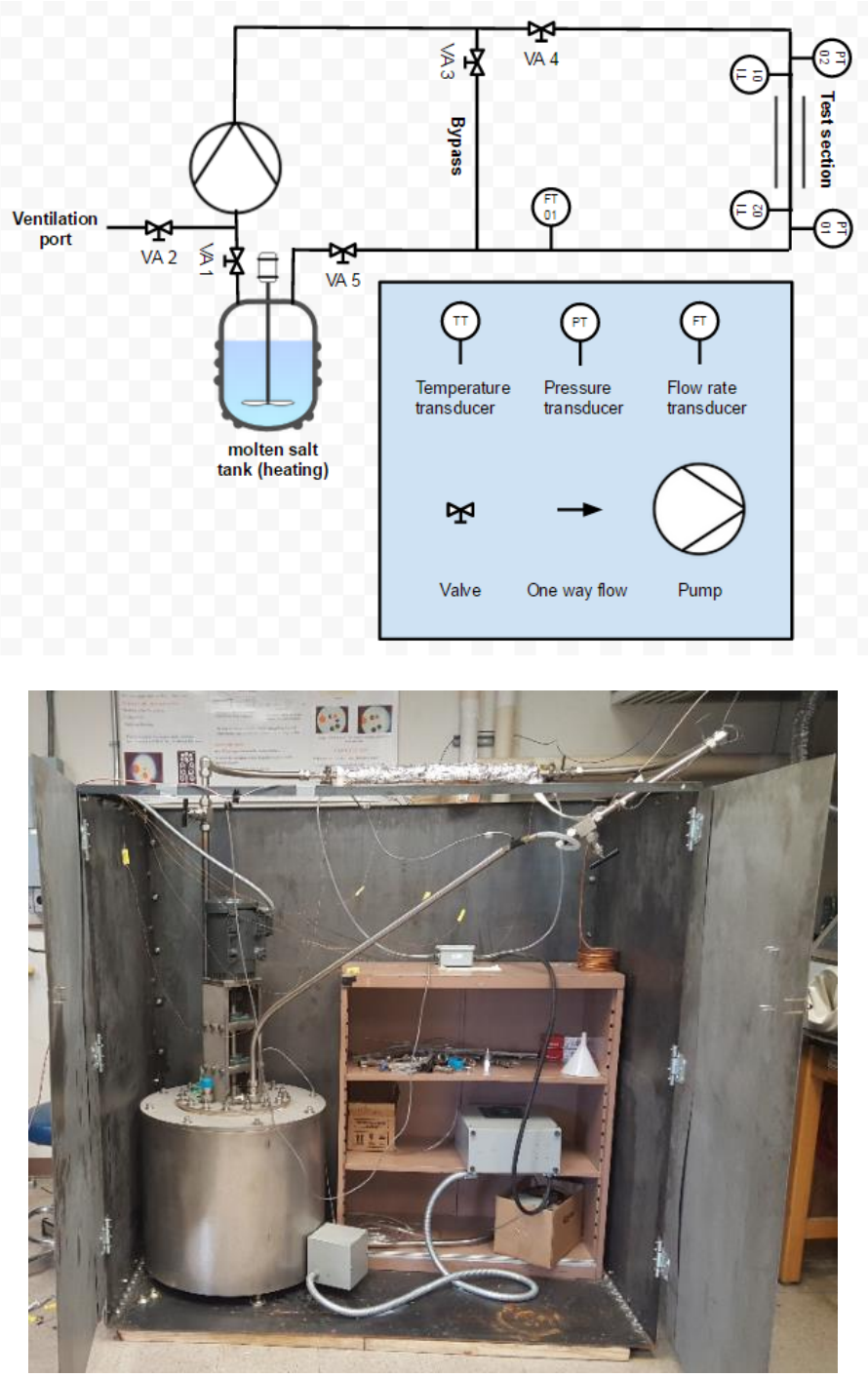

Figure 34. (a) Schematic diagram of flow loop design (top); (b) Actual flow loop system (bottom)

2.7 Summary

In this chapter, experimental methods were developed for exploring material properties and heat transfer performances of molten salt nanofluids. Both two-step and one-step methods were adopted to prepare the nanofluid sample based on binary $NaNO_3$-KNO_3 eutectic. The specific heat capacity of the nano-samples was measured using both MDSC method (with commercial instrument) and T-History method (with customized setup). The thermal conductivity of nano-samples was measured using a customized concentric cylindrical chamber with 1-D radial conduction assumption. The corrosivity of molten salt nanofluids were evaluated using "coupon bomb" design followed by ASTM descaling protocols. The thermal stability of molten salt nanofluids were evaluated with mass reduction test performed at elevated temperature (565°C) in furnace. A customized high temperature flow loop system was designed and constructed for testing the heat transfer performance of molten salt nanofluid.

3. EXPERIMENTAL RESULTS: THERMO-PHYSICAL PROPERTIES OF MOLTEN SALT NANOFLUID

3.1 Pure solar salt ($NaNO_3$-KNO_3 eutectic)

In order to evaluate the level of enhancement in the material properties of molten salt nanomaterials, the thermo-physical properties of the base material (pure solar salt) was measured. The synthesis of the pure solar salt followed the same approach described in Section 2.1 where the two salt powders ($NaNO_3$ and KNO_3) were mixed in beaker with 60:40 mass ratio and heated in furnace at 550ºC for one hour. After the heating cycle, a homogeneous eutectic mixture of $NaNO_3$ and KNO_3 in molten state was formed in the beaker. The specific heat capacity and thermal conductivity of pure solar salt was then measured using MDSC and customized apparatus for thermal conductivity measurements (as described in the previous chapter).

3.1.1 Specific heat capacity

The MDSC measurements were performed independently by collaborators in the research group of Dr. D. Shin at the University of Texas Arlington to cross-check the measurements performed in this study. The specific heat capacity of pure solar salt was measured using MDSC from 150ºC to 500ºC for a temperature ramping rate of 4ºC/minute. The measurement was repeated for four consecutive cycles of melting and solidification (the results are illustrated in Figure 35 and summarized in Table 9). The measured values are observed to show good repeatability with an average specific heat capacity of 1.467 J/(g·K) at 300ºC. The specific heat increases slightly with increasing temperature. This is

supported by the fact that the average values of specific heat capacity (in the temperature range of 250ºC to 500ºC) are slightly higher than the measured values at 300 ºC. These results are in good agreement with the literature value of 1.48 J/(g·K) [99].

The melting point and phase change enthalpy (latent heat) were also derived from isotherms obtained from the DSC experiments. The melting point is represented by the temperature at which the specific heat capacity reaches a maximum value while the latent heat was calculated by integrating specific heat with temperature in the phase change region of the isotherms. The results from the repeated cycles shows good consistency in the values of both the melting point and latent heat. The average values of melting point and latent heat of pure solar salt eutectic was found to be 223.5ºC and 121.8 J/g which is also in good agreement with the values reported in the literature [30].

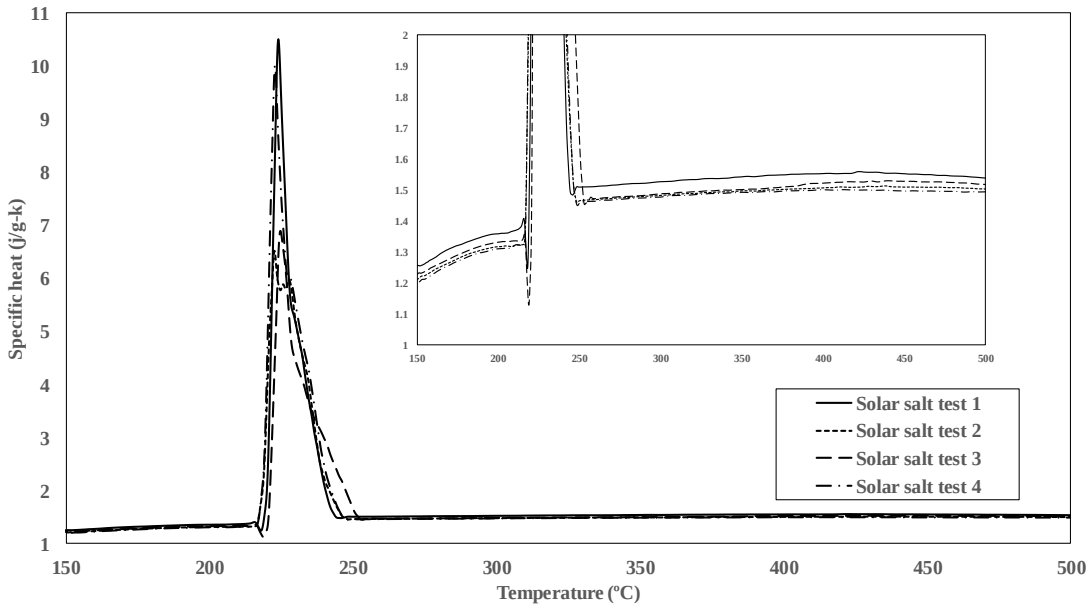

Figure 35. DSC curve for pure molten solar salt (courtesy of Dr. D. Shin research group at the University of Texas at Arlington)

Table 9. Specific heat measurement results for pure solar salt

Test No.	Specific Heat Capacity at 300ºC [J/(g·K)]	Average Specific Heat Capacity from 250ºC to 500 ºC [J/(g·K)]	Melting Point (ºC)	Latent Heat [J/g]
1	1.527	1.540	223.98	119.5
2	1.483	1.497	222.63	117.2
3	1.488	1.508	224.70	117.3
4	1.477	1.489	222.82	133.2
Average	1.494	1.509	223.53	121.8
Standard Deviation	1.3%	1.3%	0.4%	5.5%

3.1.2 Thermal conductivity

The thermal conductivity of pure solar salt was measured at three different temperatures (300 ºC, 400 ºC, 500 ºC) using the steady state 1-D radial conduction equation described in Chapter 2. At each temperature, the testing chamber was soaked in a furnace for 12 hours to ensure that the system reaches steady state. After that the temperature drop across the four pairs of thermocouples in the testing chamber were recorded for 1 hour and used for calculating thermal conductivity. Figure 37 shows the experimental results for three different temperature set points. The experimental results obtained at 300 ºC are observed to be consistent for the recordings obtained from the four pairs of thermocouples. However, the experimental results obtained at 400 ºC and 500 ºC show large variations in temperature difference between a few of the four pairs of thermocouples. This is potentially due to non-uniform radiation heat transfer between the walls of the furnace and the test apparatus. The average values of thermal conductivity

were calculated from the temperature measurements recorded by the four pairs of thermocouples (i.e., the temperature differences at each radial location) and the results are summarized in Table 10 and Figure 36. The thermal conductivity values of pure solar salt increases marginally between 300ºC to 500ºC with an average value of 0.505 W/(m·K). Literature studies have shown large variation in the values of thermal conductivity for solar salts. Considering the variations in the values of thermal conductivity reported in the literature, the experimental measurements obtained from this study are consistently are within the range of values of reported in the literature.

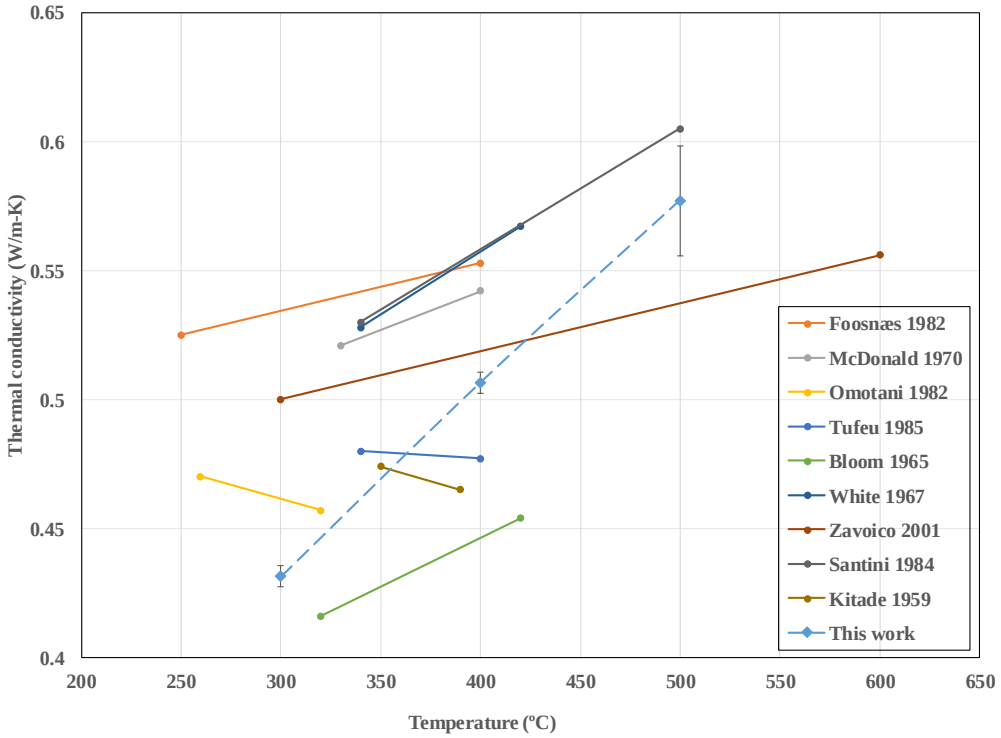

Figure 36. Comparison of solar salt thermal conductivity measurements obtained in this study with that of the literature

Table 10. Thermal conductivity measurement results for pure solar salt

Temperature (ºC)	Thermal conductivity [W/(m·K)]	Standard Deviation
300	0.431	0.9%
400	0.507	0.8%
500	0.577	3.6%
Average	0.505	11.9%

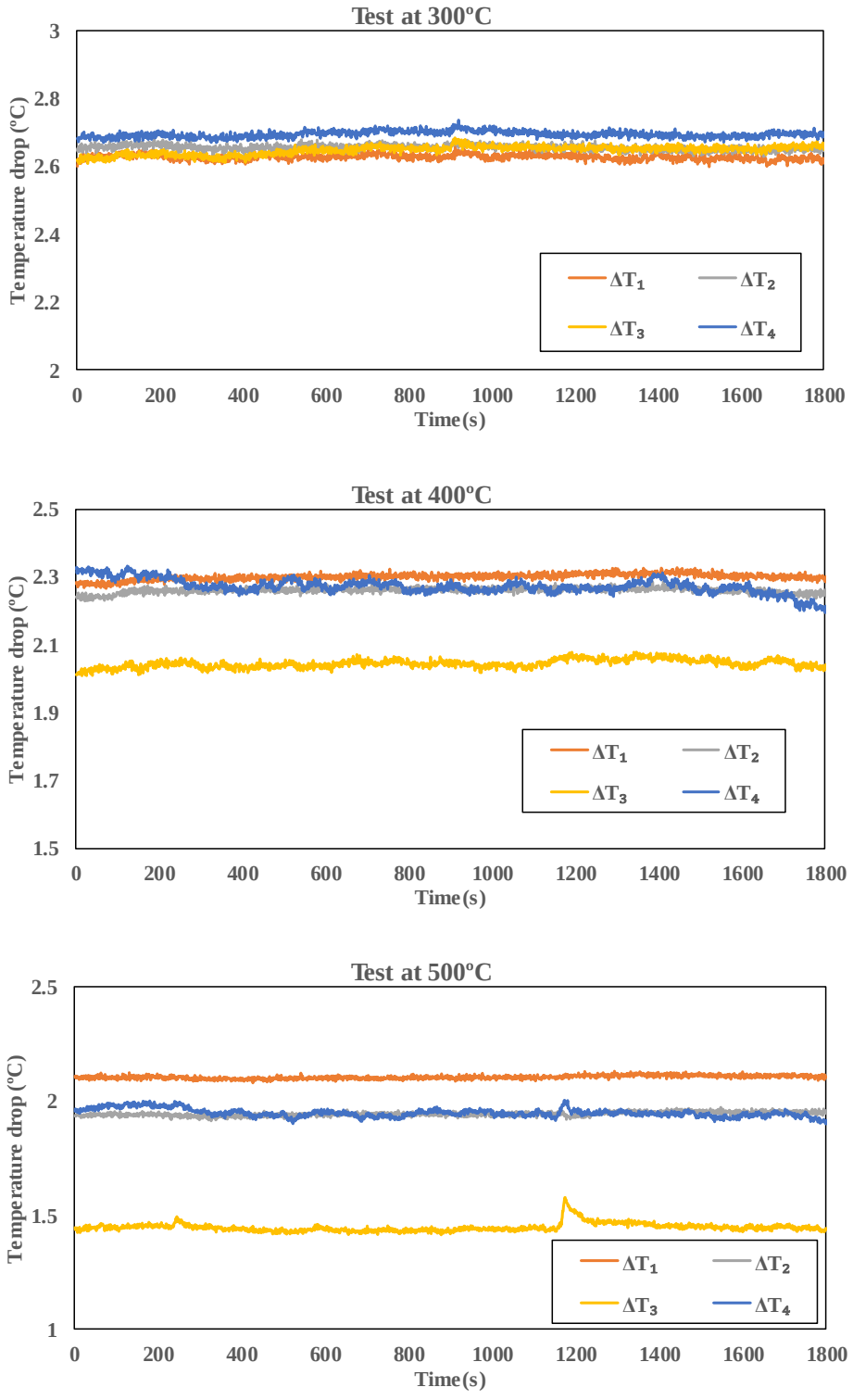

Figure 37. Measurements of temperature drop in thermal conductivity tests

3.1.3 Material characterization

Figure 38 shows the SEM image of pure solar salt from 4500x to 33000x magnifications. The images show the crystal grain boundaries in the pure salt and smooth surfaces of the crystal faces within the grain boundaries. No significant surface defects or particle clusters were observed in the pure salt sample. Such morphology is typical of inorganic salt crystals.

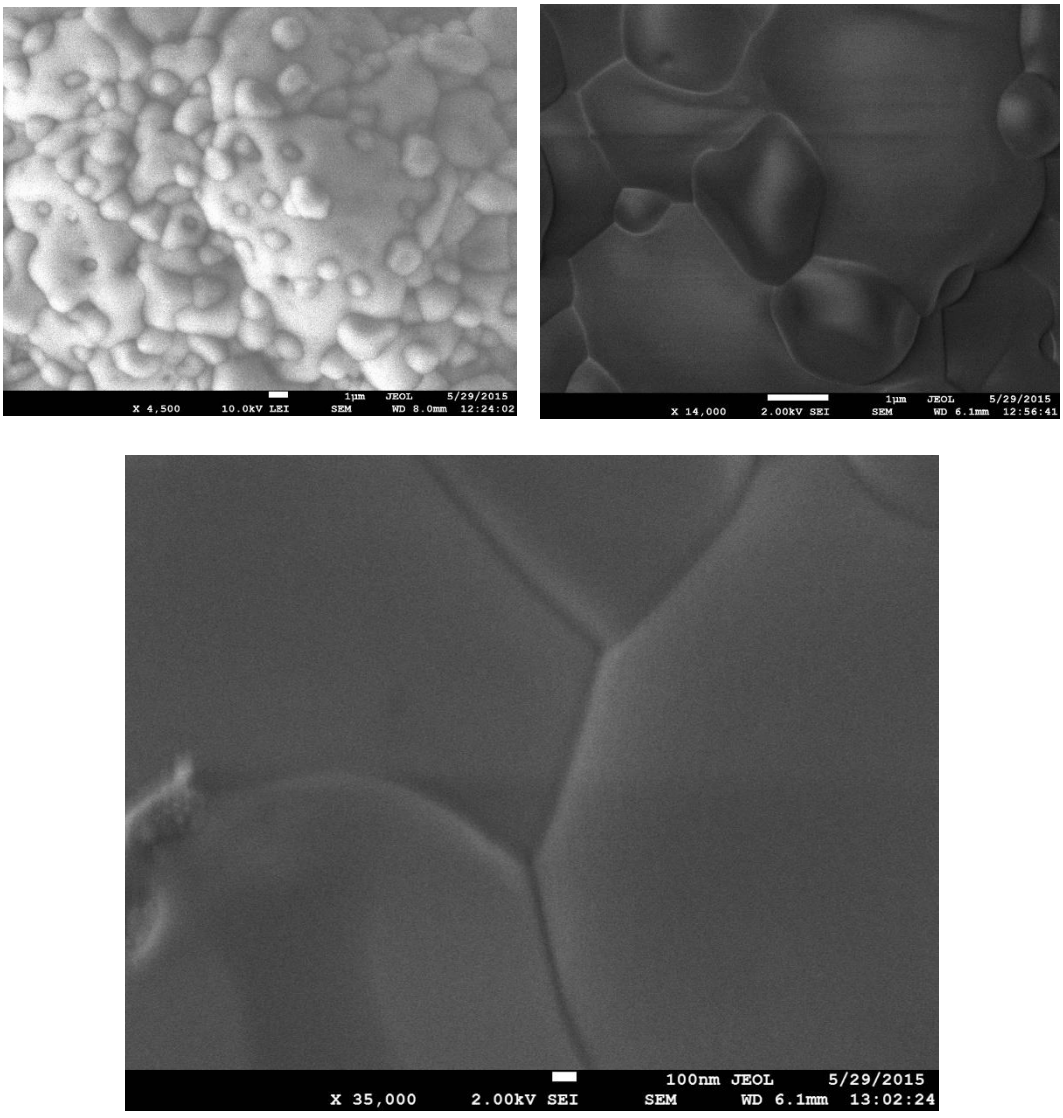

Figure 38. SEM images of pure solar salt crystal

3.2 Two step synthesis of molten salt nanofluids (SiO_2 nanoparticles)

Molten solar salt nanofluid samples were synthesized by mixing SiO_2 nanoparticles (i.e., using the traditional two-step mixing method as discussed in Chapter 2). In this synthesis protocol 35g solar salt nanofluid was realized by mixing SiO_2 nanoparticles at 1.0% mass concentration. This involved mixing 20.79 g $NaNO_3$ and 13.86 g KNO_3 were weighed and dissolved in distilled water along with 0.35 g of SiO_2 nanoparticles (5~15 nm). The nanoparticles and salts were procured from Sigma Aldrich. The mixture solution was then ultra-sonicated for 3 hours and dehydrated on hot plate at 120°C for realizing the solid state of the molten salt nanofluid.

The specific heat capacity of the synthesized solar salt nanofluid samples (with SiO_2 nanoparticles) was measured using T-History method and subsequently verified using MDSC method (assistance of Dr. D. Shin and collaboration with his research group at the University of Texas at Arlington is gratefully acknowledged for the MDSC measurements). The thermal conductivity of the samples was tested using a customized concentric cylindrical chamber apparatus (as mentioned in Chapter 2). Materials characterization of the salt samples was performed using electron microscopy techniques (i.e., the morphology of the microstructures in the solid state of the molten salt nanofluid samples was examined using SEM).

3.2.1 Specific heat capacity

3.2.1.1 T-History method

Figure 39 shows the results obtained from the one cycle of T-History experiments for both pure solar salt samples and solar salt nanofluid samples (containing SiO_2 nanoparticles with a nominal size of 5~15 nm). The salt samples were heated from 270 ºC to 550 ºC in these experiments and the temperature of these samples were plotted as a function of time. The plot show that the temperature of the pure salt sample increased at a faster rate compared to that of the molten salt nanofluid samples. At any instant in time the temperature of the pure salt sample is observed to be always higher than that of the nanofluid sample. The slower heating response of nanofluid sample under same external heating condition indicates that the nanofluid sample has a higher thermal storage capacity compared to that of the pure solar salt. The tests were repeated for ten cycles continuously (the detailed temperature ramping curves are shown in Appendix B). The results from each cycle show the same trend where at any instant in time the temperature of the pure solar salt samples was higher than that of the nanofluid samples. The values of specific heat capacity ratio (between nanofluid samples and pure salt samples) were calculated according to Equation 14 and plotted in Figure 40.

The results from repeated tests showed that the first three testing cycles yielded much higher values of specific heat capacity enhancement of the nanofluid samples (with average values in excess of 15% with standard deviation of 1~2 %). However, in subsequent cycles the average enhancement was typically less than 15% (with standard deviation of 1~3 %). This could possibly occur from the progressive agglomeration of the

nanoparticles with each cycle for the first three cycles followed by equilibration of the nanoparticles in the subsequent cycles. The specific heat capacity enhancement increases marginally with increasing temperature. The average enhancement of the specific heat capacity of the solar salt nanofluid samples (with SiO_2 nanoparticles of 5~15 nm nominal diameter at 1% mass concertation) was 9.3% over that of the pure solar salt samples.

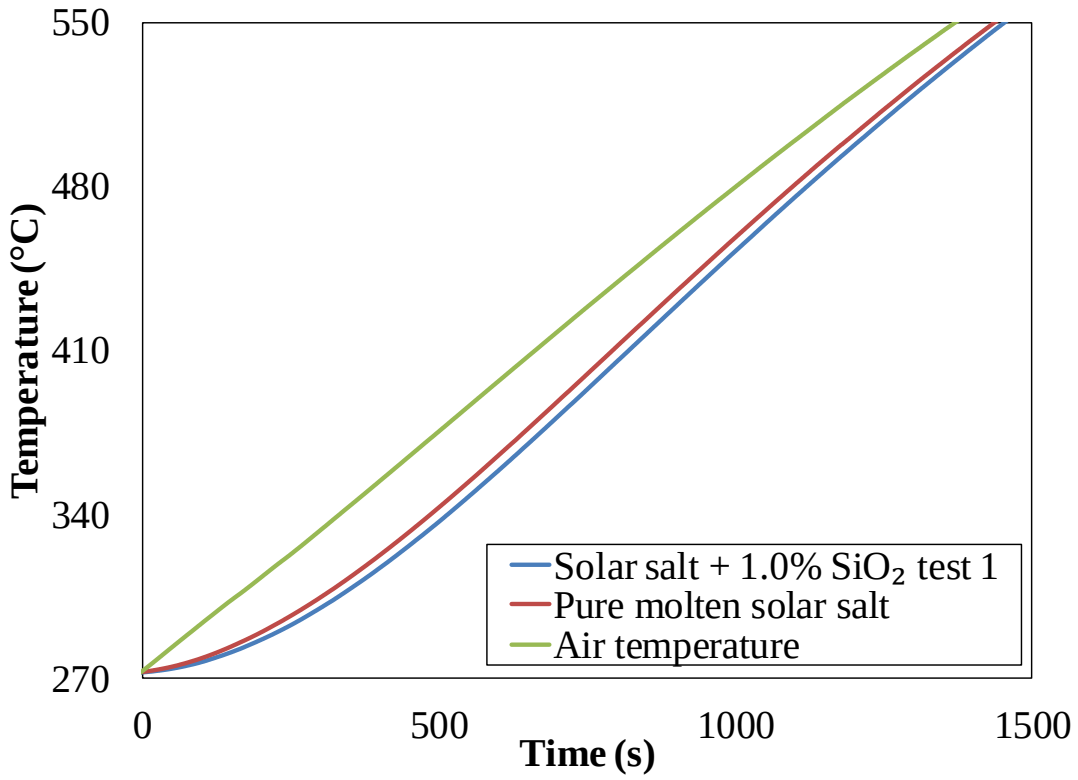

Figure 39. Plot of temperature response obtained from T-History experiments for thermocouples places in air (in the furnace), pure solar salt samples and solar salt nanofluids containing SiO_2 nanoparticles (with initial nominal diameter of 5 ~ 15 nm) at a mass concentration of 1.0%.

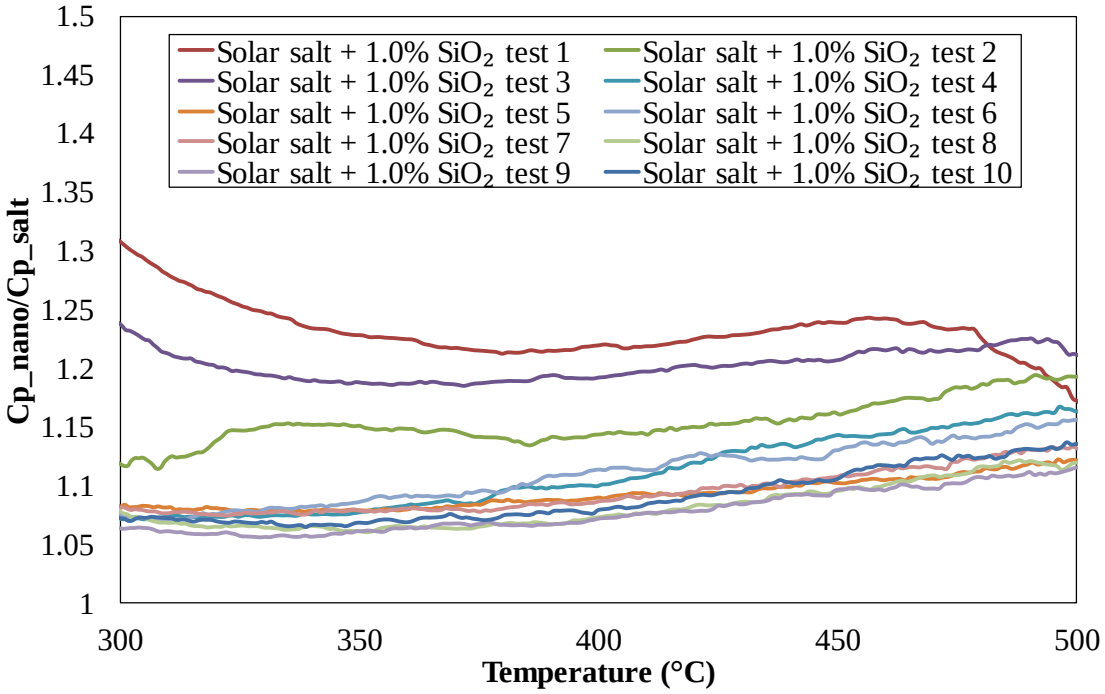

Figure 40. Plot of specific heat capacity ratio as a function of temperature (obtained from T-History experiments). The specific heat capacity of pure solar salt samples is compared to that of the molten salt nanofluid samples containing SiO_2 nanoparticles (with initial nominal diameter of 5 ~ 15 nm) at a mass concentration of 1.0%.

Table 11. Values of specific heat capacity enhancement for different cycles are listed as a function of temperature (obtained from T-History experiments). The specific heat capacity of pure solar salt samples is compared to that of the molten salt nanofluid samples containing SiO_2 nanoparticles (with initial nominal diameter of 5 ~ 15 nm) at a mass concentration of 1.0%.

Test number	300ºC	400ºC	500 ºC	Average	Standard Deviation
1	30.7%	22.0%	17.2%	23.4%	2.4%
2	11.9%	14.4%	19.3%	15.3%	1.9%
3	23.9%	19.3%	21.2%	20.4%	1.3%
4	7.3%	10.0%	16.4%	10.9%	3.2%
5	8.3%	9.0%	12.1%	9.3%	1.3%
6	7.5%	11.4%	15.7%	10.9%	2.6%
7	8.2%	8.7%	13.2%	9.4%	1.8%
8	7.8%	7.3%	12.0%	8.1%	1.9%
9	6.4%	7.2%	11.6%	7.8%	1.8%
10	7.2%	7.9%	13.6%	8.9%	2.2%
Average (for tests 4-10)	**7.5%**	**8.8%**	**13.5%**	**9.9%**	**1.8%**
Standard Deviation (for tests 4-10)	0.6%	1.4%	1.7%	1.1%	0.6%
Average (for tests 1-10)	***11.9%***	***11.7%***	***15.2%***	***13%***	***2%***
Standard Deviation (for tests 1-10)	8%	4.9%	3.1%	5.2%	0.6%
Average (for tests 1-3)	***22.2%***	***18.6%***	***19.2%***	***20%***	***1.9%***
Standard Deviation (for tests 1-3)	7.8%	3.1%	1.6%	3.3%	0.4%

3.2.1.2 MDSC Measurements

MDSC experiments were performed to validate the results obtained from the T-History experiments for the specific heat capacity measurements for the pure solar salt samples and solar salt nanofluid samples (containing SiO_2 nanoparticles with initial nominal diameter of 5~ 15 nm at a mass fraction of 1%). The same samples were prepared using the same protocol as the T-History measurements (mentioned in the previous section) and used for performing the MDSC experiments to measure the specific heat capacity. The MDSC measurements were performed independently by collaborators in the research group of Dr. D. Shin at the University of Texas Arlington to cross-check the measurements performed in this study. The measurements were performed three times on each of the three separate samples. The results from the MDSC measurements are listed in Table 12 and plotted in Figure 41. The results for the specific heat capacity measurements from the MDSC experiments have lower values of measurement uncertainty (0.1~0.2%) compared to that of the T-History experiments (1~3%). The results from the MDSC experiments show that the average value of specific heat capacity measurements was enhanced 10.4% when pure solar salt samples were mixed with SiO_2 nanoparticles (with initial nominal diameter of 5~15 nm) at a mass concentration of 1%. Hence, the results of the specific heat capacity measurements show that the T-History experiments (average enhancement of 9.9% with standard deviation of 1.1%) are consistent with the MDSC experiments (average enhancement of 10.4% with standard deviation of 1.7%).

Table 12. Values of specific heat capacity for different cycles are listed as a function of temperature (obtained from MDSC experiments). The specific heat capacity of pure solar salt samples is compared to that of the molten salt nanofluid samples containing SiO_2 nanoparticles (with initial nominal diameter of 5 ~ 15 nm) at a mass concentration of 1.0%.

Test number	Specific heat capacity [J/(g·K)]	Enhancement (%)	Uncertainty (%)
1	1.700	12.7%	0.126
2	1.663	10.2%	0.169
3	1.706	13.1%	0.118
4	1.636	8.4%	0.134
5	1.617	7.2%	0.156
6	1.687	11.8%	0.154
7	1.67	10.7%	0.195
8	1.677	11.1%	0.112
9	1.635	8.3%	0.240
Average	1.666	10.4%	0.163
Standard Deviation	1.7%	1.9%	

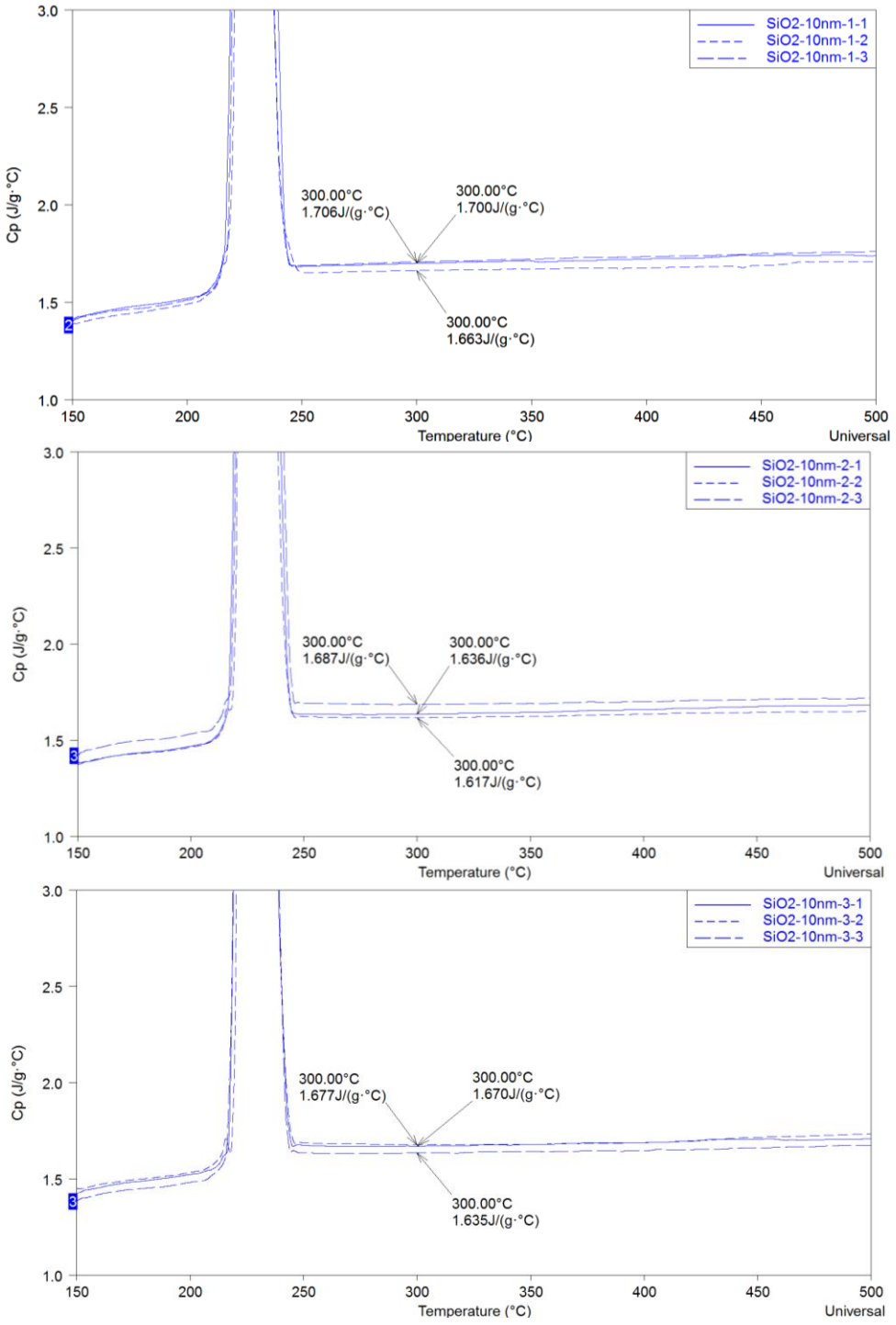

Figure 41. Plot of specific heat capacity as a function of temperature (obtained from MDSC experiments) for nanofluid samples containing SiO_2 nanoparticles (with initial nominal diameter of 5 ~ 15 nm) at a mass concentration of 1.0% (courtesy of Dr. D. Shin research group at the University of Texas at Arlington).

3.2.2 Thermal conductivity

The thermal conductivity of solar salt nanofluid samples (containing SiO_2 nanoparticles at a mass fraction of 1.0% with initial nominal diameter in the range of 5 ~ 15 nm) were measured at three different temperatures (300ºC, 400ºC, and 500ºC) using the same technique discussed earlier in Chapter 2 (i.e., using a concentric cylinder test apparatus). The average values of thermal conductivity were calculated from the average values of temperature drop recorded by the four pairs of thermocouples and are summarized in Table 13 and Figure 42.

Figure 43 shows the measurement of temperature drop at steady state conditions from the four pairs of thermocouples (the measurements were performed at three temperatures set points). A small deviation of the values of temperature drop is observed between the different pairs of thermocouples which suggests that the radial heat conduction may vary slightly in different circumferential locations. However, the average values of the measured temperature drops could still be used for calculating the representative values for the thermal conductivity of the molten salt samples under different temperature conditions since this deviation (i.e., depending on circumferential location) is small compared to the values of the temperature drop in the radial direction.

The results show that the thermal conductivity of both the pure solar salt samples and the nanofluid samples increases monotonously with increasing temperature from 300ºC to 500ºC (which is typical of most liquids). The result also showed high uncertainty in thermal conductivity measurements for the nanofluid samples. Considering the average values of the measurements the results show that the thermal conductivity was enhanced

by 34% (with a standard deviation of 17.5) for the nanofluid samples compared to that of the pure solar salt samples. For the range of temperatures used in the measurements the enhancement varied from 32 ~ 36% (with standard deviation in the range of 7.8 ~ 14.1%).

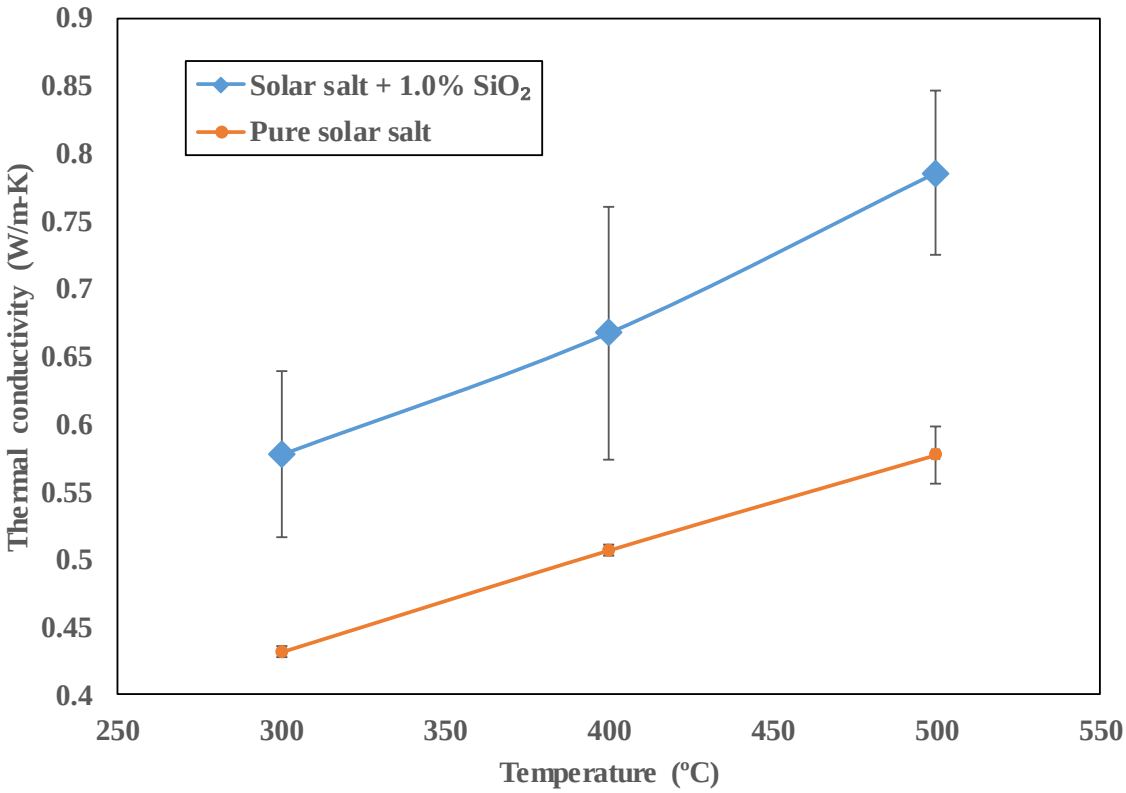

Figure 42. Plot of thermal conductivity as a function of temperature for pure solar salt samples and molten salt nanofluid samples containing SiO_2 nanoparticles (with initial nominal diameter of 5 ~ 15 nm) at a mass concentration of 1.0%.

Table 13. Thermal conductivity as a function of temperature for pure solar salt samples and molten salt nanofluid samples containing SiO_2 nanoparticles (with initial nominal diameter of 5 ~ 15 nm) at a mass concentration of 1.0%.

Temperature (°C)	Solar salt nanofluid		Pure solar salt		Enhancement (%)
	k [W/(m·K)]	Standard Deviation	*k* [W/(m·K)]	Standard Deviation	*k* [W/(m·K)]
300	0.577	10.7%	0.431	0.9%	33.9%
400	0.667	14.1%	0.507	0.8%	31.8%
500	0.786	7.8%	0.577	3.6%	36.2%
Average	0.677	12.9%	0.505	11.9%	34.1%

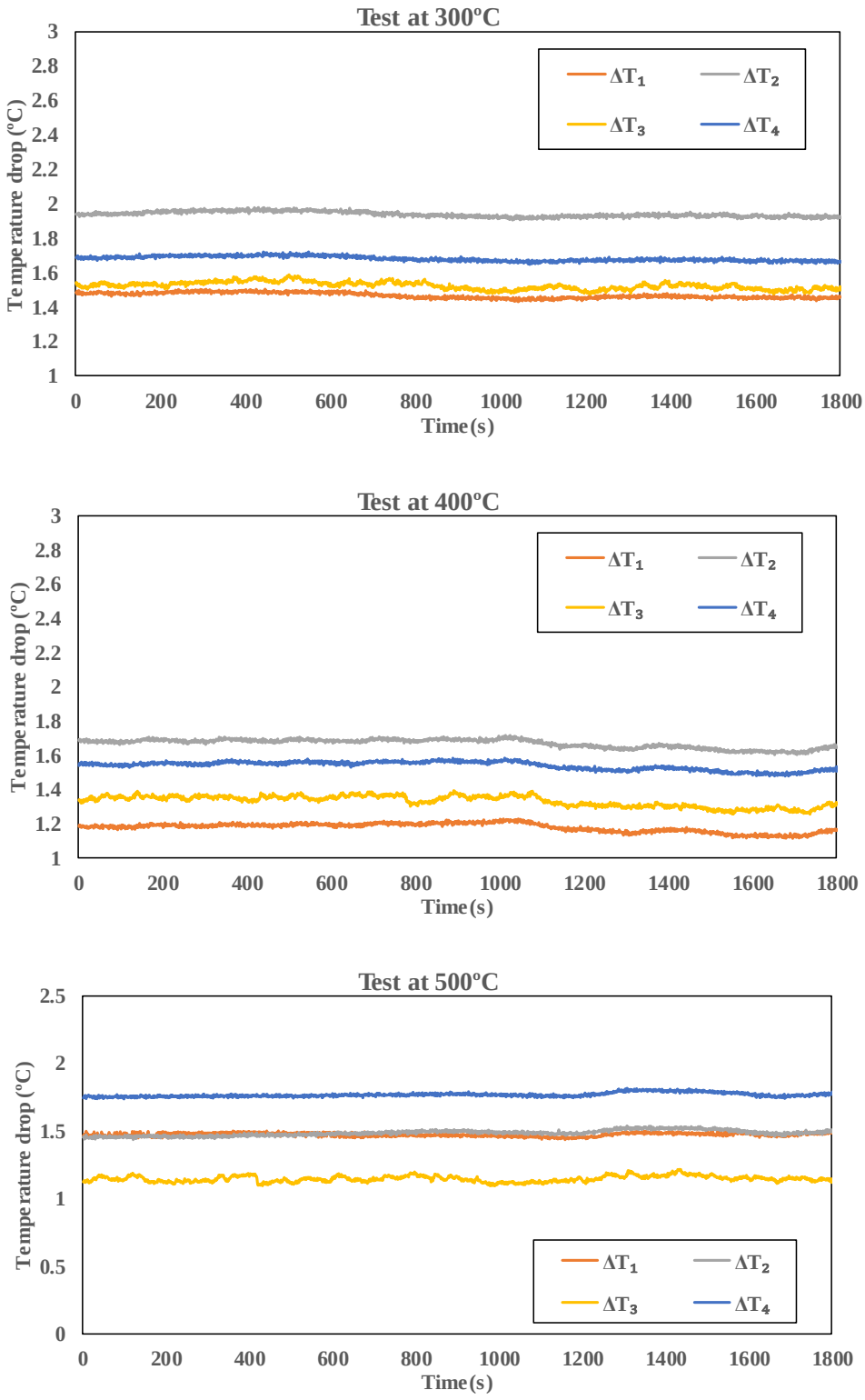

Figure 43. Measurements of temperature drop in thermal conductivity tests

3.2.3 Material characterization

Materials characterization was performed for the nanofluid samples using SEM as shown in Figure 44 below. The images show clusters of SiO_2 nanoparticles. Magnified images showed that the average size of nanoparticles is in the range of 15~50 nm (which is consistent with the size distribution specified by the manufacturer). EDS (Energy Dispersive X-Ray Spectroscopy) of the salt samples was performed using the SEM apparatus.

The portions of the salt samples containing elevated levels of Si (as shown in the EDS plots), i.e., portions of the salt sample containing SiO_2 nanoparticles induced the formation of secondary nanostructures in the salt phase. To elaborate further on this observation, as shown in the EDS plots, Spectrum 1 has lower levels of Si (which implies absence of SiO_2 nanoparticles) and the portion of the sample corresponding to Spectrum 1 does not show the existence of any secondary nanostructures. This shows that in the absence of the nanoparticle the salt does not form any secondary nanostructures. In contrast, Spectrum 2 shows significant elevation in the level of Si (which implies presence of SiO_2 nanoparticles). The portion of the sample corresponding to Spectrum 2 thus contains SiO_2 nanoparticles and shows the formation of secondary nanostructures in the form of "cauliflower" shapes in the salt material. Prior reports in the literature have also shown that the presence of these secondary nanostructures is essential for the enhancement in the specific heat capacity of the nanofluid samples ([78] [84] [100]). The SEM images show that the diameters of the nanoparticles to be in the range of 10 ~ 50 nm thus implying

partial agglomeration of the nanoparticles (since the initial range of diameters was 5 ~ 15 nm, according to manufacturer specification).

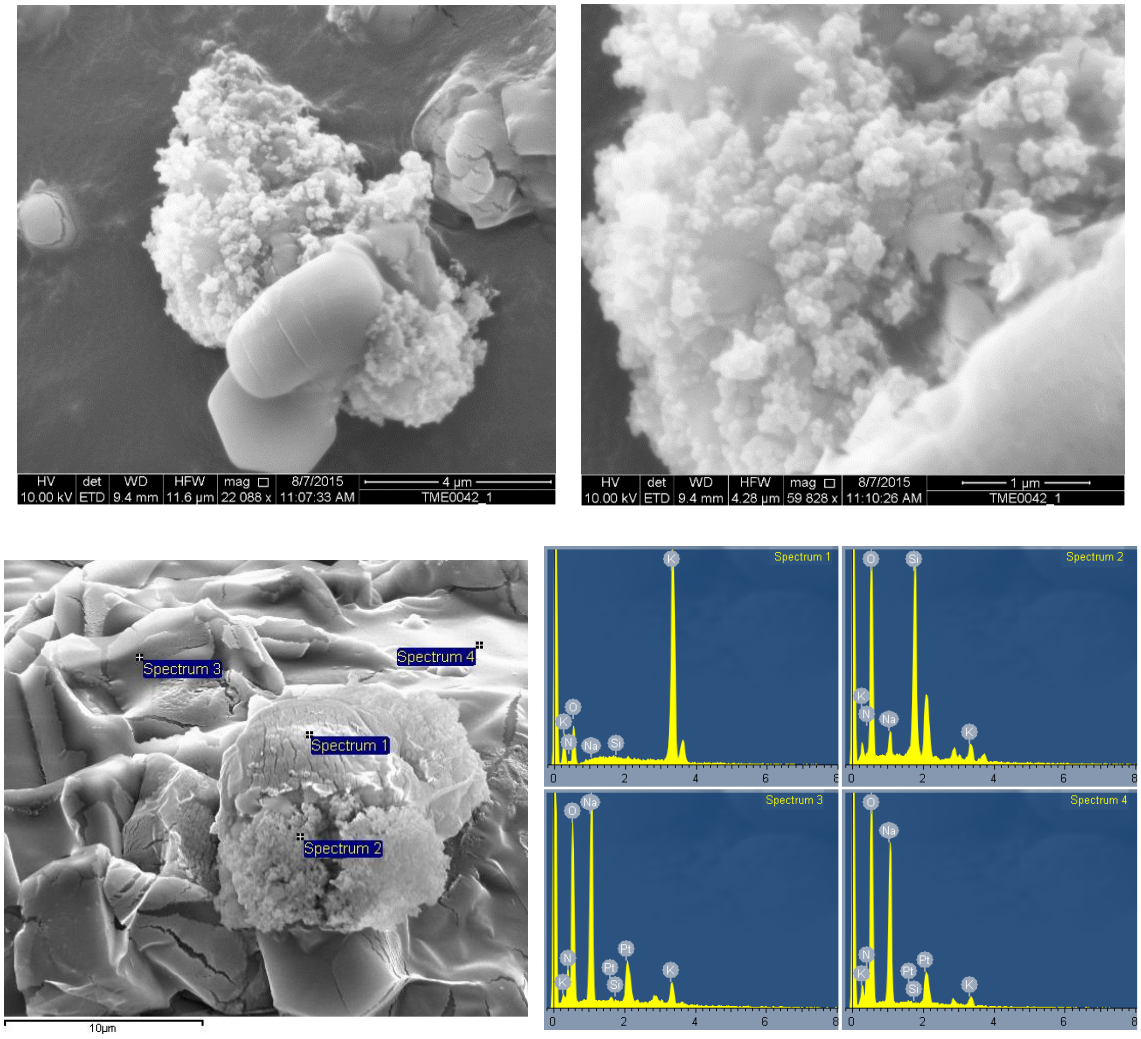

Figure 44. SEM images of molten salt (solar salt) nanofluid samples containing SiO_2 nanoparticles with initial nominal diameter of 5 ~ 15 nm at a mass concentration of 1.0% (top row and bottom left). The images show nanoparticle diameters to be in the range of 10 ~ 50 nm. Elemental analysis of the different regions in the images are obtained by using EDS (bottom right).

3.3 One-step synthesis of nanofluids (targeting Al_2O_3 nanoparticles)

Nanofluids were realized by employing a novel one-step synthesis protocol where additives (which are nanoparticle precursors) were mixed with pure molten salt samples (solar salt). When heated above a critical temperature the precursors disintegrated (thermal decomposition technique) to yield nanoparticles in-situ which were inherently dispersed in the molten salt samples.

In this study Al_2O_3 nanoparticles were synthesized in-situ in solar salt using the one-step thermal decomposition method from $Al(NO_3)_3 \cdot 9H_2O$ additive (nanoparticle precursors). The synthesis protocol was described in Chapter 2: involving thermal decomposition of the precursor that was mixed with the solar salt powder prior to heating in a furnace at 550ºC for 1 hour. Based on thermogravimetric (TGA) analysis of pure $Al(NO_3)_3 \cdot 9H_2O$ (Figure 13), the ultimate decomposition temperature of this precursor is estimated to be around 400ºC. Hence the thermal cycling implemented in this test here should ensure the completion of the thermo-chemical decomposition of the precursor, i.e., $Al(NO_3)_3 \cdot 9H_2O$ and yield Al_2O_3 nanoparticles. In this test, the target mass concentration of the Al_2O_3 nanoparticle is 1% and the amount of $Al(NO_3)_3 \cdot 9H_2O$ precursor needed was calculated accordingly as shown in Table 14. All mass concentration values were calculated with respect to the total sample mass.

Table 14. Mass of raw material needed for synthesis

	Raw material mass (g) for synthesis			Final product mass (g)		
Target nanoparticle concentration	$NaNO_3$	KNO_3	$Al(NO_3)_3 \cdot 9H_2O$	Solar salt	Al_2O_3	Total
1.0%	20.790	13.86	2.575	34.650	0.350	35

Electron microscopy images were obtained after the heating cycle (i.e., thermal decomposition of the additive) to check the size distribution of the resulting nanoparticles synthesized in-situ using the one-step synthesis protocol. The specific heat capacity values of these nanofluid samples were measured using T-History method and these results were further validated independently using MDSC experiments in another experimental facility. The thermal conductivity of the nanofluid samples synthesized in-situ using the one-step synthesis protocol were also measured using a customized concentric cylinder testing apparatus.

3.3.1 Specific heat capacity

3.3.1.1 T-History method

T-History experiments were conducted by repeated melting and solidification of the molten salt nanofluid samples. The measurements were repeated for 10 times (i.e., for 10 consecutive thermocycles) by ramping up and down the temperature of the furnace from an initial temperature of 250 ºC to a final temperature of 550 ºC. Figure 45 shows the temperature recorded by thermocouples immersed in the pure solar salt sample and nanofluid sample (for test 1) as the air temperature of the furnace was ramped from an initial temperature of 250 ºC to a final temperature of 550 ºC. The results show that starting from the same initial temperature (i.e., after thermal equilibration at 250 ºC), the temperature of the nanofluid sample increased at a slower rate than the pure solar salt sample. Hence, at any given instant, the solar salt sample was at a higher temperature than the nanofluid sample. Since both samples have similar values of mass and volume (for

both the pure solar salt samples and the nanofluid samples), the faster temperature response indicates that the pure solar salt samples have a lower heat storage capacity (specific heat capacity) compared to the nanofluid samples.

The temperature response of the nanofluid samples and the pure solar salt samples can be used for quantitative analysis for derivation of the specific heat capacity ratio using the procedure outlined in Chapter 2 and Equation 14. The temperature ramp rate and natural convection heat flux was calculated based on the recorded temperature history curves and used for the determination of the specific heat capacity ratio. The results are summarized in Figure 46 and Table 15.

It was observed that for each cycle (for the 10 cycles used for repeated measurements) there is a significant enhancement in the specific heat capacity of the nanofluid samples compared to that of the pure solar salt samples. The enhancement values are consistent for each cycle – thus demonstrating good repeatability of the experiments (the detailed temperature response of other 9 cycles can be found in Appendix C). It should also be noted that marginal deviation in enhancement values occurs for tests performed at 300ºC. This deviation is reduced as the temperature is increased. This is potentially due to more uniform thermal equilibration and uniformity of temperature distribution being achieved in the salt samples at higher temperatures. The average enhancement in the values of the specific heat capacity is 41% on treating the pure solar salt samples with additive (with a standard deviation of 2.1%).

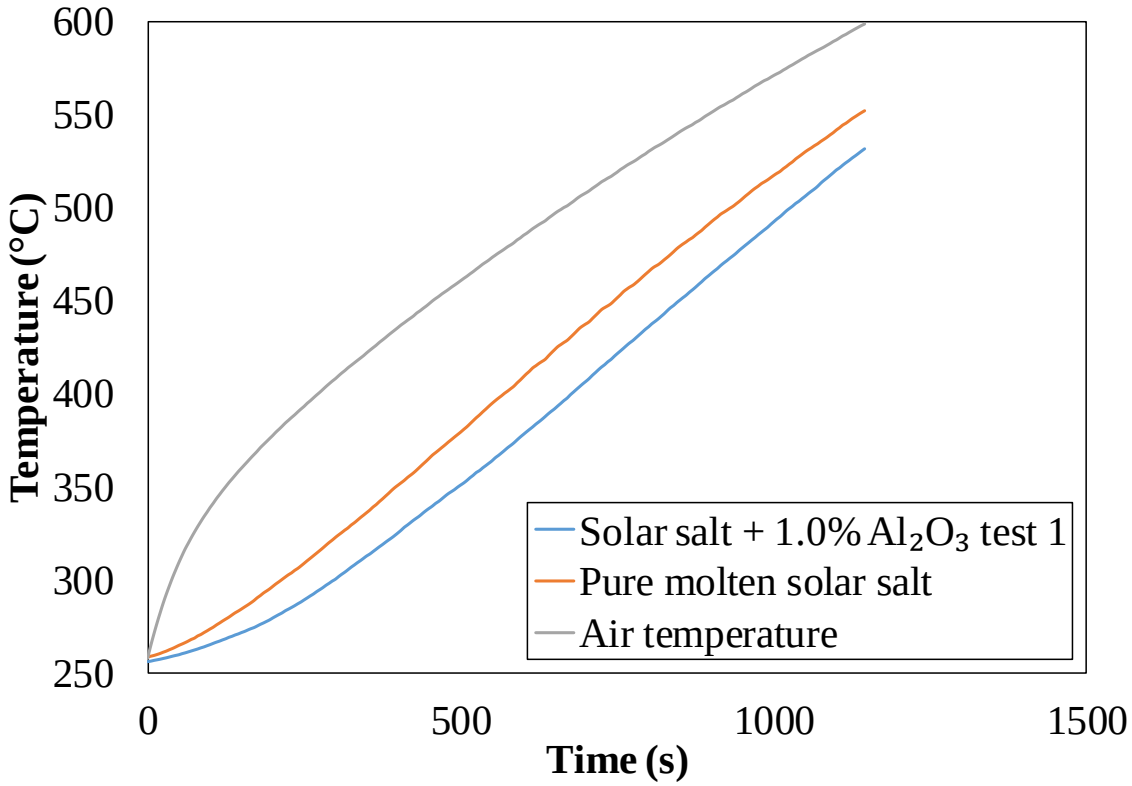

Figure 45. Plot of temperature response obtained from T-History experiments for thermocouples places in air (in the furnace), pure solar salt samples and solar salt nanofluid samples (prepared using one-step synthesis protocol). The molten salt nanofluid samples were obtained by adding $Al(NO_3)_3 \cdot 9H_2O$ at 6.9% mass fraction (as nanoparticle precursors for yielding nanofluids) to pure solar salt for a target mass fraction of 1% for the resulting Al_2O_3 nanoparticles obtained by thermal decomposition (one-step synthesis protocol)

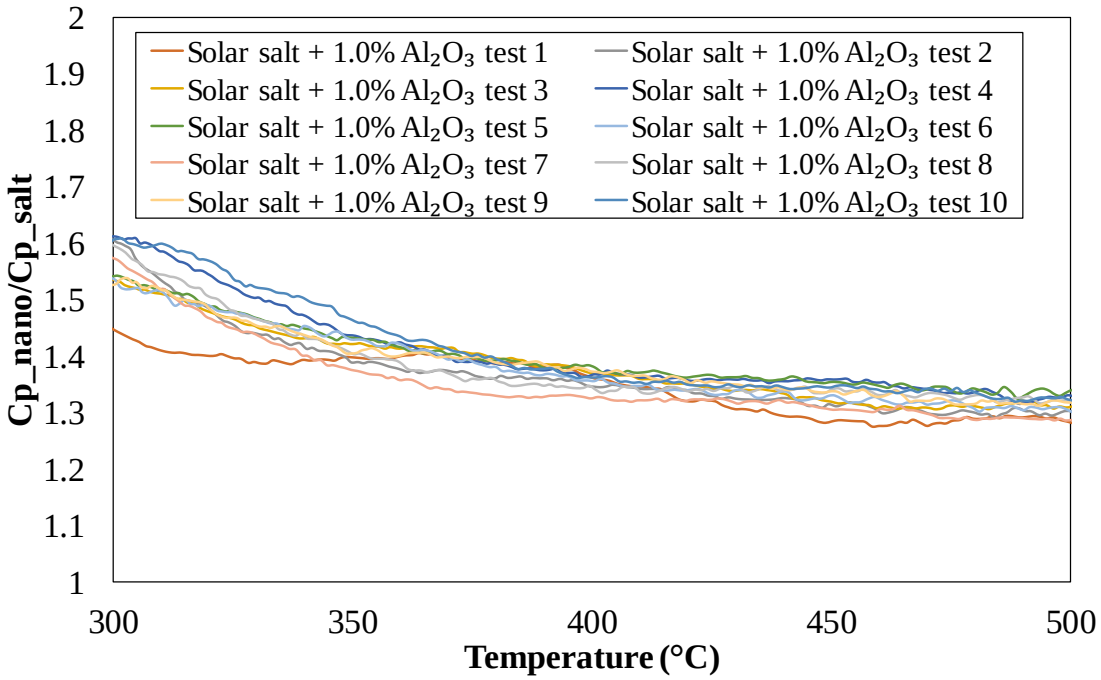

Figure 46. Plot of specific heat capacity ratio as a function of temperature (obtained from T-History experiments). The specific heat capacity of pure solar salt samples is compared to that of the solar salt nanofluid samples (prepared using one-step synthesis protocol). The molten salt nanofluid samples were obtained by adding $Al(NO_3)_3 \cdot 9H_2O$ at 6.9% mass fraction to pure solar salt for a target mass fraction of 1% for the resulting Al_2O_3 nanoparticles obtained by thermal decomposition (one-step synthesis protocol)

Table 15. Specific heat capacity enhancement as a function of temperature (obtained from T-History experiments). The specific heat capacity of pure solar salt samples is compared to that of the solar salt nanofluid samples (prepared using one-step synthesis protocol). The molten salt nanofluid samples were obtained by adding $Al(NO_3)_3 \cdot 9H_2O$ at 6.9% mass fraction to pure solar salt for a target mass fraction of 1% for the resulting Al_2O_3 nanoparticles obtained by thermal decomposition (one-step synthesis protocol)

Test number	300ºC	400ºC	500 ºC	Average	Standard Deviation
1	44.5%	36.0%	28.1%	35.1%	5.1%
2	60.3%	34.7%	30.3%	37.6%	7.7%
3	53.6%	37.0%	31.2%	38.7%	6.7%
4	61.3%	36.9%	32.8%	41.6%	8.6%
5	54.3%	38.1%	34.1%	40.3%	6.0%
6	53.8%	35.5%	30.4%	38.5%	6.9%
7	57.4%	32.6%	28.7%	36.0%	7.5%
8	59.4%	34.7%	32.0%	38.7%	7.5%
9	52.6%	37.3%	31.7%	39.1%	6.4%
10	60.7%	36.2%	32.1%	41.8%	9.2%
Average (for tests 1~10)	55.8%	35.9%	31.2%	41%	7.2%
Standard Deviation (for tests 1~10)	4.9%	1.5%	1.7%	2.1%	1.1%

3.3.1.2 MDSC validation

MDSC experiments were performed to validate the results obtained from the T-History experiments for the specific heat capacity measurements for the pure solar salt samples and solar salt samples with additive (as precursor for nanoparticles for yielding nanofluids). The same samples were prepared using the same protocol as the T-History measurements (mentioned in the previous section) and used for performing the MDSC experiments to measure the specific heat capacity. The MDSC measurements were performed independently by collaborators in the research group of Dr. D. Shin at the University of Texas Arlington to cross-check the measurements performed in this study. The measurements were performed three times on each of the three separate samples. The results from the MDSC measurements are shown in Table 16 and Figure 47. The results for the specific heat capacity measurements from the MDSC experiments have lower values of measurement uncertainty (~3%) compared to that of the T-History experiments (5~9%). The results from the MDSC experiments show that the average enhancement in the value of specific heat capacity measurements was ~32% (with a measurement uncertainty of ~3%) when pure solar salt samples were mixed with additive [$Al(NO_3)_3 \cdot 9H_2O$] at 6.9% mass fraction for yielding Al_2O_3 nanoparticles at a target mass fraction of 1%. Hence, the results of the specific heat capacity measurements show that the T-History experiments show a higher level of enhancement (average enhancement of ~41% with standard deviation of ~2%) compared to that of the MDSC experiments (average enhancement of ~32% with standard deviation of ~3%).

Table 16. Values of specific heat capacity for different cycles are listed as a function of temperature (obtained from MDSC experiments). The specific heat capacity of pure solar salt samples is compared to that of the solar salt nanofluid samples (prepared using one-step synthesis protocol). The molten salt nanofluid samples were obtained by adding $Al(NO_3)_3 \cdot 9H_2O$ at 6.9% mass fraction to pure solar salt for a target mass fraction of 1% for the resulting Al_2O_3 nanoparticles obtained by thermal decomposition (one-step synthesis protocol). (Results courtesy of Dr. D. Shin research group at the University of Texas at Arlington)

Solar salt + Al_2O_3 - 1% target				
Sample weight	Cycle	Cp at 300 °C (kJ/kg °C)	Enhancement (%)	Uncertainty (%)
200mg	1	1.999	31.5	2.7
	2	2.014	32.5	2.7
	3	2.018	32.8	2.7
	4	2.020	32.9	2.7
	5	2.030	33.6	2.7
	6	2.010	32.2	2.7
	7	2.001	31.6	2.7
	8	1.996	31.3	2.7
	9	2.000	31.6	2.7
	10	1.998	31.4	2.7
Average		2.009	32.1	2.7
STDEV error		0.004	0.248	-

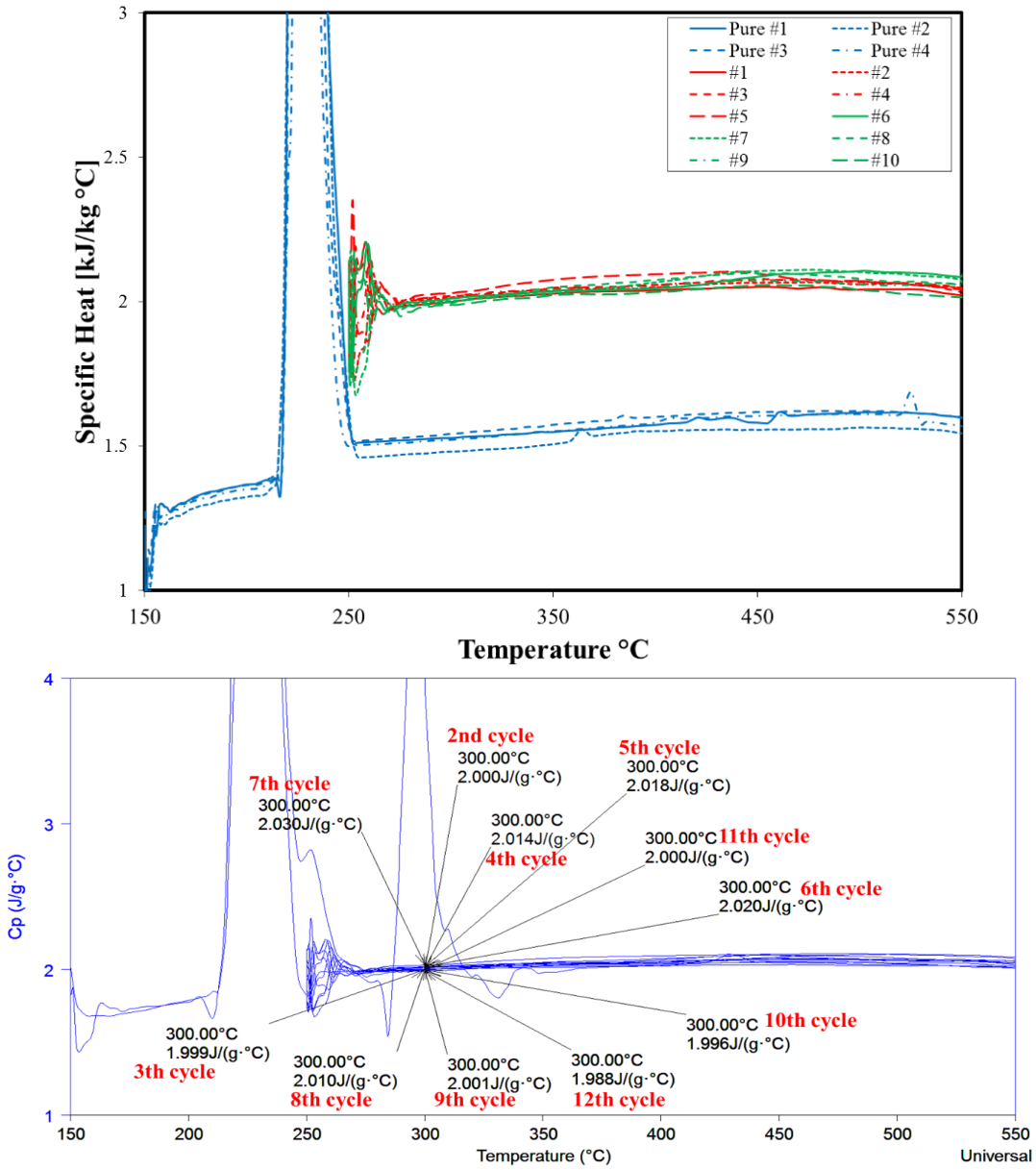

Figure 47. Plot of specific heat capacity as a function of temperature (obtained from MDSC experiments) for solar salt nanofluid samples (prepared using one-step synthesis protocol). The specific heat capacity of pure solar salt samples is compared to that of the solar salt nanofluid samples (prepared using one-step synthesis protocol). The molten salt nanofluid samples were obtained by adding $Al(NO_3)_3 \cdot 9H_2O$ at 6.9% mass fraction to pure solar salt for a target mass fraction of 1% for the resulting Al_2O_3 nanoparticles obtained by thermal decomposition (one-step synthesis protocol). (Results courtesy of Dr. D. Shin research group at the University of Texas at Arlington)

3.3.2 Thermal conductivity measurement

The thermal conductivity of solar salt nanofluid samples were measured at three different temperatures (300ºC, 400ºC, and 500ºC) using the same technique discussed earlier in Chapter 2 (i.e., using a concentric cylinder test apparatus). The nanoparticles in the nanofluids samples were derived from thermal degradation of $Al(NO_3)_3 \cdot 9H_2O$ additive (that served as precursor for Al_2O_3 nanoparticles on thermal degradation, as discussed in the synthesis protocol outlined in Chapter 2). The average values of thermal conductivity were calculated from the average values of temperature drop recorded by the four pairs of thermocouples and are summarized in Table 17 and Figure 48.

Figure 49 shows the measurement of temperature drop at steady state conditions from the four pairs of thermocouples (the measurements were performed at three temperatures set points). A small deviation of the values of temperature drop is observed between the different pairs of thermocouples which suggests that the radial heat conduction may vary slightly in different circumferential locations. However, the average values of the measured temperature drops could still be used for calculating the representative values for the thermal conductivity of the molten salt samples under different temperature conditions since this deviation depending on circumferential location is small compared to the values of the temperature drop in the radial direction.

The results show that the thermal conductivity of both the pure solar salt samples and the nanofluid samples increases monotonously with increasing temperature from 300ºC to 500ºC (which is typical of most liquids). The result also showed high uncertainty in thermal conductivity measurements for the nanofluid samples. Considering the average

values of the measurements the results show that the thermal conductivity was enhanced by ~22% in the nanofluid samples compared to that of the pure solar salt samples. For the range of temperatures used in the measurements the enhancement varied from 21 ~ 24%.

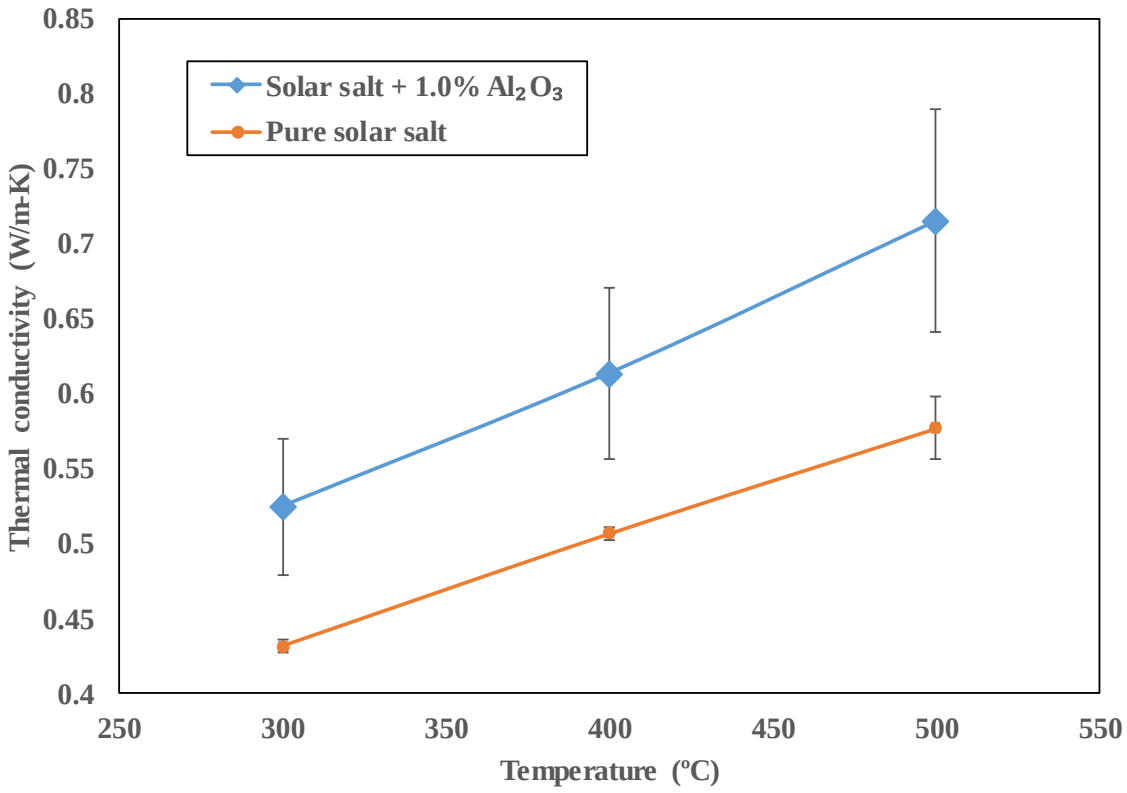

Figure 48. Plot of thermal conductivity as a function of temperature for pure solar salt samples and molten salt nanofluid samples (prepared using one-step synthesis protocol). The molten salt nanofluid samples were obtained by adding $Al(NO_3)_3 \cdot 9H_2O$ at 6.9% mass fraction (as nanoparticle precursor) to pure solar salt for a target mass fraction of 1% for the resulting Al_2O_3 nanoparticles obtained by thermal decomposition (one-step synthesis protocol)

Table 17. Thermal conductivity as a function of temperature for pure solar salt samples and molten salt nanofluid samples (prepared using one-step synthesis protocol). The molten salt nanofluid samples were obtained by adding $Al(NO_3)_3 \cdot 9H_2O$ at 6.9% mass fraction (as nanoparticle precursor) to pure solar salt for a target mass fraction of 1% for the resulting Al_2O_3 nanoparticles obtained by thermal decomposition (one-step synthesis protocol)

Temperature (°C)	Solar salt + 1.0% Al_2O_3		Pure solar salt		Enhancement (%)
	k [W/(m·K)]	Standard deviation	*k* [W/(m·K)]	Standard deviation	
300	0.525	8.6%	0.431	0.9%	21.7%
400	0.613	9.3%	0.507	0.8%	21.1%
500	0.715	10.3%	0.577	3.6%	23.9%
Average	0.618	15.9%	0.505	11.8%	22.3%

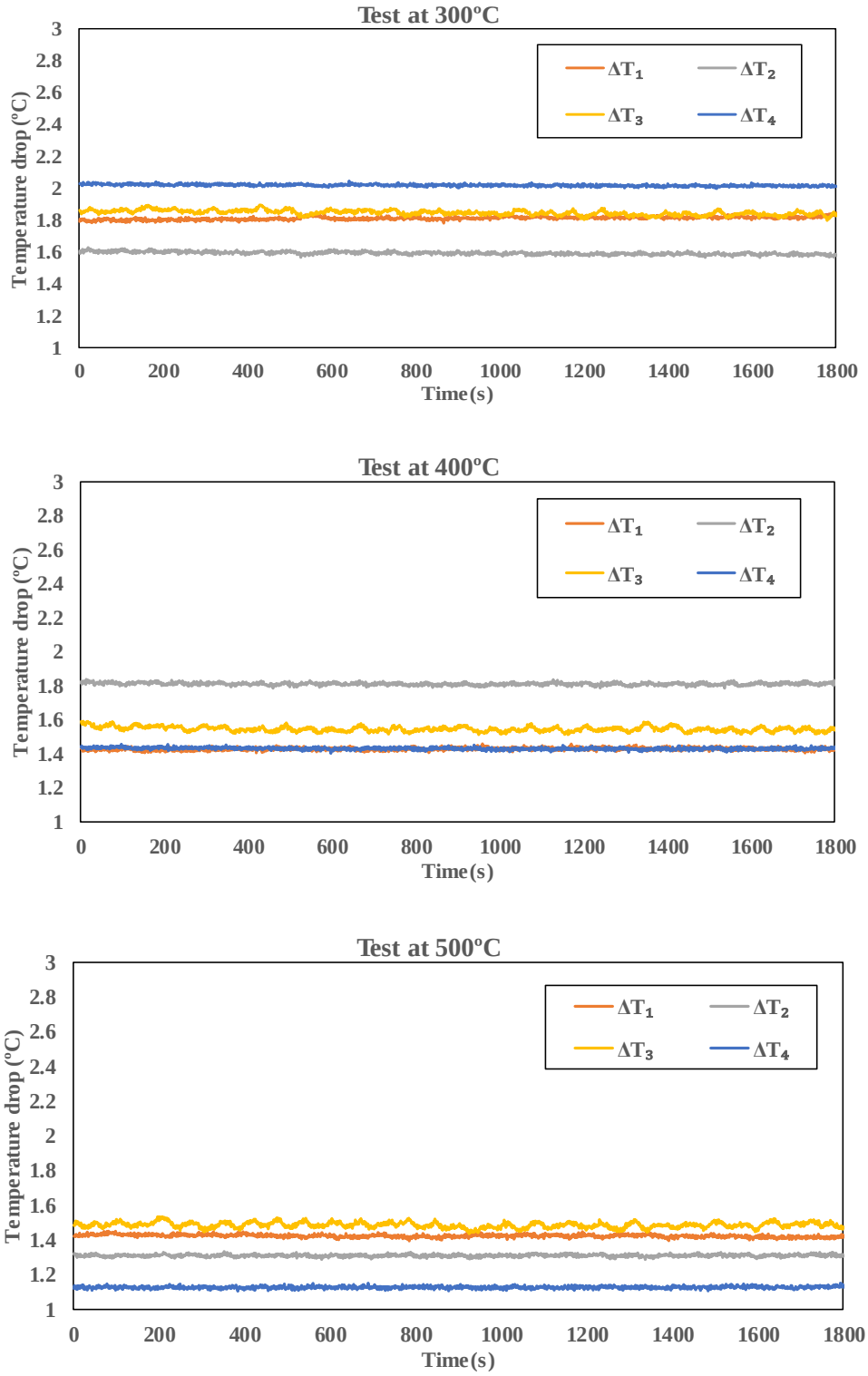

Figure 49. Measurements of temperature drop in thermal conductivity tests

3.3.3 Material characterization

The solar salt nanofluids prepared using one-step synthesis protocol (as described in Chapter 2) was tested for stability under quiescent conditions. The molten salt nanofluid samples were obtained by adding $Al(NO_3)_3 \cdot 9H_2O$ at 6.9% mass fraction (as nanoparticle precursor) to pure solar salt for a target mass fraction of 1% for the resulting Al_2O_3 nanoparticles obtained by thermal decomposition (one-step synthesis protocol). The vial containing the synthesized nanofluid was kept undisturbed in a furnace (at molten state) at 300 ºC and photographs of the suspension were obtained using a digital camera. The photographs show the milky-white colloidal suspension of the nanoparticles synthesized in-situ in the molten salt due to thermal degradation of the additive. The photographs were recorded 1 hour, 4 hours, 24 hours (1 day), 2 days, 3 days, 9 days and 14 days after synthesis of the fresh samples. The photographs are shown in Figure 50.

The top row of the photographs in Figure 50 show the colloidal suspension in the nanofluid was stable within the first 24 hours of in-situ synthesis with no noticeable sedimentation of the colloidal suspension. The bottom row of photographs shows that a slow rate of sedimentation of the nanoparticles occurred over two weeks period (with no noticeable agglomeration). This is evidenced by the clear and transparent supernatant liquid phase on the top (which may still contain nanoparticles that are not visible or apparent visually in the photographs). The height of the milky white colloidal suspension diminishes over time while appearing to be denser in complexion potentially due to sedimentation of nanoparticles in the solution. The slow sedimentation rate is consistent with the low terminal velocity of the nanoparticles in the colloidal suspension.

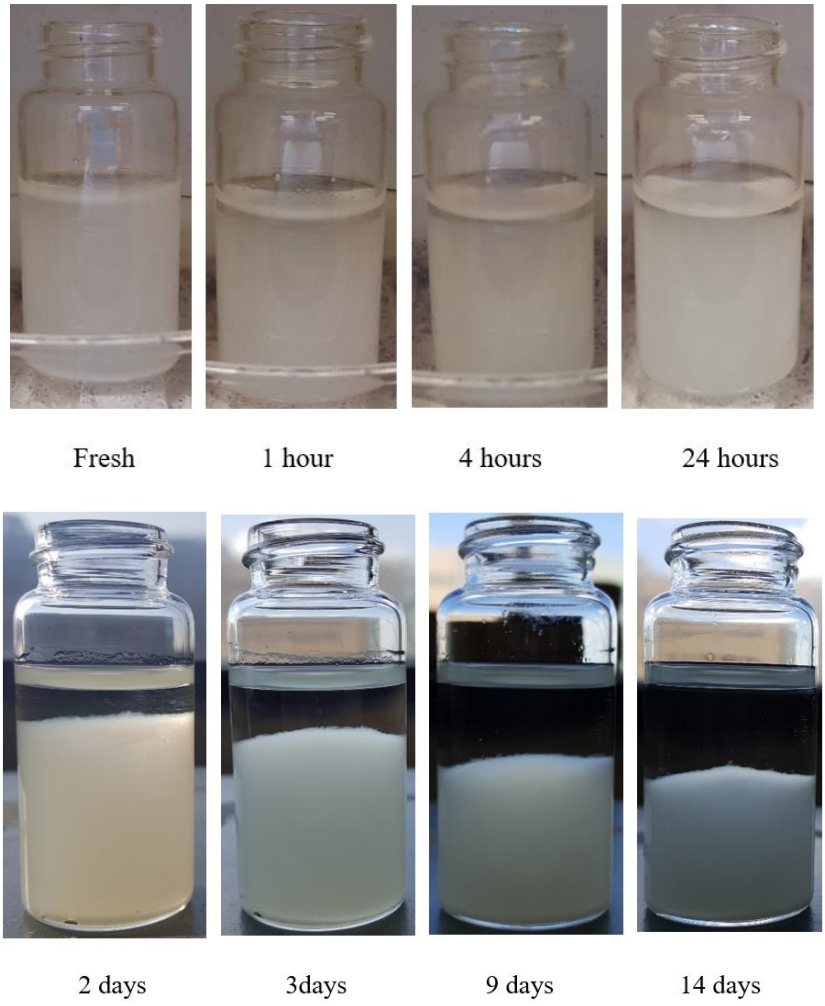

Figure 50. Photographs obtained at specific time intervals using a digital camera over a two week period for the solar salt nanofluid samples. The molten salt nanofluid samples were prepared using one-step synthesis protocol containing Al_2O_3 nanoparticles (synthesized in-situ) at a target mass concentration of 1% and derived from thermal degradation of $Al(NO_3)_3 \cdot 9H_2O$ additive (as a nanoparticle precursor) at a mass fraction of 6.9%. The solar salt nanofluid sample was prepared in a vial and the vial was placed under quiescent conditions at 300 °C in a furnace.

This demonstrates that the nanofluid samples prepared using the one-step synthesis protocol are stable and no visual evidence is obtained for the agglomeration, precipitation or coagulation of the nanoparticles over the two weeks period. However, electron microscopy images are still needed for ascertaining the small-scale structures formed in-situ within these molten salt samples (i.e., at the nano-scales) and for evaluating the size distribution of the nanoparticles synthesized in-situ (as well as, potentially secondary nanostructured induced by the nanoparticles in the solvent phase).

Materials characterization was performed using electron microscopy techniques for the nanofluid samples (prepared by one step synthesis protocol where alumina nanoparticles are generated due to thermal decomposition of aluminum nitrate precursors that were mixed apriori with solar salt as dry powders or as a wet solution). The SEM images obtained from this study are shown in Figure 51 for the solar salt nanofluid samples with a target alumina mass fraction of 1% (from alumina nitrate precursors mixed with solar salt at at a mass fraction of 6.9%). s

Although individual nanoparticles are not easily discernible in these SEM images (unlike Figure 44 for solar salt nanofluids with silica nanoparticles), clusters of needle shaped ("nano-needles") secondary nano-structures are observed in Figure 51 on higher magnification of a few locations within the samples. The SEM images show that the nominal diameter of these nano-needles is approximately 50 nm with lengths ranging from 2 ~ 3 microns (i.e., the aspect ratio of the nano-needles ranges from 40 ~ 60). These nano-needles are observed to be located in the crevices of the bulk salt phase (amorphous phase).

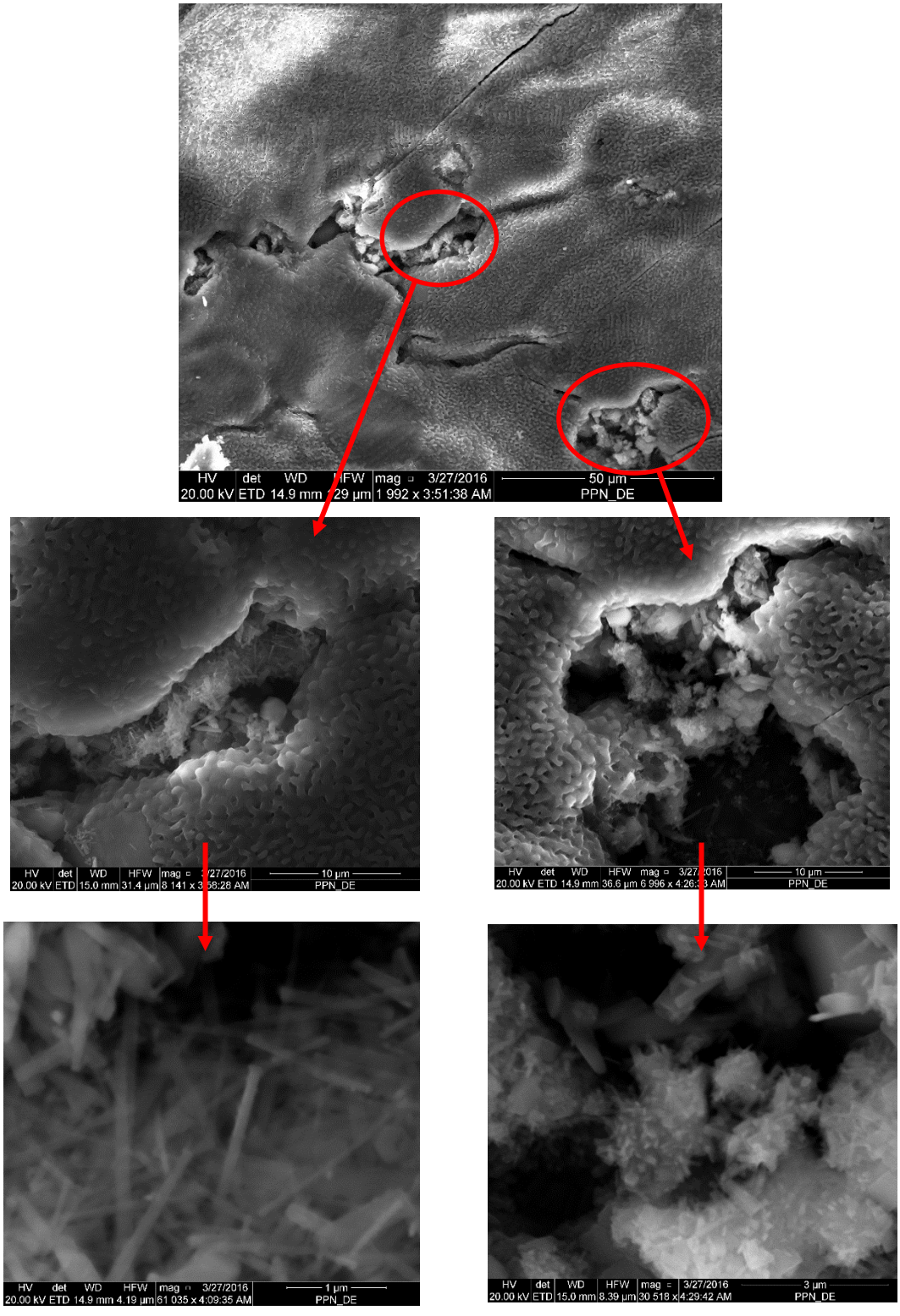

Figure 51. SEM images of solar salt nanofluid samples (one-step synthesis).

Compared to the spherical shape of the silica nanoparticles (in Figure 42), the cylindrical shape of these secondary nanostructures (nano-needles) in Figure 50 - confers significantly higher values of specific surface area (i.e., surface area per unit mass or surface area per unit volume). These nano-needles also confer the ability to form percolation networks and porous structures more easily (unlike spherical silica nanostructures). Hence, the formation of these secondary nanostructures (nano-needles) in-situ in the solar salt nanofluids augments the thermal energy storage capacity and thermal conductivity ([78] [84] [100]).

EDS (Energy Dispersive X-Ray Spectroscopy) of the solar salt nanofluid samples was also performed using the SEM apparatus, as shown in Figure 52 The results from the EDS show that the elemental composition, particularly that of Al, is fairly uniformly distributed in the solar salt nanofluid samples. The spectrums did not show any significant different in the elemental composition between the location of the amorphous region of the salt samples and in the regions where secondary nanostructures are observed (i.e., for the nano-needles). This is potentially due to homogeneous dispersion of the aluminum nitrate precursor initially in the salt (during one-step synthesis) that causes generation of fine grained alumina nanoparticles that are uniformly dispersed in the nanofluid samples (perhaps at a shallow depth from the surface). Hence, the alumina nanoparticles are not discernible in the SEM images - since the low energy electrons do not penetrate deeper into the samples; but are perceived in the EDS by the more deeply penetrating X-Rays that have higher energy.

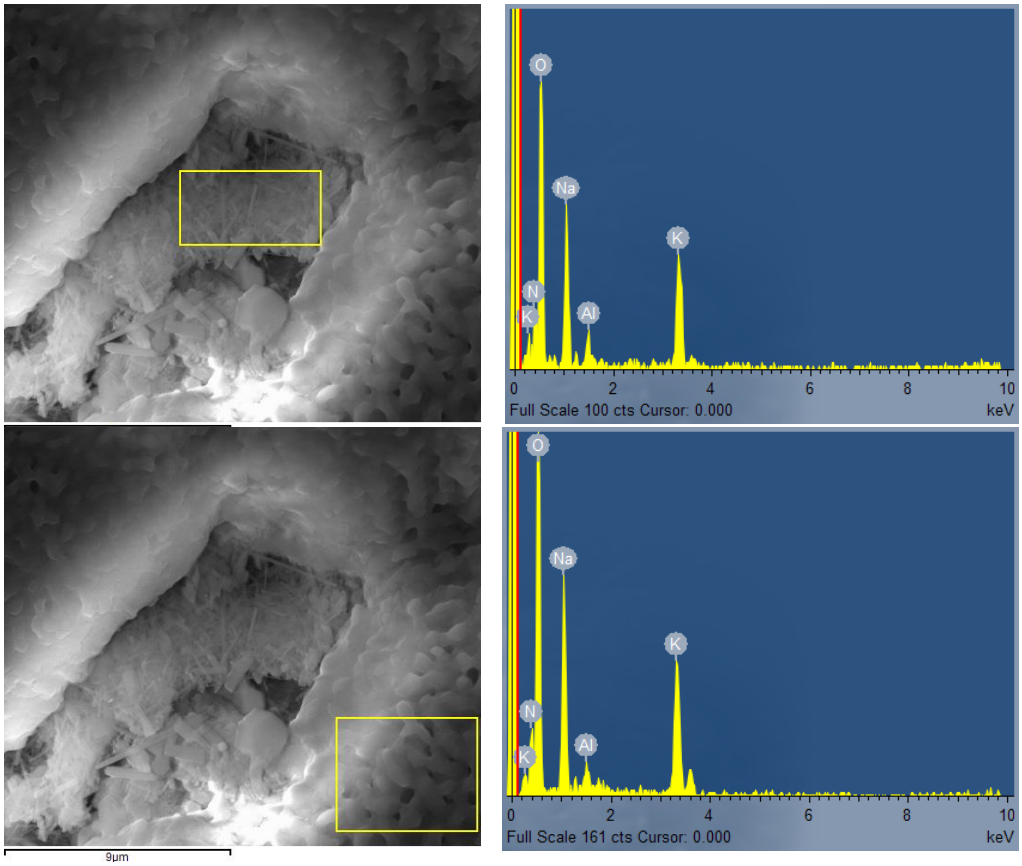

Figure 52. EDS analysis of elemental composition of solar salt nanofluid (one-step synthesis of Al_2O_3 nanoparticles in-situ)

Closer examination of SEM images obtained from another set of solar salt nanofluid samples revealed a diverse range of shapes and sizes for these secondary nanostructures (that were induced by the alumina nanoparticles formed in-situ) and are shown in Figure 53. Apart from nano-needles other secondary nanostructures in the form of long range, and loosely-packed dendritic structures were observed in the SEM images. In another case, closely-packed percolation networks were also observed in the SEM images. The mechanisms for the nucleation and growth of these secondary nanostructures are as yet unknown. However, it is evident that these secondary nanostructures may

mutually affect the formation in-situ and growth as well as the inherent kinematics and dynamics (e.g., in the form of non-Newtonian rheology of the nanofluid samples).

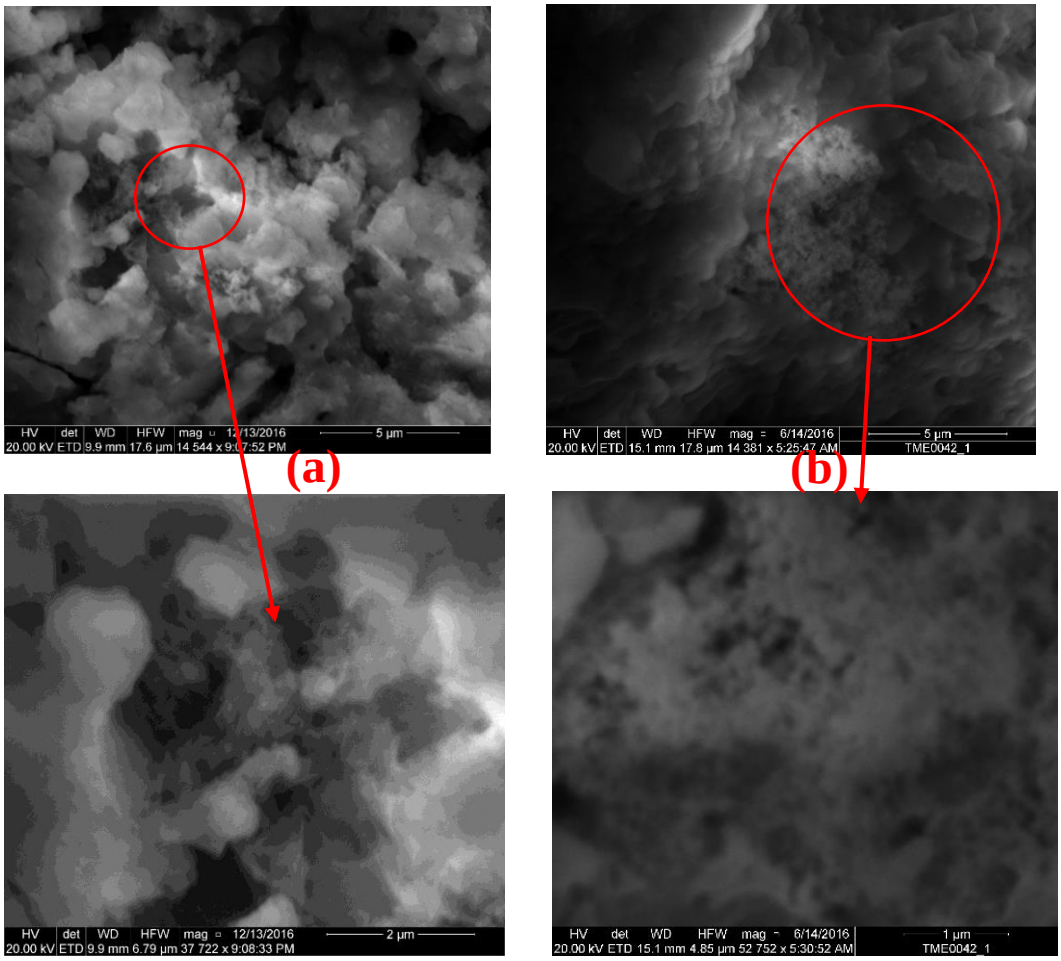

Figure 53. SEM images of solar salt nanofluid samples (one-step synthesis protocol). In addition to the cluster of single nano-needles observed in Figure 50 - the image shows a diverse range of secondary nanostructures formed in the sample – such as loosely packed dendritic (left: top and bottom) structures and closely packed percolation networks (right: top and bottom)

The solar salt nanofluid samples (prepared by one-step synthesis protocol from aluminum nitrate additive) were shipped immediately for further analysis by the research

group of Dr. D. Shin at the University of Texas Arlington (UTA). The help and support of Dr. D. Shin is gratefully acknowledged in obtaining these results. The SEM images obtained at UTA are shown in Figure 54. The images show that the secondary nanostructures (nano-needles) form fractal shapes, i.e., self-replicating tree-shaped branched nano-structures. Figure 53 shows that large flocks of inter-connected "nano-spikes" are spread over the surface of salt crystals. The diameter at the base (i.e., "stem") of these nanostructures is estimated from the images to be approximately 50 nm while the nano-spikes have diameters less than 10 nm. These fractal nanostructures observed in Figure 53 would considerably enhance the specific surface area that is packed into smaller volumes occupied by these secondary nanostructures - compared to that of the single and straight nano-needles formed in a cluster, as was observed in Figure 51.

Recent reports in the literature for molten salt nanofluids have demonstrated that the presence of nanoparticles can induce the formation of long-range secondary nanostructures in the salt phase due to preferential affinities between the nanoparticle surface and components of the salt mixture [100, 101, 102]. These secondary nanostructures can have different elemental composition than the bulk amorphous phase resulting in different values of melting point as well as significantly elevated values of thermo-physical properties owing to their high surface energy. Hence, the diverse range of shapes and sizes of the secondary nanostructures observed in these SEM images are potentially composed of the salt molecules (with a different mixture ratio than the bulk phase of the solar salt) and are induced in the vicinity of very fine-grained Al_2O_3 nanoparticles (say, less than 5 nm diameter), that are not visible in the SEM images.

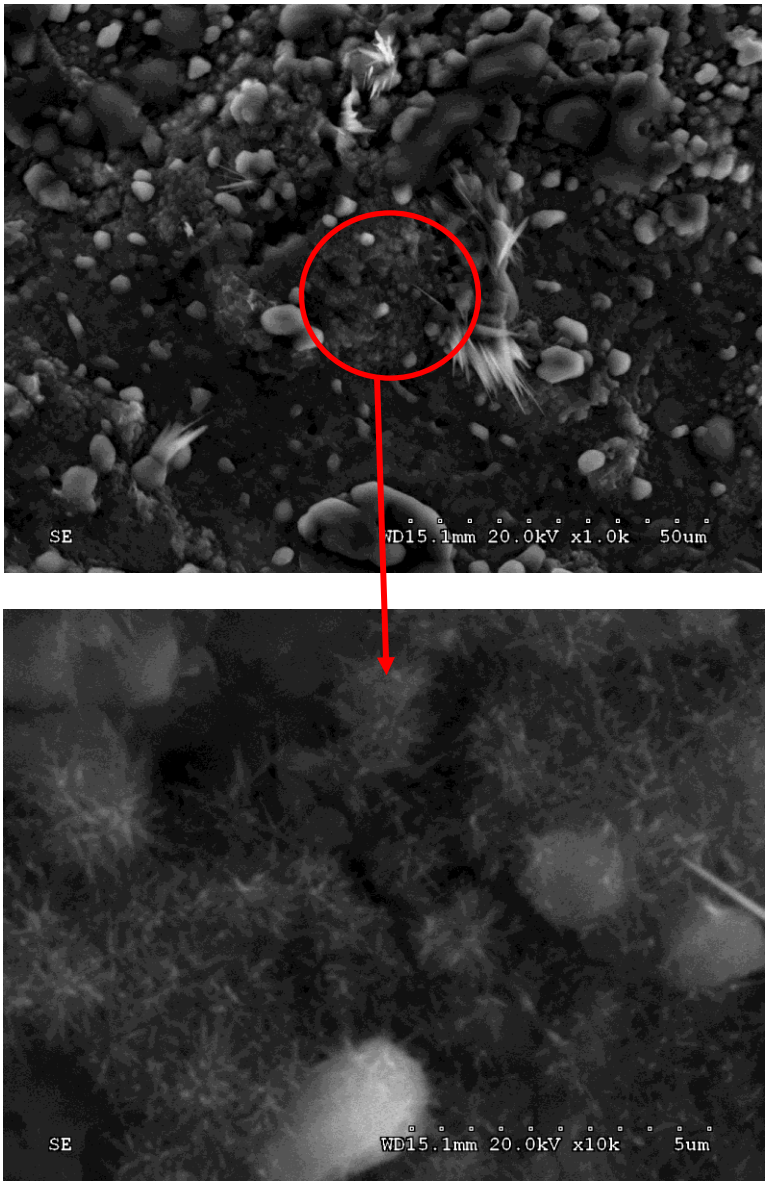

Figure 54. SEM images of solar salt nanofluid samples (one-step synthesis protocol). In addition to the cluster of single nano-needles observed in Figure 50 - the image shows other forms of secondary nanostructures: such as - fractal and dendritic structures that are formed in the sample. Images courtesy of Dr. D. Shin and his research group at the University of Texas at Arlington is gratefully acknowledged

3.4 Summary and discussion

The comparison of the thermo-physical properties of the solar salt nanofluid samples (prepared by the two-step and one-step synthesis protocols) with that of the pure solar salt samples is shown in Table 18 and Table 19. The tables show the relative enhancement in the values of the specific heat capacity and thermal conductivity of the nanofluid samples.

Table 18. Specific heat capacity enhancement of solar salt nanofluid samples with target mass concentration of 1% for the nanoparticles

Sample	300ºC	400ºC	500ºC	Average
Two-step synthesis: SiO_2 nanoparticles	7.5%	8.8%	13.5%	9.3%
One-step synthesis: Al_2O_3 nanoparticles	55.8%	35.9%	31.2%	38.7%

Table 19. Thermal conductivity measurements (units in [W/(m^2·K)]) for solar salt samples (pure and nanofluid samples) with target mass concentration of 1% for the nanoparticles. Quantities in brackets denote enhancement over that of the pure solar salt samples

Sample	300ºC	400ºC	500ºC	Average
Pure solar salt	0.431	0.507	0.577	0.505
Solar salt nanofluid, Two-step synthesis: SiO_2 nanoparticles	0.577 (33.9%)	0.667 (31.8%)	0.786 (36.2%)	0.677 (34.1%)
Solar salt nanofluid, One-step synthesis: Al_2O_3 nanoparticles	0.525 (21.7%)	0.613 (21.1%)	0.715 (23.9%)	0.618 (22.3%)

The results show that nanofluid samples have significantly enhanced specific heat capacity and thermal conductivity. The two-step method is nanomaterial synthesized from two step method has a smaller particle size and more uniform size distribution as the nanoparticle come with pre-defined shape and size. In the nanofluid samples (two-step method) the nanoparticles appear to be mono-dispersed and seemed to induce the formation of "cauliflower" shaped secondary nanostructures. In the contrast, within the nanofluid samples (single-step method) a diverse range of shapes and sizes were observed for the secondary nanostructures that were formed in-situ. These secondary nanostructures formed inter-connected and long-range structures which considerably enhances the specific surface area (and, as a result, the surface energy and therefore the specific heat capacity of the mixure). The percolation networks formed by these secondary nanostructures also provides additional pathways for thermal energy (i.e., thermal vibrations or phonons) to be transported apart from the bulk amorphous phase of the molten salt system and this, in turn, enhances the overall thermal conductivity. The secondary nanostructures therefore favor better material stability (i.e., stability of the nanoparticles to remain in suspension) due to the slower rates of sedimentation [89, 103] and lower velocity of the nanoparticles induced by Brownian motion [104, 105].

Considering that nanoparticles are expensive to procure from commercial sources (approximately \$100/ kg ~ \$1000/ kg) and that the additives (i.e., the nanoparticle precursors such as aluminum nitrate as well as other alkali salts) are considerably cheaper (approximately \$0.10/kg to \$1/kg), it is apparent that the two-step synthesis protocol bears the risk of higher material and handling costs than single-step synthesis protocol for

manufacturing molten salt nanofluids. Hence the one-step synthesis protocol may be a cheaper as well as more cost-effective technique for enhancing thermal energy storage capacity in industrial applications and thereby - enable better systemic efficiencies (as well as thermodynamic efficiencies) to be realized owing to the significant enhancement of the specific heat capacity and augmentation of thermal conductivity.

In the following section, the potential physical mechanisms responsible for the enhanced thermos-physical properties of nanofluids will be examined, especially in the realm of the formation of the secondary nanostructures.

4. ANALYSIS OF THERMOPHYSICAL PROPERTY ENHANCEMENT OF NANONETWORK DISPERSION

4.1 Specific heat capacity of nanostructure

4.1.1 Role of secondary nanostructures

In traditional mixing models, it is assumed that the specific heat capacity of a mixture (such as, a nanofluid) is a mass-fraction weighted sum of the specific heat capacity of the individual components (i.e., both the solvent phase and the constituent nanoparticles):

$$C_{total} = \frac{[MxC_n] + [(M - Mx)C_l]}{M} \tag{16}$$

where, $\boldsymbol{M}$ is the total mass of the mixture, $\boldsymbol{x}$ is the mass fraction of the nanoparticles, and $\boldsymbol{C}$ is the specific heat capacity of nanoparticle. The subscripts *n* and *l* denote the properties of the bulk liquid phase and nanoparticle, respectively. Typically, solids (and therefore nanoparticles) have significantly lower values of specific heat capacity (less than 1 J/[g·K]) compared to that of liquids, such as molten salts (e.g., in the range of 1~2 J/[g·K]). Equation 16 therefore would predict the degradation in the values of specific heat capacity of solvents when mixed with solids, especially where the solid phase is immiscible or does not form a colloidal suspension. However, experimental results contradict this prediction where specific heat capacity values are enhanced on mixing with solid nanoparticles (e.g., in the form of stable colloidal suspension) [69, 43].

Modified model were therefore developed to mitigate these discrepancies by accounting for the high surface energy of nanoparticles compared to the bulk property values of the solid phase [106, 107] and recognizing the existence of secondary

nanostructures as a distinctly separate component, termed as the "compressed phase" or "compressed layer" that is induced on the surface of the nanoparticle by molecules of the solvent phase that are adsorbed on the surface. Inclusion of the compressed layer adsorbed on nanoparticle surface [43, 85, 86] was proposed later in the literature for predicting the specific heat capacity of molten salt nanofluids. The inherent assumption in the modified model is that the compressed layer has significantly higher heat capacity due to its unique structure and composition (which may be semi-solid and may have non-Newtonian rheology even though the solvent phase may have Newtonian behavior). Hence, the net value of the specific heat capacity of molten salt nanofluid is calculated by adding the mass fraction weighted values of the specific heat capacity of the three constituents: the nanoparticle, the compressed phase and the bulk liquid phase (solvent), as shown below:

$$C_{total} = \frac{[MxC_n] + \left[\frac{Mx}{m_n} m_s C_s\right] + \left[\left(M - Mx - \frac{Mx}{m_n} m_s\right) C_l\right]}{M} \tag{17}$$

where, (m_s/m_n) is the ratio between the mass fraction of the compressed layer and the nanoparticle. The calculation of this ratio can be performed using the shape and size (i.e., morphology) of the nanoparticle.

As an example, for a spherical nanoparticle, as shown in Figure 55, the compressed layer can be assumed to form a concentric envelope around the nanoparticle of a certain thickness (δ). Based on molecular equilibration models the thickness of this compressed layer can range from 1~2 nm to as high as ~20 nm; depending on the chemical properties of the solvent.

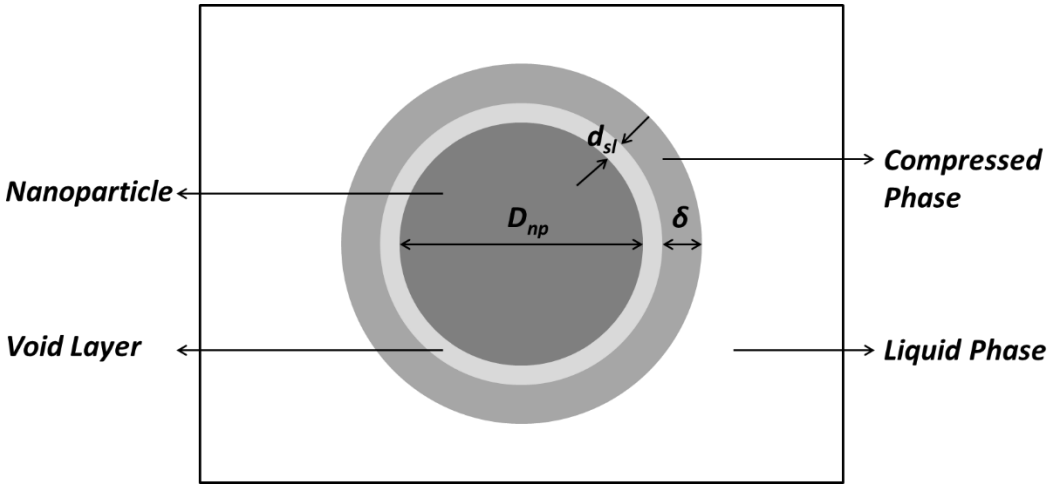

Figure 55. Schematic of compressed layer formed by surface adsorption on a spherical nanoparticle.

The space between the compressed layer and nanoparticle (e.g., equilibrium distance for molecular spacing) is denoted as d_{sl} and the diameter of the spherical nanoparticle is denoted as D_{np}. Hence, based on the geometrical characteristics of this schematic diagram, Equation 17 can be simplified as:

$$C_{total} = [x]C_n + \left[\left(x\frac{\rho_s}{\rho_n}\right)\left\{\left(1+\frac{2(\delta+d_{sl})}{D_{np}}\right)^3 - \left(1+\frac{2d_{sl}}{D_{np}}\right)^3\right\}\right]C_s + \left[1-x-\left(x\frac{\rho_s}{\rho_n}\right)\left\{\left(1+\frac{2(\delta+d_{sl})}{D_{np}}\right)^3 - \left(1+\frac{2d_{sl}}{D_{np}}\right)^3\right\}\right]C_l \quad (18)$$

From molecular dynamic simulations, the value of d_{sl} is estimated to be 0.3 nm (additional details are provided in Appendix G). The specific heat capacity of the pure molten salt and Al_2O_3 nanoparticles are 1500 J/(kg·K) and 700 J/(kg·K), respectively. The

estimation of the specific heat capacity of compressed layer is enigmatic, as currently no direct experimental measurement exists for this state of matter (and is likely to be a semi-solid phase with non-Newtonian rheology). The estimation of the specific heat capacity of compressed layer was therefore based on the proposition (or assumption) that the inter-molecular structure of the compressed phase is similar to the solid phase of the pure solvent (i.e., the molten salt or pure solar salt) as the phase transition occurs from solid to liquid. The resultant force arising from the inter-molecular interactions (e.g., the attractive and repulsive forces that vary as a function of the inter-molecular distances) causes the molecules of the solvent phase (that are confined in the compressed layer in the vicinity of the nanoparticle surface due to dominance of the adhesive forces over the cohesive forces), to be packed into smaller volumes. In other words, the mass density of the compressed phase is expected to increase over that of the bulk solvent phase. This increases the total potential energy of the atoms in the compressed layer. Due to the strong intermolecular forces in the compressed layer, the molecules of the solvent that are confined within the compressed phase have lower mobility and are therefore much more stable than the molecules in the bulk phase of the solvent (i.e., the molecules in the bulk phase of the solvent can move easily with relatively smaller energy input). As a result, chemical concentration gradients are also induced between the compressed phase and the bulk phase of the solvent. Consequently, it becomes more difficult for these atoms to gain momentum, unless the energy input is large enough to overcome the potential energy barrier of the compressed phase (this situation is akin to potential barrier for molecules to

move from solid to liquid phase at a solid-liquid interface or liquid to vapor phase for a liquid-vapor interface).

Another perspective for describing such mechanisms is achieved by segmenting the total internal energy into the kinematic energy ("KE", resulting from translational motion of the constituent molecules) and the potential energy ("PE", resulting from the relative position of the constituent molecules). The ratio between PE and KE for molecules confined in the compressed layer is much larger than that of the molecules in the bulk phase of the solvent. Thus, larger values of total energy (KE + PE) are required for increasing the KE of the molecules in the compressed phase (i.e., to the same level as the KE of the molecules in the bulk phase of the solvent). Since temperature is a direct indication of KE, this analysis essentially implies that the molecules in the compressed layer have higher values of specific heat capacity compared to that of the bulk phase of the solvent. As mentioned before, this scenario closely resembles melting process, in which a significant fraction of the energy input is expended in overcoming the intermolecular bonds in the solid phase (while very small fraction of the total energy is available for increasing the kinematic energy of each individual molecule in the solid phase as it transitions to the liquid phase). Hence, it is reasonable to approximate the specific heat capacity of compressed layer as the specific heat capacity of the pure solvent in the solid state as it transitions to the liquid state (i.e., near the melting point).

Hence, for molten salt nanofluids, the specific heat capacity of the compressed phase can be estimated to be similar to that of the solid phase near the melting point. Figure 56 shows that the specific heat capacity of the compressed phase is therefore

approximately 10 times that of the liquid phase (as shown in the peak value of the specific heat capacity of solar salt, plotted in Figure 56 based on experimental measurements). The help of Dr. Shin and his research group at the University of Texas at Arlington in obtaining Figure 56 is gratefully acknowledged).

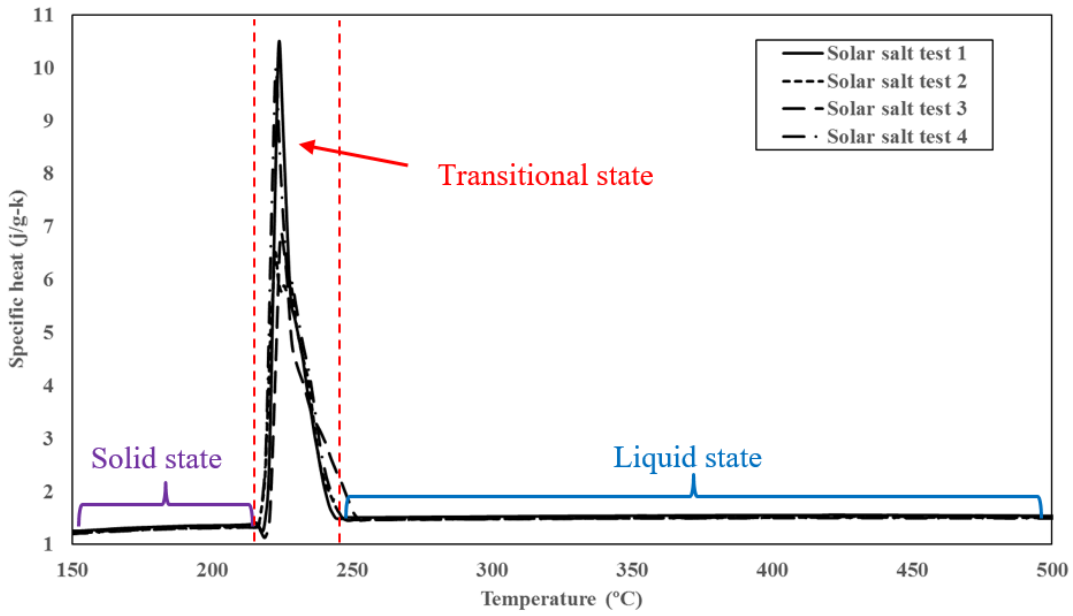

Figure 56. Typical MDSC curve for solar salt (courtesy of Dr. D. Shin and his research group at the University of Texas at Arlington, is gratefully acknowledged)

An alternative approach for estimating the specific heat capacity of the compressed phase involves a simple mathematical model based on one-dimensional oscillation of molecules, as shown in Figure 57. Figure 57 shows a one-dimensional representation of the bond interactions between one sodium ion and two collinear nitrate ions (in the form of spring-mass systems).

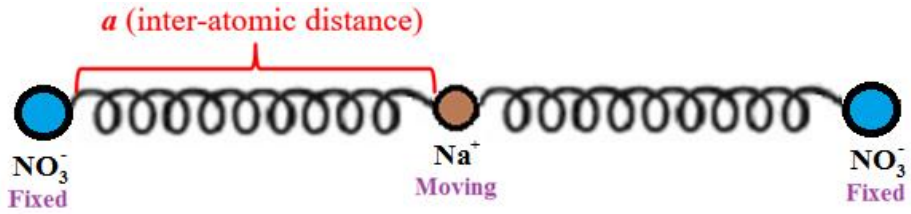

Figure 57. Schematic diagram of 1-D oscillation of sodium atom

Assuming the total potential energy associated with the moving atoms are represented by Lennard-Jones potential (V_{LJ}) [108] and electrostatic potential between a pair of charged particles as:

$$\mathrm{V}_{LJ} = 4\varepsilon\left[\left(\frac{\sigma}{r}\right)^{12} - \left(\frac{\sigma}{r}\right)^{6}\right] \tag{19}$$

$$\mathrm{V}_{e} = \frac{ke^2}{r} \tag{20}$$

where, $\boldsymbol{\varepsilon}$ is the depth of the potential well, $\boldsymbol{\sigma}$ is the finite distance at which the inter-particle potential is zero, $\boldsymbol{r}$ is the distance between the particles, $\boldsymbol{k}$ is the Coulomb's constant and $\boldsymbol{e}$ is the elementary charge of single electron.

The inter-atomic force (F_{LJ}) can then be represented by taking the gradient of Equation 19 as:

$$\mathrm{F}_{LJ} = 4\varepsilon\left[6\left(\frac{\sigma}{r}\right)^{7} - 12\left(\frac{\sigma}{r}\right)^{13}\right] \tag{21}$$

$$\mathrm{F}_{e} = \frac{ke^2}{r^2} \tag{22}$$

The trajectory of the moving sodium atom can be represented by the following equation:

$$\frac{\mathrm{d}^2x}{\mathrm{d}t^2} = \frac{4\varepsilon}{m}\left\{\left[6\left(\frac{\sigma}{a-x}\right)^7 - 12\left(\frac{\sigma}{a-x}\right)^{13}\right] - \left[6\left(\frac{\sigma}{a+x}\right)^7 - 12\left(\frac{\sigma}{a+x}\right)^{13}\right]\right\} + \frac{k}{m}\left[\frac{e^2}{(a-x)^2} - \frac{e^2}{(a+x)^2}\right] \quad (23)$$

where, $\boldsymbol{x} = 0$ is defined at the midpoint of two nitrate ions and $\boldsymbol{a}$ is the half distance between two nitrate ions. By perturbing the system with an initial velocity of the center atom at $\boldsymbol{t} = 0$, the velocity and displacement profile of the particle with respect to time can be numerically evaluated using the classic Velocity Verlet algorithm, by converting the equation into a set of first order ODEs (additional details provided in Appendix H). The intermolecular parameters for sodium nitrate were obtained from the standard library of Material Studio (Accelrys, Inc., 2008) and are summarized in Table 20. Figure 58 shows the example particle trajectory and velocity profile calculated with a = 0.5 Å and a = 1.5 Å.

Table 20. Parameters for intermolecular interactions for sodium nitrate[7]

Atom	q (e)	ε (kcal/mol)	σ (Å)
Na	+1	0.086	2.730
N	+0.95	0.080	3.900
O	-0.65	0.155	3.154

[7] The cross terms were computed using the mixing rule: $\varepsilon_{ij} = \left(\varepsilon_{ii}\varepsilon_{jj}\right)^{1/2}$, $\frac{1}{\sigma_{ij}} = \frac{1}{\sigma_{ii}} + \frac{1}{\sigma_{jj}}$

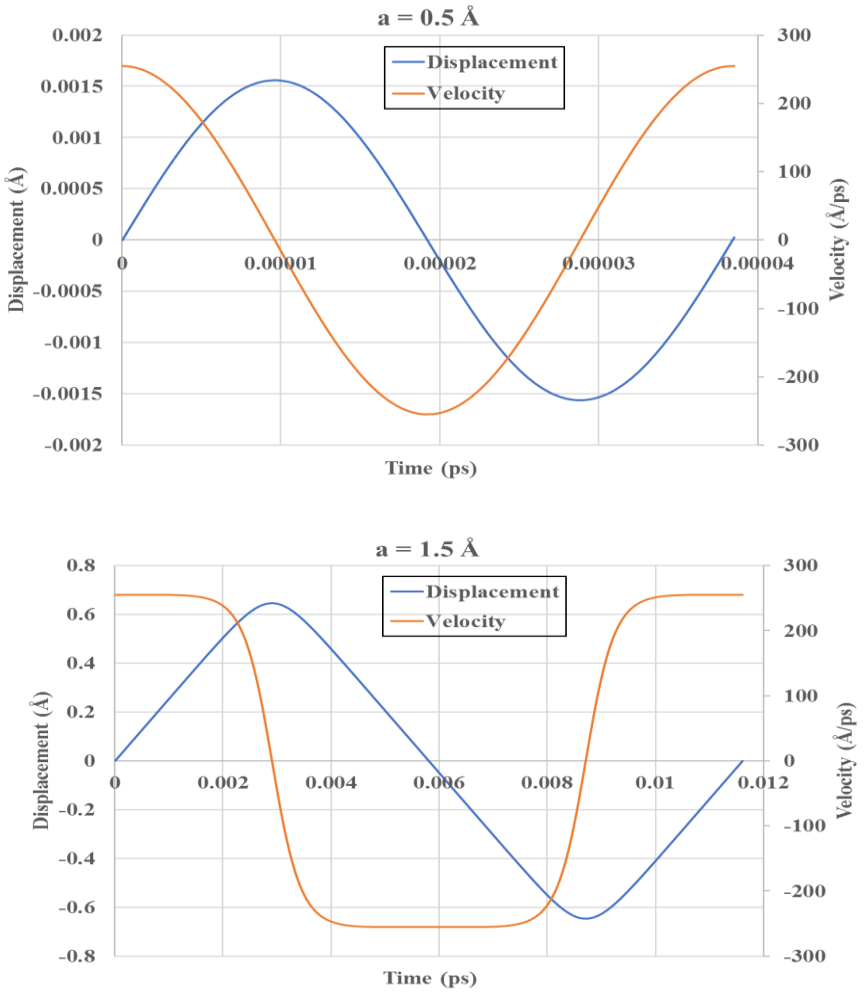

Figure 58. Displacement and velocity profile of oscillating sodium ion as a function of interatomic distance with nitrate ions: (i) a = 0.5 Å (top); (ii) a = 1.5 Å (bottom)

On reducing the intermolecular distance ***a*** from 1.5 Å to 0.5 Å the time averaged values of KE and PE obtained from these equations for one complete cycle of oscillation, it was observed that the percentage of KE (in the total internal energy) reduces dramatically as the intermolecular spacing is decreased (as shown in Figure 59 and Table 21). The predictions from this model implies that the effective specific heat capacity of closely packed molecules is increased with increase in packing density, since additional

quantities of energy is required (i.e. the total internal energy is higher) in order to maintain the system in thermal equilibrium or under isothermal conditions (i.e., for the same KE or for the same level of translational motion of the particles). Hence, this proves that the specific heat capacity of the compressed phase of the molten salt is significantly higher than that of the bulk phase.

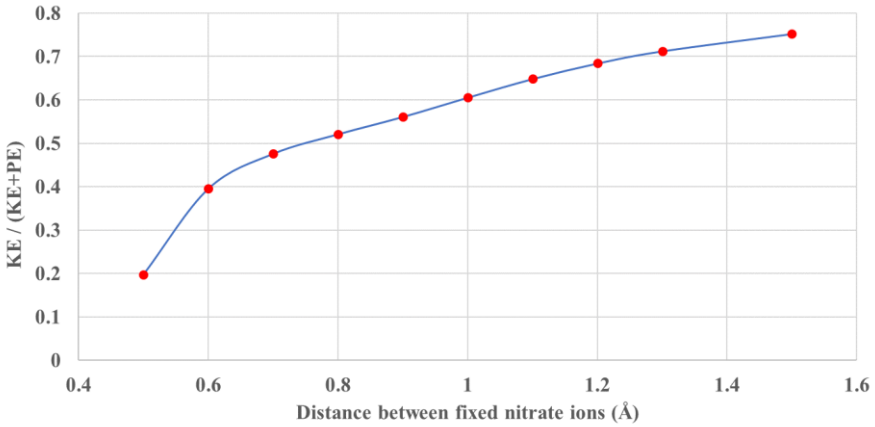

Figure 59. Plot for ratio of kinematic energy to total internal energy as a function of intermolecular distance between sodium and nitrate ions. The plot was derived from Equation 23 and the parameters listed in Table 20

Table 21. Estimation of kinematic energy (KE), potential energy (PE) and total internal energy (PE+KE) as a function of the intermolecular distance between sodium and nitrate ions. The calculated values were derived from Equation 23 and the parameters listed in Table 20

a (Å)	Energy ($\times 10^{-18}$ J)				$\frac{KE}{KE + PE}$
	KE	PE (Lennard-Jones)	PE (electrostatic)	PE (total)	
0.5	6.307	16.373	9.231	25.604	20%
0.6	6.236	1.837	7.693	9.530	40%
0.7	6.256	0.293	6.595	6.888	48%
0.8	6.351	0.0631	5.777	5.840	52%
0.9	6.608	0.019	5.153	5.172	56%
1	7.182	0.009	4.673	4.682	61%
1.1	7.938	0.006	4.299	4.304	65%
1.2	8.668	0.004	3.997	4.001	68%
1.3	9.287	0.003	3.745	3.748	71%
1.5	10.165	0.003	3.343	3.346	75%

After the nucleation of the compressed phase (e.g., due to surface adsorption of the solvent molecules on the surface of the nanoparticle), secondary nanostructures can form subsequently. In SEM images, these secondary nanostructures appear to emanate from the surface of the nanoparticles. Hence, the formation of the secondary nanostructures can be segmented into a nucleation phase and a growth phase. This is discussed next.

4.1.2 Formation of secondary nanostructures

As predicted by Equation 18, when nanoparticle size exceeds certain critical threshold, the volume fraction of the "compressed layer" on nanoparticle surface will become sufficiently small such that the proportional contribution to the net value of specific heat capacity will be negligible or insignificant. The specific heat capacity of solar salt nanofluid (with Al_2O_3 nanoparticles) is calculated as a function of nanoparticle size and mass concentration using Equation 18 (by accounting for the properties of the compressed phase) and plotted in Figure 60.

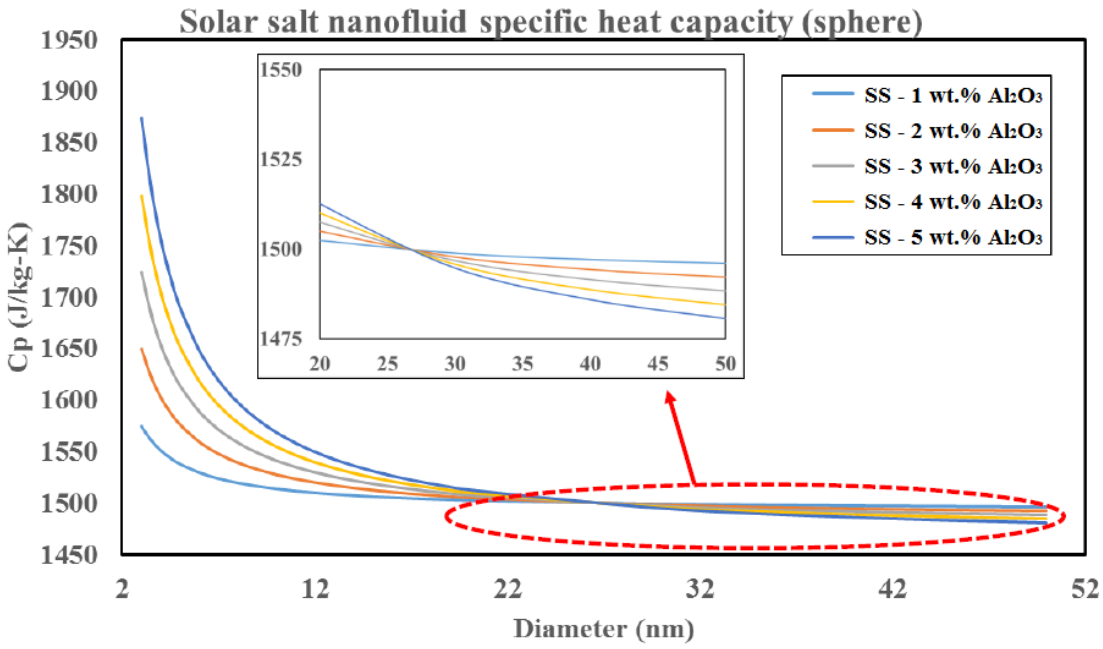

Figure 60. Numerical prediction for the values of net specific heat capacity of solar salt nanofluid (containing Al_2O_3 nanoparticles) as a function of nanoparticle size and mass concentration by assuming contribution from compressed phase, using Equation 18

The plot in Figure 60 shows that the specific heat capacity is enhanced by a significant margin for nanoparticle size decreases below a threshold value (of approximately less than 10~12 nm for spherical nanoparticles) and the level of enhancement is highly sensitive to the mass concentration of the nanoparticles for smaller nanoparticles (i.e., approximately less than 10~12 nm for spherical nanoparticles). The plots show that for nanoparticle size exceeding 20 nm there is only marginal change in the value of the specific heat capacity and the effect of the compressed phase (i.e., the contribution of the compressed phase to the net specific heat capacity) is almost negligible. This prediction is therefore inconsistent with the experimental results obtained in this study (as well as prior reports in the literature) - since significant enhancement in specific heat capacity values were observed for solar salt nanofluids with silica nanoparticles at mass concentration of 1% and for diameter of the nanoparticles ranging from 10 ~ 50 nm.

Molten salts are ionic liquids which typically dissociate into positive and negative ions. In the liquid state, the solar salt is composed of free Na^+, K^+ and NO_3^- ions. Due to the exposed crystal facets and surface defects on a solid surface (such as a nanoparticle surface), these ions can get adsorbed preferentially depending on the intermolecular affinity for each ion for a given surface. The preferential adsorption of ions on a solid surface significantly alters its apparent surface charge distribution resulting in accumulation of surface charges. Considering Al2O3 nanoparticle as an example, the NO_3^- anion could be chemisorbed to the metal cation in the particle surface with three different bonding structures [109, 110, 111] (as shown in Figure 61). The preferential adsorption of NO_3^- on the surface of the alumina nanoparticle causes progressive build up of a net

negatively charged surface potential (i.e., the nanoparticle develops a negative charge with reference to the bulk solvent phase). This in turn, induces substantial electrostatic attractive/repulsive forces near the particle surface as well as between nanoparticles in the vicinity of each surface. Various reports in the literature have demonstrated that under the influence of a strong electrostatic driving force, the ordered ionic liquid layer could extend to more than 10 nm in thickness [112, 113, 114, 115]. In certain cases, the ordered layer extends over 1000 nm, in which strong preferential alignments of molecules were revealed in the compressed layer [116]. where the adsorbed molecules can align mutually to start mimicking the underlying crystal structure of the solid surface (i.e., an epitaxial structure can form). This is shown in Figure 62 where long-range ordering of ionic liquid is simulated to occur on a charged surface.

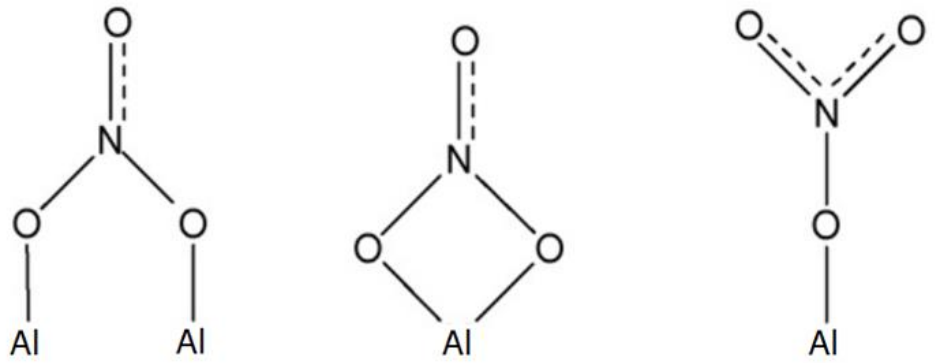

Figure 61. Possible chemisorption structure of nitrate ion on Al_2O_3 surface [109, 110, 111]

Mutual interactions in multi-body and multi-component systems, can cause these ordered layers to extend from the surface of each nanoparticle and form “bridges” to other

nanoparticles in the vicinity. These bridges (i.e., the secondary nanostructures) cause the nanoparticles to become inter-connected and form percolation networks (as shown in the schematic of Figure 63). Such phenomena have also been observed in a number of studies reported in the literature [84, 101].

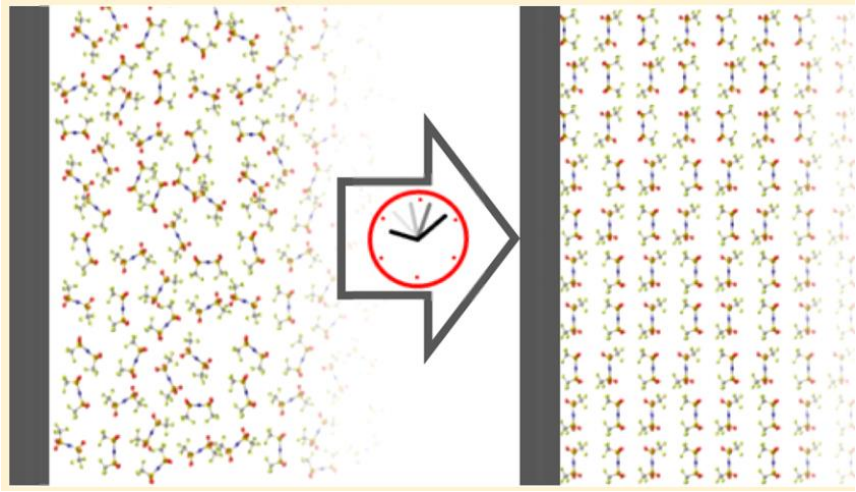

Figure 62. Long-range ordering of ionic liquid near charged surface [116]

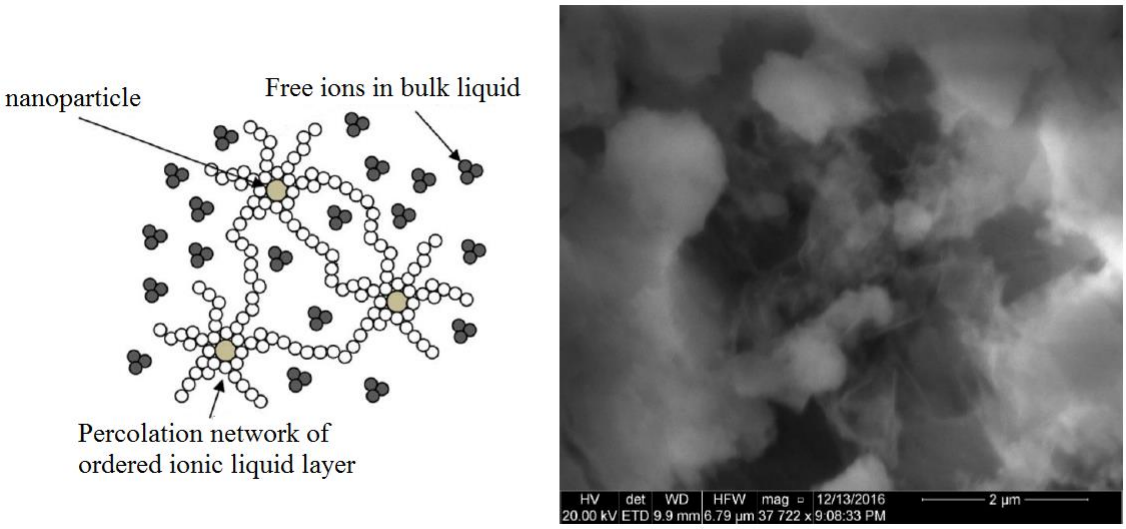

Figure 63. Formation of secondary nanostructure (percolation network) by extended ordering of molecules from the compressed phase formed on the surface of nanoparticles. (LEFT) Schematic showing the secondary nanostructures forming a percolation network between nanoparticles from free ions (or molecules) in the bulk phase of the solvent. (RIGHT) SEM image showing percolation network formed by secondary nanostructures in solar slat nanofluids with alumna nanoparticles (single-step synthesis protocol)

Considering that long-range secondary nanostructures observed in the solar salt nanofluid samples (Figure 63), Equation 18 could be modified to predict the net heat capacity of molten salt nanofluids by incorporating the additional effect arising from the long-range nanostructures induced in the molten salt, as follows:

$$C_{total} = \frac{[MxC_n] + \left[\frac{Mx}{m_n} m_s C_s\right] + \left[\frac{Mx}{m_n} m_f C_f\right] + \left[\left(M - Mx - \frac{Mx}{m_n} m_s - \frac{Mx}{m_n} m_f\right) C_l\right]}{M} \quad (24)$$

where, $\boldsymbol{m_f/m_n}$ is the ratio of mass fraction between induced long-range nanostructures and nanoparticle, while $\boldsymbol{C_f}$ is the heat capacity of the long-range nanostructure.

Kuznetsov [117] performed an analytical study of the heat capacity of fractal nanostructure based on Debye approximation and showed that materials confined at the nanoscale (especially fractal nanostructures) have a much higher specific heat capacity. The author elaborated on two unique features of materials confined to nanoscale dimensions that significantly modulated the resulting enhancement in the values of specific heat capacity, which are summarized as follows:

(1) These nanostructures have a lower Euclidean and phonon spectrum dimension compared to that of the bulk phase of these materials - which result in an excess density of vibrational states;

(2) In contrast to crystals having infinitely long wavelength spectrum, the maximum phonon wavelength λ_{max} is limited by the critical dimension (i.e., the length-scale of the nanostructure size L_N). This creates a lower bound for the oscillation frequency ω_{min} and hence increases the phono spectrum density in nanostructures. C_f could be calculated analytically as a function of phonon spectrum dimension and nanostructure size [117], as follows

$$C_f = \frac{3d_f n k_B}{\left(\frac{\theta_H}{T}\right)^{d_f} - \left(\frac{\theta_N}{T}\right)^{d_f}} \int_{x_{min}}^{x_{max}} \frac{x^{d_f+1} e^x}{(e^x - 1)^2} \mathrm{dx} \tag{25}$$

The determination of m_f/m_n would require some additional technique and exploration in the future for generalizing the effect (e.g., by performing digital image analyses of the SEM images). Nevertheless, if we consider the secondary nanostructures to be of the same composition as the compressed layer and approximate the effective

volume of secondary nanostructure as an extended shell that envelopes the nanoparticle (say with a shell thickness of ~10 nm), the prediction using Equation 18 showed that even with large sized nanoparticle (say, for a spherical nanoparticle with a diameter of ~50 nm), the net value of the specific heat capacity of the nanofluid can be effectively enhanced by more than 13%. The results from these calculations for the net value of specific heat capacity are plotted in Figure 64 as a function of nanoparticle size and mass concentration.

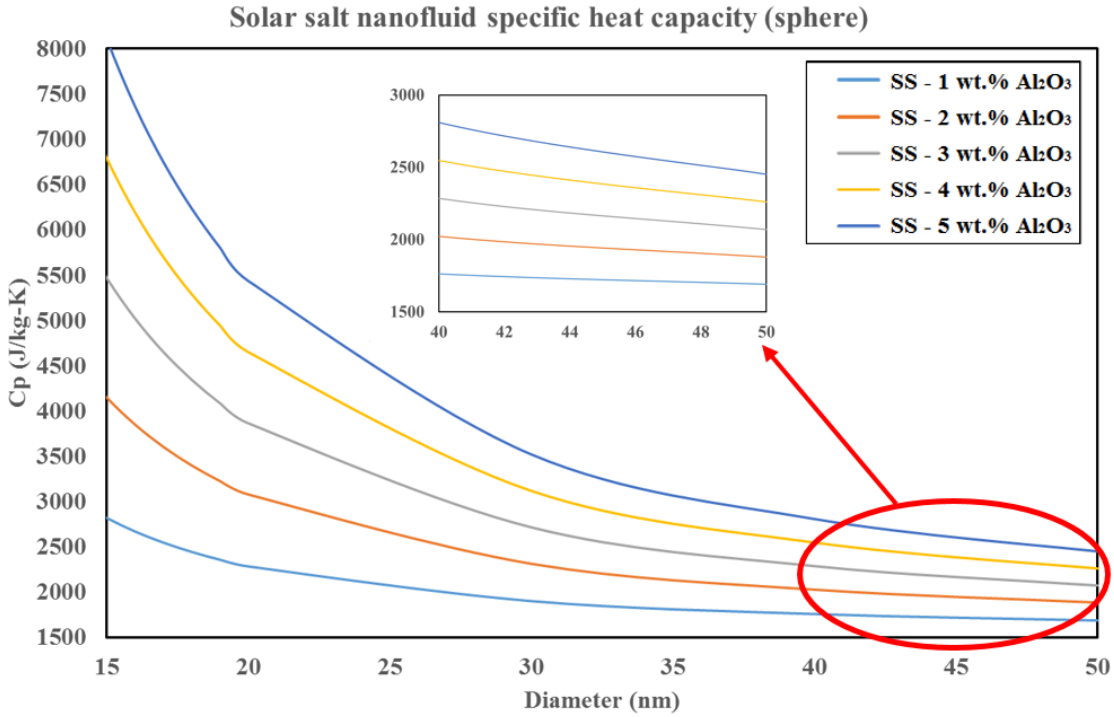

Figure 64. Numerical prediction for the values of net specific heat capacity of solar salt nanofluid (containing Al_2O_3 nanoparticles) as a function of nanoparticle size and mass concentration by assuming contribution from compressed phase, using Equation 24.

Hence, the endeavor to estimate the specific heat capacity of nanofluids, particularly for molten salt nanofluids, need to account for the material property values as well as the molecular structure of the solvent molecules in the compressed phase and the

secondary nanostructures that can be induced by the presence of the nanoparticles in the solvent medium. It is possible that the chemical composition and molecular level ordering of the compressed phase and secondary nanostructures can be very different from each other as well as from the bulk phase of the solvent.

4.2 Thermal conductivity of nanostructure

4.2.1 Conventional models

Brownian motion has been shown to contribute significantly to the thermal transport phenomena in nanofluids. In addition, intermolecular interactions at the surface of a nanoparticle with solvent phase has also been accounted to be a significant parameter in estimating the thermal impedance networks inherent in nanofluids (e.g., the role of Kaptiza resistance). Other parameters have also been explored in the literature for estimating the thermal properties of nanofluids (e.g., agglomeration, clustering, formation of fractal networks, etc.). However, it is unclear which of these parameters dominates the modulation of the effective thermal conductivity of nanofluids. Pang [118] proposed a new correlation for predicting the thermal conductivity of nanofluids which combined the effect of nano-scale percolation networks and convection of the solvent phase in the vicinity of the nanoparticles, and is shown below:

$$k_{\text{eff}} = \frac{k_{nf}}{k_{bf}} = \frac{3\emptyset_a K_{ba} + (1-\emptyset_a)(K_{ba}+2)}{3\emptyset_a + (1-\emptyset_a)(K_{ba}+2)} + A\emptyset_a \text{Re}_a^m \text{Pr}^{0.333} \quad (26)$$

where, $\emptyset_a$ is the volume fraction of the nanoparticle in the fluid, K_{ba} is the ratio of thermal conductivity between the nanoparticle and base fluid, A and m are constants determined from experiments and Reynolds number is determined from the nano-convection of liquid near the particles [105], as follows:

$$\mathrm{Re} = \frac{1}{v}\sqrt{\frac{18k_bT}{\pi\rho_N d_N}} \tag{27}$$

where, k_b is Boltzmann constant, T is the liquid temperature, ρ_N is the density of the nanoparticle and d_N is the diameter of the nanoparticle.

A selected number of numerical models for predicting the thermal conductivity of nanofluids was culled from the literature and are listed in Table 22. The experimental data for the thermal conductivity measurements for the solar salt nanofluids obtained in this study are used to validate the models reported in the literature, as shown in Figure 65. For the solar salt nanofluids (SiO_2 nanoparticles, two-step synthesis protocol) a close match between the measured values of thermal conductivity and predictions from Equation 26 was observed (i.e., by using $A = 180$ and $m = 0.5$). However, all the correlations selected in this exercise were found to underestimate the measured values of the thermal conductivity of solar salt nanofluids (target Al_2O_3 nanoparticles from aluminum nitrate additive, one-step synthesis protocol). This is most likely due to the formation of secondary nanostructures (percolation) in this nanofluid - which further enhances the heat transport in the colloidal system and these effects are not accounted for in the models available in the literature. The formation of percolation networks (as additional pathways for heat conduction with potentially significantly higher values of thermal conductivity)

provides means for more efficient heat removal than in the bulk phase of the solvent. The percolation networks arising from the formation of the secondary nanostructures (dendritic structures, fractal structures, nano-needles in the form of “nano-fins”, etc.) are therefore believed to be the dominant parameter for the anomalous enhancement in thermal conductivity of the nanofluids obtained by the single-step synthesis protocol. However, addition studies are needed to characterize the structure and morphology as well as composition of the percolation networks formed by the secondary nanostructures in order to develop a more mature numerical model for the prediction of effective thermal conductivity of nanofluids.

Table 22. Selected correlations for nanofluid thermal conductivity

Maxwell correlation (spherical) [119]	$\frac{k}{k_f} = \frac{1 + 2\beta\emptyset}{1 - \beta\emptyset},\ \beta = \frac{k_p - k_f}{k_p + 2k_f}$	(28)
Hamilton - Crosser [120]	$\frac{k}{k_f} = \frac{k_p + (n-1)k_f - (n-1)(k_f - k_p)\varphi}{k_p + (n-1)k_f + (k_f - k_p)\varphi}$	(29)
	$n = \frac{3}{\psi},\ \psi = \begin{cases} 1 & \text{for sphereical particle} \\ 0.5 & \text{for prolate ellopsoid} \end{cases}$	(30)
Xuan & Li [47]	$\frac{k}{k_f} = \frac{k_p + 2k_f - 2(k_f - k_p)\varphi}{k_p + 2k_f + (k_f - k_p)\varphi} + \frac{\rho_p \varphi c_p}{2k_f}\sqrt{\frac{k_B T}{3\pi r_c \mu}}$	(31)
Prasher [105]	$\frac{k}{k_f} = (1 + ARe^m Pr^{0.333}\phi)\left[\frac{(1+2\alpha) + 2\phi(1-\alpha)}{(1+2\alpha) - \phi(1-\alpha)}\right]$	(32)
	$\mathrm{Re} = \frac{\rho_f}{\mu_f}\sqrt{\frac{18k_b T}{\pi\rho_N d_N}},\ \alpha = \frac{2R_b k_m}{d}$	(33)
Pang & Lee [118]	$\frac{k}{k_f} = \frac{3\phi\frac{k_p}{k_f} + (1-\phi)\left(\frac{k_p}{k_f} + 2\right)}{3\phi + (1-\phi)\left(\frac{k_p}{k_f} + 2\right)} + ARe^m Pr^{0.333}\phi$	(34)

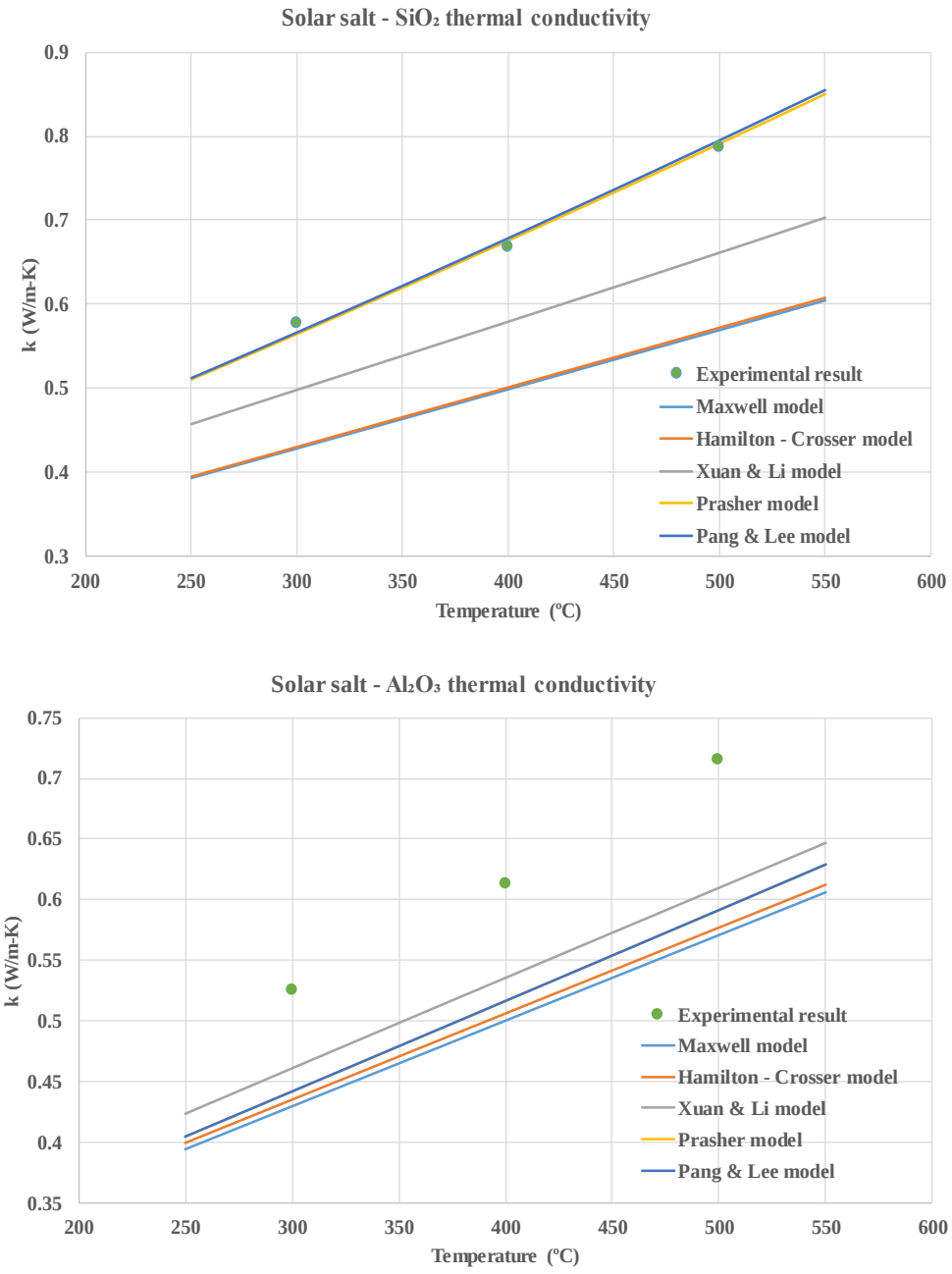

Figure 65. Experimental validation of predictions for thermal conductivity of nanofluids explored in this study. (TOP) Solar salt nanofluids prepared using two-step synthesis protocol (SiO_2 nanoparticles). (BOTTOM) Solar salt nanofluids prepared using one-step synthesis protocol (target Al_2O_3 nanoparticles)

4.2.2 Percolation model

In order to properly characterize the heat conduction in nano-network, a two-stage dispersed-aggregate model was developed here, in which periodic structures were employed for analyzing the heat transport in both aggregated clusters and the liquid dispersion. Therefore, the characteristics of heat conduction in nanofluid can be represented by the performance in a single unit cell. It shall also be shown that when nano-network was formed in the nanofluid system, the effect of Brownian motion becomes negligible. Hence, the effective thermal conductivity of the nanofluid can be calculated merely as a function of permeability, volume fraction and thermal conductivity of the nano-cluster.

4.2.2.1 Model construction

Stage I – Effective thermal conductivity of single nano-cluster

We considered a uniform cross-bar network structure in the aggregate, in which the nanoparticles are interconnected with a periodic pattern (Figure 66 a). Such structure could be treated as repeated patterns of a single cubic cell will the nano-fillings stretching out to six surfaces (Figure 66 b). The effective thermal conductivity of the assembly (with large enough number of cells) could then be represented by the value in each single cell, considering the periodicity of the structure. The volume fraction of the nano-network filling is given by

$$\emptyset = \frac{3\pi}{4\eta_{LD}^2} - \frac{\sqrt{2}}{\eta_{LD}^3} \tag{35}$$

where, $\boldsymbol{\eta_{LD}}$ is the ratio between unit cell length and nano-network stem diameter. The steady state heat transport in the cubic cell is governed by the isotropic conduction equation $\vec{\nabla}T = 0$

To evaluate the effective thermal conductivity of the single cell, we consider the case of heat flux flowing in *y*-direction which mimics the 1-D conduction scenario. In this case, periodic boundary conditions are applied on all *xy* and *yz* faces (light blue surfaces in Figure 66 b) and isothermal boundary conditions are applied on *xz* faces (orange surfaces in Figure 66 a). By solving the temperature field inside the single cell, the effective thermal conductivity of the composite can be expressed as

$$k_{\text{eff,cluster}} = q_{\text{avg}} \cdot \frac{L_{cell}}{T_{\text{front}} - T_{\text{rear}}} \tag{36}$$

where, $\boldsymbol{q_{avg}}$ is the average heat flux at front face, $\boldsymbol{L_{cell}}$ is the side length of the unit cell, $\boldsymbol{T_{front}}$ and $\boldsymbol{T_{rear}}$ are the boundary temperature at front and rear faces.

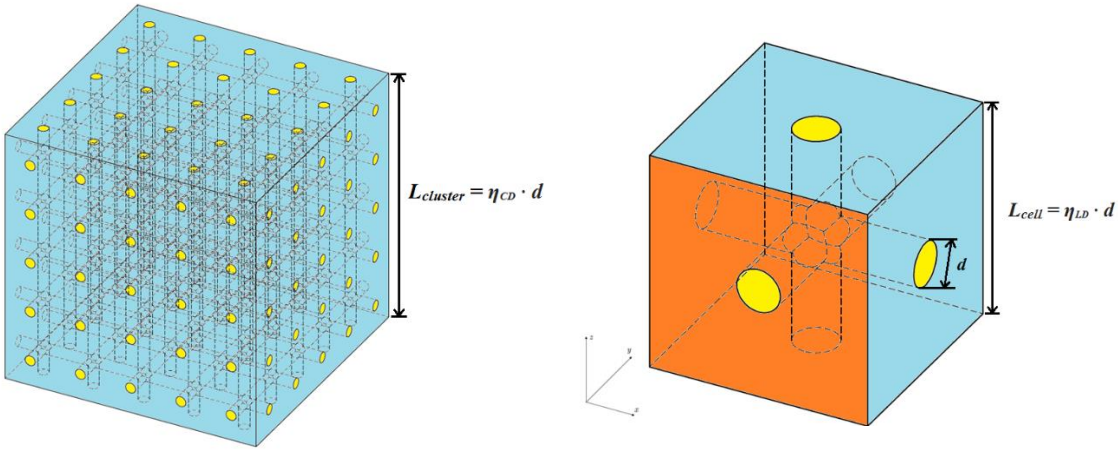

Figure 66. (a) Nano-aggregate structure with repeated pattern (left); (b) Single unit cell of nanofluid composite (right). The yellow color represents nano-fillings and the blue color represents the base fluid

Stage II – Effective thermal conductivity of nanofluid

A nanofluid system can be considered as nano-clusters dispersed in the base fluid. Each nano-cluster could have distinct size, shape and volume. With known effective thermal conductivity of each individual cluster, the effective thermal conductivity of overall nanofluid system can be then evaluated using classical dispersed system correlations. Each nano-cluster now can be treated as a dispersed entity with effective thermal conductivity of k_{eff} and effective radius of r_{eff}. The total thermal conductivity of the nanofluid system can then be calculated using the classical equations for multi-phase dispersed system such as Maxwell equation [119] or Lewis-Nielsen equation [121].

Maxwell-Garnett model:

$$\frac{k_{\text{eff}}}{k_f} = \frac{k_p + 2k_f + 2\emptyset(k_p - k_f)}{k_p + 2k_f - \emptyset(k_p - k_f)} \tag{37}$$

where, $\boldsymbol{k_f}$ and $\boldsymbol{k_p}$ are the thermal conductivity of the base fluid and nanoparticles respectively.

Lewis-Nielson model:

$$\frac{k_{\text{eff}}}{k_f} = \frac{1 + AB\emptyset}{1 - B\psi\emptyset} \tag{38a}$$

where

$$B = \left(\frac{k_p/k_f - 1}{k_p/k_f + A}\right) \tag{38b}$$

$$\psi = 1 + \left(\frac{1 - \emptyset_m}{\emptyset_m^2}\right)\emptyset \tag{38c}$$

where, $\boldsymbol{A}$ is shape coefficient (1.5 for sphere), $\emptyset_{\boldsymbol{m}}$ is the maximum packing volume fraction (0.637 for close packing of spheres)

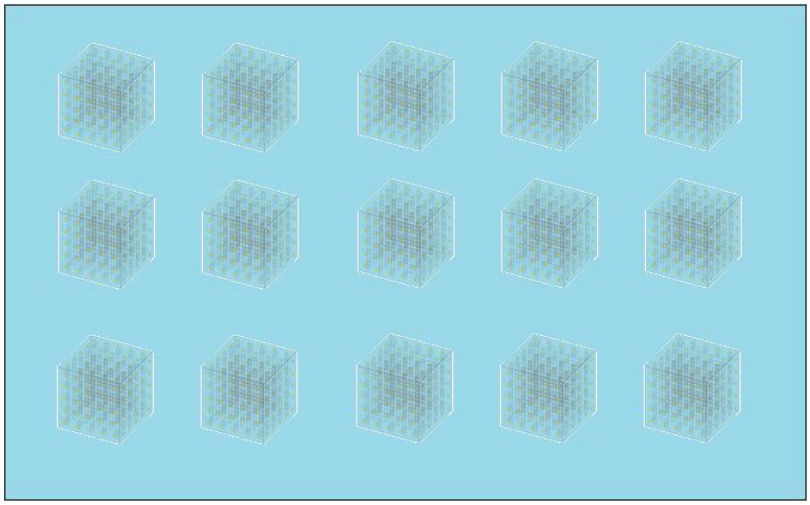

Figure 67. Schematic of the dispersed nano-cluster in the base fluid

4.2.2.2 Numerical analysis

Mathematical formulation

The thermal analysis of single cubic cell was performed using finite-volume software STAR-CCM+. The heat transfer is governed by stationary conduction equations while the temperature gradient jumps across the two-phase interface. Mathematically, these are expressed as

$$\frac{\partial^2 T_f}{\partial x^2} + \frac{\partial^2 T_f}{\partial y^2} + \frac{\partial^2 T_f}{\partial z^2} = 0 \tag{39a}$$

$$\frac{\partial^2 T_p}{\partial x^2} + \frac{\partial^2 T_p}{\partial y^2} + \frac{\partial^2 T_p}{\partial z^2} = 0 \tag{39b}$$

where, T_f and T_p are continuous temperature functions in each domain (base fluid and nano-network). The boundary conditions are set as describe earlier:

$$T_{x=0} = T_{x=L}, \qquad \left(\frac{\partial T}{\partial x}\right)_{x=0} = \left(\frac{\partial T}{\partial x}\right)_{x=L} \tag{40a}$$

$$T_{z=0} = T_{z=L}, \qquad \left(\frac{\partial T}{\partial x}\right)_{z=0} = \left(\frac{\partial T}{\partial x}\right)_{z=L} \tag{40b}$$

$$T_{y=0} = T_1 \tag{40c}$$

$$T_{y=L} = T_2 \tag{40d}$$

Coupling equations at interfaces gives:

$$(T_{\mathrm{f}})_{\mathrm{interface}} = (T_p)_{\mathrm{interface}} \tag{41a}$$

$$k_{\mathrm{f}}\left(\frac{\partial T_f}{\partial \vec{n}}\right)_{\mathrm{interface}} = k_{\mathrm{p}}\left(\frac{\partial T_p}{\partial \vec{n}}\right)_{\mathrm{interface}} \tag{41b}$$

where, $\vec{\boldsymbol{n}}$ is the normal vector at the solid-liquid interface.

Model setup for single nano-cluster (Stage I)

In the study, the temperature field in the domain was first solved with the prescribed boundary conditions, then the average surface heat flux at inlet face was calculated and plugged into equation 36 for evaluating the effective thermal conductivity of the cubic cell. The simulation domain was construed in STAR-CCM+ with constant property as shown in Figure 68. The stem diameter of the network filling material is set as 0.02 m, the thermal conductivity of the filling material is set as 0.6 W/(m·K), the temperature at inlet and outlet face were set at 302 K and 300 K.

The effective thermal conductivity is evaluated against two parameters: (i) the ratio of cell length over network diameter ($\eta_{LD} = L/d$); (ii) the thermal conductivity ratio between network and matrix material ($\lambda = k_p/k_f$). The pilot study was performed with $\eta_{LD} = 1.5$ and $\lambda = 50$. The geometry was meshed using polyhedrons with base size of 5×10^{-4} m and surface growth rate of 1.3. The pilot simulation result was validated with: (i) mesh convergence study; (ii) multi-cell-geometry study. After the pilot study was validated, a parametric study was performed with η_{LD} varying from 1.5 ~ 1000 and λ varying from 1.1 ~ 5. The effective thermal conductivity of the composite under different conditions are then calculated correspondingly and analyzed using regression fitting.

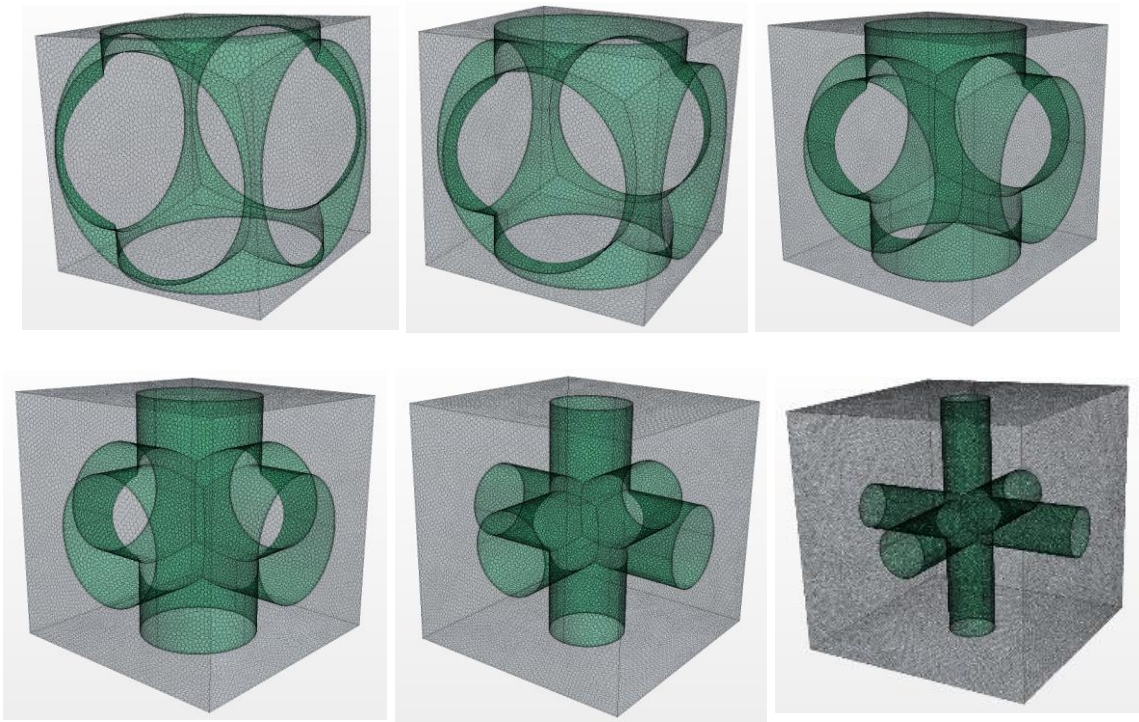

Figure 68. Mesh of single cubic cell for parametric study

Model setup for dispersed non-interacting system (Stage II)

Now consider the case of multiple nano-clusters dispersed in the base fluid as shown in Figure 67, each cluster can be treated as an independent, non-interacting entity with effective thermal conductivity of $\boldsymbol{k}_{\mathbf{cluster}}$. To investigate the heat transport behavior in the non-interacting nano-dispersion system, a simple body center cubic geometry was employed for the numerical study (Figure 69). The sphere in the center of the cell is representative of the effective volume occupied by the inter-connected nano cluster. A similar approach was adopted to calculate the effective thermal conductivity of the dispersed system, in which periodic boundary conditions were assigned to four side faces while isothermal boundary conditions were assigned to front and rear faces. The effective thermal conductivity of the system is calculated with varying thermal conductivity ratio between the two material and volume fraction.

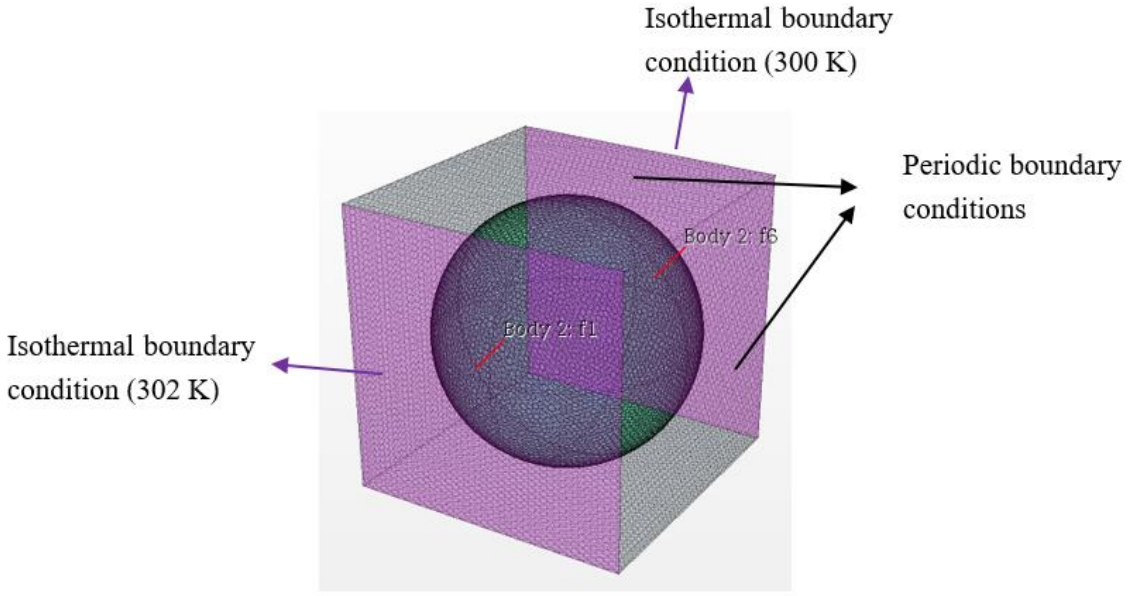

Figure 69. Configuration for single cubic cell of dispersed system

4.2.2.3 Results

Pilot study for nano-cluster

Figure 70 shows the temperature profile of different cross section planes obtained in the pilot simulation study (with $\eta_{LD} = 1.5$ and $\lambda = 50$). Overall the temperature profile revealed symmetric characteristic between inlet and outlet surface. It is also evident to notice that the temperature gradient becomes zero at top and bottom boundaries, which suggests that the periodic boundary condition is equivalent to insulated boundary condition in this study. Towards the right-most boundary plane, it is noticed that the temperature gradient tends to converge to the center filling region. This suggests the heat tends to flow from matrix region (base fluid) to filling region (nano-network). Towards the center plane, however, the direction of temperature gradient tends to point to top and bottom faces. These directions are in accordance with the two branches of network which stretches to up and down directions. Figure 71 shows the heat flux streamline inside the composite cell which is in accordance with the temperature profile.

Table 23 shows distribution of boundary heat transfer magnitude at inlet surface. It was found that more than 95% heat flows through the high conducting filling region, which only occupied 34.9% of the surface area at inlet. In other word, the presence of the high conducting filling network structure served as “high-speed channels” for the heat to transport fast through the medium. By calculating the average heat flux at inlet face, it was found that the effective thermal conductivity of the single cubic cell is 14.28 W/(m·K), which is more than 20 times of the matrix property (base fluid).

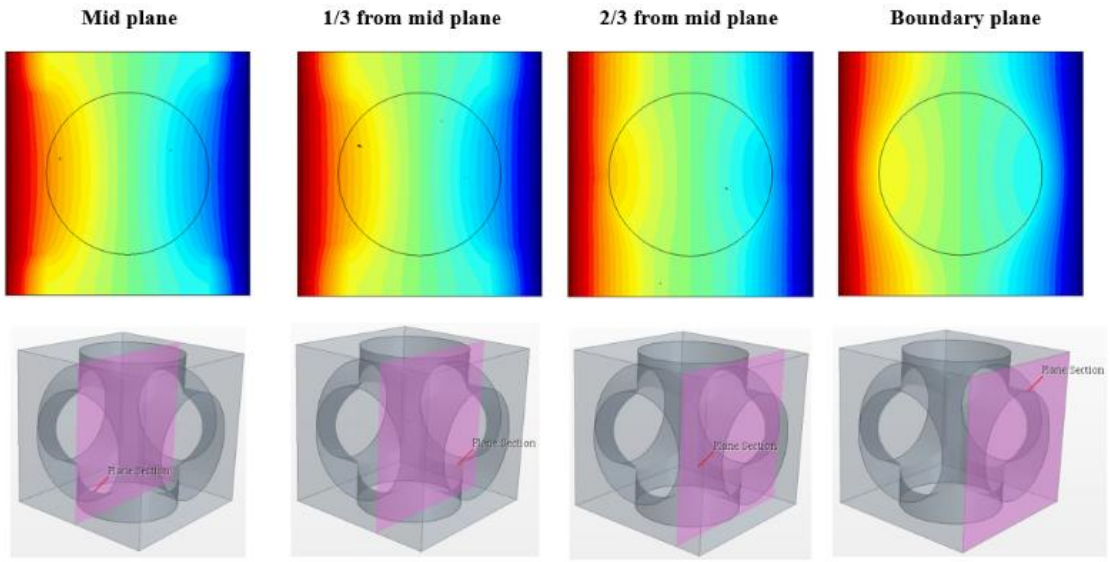

Figure 70. Cross section temperature profile of pilot study

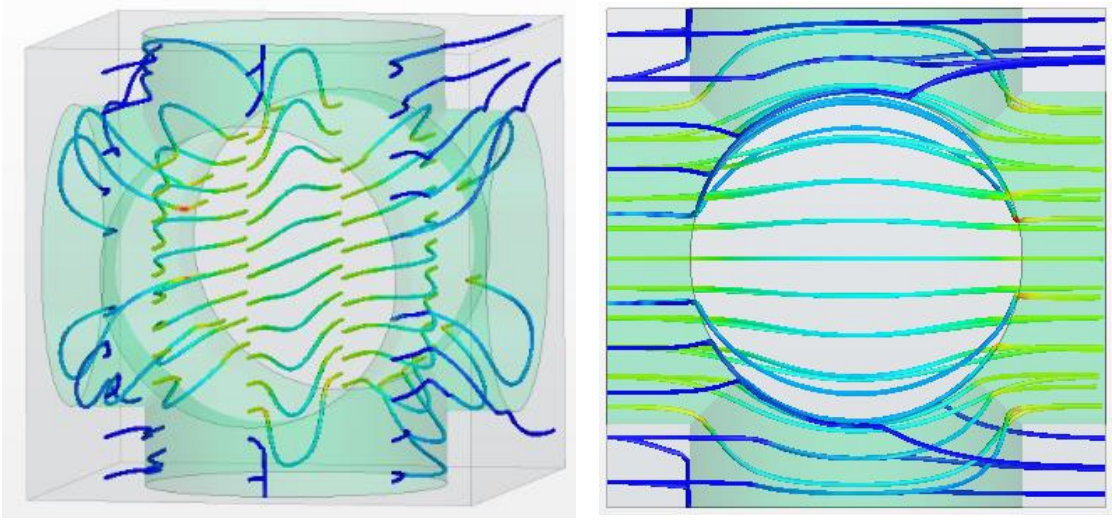

Figure 71. Heat flux streamline

Table 23. Heat flow distribution at inlet face

	Heat flux [(W/m^2)]	Area [(×10^{-4} m^2)]	Total heat transfer [(W)]
Overall	951.8	9.00	0.856
Through matrix	63.6	5.86	0.037
Through filling	2610.6	3.14	0.819

To validate the accuracy of the pilot simulation result, a mesh convergence study was performed in which the base mesh size was reduced from 5×10^{-4} m to 2×10^{-4} m. The number of meshing cells was hence increased from 291501 to 3378839. The average inlet heat flux calculated from the dense-mesh simulation remained same within two decimal places, which suggests that the pilot study with the designated meshing size is highly accurate with negligible numerical error.

To validate if the simulation result from single cell is representative of the overall nanonetwork system characteristic, a 5×5×5 super cell was constructed with front surface temperature set at 310 K (Figure 72). Figure 73 shows the comparison of temperature profile obtained between single cell geometry and super cell geometry. It was found that the temperature characteristics in single cell and multi-cell configuration is in highly agreement. In the multi-cell study, the temperature profile is self-repetitive in directions both orthogonal and parallel to the heat flow. Also, the temperature profile in the single cell study is resembling of the feature in each cubic cell in the multi-cell study on both boundary and mid cross section plane. This indicates that the heat transfer in multi-cell

configuration follows the same characteristic in the single cell configuration. The average inlet heat flux from the multi-cell study was calculated to be 948.83 W/m^2, which yields an effective thermal conductivity of 14.23 W/(m·K). Such value is in good match with the prediction from single cell pilot study, which suggests that the periodicity was conserved in the simulation study.

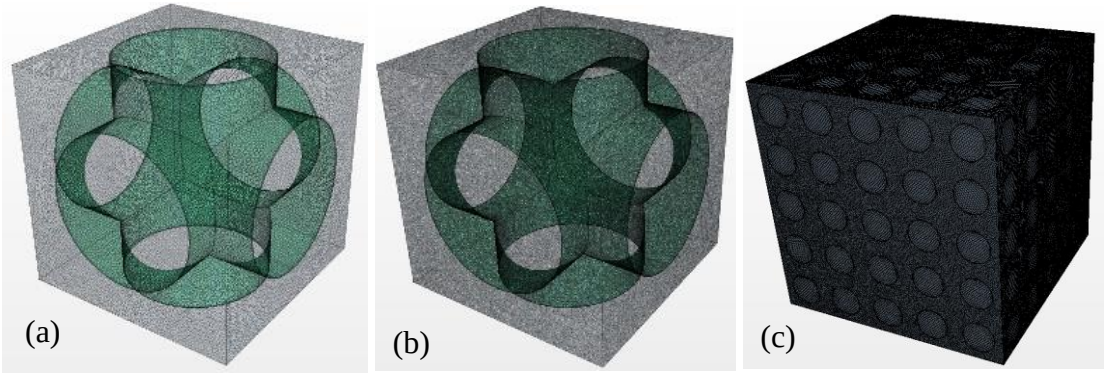

Figure 72. Validation test: (a) pilot study; (b) mesh convergence study; (c) Multi-cell study

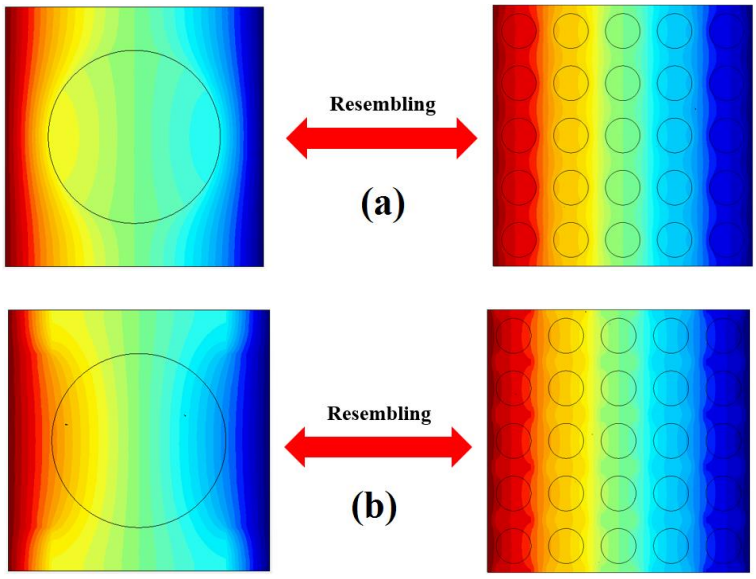

Figure 73. Comparison of temperature profile between single cell and super cell simulation: (a) boundary plane; (b) center plane

Parametric study for nano-cluster

Effective thermal conductivity of the aggregate network system was computed by the same method employed in the pilot study, as a function of two parameters η_{LD} and λ. Table 24 and Figure 74 shows the result from the parametric study under different conditions, in which **φ** is the volume fraction of networking fitting in the cubic cell. It was found that with fixed geometry, the percentage enhancement in thermal conductivity (***k*** $_{eff}$ **/** ***k*** $_{fluid}$) increases linearly with the thermal conductivity of network filling. With increasing volume ratio, the contribution of the network filling becomes more dominating and the overall enhancement in thermal conductivity is approaching the ratio between network thermal conductivity and base fluid thermal conductivity. By performing regression fitting to the calculated result, the following correlation is obtained for predicting the effective thermal conductivity of network-filled-composite:

$$\frac{k_{\text{eff,cluster}}}{k_{\text{fluid}}} = (0.695\varphi^2 + 0.302\varphi)\left(\frac{k_{\text{network}}}{k_{\text{fluid}}} - 1\right) + 1 \qquad (42)$$

When the volume fraction of network filling is 0%, $\frac{k_{\text{eff,cluster}}}{k_{\text{fluid}}}$ is equivalent to 1 suggesting that the effective thermal conductivity of the cell is same with the base fluid. When the volume fraction of network filling is 100%, $\frac{k_{\text{eff,cluster}}}{k_{\text{fluid}}} = \frac{k_{\text{network}}}{k_{\text{fluid}}}$ suggesting that the effective thermal conductivity of the cell is equivalent to the value of the network filling material.

Table 24. Parametric study result of composite effective thermal conductivity

$k_{\text{eff,cluster}}$ [W/(m·K)]		Volume fraction of network filling					
		8.3%	**20.9%**	**41.2%**	**62.8%**	**78.4%**	**88.5%**
$k_{network}$ [W/(m·K)]	**0.9**	0.62	0.66	0.71	0.78	0.83	0.86
	1.2	0.64	0.70	0.81	0.95	1.05	1.12
	1.8	0.67	0.79	1.00	1.26	1.47	1.62
	3	0.72	0.93	1.33	1.85	2.29	2.62
	4.5	0.78	1.09	1.71	2.56	3.30	3.85
	6	0.83	1.25	2.09	3.26	4.31	5.08
	9	0.94	1.56	2.83	4.65	6.30	7.53
	12	1.04	1.86	3.57	6.03	8.29	9.99
	18	1.25	2.47	5.03	8.78	12.27	14.89
	30	1.66	3.67	7.95	14.28	20.21	24.69
	45	2.17	5.18	11.59	21.14	30.14	36.94
	60	2.68	6.68	15.24	28.00	40.06	49.18
	90	3.70	9.68	22.52	41.73	59.91	73.67
	120	4.72	12.68	29.80	55.45	79.75	98.17
	180	6.76	18.69	44.36	82.89	119.44	147.15
	240	8.80	24.70	58.93	110.34	159.13	196.13
	300	10.84	30.70	73.49	137.78	198.82	245.12

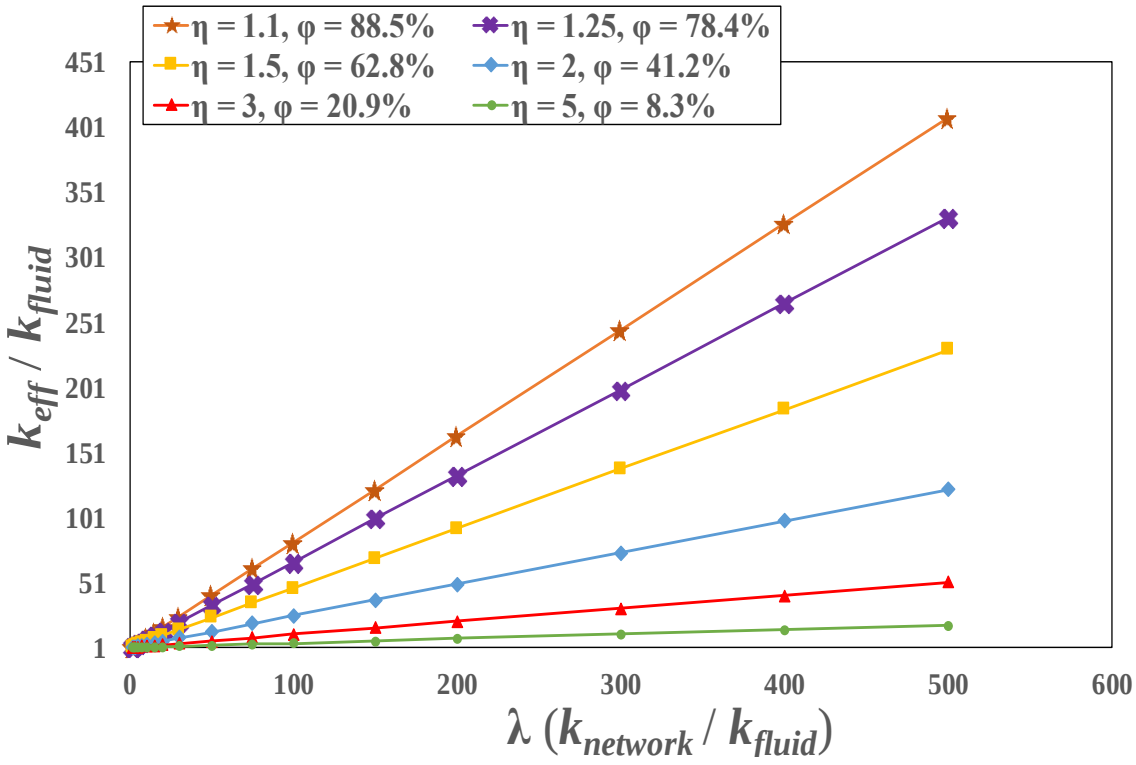

Figure 74. Summary of parametric study result in single cluster cell

Parametric study for dispersed system

Thermal conductivity of dispersed, non-interacting system was calculated under different conditions using the BCC model shown in Figure 69. Figure 75 shows the results from the parametric numerical simulation in comparison with the analytical predictions obtained using Maxwell-Garnett equation [119] and Lewis-Nielsen equation [121]. Different from the characteristic observed in single network cluster, the effective thermal conductivity of dispersed composite tends to converge to a constant value with increasing thermal conductivity of filling sphere. It was found that the classical models gave good

predictions of the dispersed composite thermal conductivity with low volume fraction. With high volume fraction, however, both model gave quite high error in the prediction. The Maxwell-Garnett model underestimates the composite thermal conductivity while the Lewis-Nielsen model overestimates the value by significant margin. To accurately capture the heat transport behavior over entire volume fraction range, the following empirical correlation was obtained via regression fitting from the simulation results:

$$\frac{k_{\text{eff,disperse}}}{k_{\text{fluid}}} = A + \frac{B}{k_{\text{sphere}}/k_{\text{fluid}} + C} \tag{43}$$

where, A, B and C are parameters fitted against the volume fraction using polynomials as

$$\begin{aligned} A &= a_0 + a_1\emptyset + a_2\emptyset^2 + a_3\emptyset^3 + a_4\emptyset^4 \\ B &= b_0 + b_1\emptyset + b_2\emptyset^2 + b_3\emptyset^3 + b_4\emptyset^4 \\ C &= c_0 + c_1\emptyset + c_2\emptyset^2 + c_3\emptyset^3 + c_4\emptyset^4 \end{aligned} \tag{44}$$

and the coefficients are listed in Table 25.

Table 25. Coefficients for parametric fitting

	0	1	2	3	4
a	1.000	2.886	5.194	-12.452	40.963
b	-0.004	-7.697	-48.426	200.481	-587.136
c	1.974	2.971	7.334	-28.969	92.980

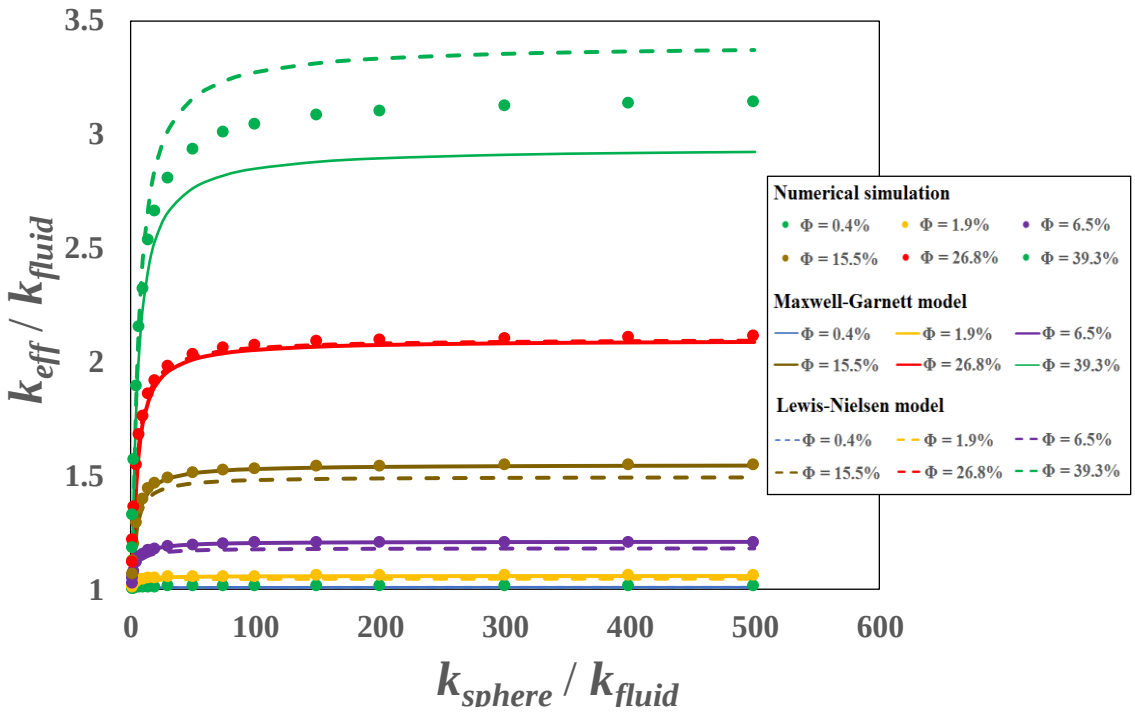

Figure 75. Summary of parametric study result in dispersed composite

It should be noted that the volume fraction Φ used in equation 44 is calculated based on the effective volume occupied by each network cluster in the nanofluid system. Such value is given by

$$V_{\text{cluster}} = \frac{V_{\text{network}}}{\varphi_{\text{network-in-cluster}}} \tag{45}$$

where, $V_{network}$ refers the volume of the network filling material while φ is the volume fraction of these networking filling in each cluster. To distinguish the different volume fraction concept used here, the volume fraction of network material in each cluster is replace by the permeability of the cluster as

$$\kappa_{\text{cluster}} = 1 - \varphi_{\text{network-in-cluster}} \tag{46}$$

In other word, the permeability of the cluster describes the "void" volume fraction in each cluster occupied by base fluid. Combining equations 43~46, the effective thermal conductivity of nanofluid with dispersed nano-network clusters can now be expressed as

$$\frac{\boldsymbol{k_{\text{eff,system}}}}{\boldsymbol{k_{\text{fluid}}}} = \boldsymbol{A}\left(\frac{\boldsymbol{\varphi}}{\boldsymbol{1-\kappa}}\right) + \frac{\boldsymbol{B}\left(\frac{\boldsymbol{\varphi}}{\boldsymbol{1-\kappa}}\right)}{[\boldsymbol{0.695(1-\kappa)^2 + 0.302(1-\kappa)}]\left(\frac{\boldsymbol{k_{\text{network}}}}{\boldsymbol{k_{\text{fluid}}}} - \boldsymbol{1}\right) + \boldsymbol{1} + \boldsymbol{C}\left(\frac{\boldsymbol{\varphi}}{\boldsymbol{1-\kappa}}\right)} \tag{47}$$

where, $\boldsymbol{\kappa}$ is the permeability in nano-network structure and $\boldsymbol{\varphi}$ is the volume fraction of nano-network in the nanofluid system.

4.2.2.4 Discussion

Effect of permeability

With increasing permeability, the network structure becomes looser, hence the space spanned by the nano-network with same volume becomes larger. This leads to increased volume fraction in space to be "connected" by the nano-network. At low permeability condition, on the contrary, very limited space in the nanofluid system are connected by the nano-network. However, the local-density of the nanostructure is much higher than that of the high permeability case, which give rise to higher local thermal conductivity. In general, increasing permeability should leverage the high thermal conductivity of nanostructure into the overall enhancement in nanofluid system more effectively.

Figure 76 shows the effect of permeability on the nanofluid thermal conductivity under different conditions. It is evident to notice that when the thermal conductivity ratio between nano-network and fluid is small ($k_{nano} / k_{fluid} < 10$), the permeability has negligible effect on the nanofluid thermal conductivity. When the ratio is large ($k_{nano} / k_{fluid} > 20$), however, the increment in nano-cluster permeability can bring drastically enhancement to the nanofluid thermal conductivity. It is also interesting to notice that under low permeability scenario, the overall thermal conductivity enhancement is quite limited regardless of the high thermal conductivity of the nano-network. When permeability is high, however, the nanofluid thermal conductivity is enhanced by significant percentage. Such prediction is in agreement with the underlying heat transport behavior in low and high permeability cases.

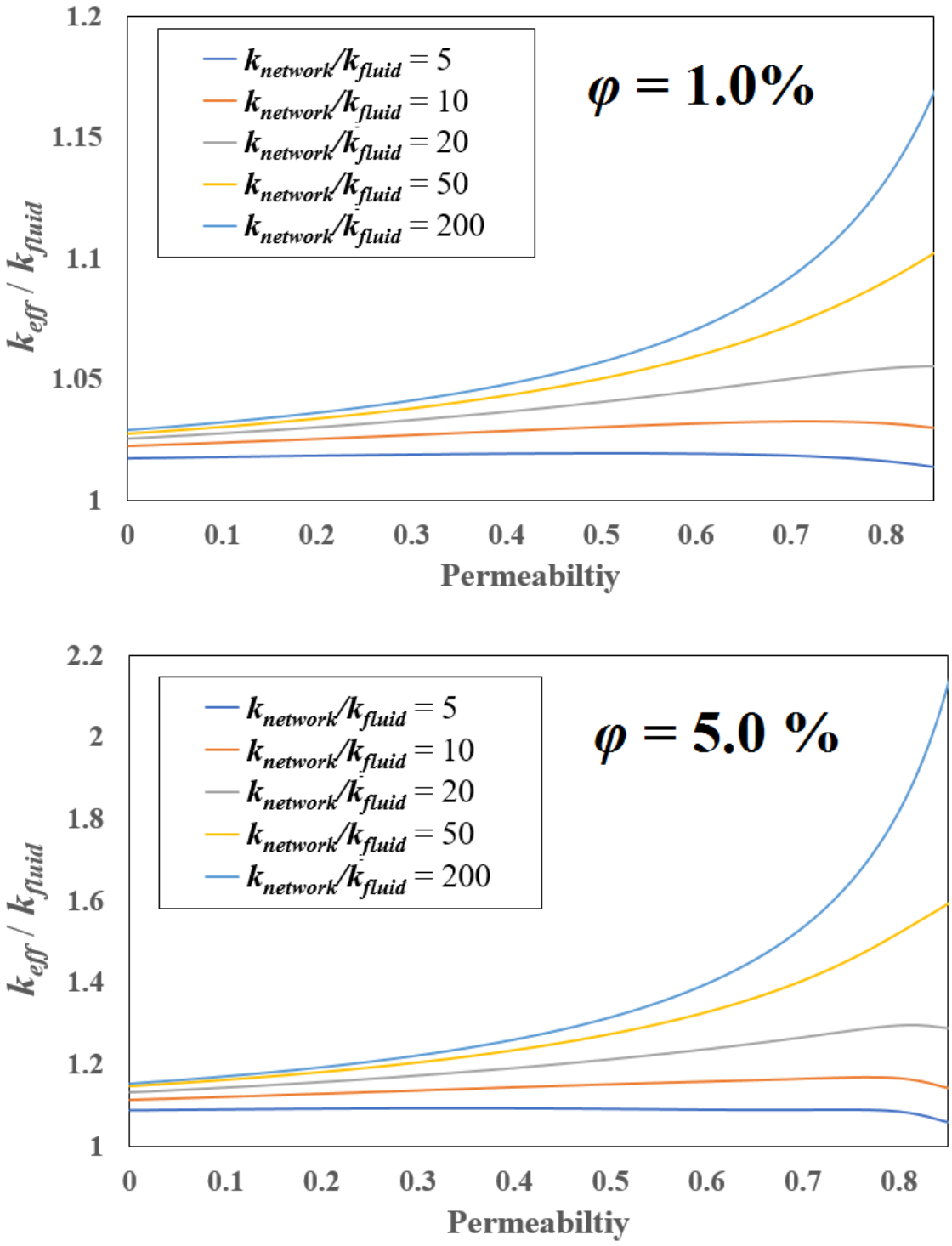

Figure 76. Effect of permeability on nanofluid thermal conductivity

Effect of volume fraction

The effect of volume fraction on nanofluid thermal conductivity is shown in Figure 77. It should be noted that the volume fraction of nano-network should not exceed (1-permeabiltiy). In general, the overall thermal conductivity increases with increasing volume fraction. However, it is observed that the increasing rate of nanofluid thermal conductivity is slow at low volume fraction. Also, when permeability is high, the volume fraction becomes the dominating factor for determining the nanofluid thermal conductivity. The thermal conductivity ratio between nano-network and fluid (k_{nano} / k_{fluid}) does not seem to affect the overall thermal conductivity enhancement significantly. Such characteristic is particular evident when both permeability and volume ratio are high (φ = 0.3, permeability = 0.7) where the overall effective thermal conductivity becomes almost independent of k_{nano} / k_{fluid}.

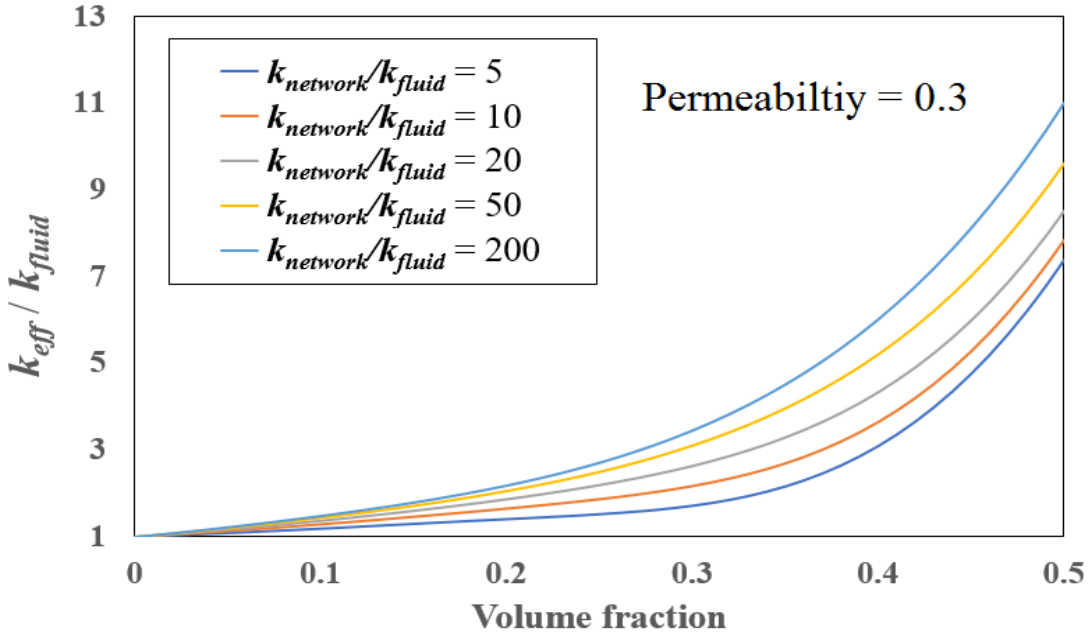

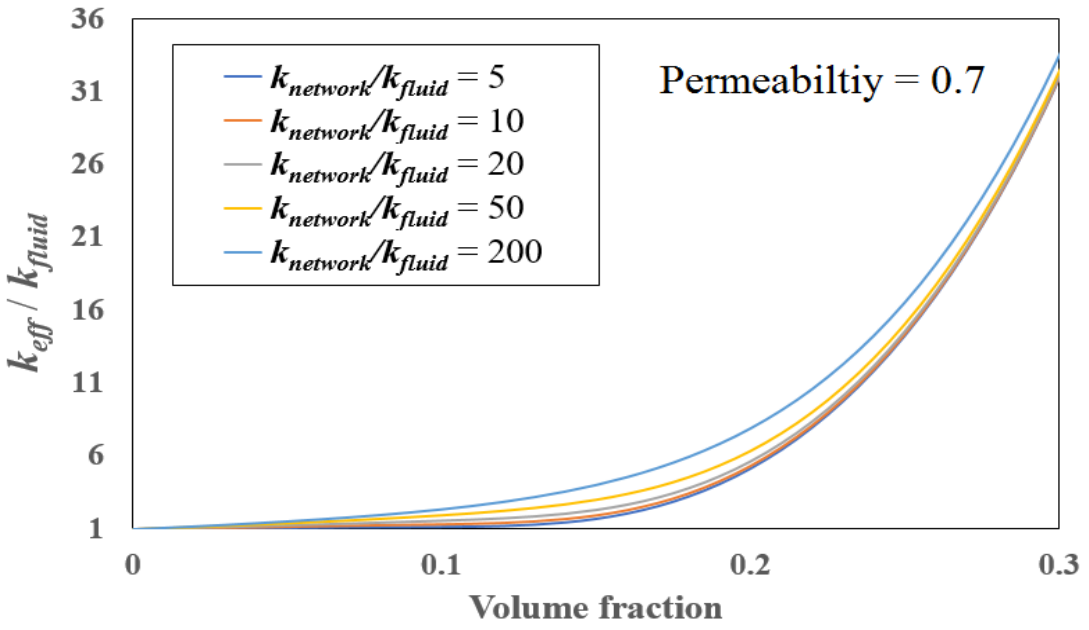

Figure 77. Effect of volume fraction on nanofluid thermal conductivity

Effect of Brownian motion

The effect of Brownian motion has not been considered in this study. This is primarily due to the reason that when nano-networks are formed in the nanofluid system, the effective mass of the clusters are large enough such that the Brownian velocity is negligible. In such scenario, the contribution of Brownian motion induced convection effect becomes trivial. The mathematical analysis follows similar procedure as proposed by Prasher [105], in which the effect of Brownian motion induced nano-convection can be treated as creeping flow passing spherical particles. By equivalating the convection effect as conduction through semi-infinite medium model, the effective thermal conductivity of the medium (base fluid) could be derived as

$$k_m = k_f[1 + (1/4)\mathrm{Re}\times\mathrm{Pr}] \tag{48}$$

in which the Reynolds number is given by

$$\mathrm{Re} = \frac{\rho_f v_{\mathrm{Brownian}} d}{\mu_f} \tag{49}$$

Here $\boldsymbol{d}$ is the diameter of each single stem in the nano-network, $\boldsymbol{k_f}$ is the thermal conductivity of base fluid, and $\boldsymbol{v_{\mathrm{Brownian}}}$ is the relative velocity of fluid with respect to the nano-cluster induced by the Brownian motion of the fluid molecules. The Brownian velocity of nano-cluster can be calculated by

$$v_{\mathrm{Brownian}} = \sqrt{\frac{3k_B T}{m}} \tag{50}$$

where, k_B is Boltzmann constant, T is temperature, and m is the mass of the overall nano-cluster. It can be easily seen that the effect of Brownian motion is more dominating when particle mass is small (i.e., well-dispersed fine particles), and such effect becomes weaker with increasing size of nano-cluster.

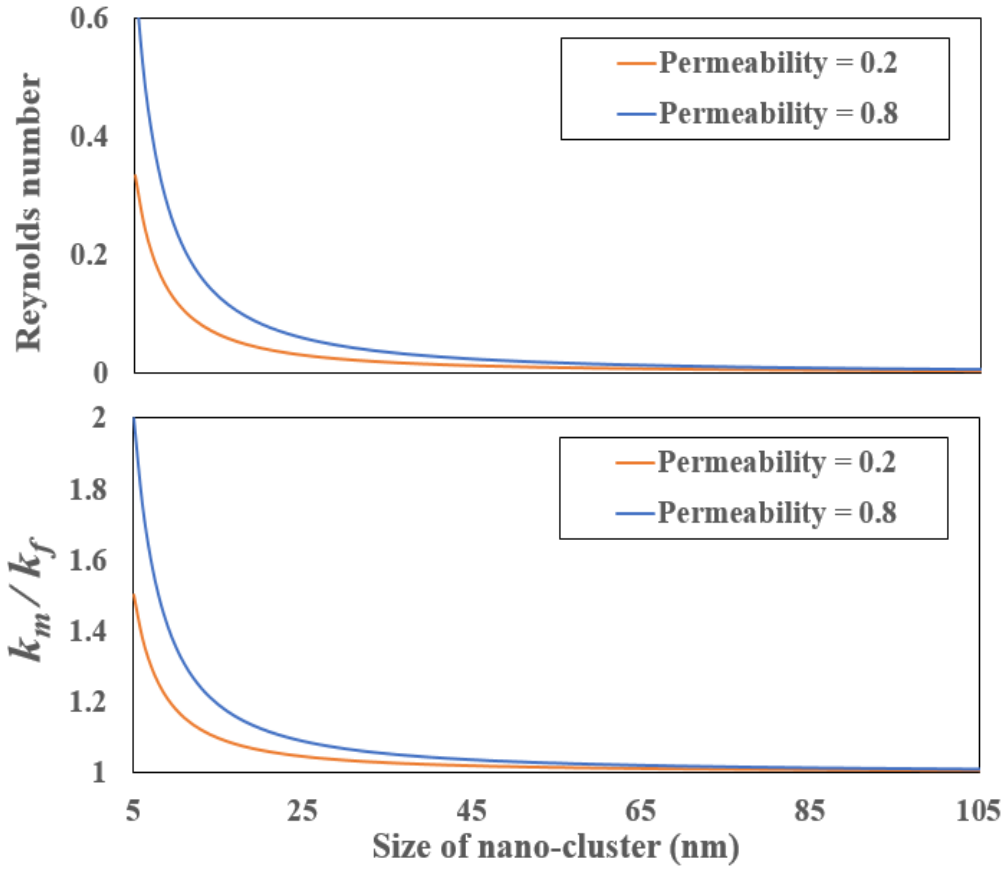

Figure 78. Effect of nano-cluster size on Reynolds number and effective thermal conductivity of liquid medium

Figure 78 shows the variation of Reynolds number and k_m / k_f as a function of nano-cluster size for aqueous copper nanofluid at room temperature under two

permeability conditions. The diameter of single stem in the nano-network is set as 10 nm. It is noticed that when the average size of nano-cluster is less than 25 nm, the Reynolds number of Brownian convection is large enough such that the effective thermal conductivity of liquid medium is enhanced for more than 10%. When the size exceeds 35 nm however, the enhancement in effective thermal conductivity of liquid medium is less than 5%. Considering that the size of nano-clusters is generally more than 100 nm, the Brownian motion Reynolds number is less than 0.01 and the nano-convection does not bring any significant enhancement to the heat transport.

4.3 Summary

In this chapter, theoretical models were proposed to explain the anomalous enhancement observed in specific heat capacity and thermal conductivity of molten salt nanofluid. It was inferred that the formation of secondary nano-network structure is the primary contributor to the increment in both energy storage capacity and heat transport rate. Mathematical correlations were derived for predicting the effective specific heat capacity and thermal conductivity in molten salt nanofluid systems. The analytical predictions are in good agreement with the experimental measurements.

5. EXPERIMENTAL RESULTS: EFFECT OF SYNTHESIS CONDITIONS ON MATERIALS PROPERTIES

5.1 Effect of concentration

The effect of variation of nanoparticle concentrations on the specific heat capacity of the nanomaterials was examined for solar salt based nanofluids derived from aluminum nitrate additives (with target mass fraction of alumina nanoparticles at 0.5%, 1% and 1.5%). The synthesis procedure is described in Chapter 2. Briefly, the pure solar salt samples are mixed in powder form with aluminum nitrate additive (which serves as a precursor for generating alumina nanoparticles when heated in furnace at 550ºC for 1 hour). Based on the thermogravimetric analysis (TGA) analysis of pure samples of $Al(NO_3)_3 \cdot 9H_2O$ (as shown in Figure 13) the decomposition of these additives should be complete after the thermal decomposition step and be able to yield Al_2O_3 nanoparticles for the desired target mass concentration. Table 26 summarizes the quantity of additives that are used for synthesis for each desired target mass fraction of alumina nanoparticles (the mass fraction of $Al(NO_3)_3 \cdot 9H_2O$ additives listed in Table 26 as nanoparticle precursors was determined from the stoichiometric values for the target mass fraction of Al_2O_3 nanoparticles based on the assumption of complete thermal degradation of the additives/ precursors).

Table 26. Mass of raw material needed for synthesis

	Raw material mass (g) for synthesis			Final product mass (g)		
Target nanoparticle concentration	$NaNO_3$	KNO_3	$Al(NO_3)_3 \cdot 9H_2O$	Solar salt	Al_2O_3	Total
0.5%	20.895	13.93	1.287	34.825	0.175	35
1.0%	20.790	13.86	2.575	34.650	0.350	35
1.5%	20.685	13.79	3.862	34.475	0.525	35

The specific heat capacities of the samples were measured using the T-History method discussed previously and the sample morphologies were characterized using SEM.

5.1.1 Specific heat capacity

Figure 79 shows the thermocouple response recorded during T-History experiments for temperature of air, reference sample (pure solar salt) and test sample (pure solar salt nanofluid with alumina nanoparticles generated from thermal decomposition of aluminum nitrate additives). The samples were synthesized for three different concentrations of the alumina nitrate additive (3.5%, 6.9% and 10.1%; with target mass fraction of the alumina nanoparticles of 0.5%, 1% and 1.5%). The T-History experiments were performed for exactly the same condition as discussed in Chapter 2.3 (i.e., all of the samples were heated from 250ºC to 550ºC for 10 consecutive cycles and the temperature response of the thermocouples were recorded for further analyses). The results in Figure 79 show that for all the tests the rate of increase in temperature for the nanomaterial samples was always slower than that of the pure solar salt samples (for all of the concentrations used in this study). However, there is a marginal difference between the

temperature rates for both pure solar salt samples and the nanofluid samples (for a target mass fraction of alumina nanoparticles of 0.5%). This indicates that the specific heat capacity of the nanofluid samples (for a target mass fraction of alumina nanoparticles of 0.5%) is the lowest of the three mass concentrations targeted in this study. In addition, the specific heat capacity of the nanofluid samples (for a target mass fraction of alumina nanoparticles of 1%) is the highest of the three mass concentrations (for the three temperature values of 300 °C, 400 °C and 500 °C) that were targeted in this study.

Figure 80 and Table 27 shows the plots for the calculated values enhancement of the specific heat capacity values for the three target mass concentrations for nanoparticles for the solar salt nanofluids explored in this study (the details of these calculations are tabulated in Appendix C). The plots show that the level of enhancement is reduced as the temperature increases. The specific heat capacity values were enhanced significantly for nanofluid samples with 1.0% and 1.5% target mass concentration of Al_2O_3 nanoparticles (the average value of enhancement was 38.7% and 31.8%, respectively). For the nanofluid sample with 0.5% target mass concentration of Al_2O_3 nanoparticles, the average enhancement is only 17.5%. It is inferred from these results that the optimum concentration for maximizing the specific heat capacity enhancement for the solar salt nanofluids is in excess of 0.5% and less than or equal to 1%.

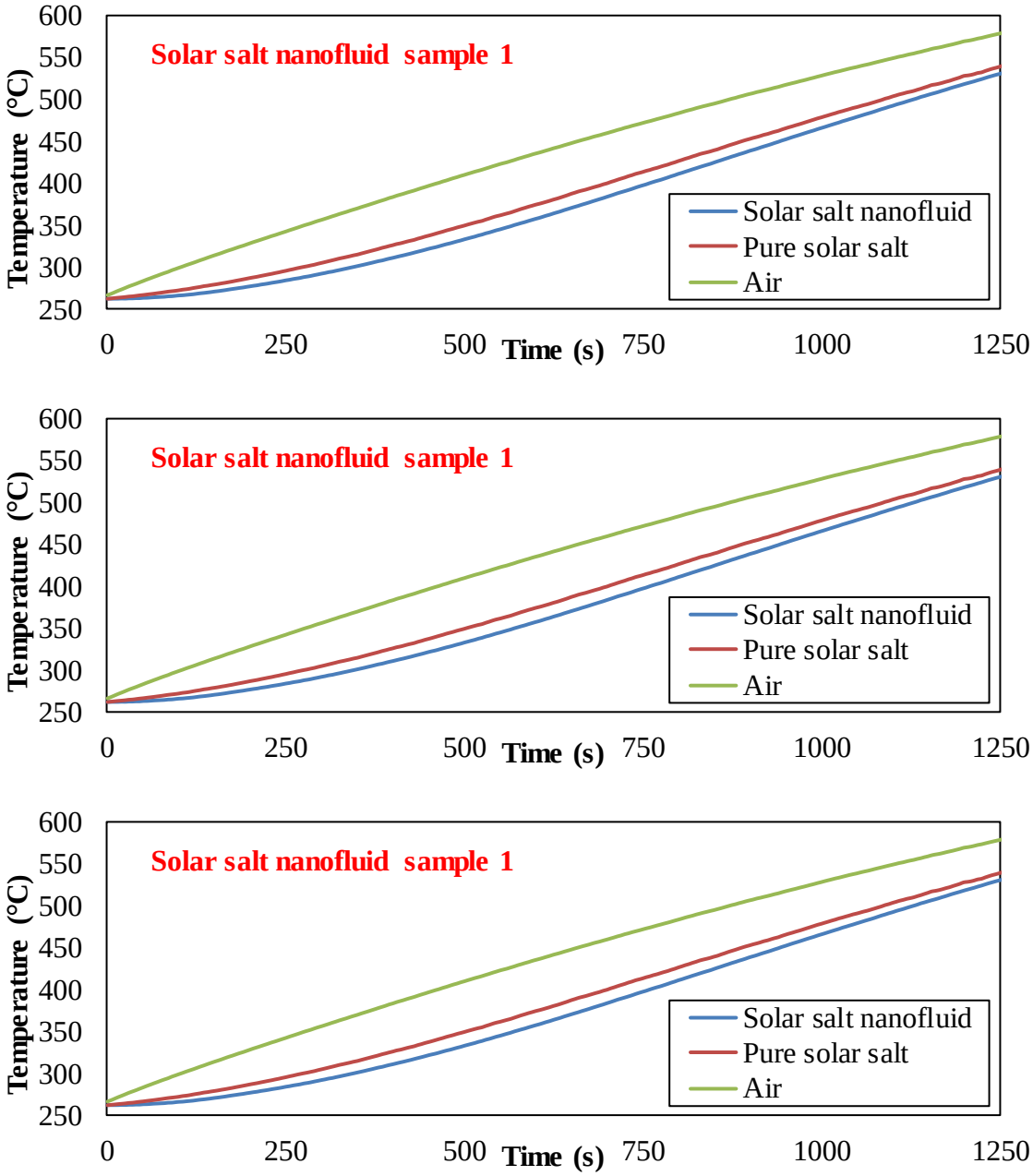

Figure 79. Thermocouple response recorded during T-History experiments for temperature of air, reference sample (pure solar salt) and test sample (pure solar salt nanofluid with alumina nanoparticles generated from thermal decomposition of aluminum nitrate additives). The mass fraction of additive (alumina nitrate) used and the target mass fraction alumina nanoparticles, are: (TOP ROW) 3.5 % and 0.5%, respectively; (MIDDLE ROW) 6.9% and 1%, respectively; and (BOTTOM ROW) 10.1% and 1.5%, respectively.

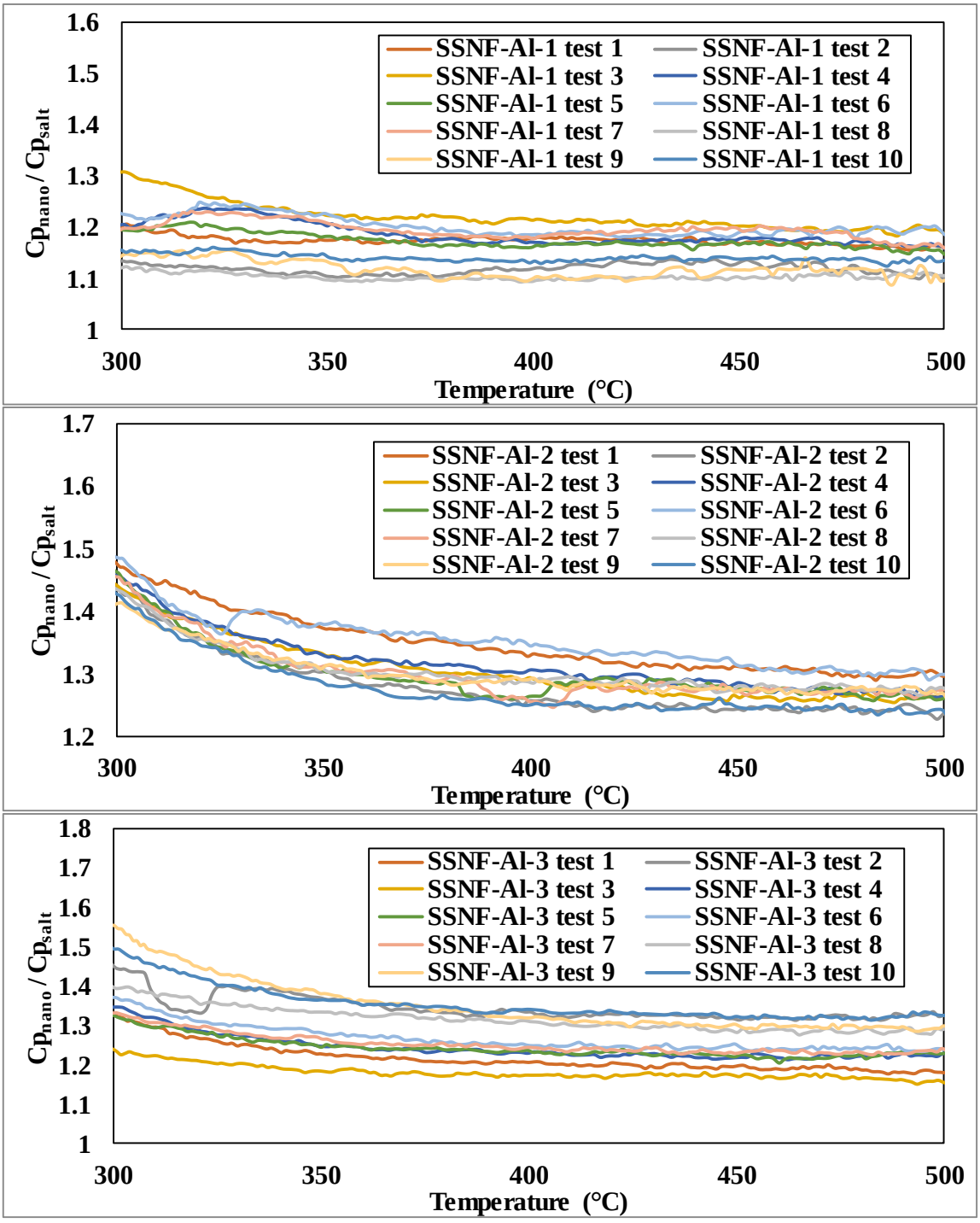

Figure 80. Specific heat capacity ratio of nanofluid samples with respect to pure solar salt. The mass fraction of additive (alumina nitrate) used and the target mass fraction alumina nanoparticles, are: (TOP ROW) 3.5 % and 0.5%; (MIDDLE ROW) 6.9% and 1%; and (BOTTOM ROW) 10.1% and 1.5%, respectively

Table 27. Specific heat capacity enhancement of nanofluid samples with respect to pure solar salt. The mass fraction of precursor used and the target mass fraction of alumina nanoparticles, are: (TOP TABLE) 3.5 % and 0.5%; (MIDDLE TABLE) 6.9% and 1%; and (BOTTOM TABLE) 10.1% and 1.5%, respectively

SSNF-Al-1 specific heat enhancement

Test number	300ºC	400ºC	500 ºC	Average	Standard deviation
1	37.9%	17.6%	11.4%	20.8%	7.0%
2	28.2%	13.2%	9.7%	15.9%	6.0%
3	42.5%	18.1%	11.1%	20.8%	8.0%
4	26.3%	11.3%	6.6%	13.6%	5.1%
5	39.7%	19.5%	13.1%	22.1%	7.2%
6	39.3%	15.8%	8.5%	18.9%	7.9%
7	30.6%	16.6%	10.1%	17.7%	6.2%
8	28.1%	11.3%	6.0%	13.8%	6.3%
9	32.0%	12.5%	7.6%	15.3%	7.2%
10	36.0%	13.9%	7.0%	15.7%	7.8%
Avg	34.1%	15.0%	9.1%	17.5%	6.9%

SSNF-Al-2 specific heat enhancement

Test number	300ºC	400ºC	500 ºC	Average	Standard deviation
1	44.5%	36.0%	28.1%	35.1%	5.1%
2	60.3%	34.7%	30.3%	37.6%	7.7%
3	53.6%	37.0%	31.2%	38.7%	6.7%
4	61.3%	36.9%	32.8%	41.6%	8.6%
5	54.3%	38.1%	34.1%	40.3%	6.0%
6	53.8%	35.5%	30.4%	38.5%	6.9%
7	57.4%	32.6%	28.7%	36.0%	7.5%
8	59.4%	34.7%	32.0%	38.7%	7.5%
9	52.6%	37.3%	31.7%	39.1%	6.4%
10	60.7%	36.2%	32.1%	41.8%	9.2%
Avg	55.8%	35.9%	31.2%	38.7%	7.2%

SSNF-Al-3 specific heat enhancement

Test number	300ºC	400ºC	500 ºC	Average	Standard deviation
1	46.5%	27.8%	20.2%	29.4%	7.0%
2	67.6%	29.6%	20.5%	32.8%	10.8%
3	53.1%	27.9%	20.3%	30.6%	8.3%
4	58.0%	28.7%	20.6%	31.2%	9.3%
5	52.1%	27.6%	21.6%	30.6%	7.9%
6	73.2%	30.9%	22.4%	35.6%	12.0%
7	58.6%	28.6%	22.3%	32.4%	9.7%
8	64.2%	27.7%	20.1%	32.3%	10.8%
9	56.1%	26.3%	19.6%	30.3%	9.4%
10	57.2%	28.8%	22.2%	32.2%	9.1%
Avg	58.7%	28.4%	21.0%	31.8%	9.5%

5.1.2 Material characterization

Figure 81 ~ Figure 83 shows the SEM images of solar salt nanofluid samples at varying levels of magnifications. At low magnification (~400×), ridge-shaped microstructures are observed in these images and the number of these ridge microstructures increases drastically with increasing value of the mass concentrations of the alumina nitrate additive (i.e., with increasing values of the target mass concentration of the alumina nanoparticles). Another interesting observation is that the fraction of the total area occupied by these ridge microstructures also increases significantly with increase in the mass concentration of the additive (i.e., increase in the target value of the mass concentration of the nanoparticles). For example, for the nanofluid sample with target mass concentration of nanoparticles of 1.5% more than 50% of the total number of pixels in the SEM image is occupied by the ridge-shaped microstructures. This is indicative of the formation of underlying secondary nanostructures induced by the presence of the alumina nanoparticles (synthesized by the thermal degradation of the aluminum nitrate additives).

At higher values of magnification (~40000×), the images show the presence of secondary nanostructures (percolation networks) in the solar salt nanofluid samples. The alumina nanoparticles are not apparent in these SEM images – however, their presence is indicated indirectly by the formation of the secondary nanostructures that are inherent in the ridge-shaped microstructures. This suggests that the nanoparticles are fully enveloped by the induced secondary nanostructures. The size of the stem (i.e., length) of these nanostructures was estimated to be ~50 nm from the SEM images obtained at higher

magnification. With increasing values of the target mass concentration of the nanoparticles, the percolation networks in the SEM images - obtained at higher magnification - were observed to be denser (i.e., regions with the amorphous phase intervening the percolation networks was observed to decrease). This is indicative of the merger and aggregation of the secondary nanostructure induced by the nanoparticles. This is probably due to higher nucleation density of the alumina nanoparticles at higher concentration of the aluminum nitrate additive. This could also lead to higher propensity for agglomeration and precipitation of the nanoparticles at higher mass concentrations (i.e., for mass fractions exceeding 1%). Hence, the level of enhancement of the specific heat capacity was reduced for the solar salt nanofluid samples with target mass fractions of nanoparticles exceeding 1%.

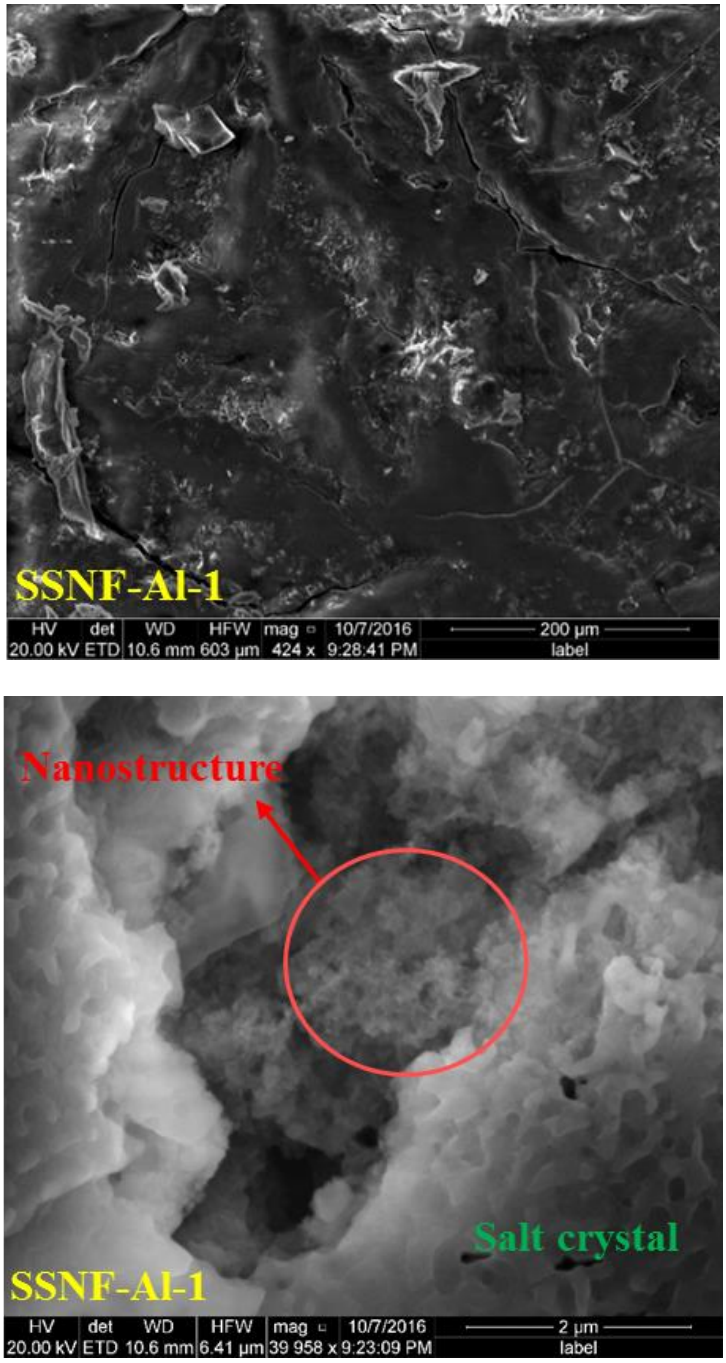

Figure 81. SEM image of nanofluid sample. The mass fraction of additive (alumina nitrate) used and the target mass fraction alumina nanoparticles are 3.5 % and 0.5%, respectively.

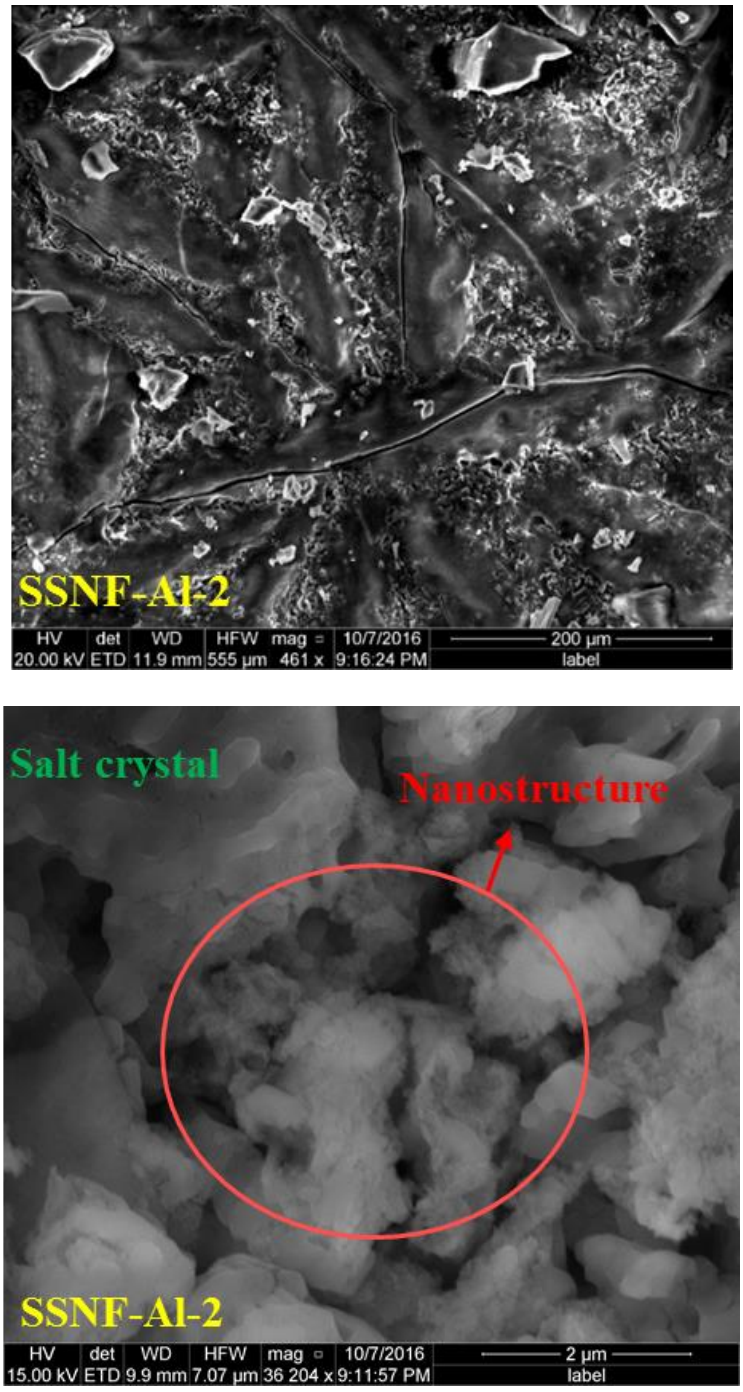

Figure 82. SEM image of nanofluid sample. The mass fraction of additive (alumina nitrate) used and the target mass fraction alumina nanoparticles are 6.9 % and 1%, respectively.

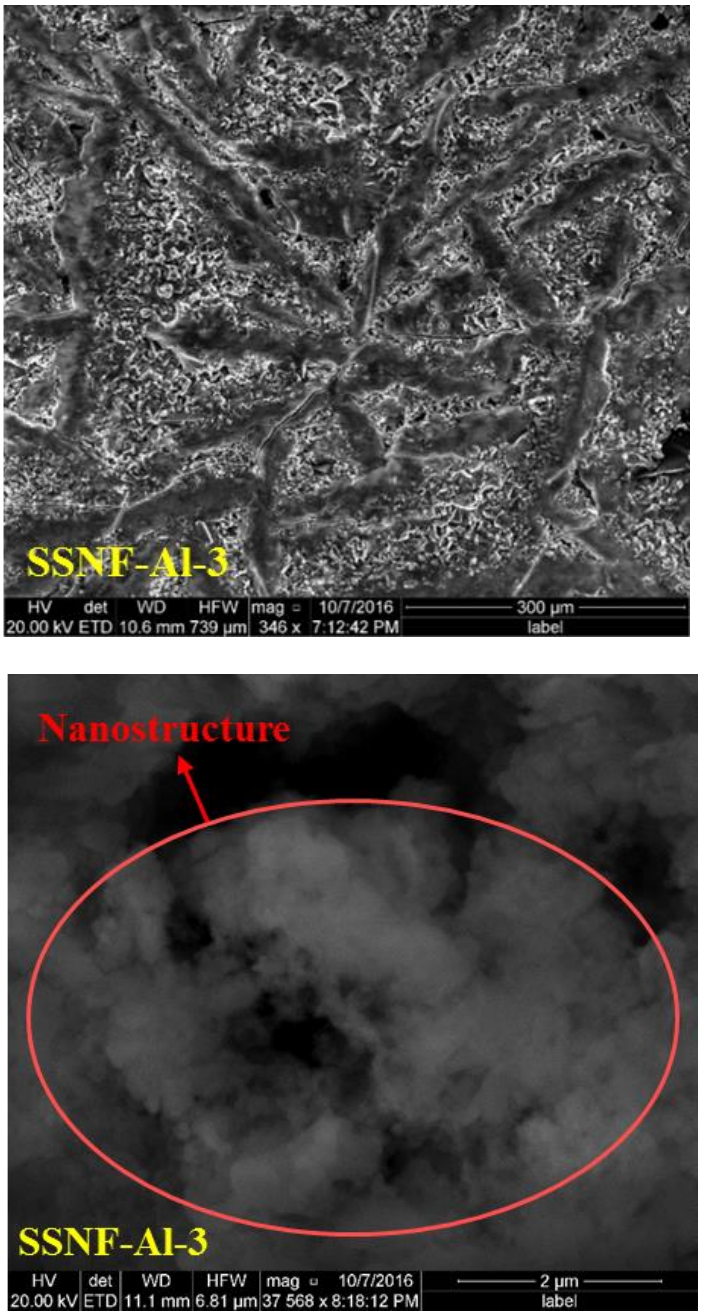

Figure 83. SEM image of nanofluid sample. The mass fraction of additive (alumina nitrate) used and the target mass fraction alumina nanoparticles are 10.1 % and 1.5%, respectively.

5.2 Effect of additive material (as nanoparticle precursor)

The effect of additive material (as nanoparticle precursor) on the specific heat capacity of the solar salt samples (and the resulting morphology) was examined for three different materials. This study was designed using two different additives for targeted synthesis of MgO nanoparticles in-situ and one additive for targeted synthesis of ZnO nanoparticles in-situ for the one-step synthesis of solar salt nanofluid samples.

5.2.1 Solar salt with Magnesium based precursor

To synthesize the solar salt nanofluids (with MgO nanoparticles synthesized in-situ at a target mass fraction 1%) using the one-step thermal decomposition method described earlier, two different additives (as nanoparticle precursors) were selected: magnesium nitrate hexahydrate and magnesium acetate tetrahydrate. These additives were mixed with pure solar salt samples before heating in a furnace for 1 hour to achieve complete thermal decomposition for the in-situ synthesis of the MgO nanoparticles. The synthesis temperature was determined based on the decomposition temperature of each precursor, as indicated by the plots obtained from the thermogravimetric analyses (TGA) experiments. In the TGA experiments - magnesium nitrate was found to decompose completely at 530ºC while magnesium acetate was found to decompose completely at 400ºC. The specific heat capacity and morphology was determined using the T-History method and SEM images, respectively.

Table 28. Mass of chemicals needed for in-situ synthesis of solar salt nanofluids (with target mass fraction of 1% for the MgO nanoparticles)

	Raw material mass for synthesis			Final product mass (g)		
Synthesis temperature	$NaNO_3$	KNO_3	Precursor	Solar salt	MgO	Total
550ºC	20.790 g	13.86 g	2.227 g $Mg(NO_3)_2 \cdot 6H_2O$	34.65 g	0.35 g	35 g
			1.862 g $Mg(CH_3COO)_2 \cdot 4H_2O$			

5.2.1.1 Specific heat capacity

T-History experiments were performed by repeated heating and cooling of the molten salt nanofluid samples and pure salt samples that were placed inside a furnace (with automated temperature control). The measurements were repeated 4 times (i.e., for 4 consecutive thermocycles) by ramping up the temperature of the furnace from an initial temperature of 250 ºC to a final temperature of 550 ºC. Figure 84 shows the temperature recorded by thermocouples immersed in the pure solar salt sample and nanofluid sample (for test 1) as the air temperature of the furnace was ramped from an initial temperature of 250 ºC to a final temperature of 550 ºC. The results show that starting from the same initial temperature (i.e., after thermal equilibration at 250 ºC), the temperature of the nanofluid sample increased at the same rate as that of the pure solar salt sample. Hence, at any given instant, the solar salt sample was at a similar temperature as that of the nanofluid sample. Since both samples have similar values of mass and volume (for both the pure solar salt samples and the nanofluid samples), the similar temperature response indicates that the pure solar salt samples have the same heat storage capacity (specific heat capacity) compared to that of the nanofluid samples.

For the solar salt nanofluid samples synthesized using magnesium acetate, similar trend was observed in the T-History tests. In repeated heating cycles, the temperature ramp rates of both the pure solar salt samples and solar salt nanofluid samples were similar. Although a slight temperature difference of ~2ºC existed between the pure salt samples and the solar salt nanofluid samples (i.e., in the quasi-steady state during the heating cycle), this value is too small compared to the temperature difference between salt samples and the air temperature inside furnace. Hence, this temperature differential can be neglected in the analyses of the specific heat capacity calculations. The results from the calculation of the specific heat capacity ratio are shown in Figure 87. Figure 87 conclusively shows that there was no significant enhancement in the specific heat capacity of the solar salt nanofluid samples in the measurements performed for the four consecutive thermocycles.

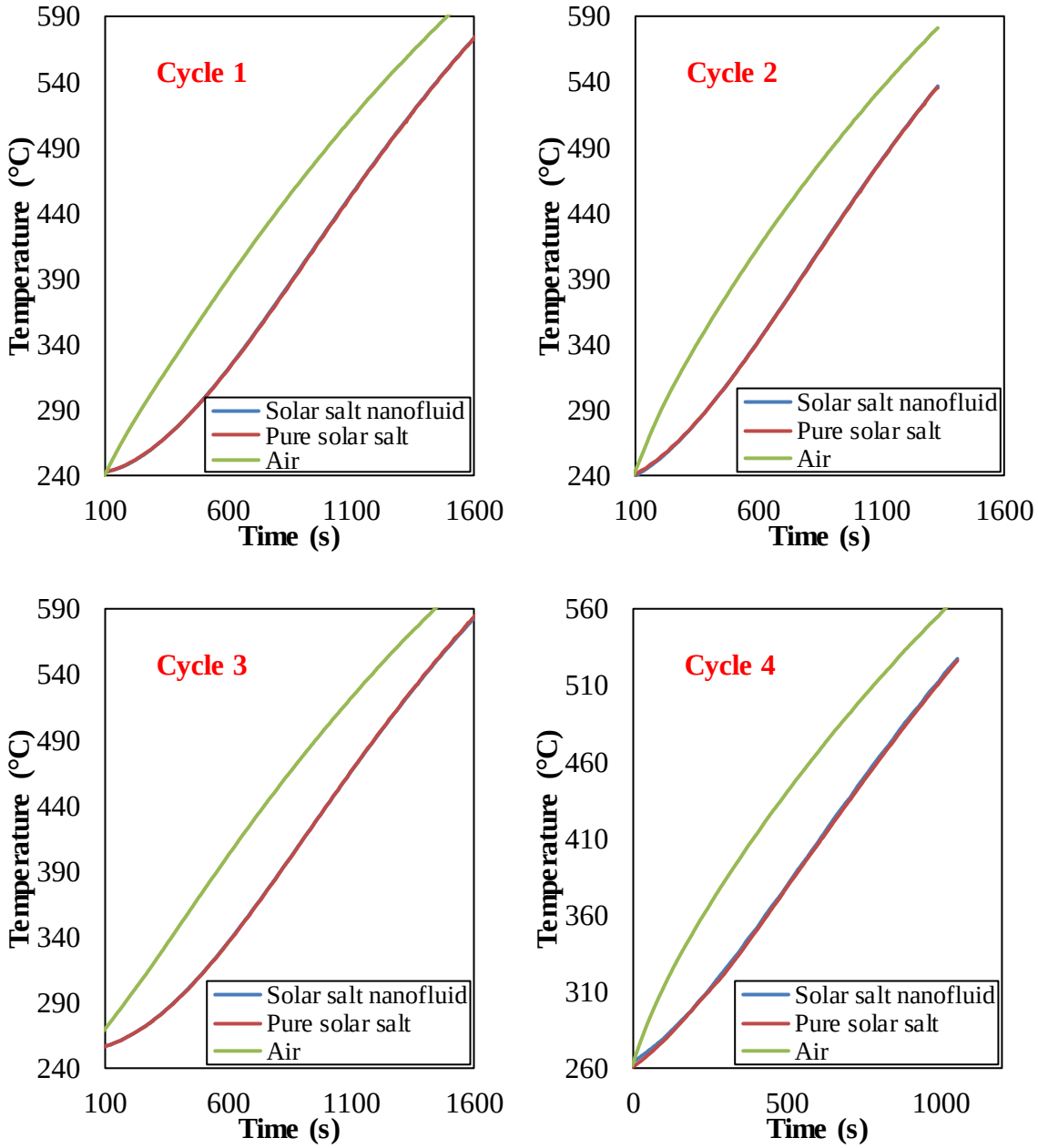

Figure 84. Plot of temperature response obtained from T-History experiments for thermocouples places in air (in the furnace), pure solar salt samples and solar salt nanofluid samples (prepared using one-step synthesis protocol). The molten salt nanofluid samples were obtained by adding $Mg(NO_3)_2 \cdot 6H_2O$ at 6% mass fraction (as nanoparticle precursors for yielding nanofluids) to pure solar salt for a target mass fraction of 1% for the resulting MgO nanoparticles obtained by thermal decomposition (one-step synthesis protocol)

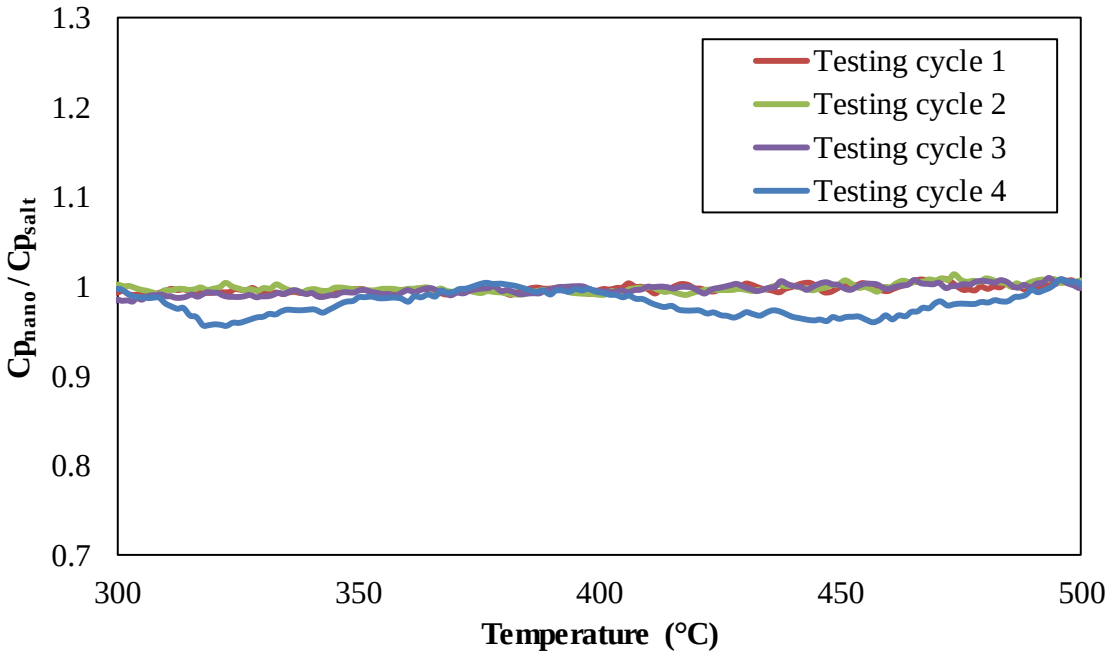

Figure 85. Plot of specific heat capacity ratio as a function of temperature (obtained from T-History experiments). The molten salt nanofluid samples were obtained by adding $Mg(NO_3)_2 \cdot 6H_2O$ at 6% mass fraction (as nanoparticle precursors for yielding nanofluids) to pure solar salt for a target mass fraction of 1% for the resulting MgO nanoparticles obtained by thermal decomposition (one-step synthesis protocol)

Table 29. Specific heat capacity enhancement of nanofluid samples with respect to pure solar salt. The molten salt nanofluid samples were obtained by adding $Mg(NO_3)_2 \cdot 6H_2O$ at 6% mass fraction (as nanoparticle precursors for yielding nanofluids) to pure solar salt for a target mass fraction of 1% for the resulting MgO nanoparticles

Test number	300ºC	400ºC	500 ºC	Average	Standard Deviation
1	-0.7%	-0.6%	-0.1%	-0.3%	0.4%
2	0.2%	-0.9%	0.7%	-0.1%	0.5%
3	-1.4%	-0.4%	-0.1%	-0.4%	0.4%
4	-0.4%	-0.7%	0.4%	0.5%	2.7%
Average	-0.6%	-0.7%	0.2%	-0.1%	1.4%
Standard Deviation	0.6%	0.2%	0.3%	0.4%	

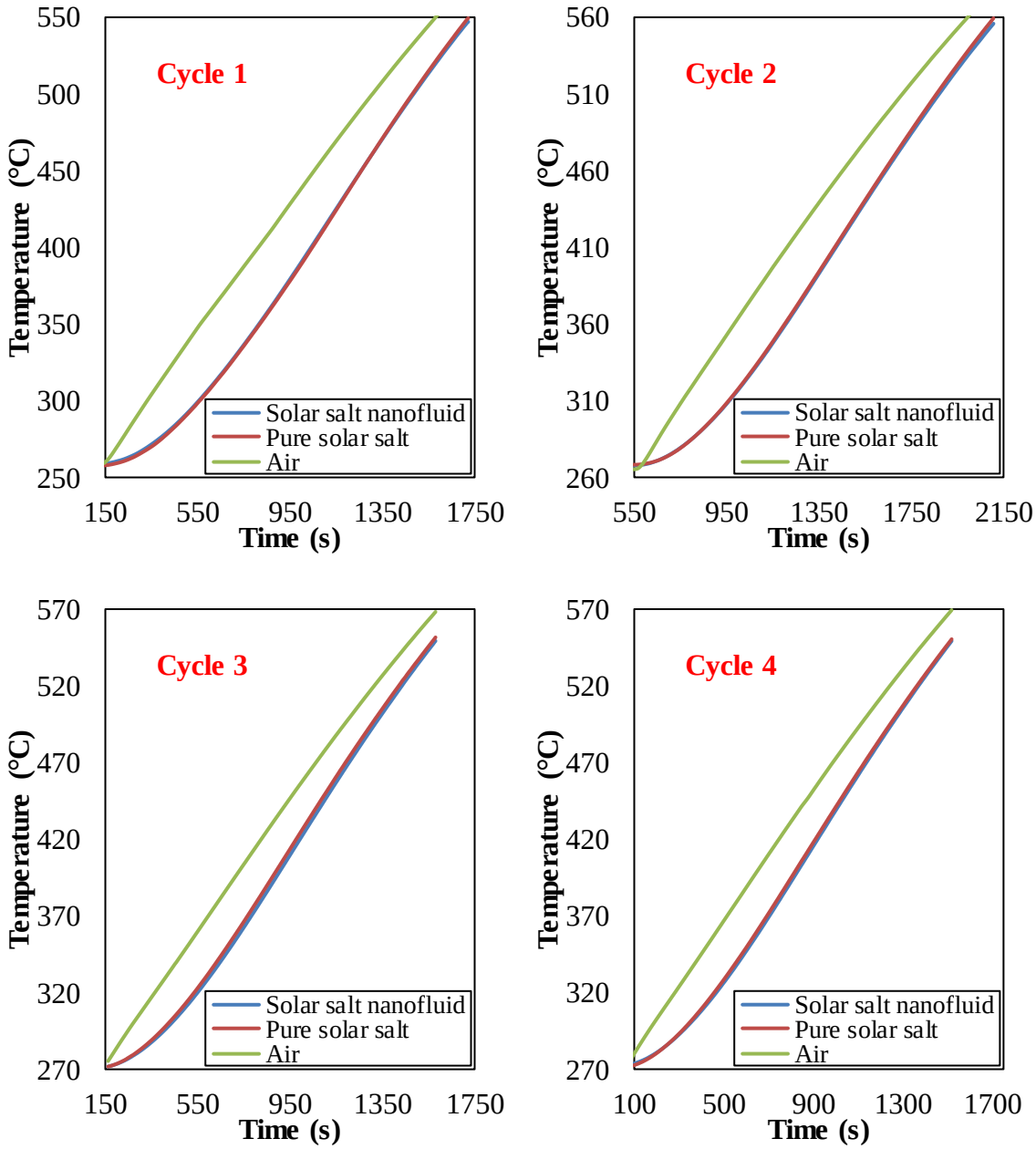

Figure 86. Plot of temperature response obtained from T-History experiments for thermocouples places in air (in the furnace), pure solar salt samples and solar salt nanofluid samples (prepared using one-step synthesis protocol). The molten salt nanofluid samples were obtained by adding $Mg(CH_3COO)_2{\cdot}4H_2O$ at 5.1% mass fraction (as nanoparticle precursors for yielding nanofluids) to pure solar salt for a target mass fraction of 1% for the resulting MgO nanoparticles obtained by thermal decomposition (one-step synthesis protocol).

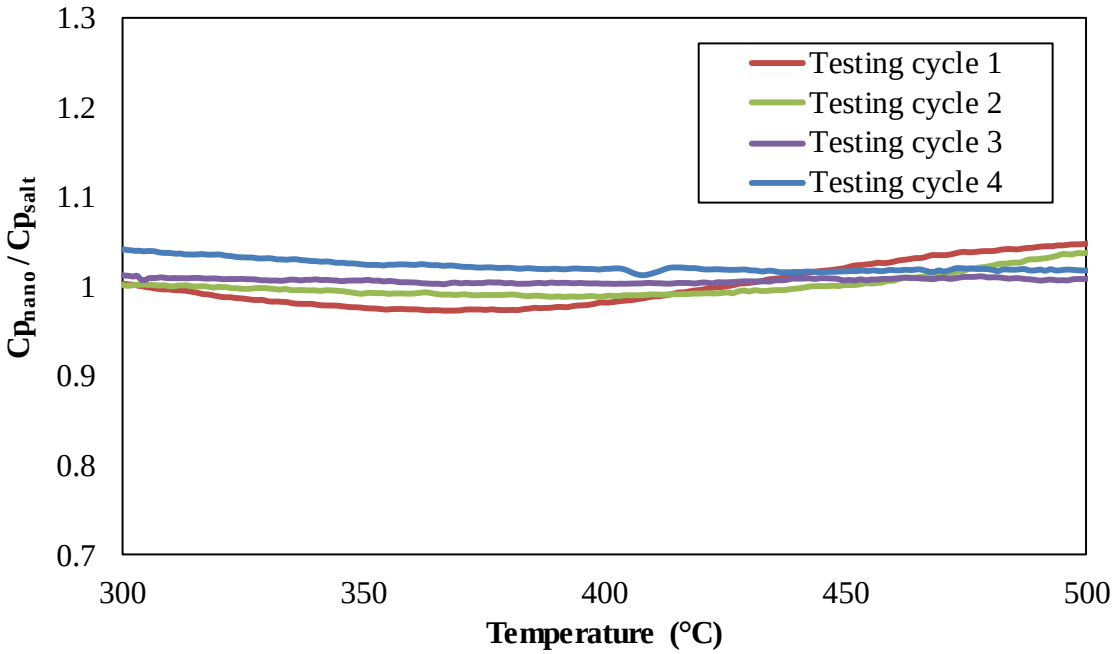

Figure 87. Plot of specific heat capacity ratio as a function of temperature (obtained from T-History experiments). The molten salt nanofluid samples were obtained by adding $Mg(CH_3COO)_2{\cdot}4H_2O$ at 5.1% mass fraction (as nanoparticle precursors for yielding nanofluids) to pure solar salt for a target mass fraction of 1% for the resulting MgO nanoparticles obtained by thermal decomposition (one-step synthesis protocol)

Table 30. Specific heat capacity enhancement of nanofluid samples with respect to pure solar salt. The molten salt nanofluid samples were obtained by adding $Mg(CH_3COO)_2{\cdot}4H_2O$ at 5.1% mass fraction (as nanoparticle precursors for yielding nanofluids to pure solar salt for a target mass fraction of 1% for the resulting MgO nanoparticles

Test number	300ºC	400ºC	500 ºC	Average	Standard Deviation
1	0.2%	-1.8%	4.8%	0.0%	2.4%
2	0.3%	-1.1%	3.9%	0.1%	1.3%
3	1.2%	0.3%	0.9%	0.7%	0.2%
4	4.2%	2.0%	1.8%	2.4%	0.7%
Average	1.5%	-0.2%	2.8%	0.8%	1.7%
Standard Deviation	1.6%	1.5%	1.6%	1.0%	

5.2.1.2 Material characterization

The solar salt nanofluids containing MgO particles at target mass concentration of 1% (generated from two different additives: magnesium nitrate or magnesium acetate) showed very low stability. This was evidenced by the rapid precipitation of the synthesized particles within one hour of completion of the synthesis steps. As shown in Figure 88 the fresh solar salt sample (generated by adding magnesium nitrate) appeared to yield a well dispersed colloidal suspension. However, after the first thermos-cycle in the T-History experiments the bulk of the sample in the vial appeared to be a clear and transparent liquid while a dense sediment was observed at the bottom of the vial. Similar images were obtained for solar salt samples that were mixed with magnesium acetate additive (as a precursor for MgO nanoparticles). However, a distinct sediment layer was observed in the bottom of the vial within one hour of synthesis in the furnace. Such fast precipitation rate suggests that the MgO particles synthesized in-situ were in-situ potentially due to agglomeration resulting in precipitates that were of micro-scale dimensions rather than nano-scale dimensions (i.e., the diameter of the particles probably exceeded 1000 nm or 1 micron).

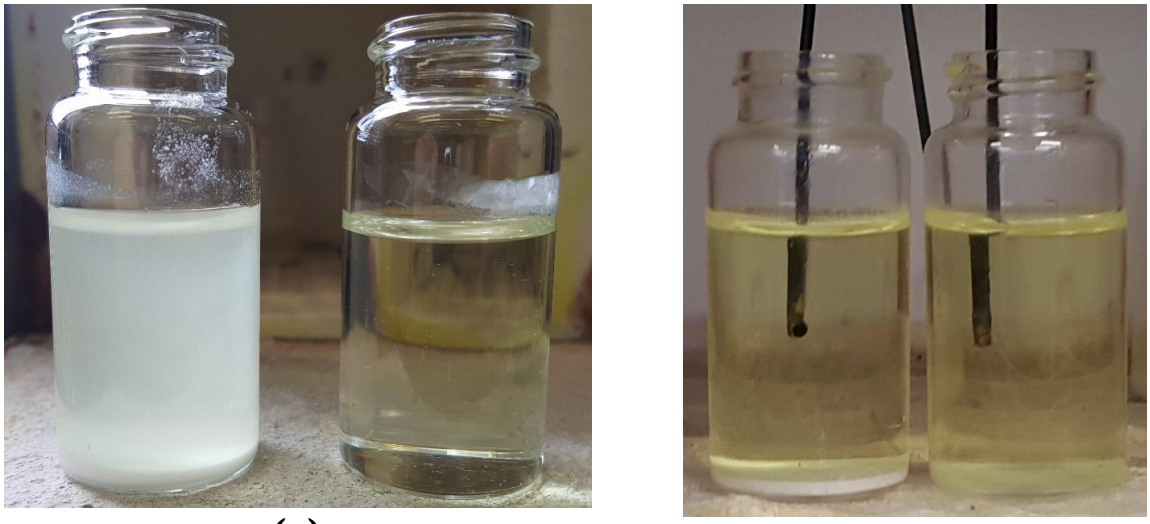

(a) **(b)**

Figure 88. Observation of pure solar salt and solar salt with magnesium acetate additive. (a) Right vial contains pure solar salt sample and left vial contains solar salt with additive (immediately after thermal decomposition for in-situ synthesis). The image shows a colloidal suspension in the left vial. (b) Right vial contains pure solar salt sample and left vial contains solar salt with additives (immediately after the first cycle of T-History experiment). The image shows a dense sediment formed at the bottom of right vial with a clear and transparent liquid layer on top. This shows that the particles synthesized in-situ form an unstable colloidal solution which precipitate rapidly on being subjected to thermocycling and therefore the specific heat capacity is not enhanced.

Figure 89. Observation of solar salt sample with magnesium nitrate additive. Image on the right shows solar salt with additive (immediately after thermal decomposition for in-situ synthesis). The image shows a colloidal suspension in the vial. The image on the right shows a dense sediment formed at the bottom of the vial with a clear and transparent liquid layer on top. This shows that the particles synthesized in-situ form an unstable colloidal solution which precipitate rapidly and therefore the specific heat capacity is not enhanced.

Materials characterization of the MgO particles were performed using SEM as shown in the figure below. At low-magnification the SEM images show that MgO particles are scattered in different regions of the solar salt samples. At high magnification the SEM images reveal that the size of these particles ranges from 0.5~2.0 μm (hence these are not nanoparticles). The chemical composition of these micron sized particles was confirmed using EDS analysis and are shown in Figure 90. Figure 90 shows the existence of prominence peaks in the spectrum corresponding to Mg at locations where the particles are visible in the images (while the Mg peak is non-existent at locations where the particles are not present). Despite of the micro-scale size of the particles, no specific structure of

MgO clusters were observed in the samples - as all of these particles were isolated from each other. Such a morphology is consistent with the absence of any enhancement in the specific heat capacity of these samples.

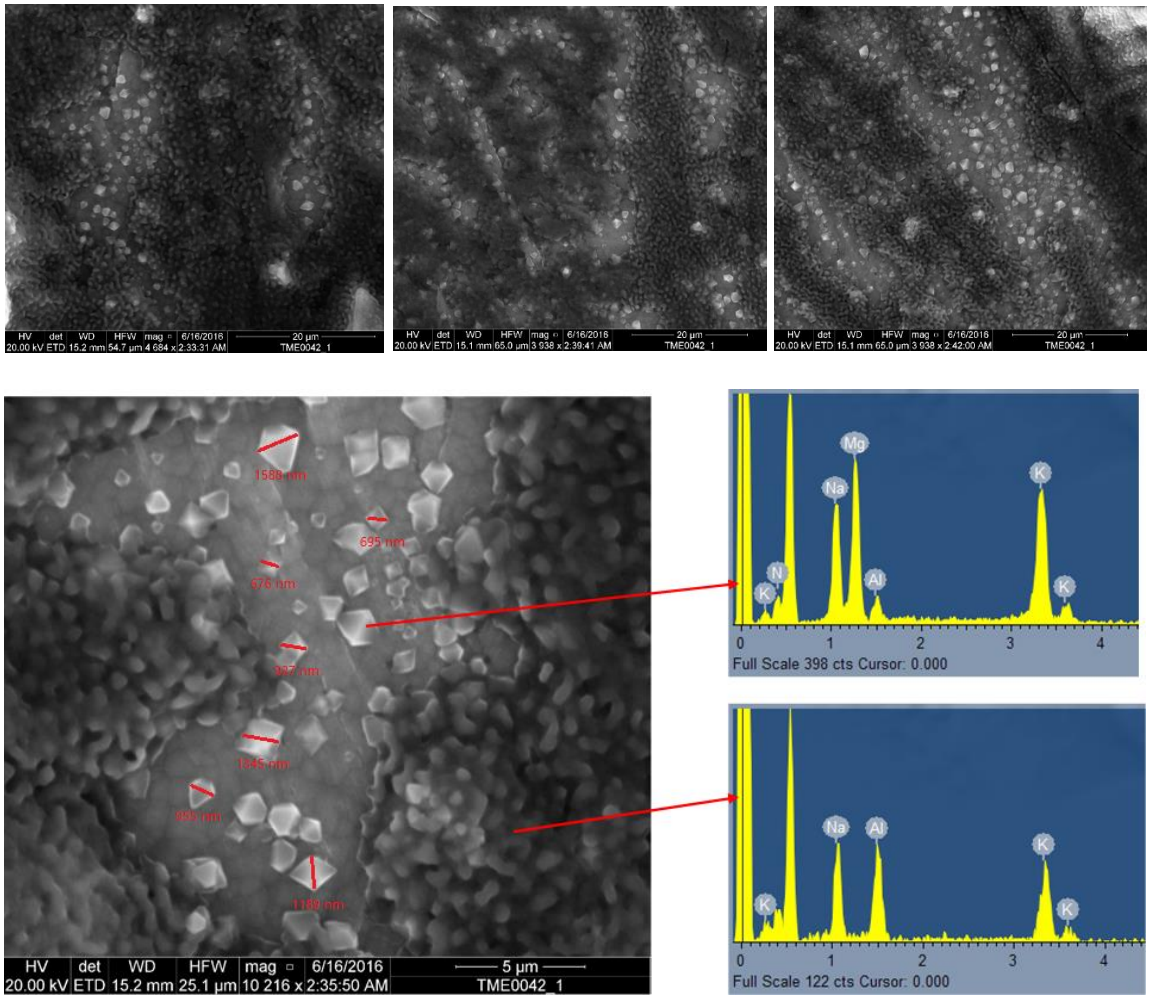

Figure 90. SEM images of molten salt (solar salt) samples containing MgO with nominal diameter of 1 ~ 3 microns at a target mass concentration of 1.0% (Bottom Right) Elemental analysis of the different regions in the images are obtained by using EDS.

5.2.1.3 Parametric study for one-step synthesis protocol

Addition experiments were performed for synthesis of nanoparticles in-situ from additives (i.e., magnesium nitrate hexahydrate as a precursor) by varying the synthesis temperature and thermal treatment time (for thermal degradation of the additive). All of these samples were prepared for deriving MgO particles at a target mass concentration of 1% (as shown in Table 28). Table 31 summarizes the values of the variables that were explored with the motivation of obtaining solar salt nanofluids using the one-step synthesis protocol.

Table 31. Summary of variables explored for synthesis of MgO particles from $Mg(NO_3)_2 \cdot 6H_2O$ additives (as precursor) mixed with solar salt and the resulting specific heat capacity values

Synthesis temperature	Synthesis time	Specific heat capacity		Repeat cycles
		Enhancement	Uncertainty	
550 ºC	10 hrs	-1.1%	1.4%	4
600 ºC	10 hrs	0.9%	1.5%	4
650 ºC	1 hr	-0.8%	3.4%	1
	2 hrs	-0.9%	1.0%	1
	3 hrs	-1.5%	2.6%	1
	4 hrs	-3.5%	1.3%	1
700 ºC	1 hr	-4.9%	2.7%	1
	2 hrs	-6.6%	2.3%	1

The results show that the for the range of synthesis conditions used in this study the additive did not yield any enhancement in the specific heat capacity of the solar salt samples. This is potentially caused by nucleation and rapid growth as well as agglomeration of the MgO particles that cause the nanoparticles to aggregate into micron-

sized particles (and as a result the material property enhancements are not observed in these samples of solar salt with additives) The detailed information on the thermal and materials characterization of these samples are included in Appendix D.

5.2.2 Solar salt with Zinc base precursor

The solar salt samples were treated with $Zn(NO_3)_2 \cdot 6H_2O$ additive for the targeted synthesis of ZnO nanoparticles in-situ using the one-step synthesis protocol described in Chapter 2. The solar salt powder was mixed with the zin nitrate hexahydrate additive and heated in a furnace at 550ºC (since TGA showed that the ultimate decomposition temperature of $Zn(NO_3)_2 \cdot 6H_2O$ was 400 ºC - where zinc nitrate decomposes completely into ZnO). The target mass concentration of ZnO in this study was 1.0%. The mass fraction of the additive required for achieving the target mass fraction of ZnO particles is 3.6% and the values of the individual components used for the one-step synthesis protocol are summarized in Table 32. The specific heat capacity and thermal conductivity of the samples were explored using the T-History method and concentric cylindrical chamber test apparatus, respectively (as described in Chapter 2). The morphology and particle size distribution of the synthesized samples were examined using SEM.

Table 32. Mass of chemicals needed for solar salt-ZnO nanofluid synthesis

	Raw material mass for synthesis (g)			Final product mass (g)		
Synthesis temperature	$NaNO_3$	KNO_3	$Zn(NO_3)_2 \cdot 6H_2O$	Solar salt	ZnO	Total
550ºC	20.79	13.86	1.279	34.65	0.35	35

5.2.2.1 Specific heat capacity

T-History experiments were performed by repeated heating and cooling of the molten salt nanofluid samples and pure salt samples that were placed inside a furnace (with automated temperature control). The measurements were repeated 4 times (i.e., for 4 consecutive thermocycles) by ramping up the temperature of the furnace from an initial temperature of 250 ºC to a final temperature of 550 ºC. Figure 91 shows the temperature recorded by thermocouples immersed in the pure solar salt sample and nanofluid sample (for test 1) as the air temperature of the furnace was ramped from an initial temperature of 250 ºC to a final temperature of 550 ºC. The results show that starting from the same initial temperature (i.e., after thermal equilibration at 250 ºC), the temperature of the nanofluid sample increased at the same rate as that of the pure solar salt sample. Hence, at any given instant, the solar salt sample was at a similar temperature as that of the nanofluid sample. Since both samples have similar values of mass and volume (for both the pure solar salt samples and the nanofluid samples), the similar temperature response indicates that the pure solar salt samples have the same heat storage capacity (specific heat capacity) compared to that of the nanofluid samples. The results from the calculation of the specific heat capacity ratio are shown in Figure 92. Figure 92 conclusively shows that there was no significant enhancement in the specific heat capacity of the solar salt nanofluid samples in the measurements performed for the four consecutive thermocycles (with the enhancement being less than 10%).

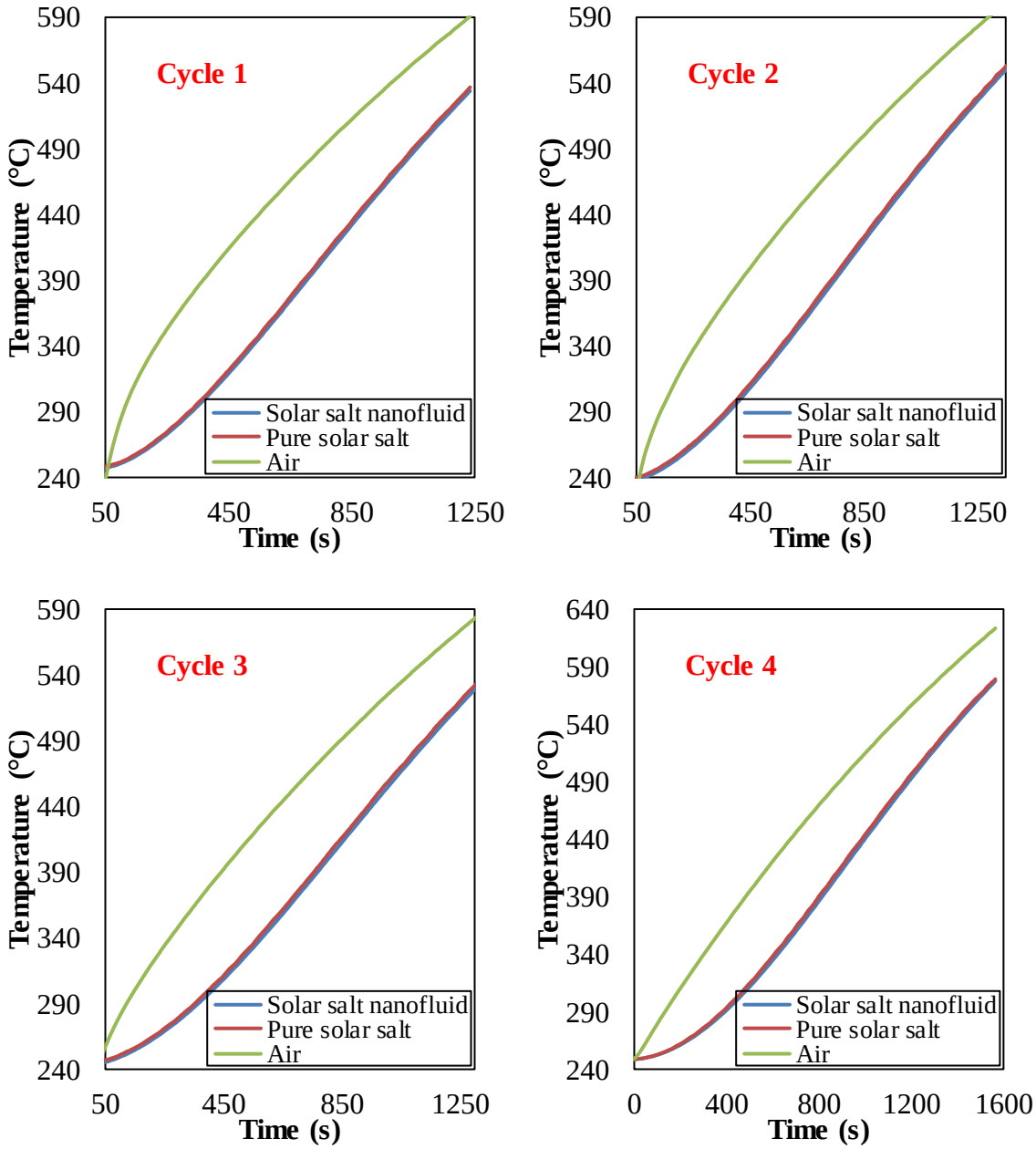

Figure 91. Plot of temperature response obtained from T-History experiments for thermocouples places in air (in the furnace), pure solar salt samples and solar salt samples with additives (prepared using one-step synthesis protocol). The molten salt samples were obtained by adding $Zn(NO_3)_2 \cdot 6H_2O$ at 3.6% mass fraction (as nanoparticle precursors for yielding nanofluids) to pure solar salt for a target mass fraction of 1% for the resulting ZnO particles that were obtained by thermal decomposition (one-step synthesis protocol)

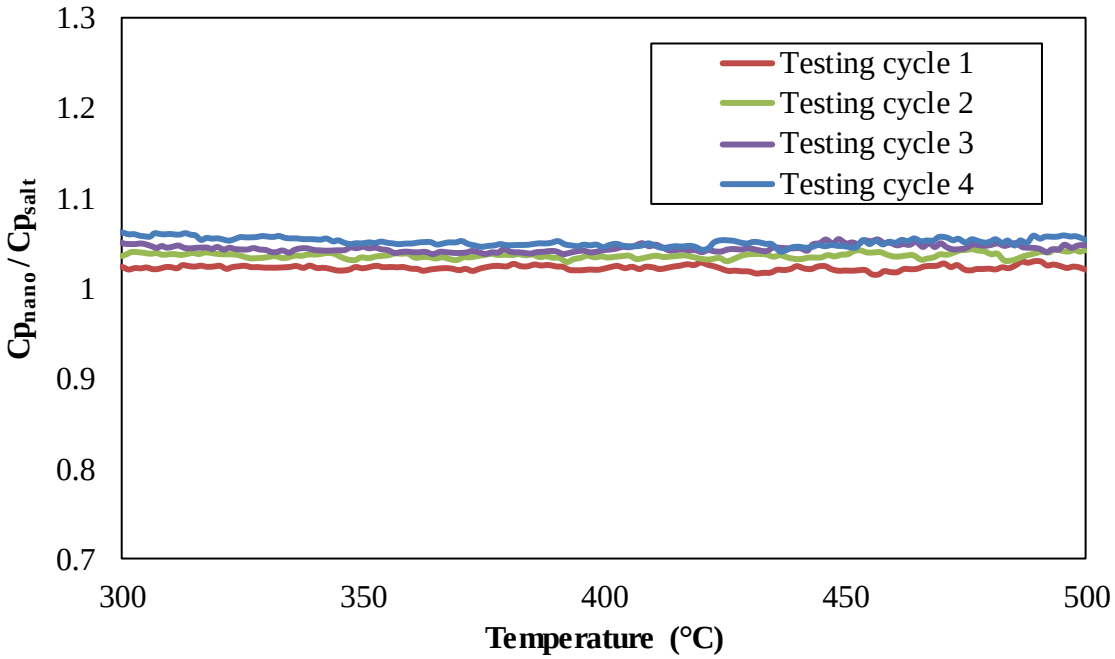

Figure 92. Plot of specific heat capacity ratio as a function of temperature (obtained from T-History experiments). The molten salt samples were obtained by adding $Zn(NO_3)_2 \cdot 6H_2O$ at 3.6% mass fraction (as nanoparticle precursors for yielding nanofluids) to pure solar salt for a target mass fraction of 1% for the resulting ZnO particles that were obtained by thermal decomposition (one-step synthesis protocol)

Table 33. Specific heat capacity enhancement of nanofluid samples with respect to pure solar salt. The molten salt nanofluid samples were obtained by adding $Zn(NO_3)_2 \cdot 6H_2O$ at 3.6% mass fraction (as nanoparticle precursors for yielding nanofluids) to pure solar salt for a target mass fraction of 1% for the resulting ZnO particles

Test number	300ºC	400ºC	500 ºC	Average	Standard Deviation
1	2.4%	2.2%	2.2%	2.3%	0.3%
2	3.5%	3.5%	4.2%	3.6%	0.3%
3	5.0%	4.3%	4.7%	4.5%	0.4%
4	6.2%	4.6%	5.4%	2.1%	0.7%
Average	4.3%	3.6%	4.1%	3.1%	1.1%
Standard Deviation	1.4%	0.9%	1.2%	1.0%	

5.2.2.2 Material characterization

The solar salt nanofluids containing ZnO particles at target mass concentration of 1% (generated from thermal degradation of zinc nitrate hexahydrate additive) showed very low stability. This was evidenced by the rapid precipitation of the synthesized particles after completion of the synthesis steps. As shown in Figure 93, the fresh solar salt sample (generated by adding zinc nitrate) appeared to yield a well dispersed colloidal suspension. However, after the first thermo-cycle in the T-History experiments the bulk of the sample in the vial appeared to be a translucent colloidal liquid while a dense sediment was observed at the bottom of the vial. Such fast precipitation rate of the ZnO particles synthesized in-situ were potentially due to agglomeration resulting in precipitates that were of micro-scale dimensions rather than nano-scale dimensions (i.e., the diameter of the particles probably exceeded 1000 nm or 1 micron).

Materials characterization of the ZnO particles were performed using SEM as shown in the Figure 94 below. At low-magnification the SEM images show that ZnO particles are scattered in different regions of the solar salt samples. At high magnification, the SEM images reveal that the size of these particles ranges from 1~5 μm (hence these are not nanoparticles). Despite of the micro-scale size of the particles, no specific structure of ZnO clusters were observed in the samples - as all of these particles were isolated from each other. Such a morphology is consistent with the absence of any enhancement in the specific heat capacity of these samples. However, the EDS analysis has not been effective in detecting the presence of Zn element in the sample. This is due to the fact that the

characteristic wavelength of zinc is very close to that of sodium (as shown in Figure 95), which makes it difficult to differentiate these two elements in the EDS spectrum.

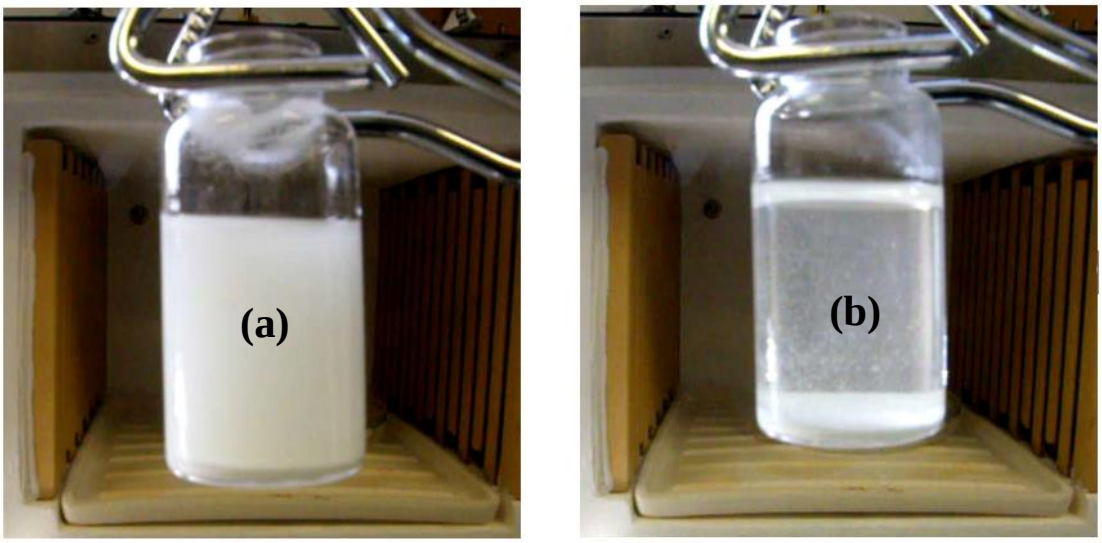

Figure 93. Observation of pure solar salt and solar salt with zinc nitrate additive. (a) Vial contains solar salt with additive (immediately after thermal decomposition for in-situ synthesis of ZnO). The image shows a colloidal suspension in the vial. (b) Vial contains solar salt with additives (immediately after the first cycle of T-History experiment). The image shows a dense sediment formed at the bottom of right vial with a translucent liquid layer on top. This shows that the particles synthesized in-situ form an unstable colloidal solution which precipitate rapidly on being subjected to thermocycling and therefore the specific heat capacity is not enhanced

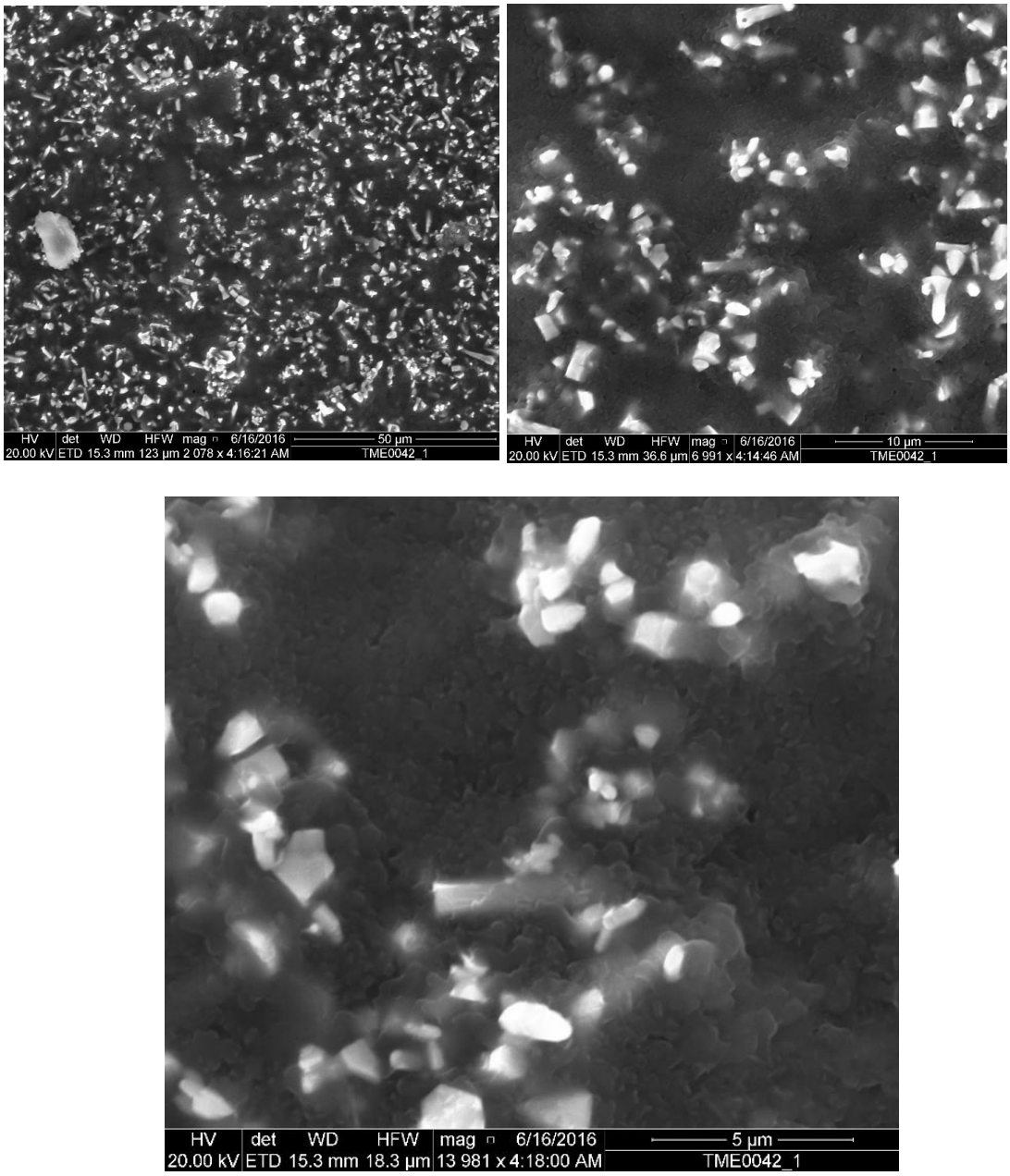

Figure 94. SEM images of molten salt (solar salt) samples containing ZnO particles with nominal diameter of 1 ~ 3 microns at a target mass concentration of 1%

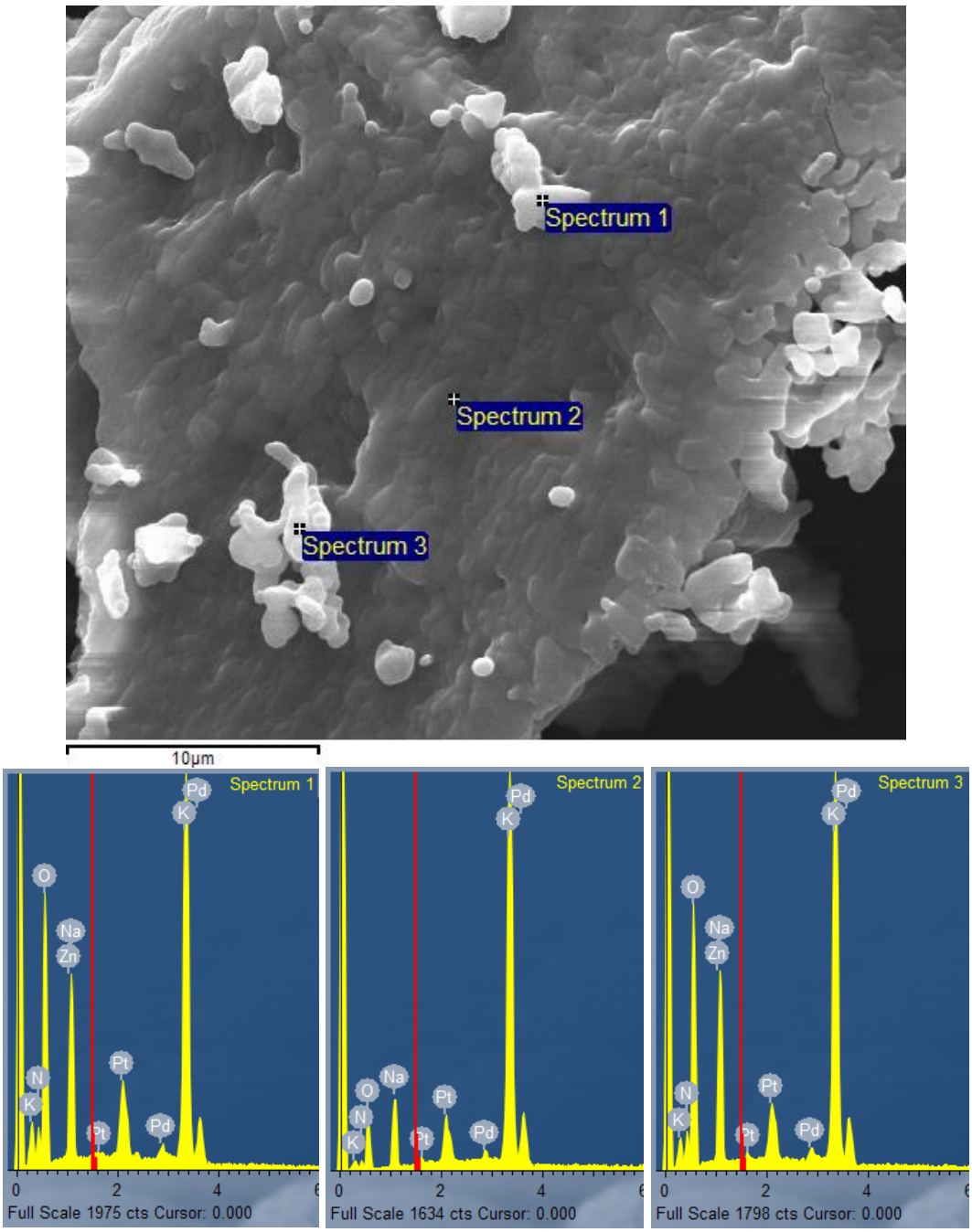

Figure 95. EDS spectrum of molten salt (solar salt) samples containing ZnO particles analyzed at three different locations

5.3 Effect of dispersing agent

Dispersing agents can be used for stabilizing colloidal suspensions. These dispersants are designed to attach to the surface of the colloidal particles (e.g., nanoparticles) for creating mutual repulsion and thus prevents their agglomeration. Surfactants are typically used for stabilizing colloidal suspensions - such as: poly-vinyl-pyrrolidone (PVP), cetyl- trimethyl-ammonium-bromide (CTAB), sodium-dodecyl-sulfate (SDS). These are organic materials which typically disintegrate readily at higher temperatures (and are oxidized by nitrate ions). Sodium phosphate has been widely used as inorganic dispersing agent (e.g., for flocculation of powders such as clay and soil; as well as a dispersant of pigments in paints) and in laboratory procedures to sustain suspensions for prolonged periods especially when measurements for particle size distribution are performed [122, 123]. In this study, synthesis experiments were performed to estimate the contribution of the dispersing agent for stabilizing the nanoparticles synthesized in-situ (i.e., to prevent their rapid agglomeration and precipitation). These solar salt samples with dispersing agents as well as additives (as precursors for the synthesis of nanoparticles in situ by thermal decomposition) were used for measuring their thermo-physical properties.

5.3.1 Sample preparation

The sample preparation for these set of molten salt nanofluids containing two different additives (nanoparticle dispersant and nanoparticle precursors) was implemented using the one-step synthesis protocol (as discussed in Chapter 2). The pure solar salt

(composed of 60% by mass of $NaNO_3$ and 40% by mass of KNO_3) served as the pure solvent. The additives for nanoparticle precursors (e.g., aluminum nitrate and magnesium nitrate) were mixed with the solar salt powder for obtaining nanofluid with target mass fraction of 1% for the ceramic nanoparticles that were generated by thermal degradation on baking at elevated temperatures in a furnace. In addition, sodium metaphosphate ($NaPO_3$) was added to the powder mixture (solar salt and nanoparticle precursor) to serve as the dispersing agent. The sodium metaphosphate was added at a mass fraction in the powder mixture to achieve a target mass ratio of 1:1 with the nanoparticles (that were to be generated in-situ). This mass ratio (of 1:1) was selected to ensure that better dispersal of the generated nanoparticles could be achieved in the nanofluids yielded in this one-step synthesis protocol. The amount of raw materials used in this synthesis experiment are list in Table 34.

The whole mixture was then subjected to thermal treatment (baking step) at 550°C. The specific heat capacity and thermal conductivity of each molten salt nanomaterial was investigated using T-History method and a customized concentric cylinder chamber test apparatus. The sample morphology and particle size distribution was investigated using SEM.

Table 34. Mass of raw material needed for synthesis at 550°C

Raw material mass for synthesis				Final product mass			
$NaNO_3$	KNO_3	Precursor	$NaPO_3$	Solar salt	Metal oxide particle	NaPO3	Total
20.79 g	13.86 g	2.575g $Al(NO_3)_3 \cdot 9H_2O$ 2.227 g $Mg(NO_3)_2 \cdot 6H_2O$	0.35g	34.65 g	0.35 g	0.35g	35.35 g

5.3.2 Specific heat capacity

T-History experiments were conducted by repeated heating and cooling of the molten salt nanofluid samples. The nanofluid samples were originally mixed with sodium metaphosphate power prior to in-situ synthesis of the nanoparticles by the thermal decomposition of the additive (nanoparticle precursor). The measurements were repeated for 5 times (i.e., for 5 consecutive thermocycles) by ramping up and down the temperature of the furnace from an initial temperature of 250 ºC to a final temperature of 550 ºC. Figure 96 shows the temperature recorded by thermocouples immersed in the pure solar salt sample and the nanofluid samples (for test 1) as the air temperature of the furnace was ramped from an initial temperature of 250 ºC to a final temperature of 550 ºC. The results show that starting from the same initial temperature (i.e., after thermal equilibration at 250 ºC), the temperature of the nanofluid sample increased at a slower rate than the pure solar salt sample. Hence, at any given instant, the pure solar salt sample was at a higher temperature than the nanofluid sample. Since both samples have similar values of mass and volume (for both the pure solar salt samples and the nanofluid samples), the faster temperature response indicates that the pure solar salt samples have a lower heat storage capacity (specific heat capacity) compared to the nanofluid samples.

The temperature ramp rate and natural convection heat flux was calculated based on the recorded temperature history curves and were used for the determination of the specific heat capacity ratio. The results are summarized in Figure 97.

For solar salt nanofluid samples (containing alumna nanoparticles at a target mass fraction of 1% and with sodium metaphosphate as the additive that served as dispersing

agent) the enhancement in the specific heat capacity was in the range of 20 ~ 40% (which is similar to that of the solar salt alumina nanofluid samples without the dispersing agent). Hence, for the solar salt-Al_2O_3 nanofluid samples, the specific heat capacity enhancement for sodium metaphosphate doped sample was found to be at a similar level with the nanofluid sample synthesized without the dispersing agent.

In contrast, for the solar salt nanofluid samples (with MgO nanoparticles synthesized in-situ at a target mass fraction of 1%), the additive (dispersing agent) has a significant effect on the specific heat capacity enhancement (which is in the range of 30~40% for repeat tests and 50~60% for test number 1).

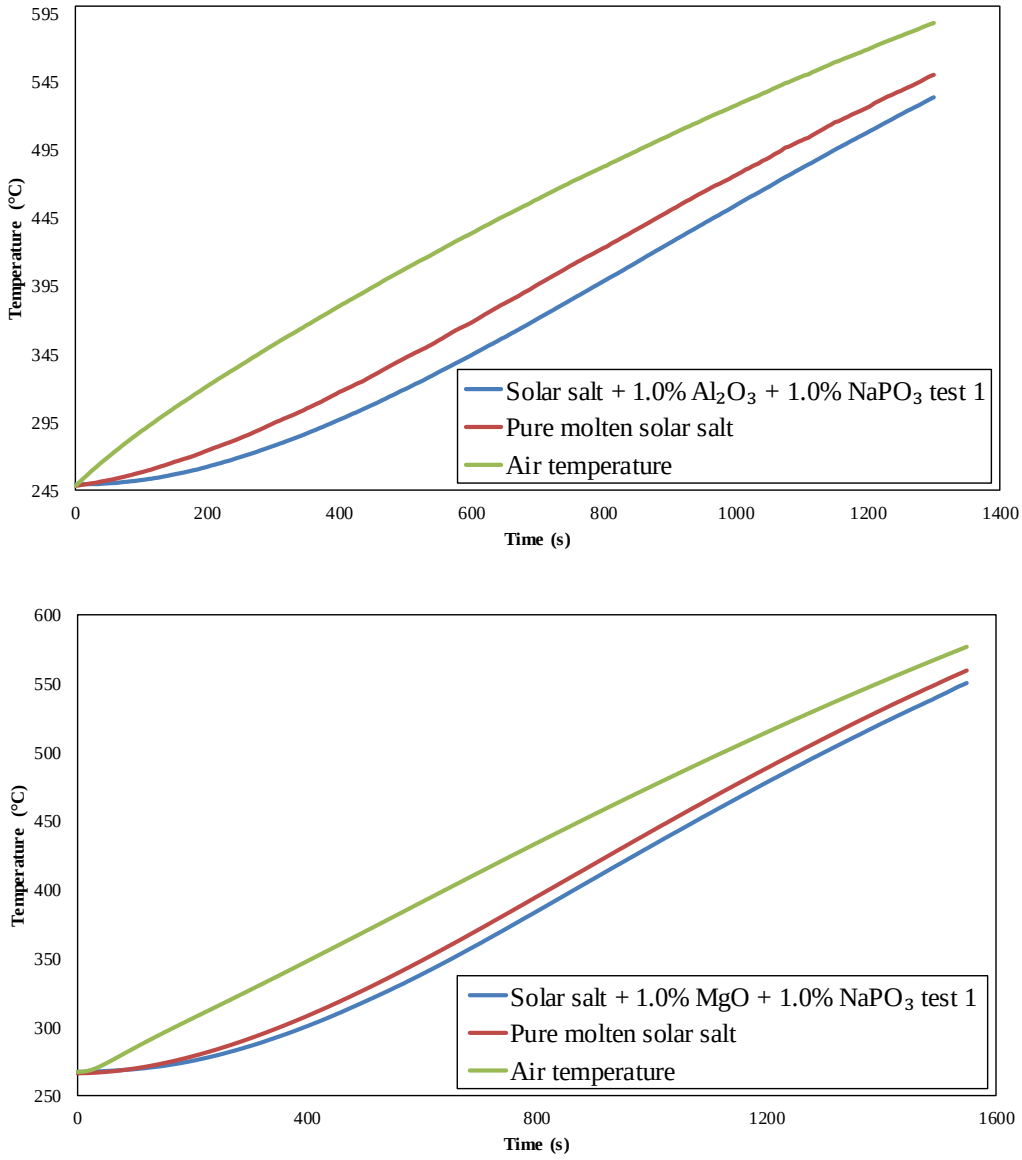

Figure 96. Plot of temperature response obtained from T-History experiments for thermocouples places in air (in the furnace), pure solar salt samples and solar salt nanofluid samples (prepared using one-step synthesis protocol with NaPO3 added as dispersing agent). (TOP) The molten salt nanofluid samples were obtained by adding $Al(NO_3)_3 \cdot 9H_2O$ at 6.9% mass fraction (as nanoparticle precursors for yielding nanofluids) to pure solar salt for a target mass fraction of 1% for the resulting Al_2O_3 nanoparticles (one-step synthesis protocol). (BOTTOM) The molten salt nanofluid samples were obtained by adding $Mg(NO_3)_2 \cdot 9H_2O$ at 3.6% mass fraction (as nanoparticle precursors for yielding nanofluids) to pure solar salt for a target mass fraction of 1% for the resulting MgO nanoparticles (one-step synthesis protocol).

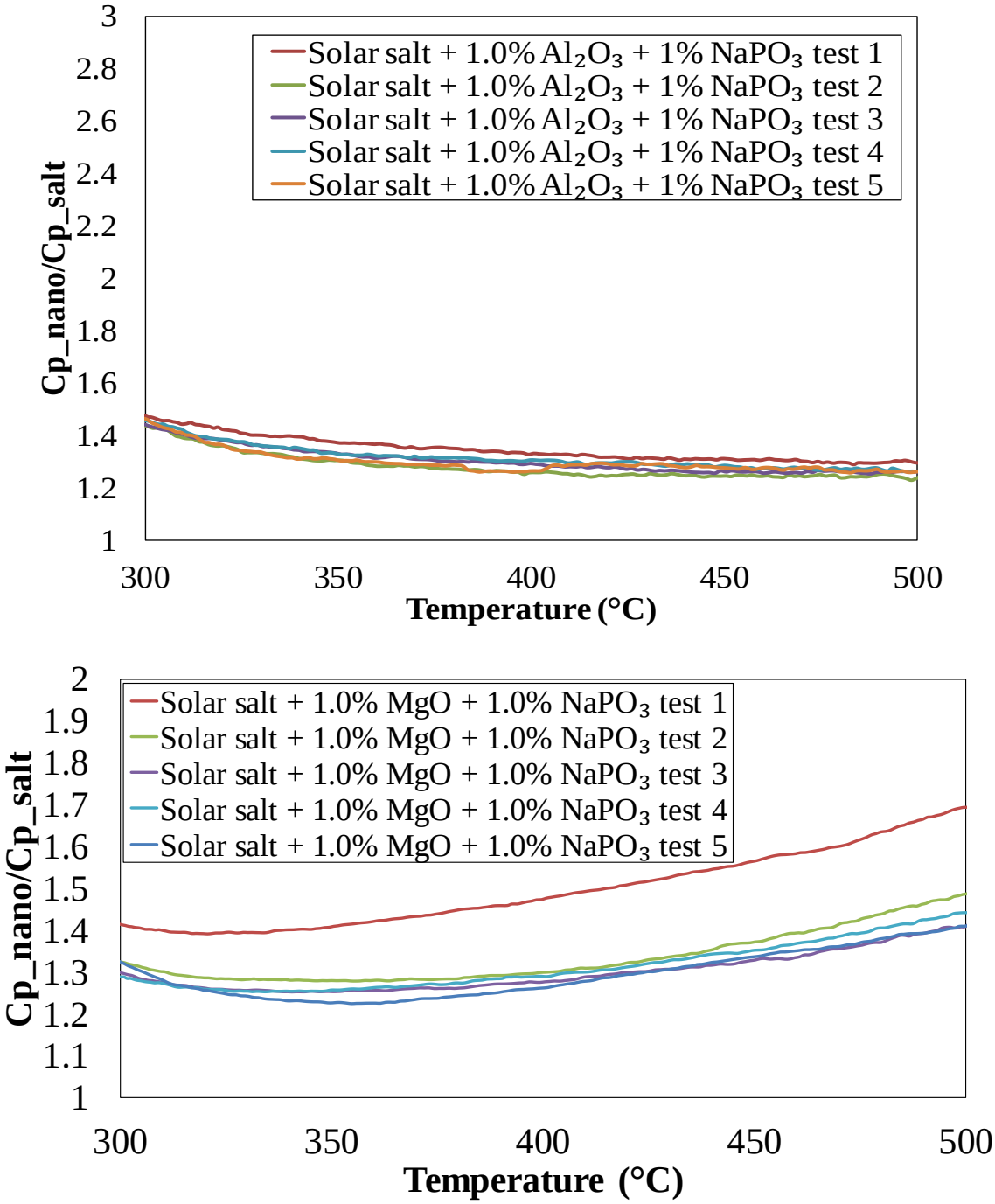

Figure 97. Plot of specific heat capacity ratio as a function of temperature (obtained from T-History experiments) for solar salt nanofluid samples (prepared using one-step synthesis protocol with $NaPO_3$ as dispersing agent). (TOP) Target mass fraction of 1% for the resulting Al_2O_3 nanoparticles. (BOTTOM) Target mass fraction of 1% for the resulting MgO nanoparticles.

Table 35. Specific heat capacity enhancement as a function of temperature (obtained from T-History experiments) for solar salt nanofluid samples (prepared using one-step synthesis protocol with $NaPO_3$ as dispersing agent). (TOP) Target mass fraction of 1% for the resulting Al_2O_3 nanoparticles. (BOTTOM) Target mass fraction of 1% for the resulting MgO nanoparticles.

Test number	300ºC	400ºC	500 ºC	Average	Standard Deviation
1	47.9%	32.7%	29.6%	35.0%	5.0%
2	43.9%	25.7%	23.5%	28.3%	5.1%
3	44.4%	29.4%	26.3%	30.7%	5.0%
4	45.7%	30.6%	26.3%	31.8%	4.7%
5	46.2%	26.5%	26.3%	30.1%	4.4%
Average	45.6%	29.0%	26.4%	31.2%	4.8%
Standard Deviation	1.4%	2.6%	1.9%	2.2%	

Test number	300ºC	400ºC	500 ºC	Average	Standard Deviation
1	41.3%	47.4%	69.4%	49.1%	9.0%
2	32.5%	30.0%	48.7%	33.4%	6.1%
3	29.9%	27.7%	40.9%	29.9%	4.5%
4	28.8%	29.0%	44.2%	31.1%	5.6%
5	32.4%	26.4%	41.1%	29.4%	5.5%
Average (for tests 1~5)	33.0%	32.1%	48.9%	34.6%	7.1%
Standard Deviation (for tests 1~5)	4.4%	7.7%	10.7%	7.4%	
Average (for tests 2~5)	30.9%	28.3%	43.7%	31.0%	5.5%
Standard Deviation (for tests 2~5)	1.6%	1.4%	3.1%	1.5%	

5.3.3 Material characterization

Figure 98 shows the comparison of SEM images of the solar salt nanofluids with and without addition of NaPO3 as a dispersing agent (with target mass fraction of 1% for the MgO particles obtained by thermal decomposition of magnesium nitrate). Both samples revealed uniform distribution of MgO particles in the salt system. However, the images show that the addition of sodium metaphosphate results in drastic reduction in the size of the MgO particles formed in the molten salt (solar salt). In the absence of sodium metaphosphate, the nominal size of the MgO particles is ~1.5 μm (as shown in Figure 90). By adding sodium metaphosphate, the nominal size of MgO particles is reduced to ~100 nm (or less) as shown in Figure 99. This suggests that sodium metaphosphate could effectively resist the agglomeration of MgO nanoparticles in the one-step synthesis protocol. The transport mechanisms respnsible for specific heat capacity enhancement can potentially be fortified due to the finer nanoparticles possessing higher surface-to-volume ratios as well as increased stability which results in enhanced energy density in the molten salt system. These results are consistent with the specific heat capacity measurements using T-History method for the alumina nanoparticles.

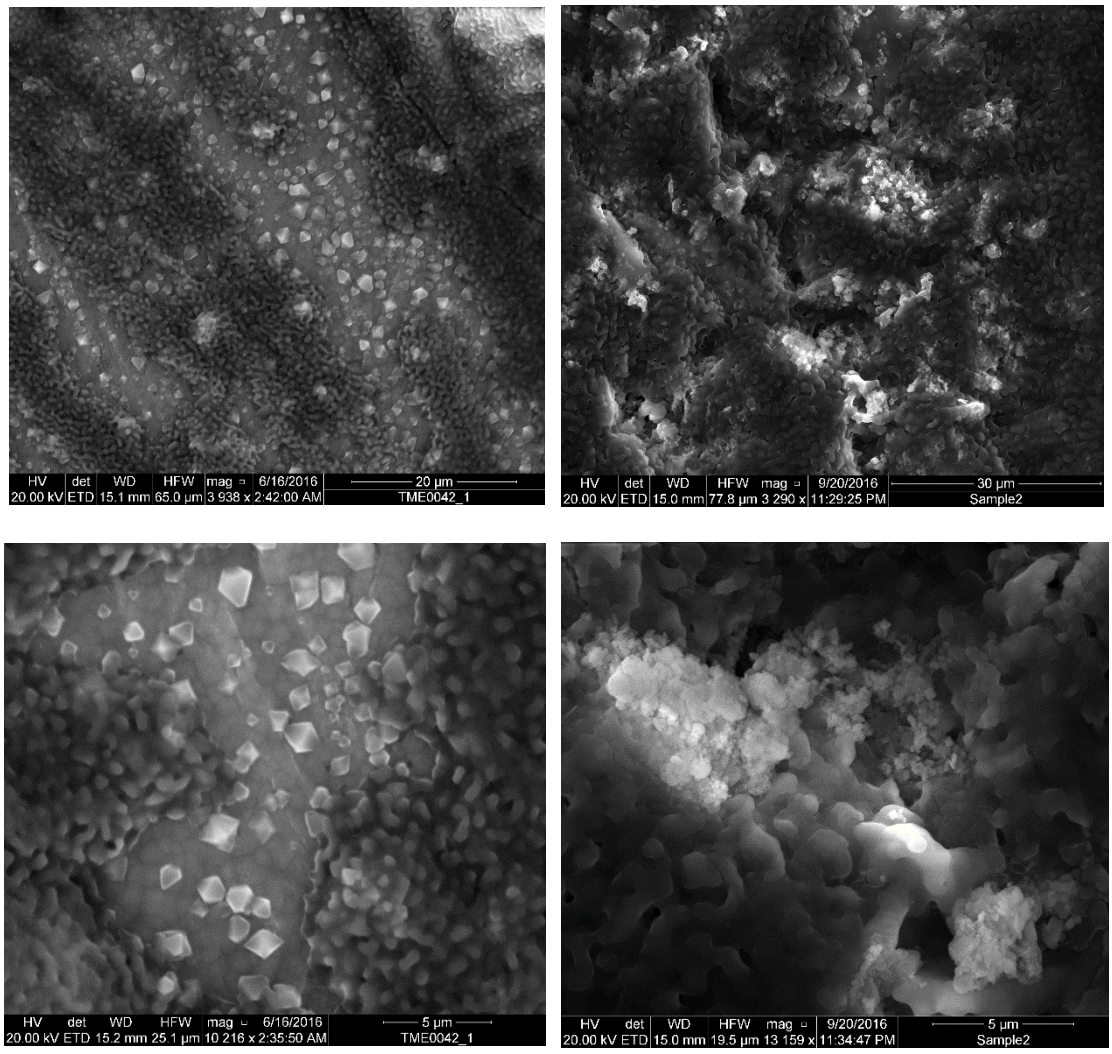

Figure 98. SEM images of solar salt nanofluid samples (one-step synthesis protocol) showing that addition of $NaPO_3$ as dispersant (to stabilize colloidal nanofluid samples) results in drastic reduction in the size of the MgO particles (at a target mass fraction of 1%) that were obtained from magnesium nitrate additive (nanoparticle precursors). (LEFT) Samples without $NaPO_3$. (RIGHT) Samples with $NaPO_3$.

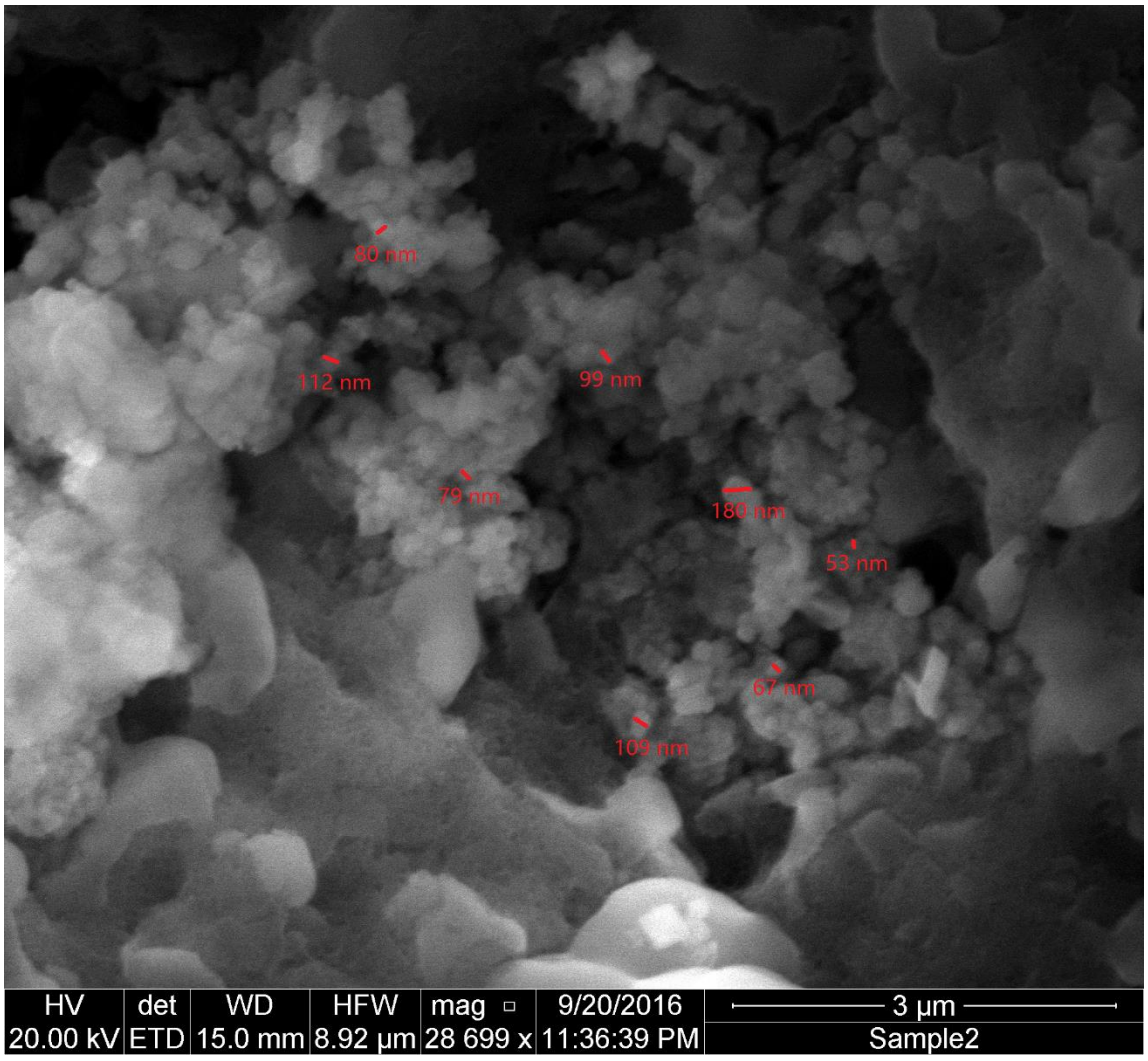

Figure 99. SEM image showing measurement of size of MgO nanoparticles synthesized in-situ from magnesium nitrate additives as nanoparticle precursors (i.e., using one-step synthesis protocol with $NaPO_3$ additives in the mixture to serve as dispersing agent) in solar salt nanofluid samples. The measurements show that the MgO nanoparticles are mostly less than 100 nm in diameter.

5.4 Summary and discussion

Considering the results obtained in this study involving the one-step synthesis protocol the following trends were observed:

- The specific heat capacity enhancement of molten salt nanofluid is not monotonic with particle concentration. Optimum value of mass concentration for nanoparticles is approximately in the vicinity of 1% (or in the range between 0.5% ~ 1%).
- Aluminum nitrate as additive to solar salt yielded nanoparticles that resulted in significant specific heat capacity enhancement. In contrast, the other additives considered in this study (zinc nitrate, magnesium nitrate and magnesium acetate) failed to yield nanoparticles of significant mass fraction and yielded micro-sized particles instead – as a result these additives failed to produce any significant enhancement in the specific heat capacity of solar salt samples.
- Dispersing agent ($NaPO_3$) enabled the additive (magnesium nitrate) to yield nanoparticles and as a result the specific heat capacity of solar salt was enhanced significantly.

As stated in Chapter 4.1, the enhancement of total specific heat capacity for molten salt nanofluids results from the formation of compressed layer on the surface of the nanoparticle (due to surface adsorption) and this compressed layer also induces the formation of secondary nanostructures which in turn can form a percolation network (this percolation network of the secondary nanostructures appears in SEM images to form a

interconnected network between the adjacent nanoparticles). Equation 24 and Figure 64, implies that the specific heat capacity enhancement should increase monotonically with nanoparticle concentration, which is inconsistent with the experimental results presented in Chapter 5.1 where the optimum value of mass fraction of the nanoparticles was observed to be 1% and the specific heat capacity was observed to decrease at mass fraction of 1.5%. To resolve this ambiguity, it is proposed that in addition to the mass fraction of the nanoparticles being a key parameter for determining the mass fraction of the secondary nanostructures – the mass fraction of the secondary nanostructures is also modulated by other factors (namely – the statistical distribution of the distance between the ensemble of nanoparticles in a sample of molten salt nanofluids).

In a nanofluid sample (i.e., a stable nanoparticle colloidal suspension), the average value of the inter-particle distance shrinks with increasing mass fraction of the nanoparticles (for a fixed size of the nanoparticles). If the secondary nanostructures are confined to the space between nanoparticles then the mass fraction of the secondary nanostructures should be reduced as the distance between the nanoparticles is reduced. Considering a simplified scenario in which all nanoparticles of the same size are distributed uniformly in a molten salt nanofluid sample and where all the percolation network formed by the secondary nanostructures of a fixed diameter (say, in the form of cylindrical shape of a fixed diameter) are confined to the shortest distance between any two adjacent nanoparticles (as shown in Figure 100), the volume of the secondary nanostructures ($V_{secondary}$) is then proportional to the inter-particle distance

($A_{inter-particle}$) and mass fraction of the nanoparticles (φ_{np}), as shown in the following equation:

$$V_{secondary} \propto A_{inter-particle} \cdot \varphi_{np} \tag{51}$$

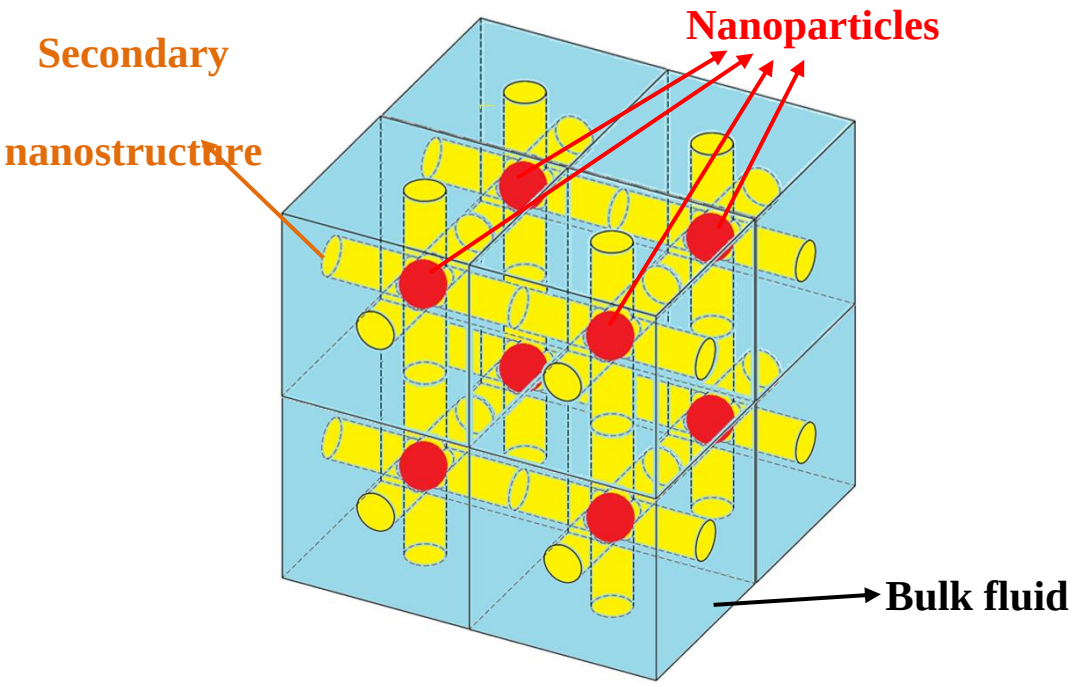

Figure 100. Conceptual model of percolation network formed by the secondary nanostructures (in yellow) between adjacent nanoparticles (in red) in a nanofluid sample (the bulk of the solvent phase is in blue color). The diameter of the nanoparticles and the percolation network are shown to be of the same fixed size.

Assuming homogeneous distribution of the nanoparticles of a fixed size, the inter-particle distance is negatively related to nanoparticle concentration as:

$$A_{inter-particle} \propto \frac{1-\varphi_{np}^{1/3}}{\varphi_{np}^{1/3}} \tag{52}$$

which yields

$$V_{secondary} \propto {\varphi_{np}}^{2/3}\left(1-{\varphi_{np}}^{1/3}\right) \tag{53}$$

Based on Equation 53 the variation of the volume of nanostructure with nanoparticle concentration (mass fraction) is plotted in Figure 101. The plot shows that the volume fraction of secondary nanostructure starts to decline when nanoparticle concentration exceeds 30%.

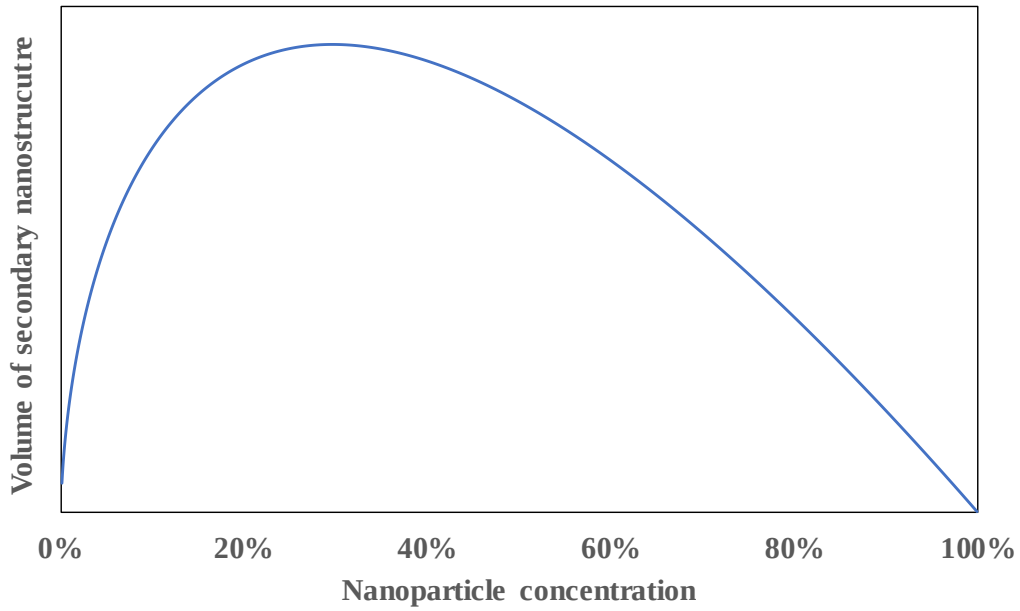

Figure 101. Plot of volume fraction of secondary nanostructures as a function of the mass fraction of the nanoparticles (of a fixed size and distributed uniformly in the volume of the nanofluid sample), based on Equation 53

In reality, the nanoparticles are not distributed uniformly in the molten salt nanofluid samples. SEM images show that the nanoparticles tend to cluster into closely packed ensembles (or parcels) and each of these parcels are dispersed throughout the volume of the nanofluid samples in discrete groups. Secondary nanostructures are observed to form between the nanoparticles in each parcel. However, secondary nanostructures are not generally apparent between different parcels. Such configuration of discrete parcels therefore results in higher values of effective nanoparticle concentration (i.e., the local values of mass fraction in each of these parcels are significantly higher than that of the global average value). Consequently, the optimum value (i.e., the global average value) of the mass concentration of the nanoparticles is achieved at ~1% while the local value of mass fraction for the nanoparticles (in a parcel) is probably in the vicinity of ~30%, as predicted in Figure 101 (30%). In addition, it can be observed in Figure 94~Figure 97 that as the global average value of the mass fraction of the nanoparticles is increased from 0.5% to 1.5%, the void space between the nanoparticles in a parcel is reduced significantly. Hence, from a purely geometric consideration - it is suggested that the optimum value of the mass fraction of the nanoparticles for maximizing the volume (or mass fraction) of the secondary nanostructures is in the range of 0.5% to 1%.

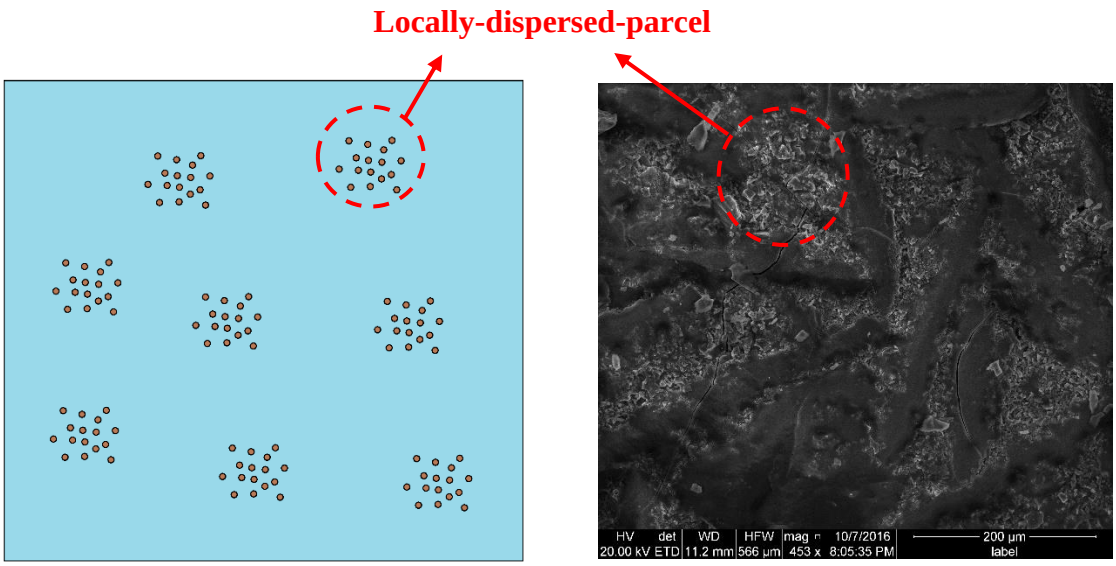

Figure 102. Heterogeneous distribution of nanoparticles in a molten salt nanofluid sample showing locally-dispersed nanoparticles in each parcel and the parcels are dispersed throughout the sample in a heterogeneous configuration. (LEFT) Schematic diagram. (RIGHT) SEM image of solar salt nanofluid sample obtained by one-step synthesis protocol from aluminum nitrate additive (with a target mass fraction of 1% for alumina nanoparticles)

6. EXPERIMENTAL RESULTS: CORROSIVITY AND THERMAL STABILITY

The material compatibility and stability of the solar salt samples was explored (with and without additives as well as with and without nanoparticles). This was performed to ascertain if the materials developed in this study are suitable for applications in solar thermal power generation as well as other industrial applications of molten salts.

6.1 Corrosion Tests

The compatibility of the solar salt samples to stainless steel coupons was evaluated by performing corrosion experiments that utilized a standardized test protocol. The test protocol involved the exposure of test coupons of stainless steel at 565ºC to the solar salt samples confined in a specified container for 120 hours. The mass loss of the test coupons after 120 hours was measured. The descaling of the corrosion products was found to be unreliable when treated with hydrochloric acid solution. Hence, the standardized test protocol was refined in this study for obtaining reliable experimental data by using different chemicals for descaling the test coupons.

6.1.1 Mass loss

Figure 103 shows image of the test coupons after heating at 565 ºC for 120 hours in different environments: (a) in air (control experiment); (b) in pure solar salt; (c) in solar salt nanofluid obtained by mixed with silica nanoparticles at a mass fraction of 1% (with initial nominal diameter of 5~15 nm and final nominal diameter of 10~50 nm); and (d) solar salt nanofluid with aluminum nitrate additive at a mass fraction of 6.9% (for a target

mass fraction of 1% for alumina nanoparticles at 50~100 nm diameter). The image shows that the samples heated in contact with air had the least amount of corrosion. The other images show the formation of dark colored scales due to highly oxidizing environment caused by exposure to solar salt samples.

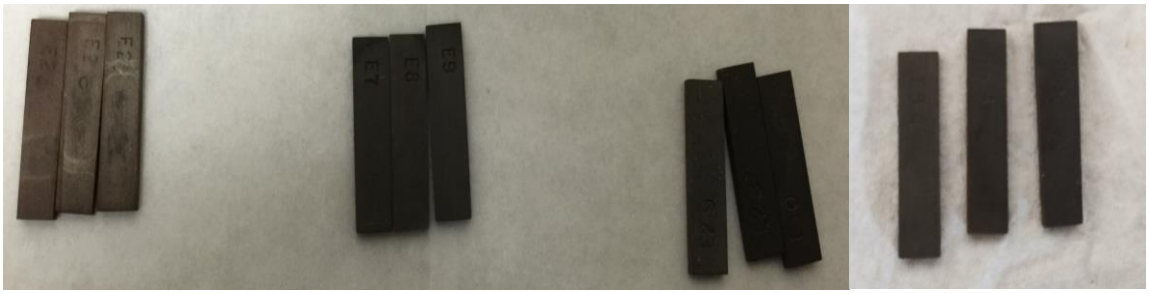

Figure 103. Image of the test coupons after heating at 565 ºC for 120 hours in different environments (from left to right): (a) in air (control experiment); (b) in pure solar salt; (c) in solar salt nanofluid (with silica nanoparticles at a mass fraction of 1%); and (d) solar salt nanofluid with aluminum nitrate additive at a mass fraction of 6.9% (for a target mass fraction of 1% for alumina nanoparticles)

6.1.1.1 HCl descaling protocol

The first attempt to descale corroded metal was achieved by immersing the coupons in HCl solution (10% mass fraction) for 30 minutes. Figure 104 shows the images of the corrosion test coupons and the change in sample morphology (the dark surface of the samples become bright and shiny after the descaling process). This indicates that the descaling protocol (using HCl solution) effectively removed all of the corrosion byproducts.

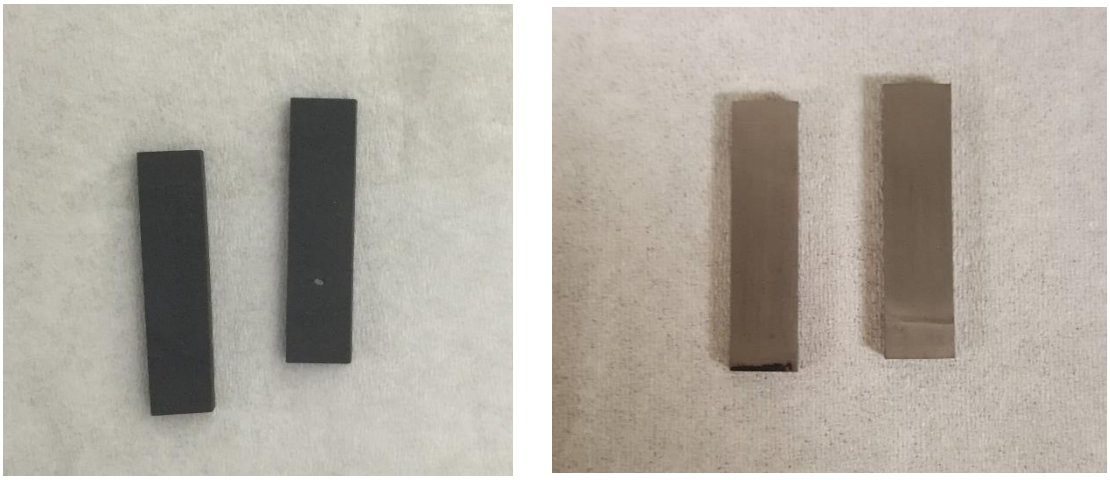

Figure 104. Images of the corrosion test coupons (in pure molten salt) showing the change in sample morphology on descaling with HCl solution. (LEFT) Before descaling. (RIGHT) After descaling.

The measured values of mass loss for each coupon are plotted in Figure 105. The mass loss values were measured for samples descaled in HCl solution for 30 minutes and 120 minutes. Three test coupons were used for each sample to verify the repeatability of the experiments. The plots show that the samples from the control experiment (samples heated in air) showed lower levels of corrosion than the samples exposed to the pure solar salt samples and solar salt nanofluid samples (with silica nanoparticles). Surprisingly, the samples from the control experiment (samples heated in air) showed similar levels of mass loss to corrosion as the samples exposed to solar salt with aluminum nitrate additivies (with target mass fraction of 1% for alumina nanoparticles). It was observed that one of the coupons exposed to solar salt nanofluid (with silica nanoparticles) displayed abnormally high degree of mass loss. This could potentially occur if the test coupon accidentally touched the surface of the container leading to galvanic corrosion (which

accelerates the electron migration process or due to more rapid descaling than the other test coupons).

From the results obtained for descaling period of 30 minutes and plotted in Figure 105, it is observed that the mass loss per unit area for stainless steel in pure solar salt samples is ~1.41 mg/cm^2. This value is much higher than the results reported by Bradshaw [95] who performed the corrosion tests under similar experimental condition and found an average mass loss of 0.50 mg/cm^2. who reported an average mass loss of 0.50 mg/cm^2 for corrosion experiments performed under similar experimental conditions. However, Bradshaw had used boiling alkaline permanganate (instead of immersing in HCl solution) for descaling which could cause lower rates of mass loss during the descaling step. It is worth noting that for the sample coupons in the control experiments (i.e., heated in air) the average mass loss was 0.8 mg/cm^2 after descaling in HCl solution. To elucidate whether the mass loss measured in these experiments is only from descaling the byproducts of corrosion or if the bare metal was being corroded by the HCl solution, the coupons were descaled for additional 1.5 hours and the mass loss values were measured. The results show that the average values of mass loss per unit area for control test coupons (i.e., heated in air) increased from 0.80 mg/cm^2 to 0.97 mg/cm^2 while that for the test coupons exposed to pure solar salt test increased from 1.41 mg/cm^2 to 1.63 mg/cm^2. The extended period of descaling did not cause significant increments in the total mass loss values and hence it is believed that the mass loss values measured for a descaling period of 30 minutes were primarily due to removal of corrosion products.

The results plotted in Figure 105 show that adding silica nanoparticles did not cause any significant changes to the corrosivity of the pure solar salt nanofluid samples (prepared using the two-step synthesis protocol) since the mass loss values were of similar magnitude for test coupons placed in both pure solar salt samples and solar salt nanofluids samples containing silica nanoparticles. In contrast, the presence of alumina nanoparticles significantly reduced the corrosivity of the solar salt nanofluid samples (prepared using the one-step synthesis protocol by mixing with aluminum nitrate additive) by ~ 50%. After decaling for 30 minutes the average mass loss of the coupons immersed in solar salt nanofluid (with silica nanoparticles) is measured to be 1.60 mg/cm^2 while that of the coupons immersed in solar salt nanofluids (with alumina nanoparticles) is 0.74 mg/cm^2. This result contradicts the results reported by Iyer [124] showing that the addition of silica nanoparticles reduced the mass loss due to corrosion by 50%.

The measurements performed for extended periods of descaling (for 120 minutes) showed similar trends as the results obtained for the descaling period of 30 minutes. The mass loss of coupons immersed in solar salt nanofluid (with silica nanoparticles) increased from 1.60 mg/cm^2 to 1.93 mg/cm^2 (which is even higher than that of the coupons immersed in pure solar salt). The mass loss of coupons immersed in solar salt nanofluids (with aluminum nitrate additives for target mass fraction of 1% for alumina nanoparticles) was similar to that of the test coupons exposed to air (control experiments). Hence, it is inferred that the Al_2O_3 nanoparticles (produced from the one-step synthesis protocol) effectively passivated the surfaces of the stainless steel coupons and protected the coupons from corrosion by the molten salt.

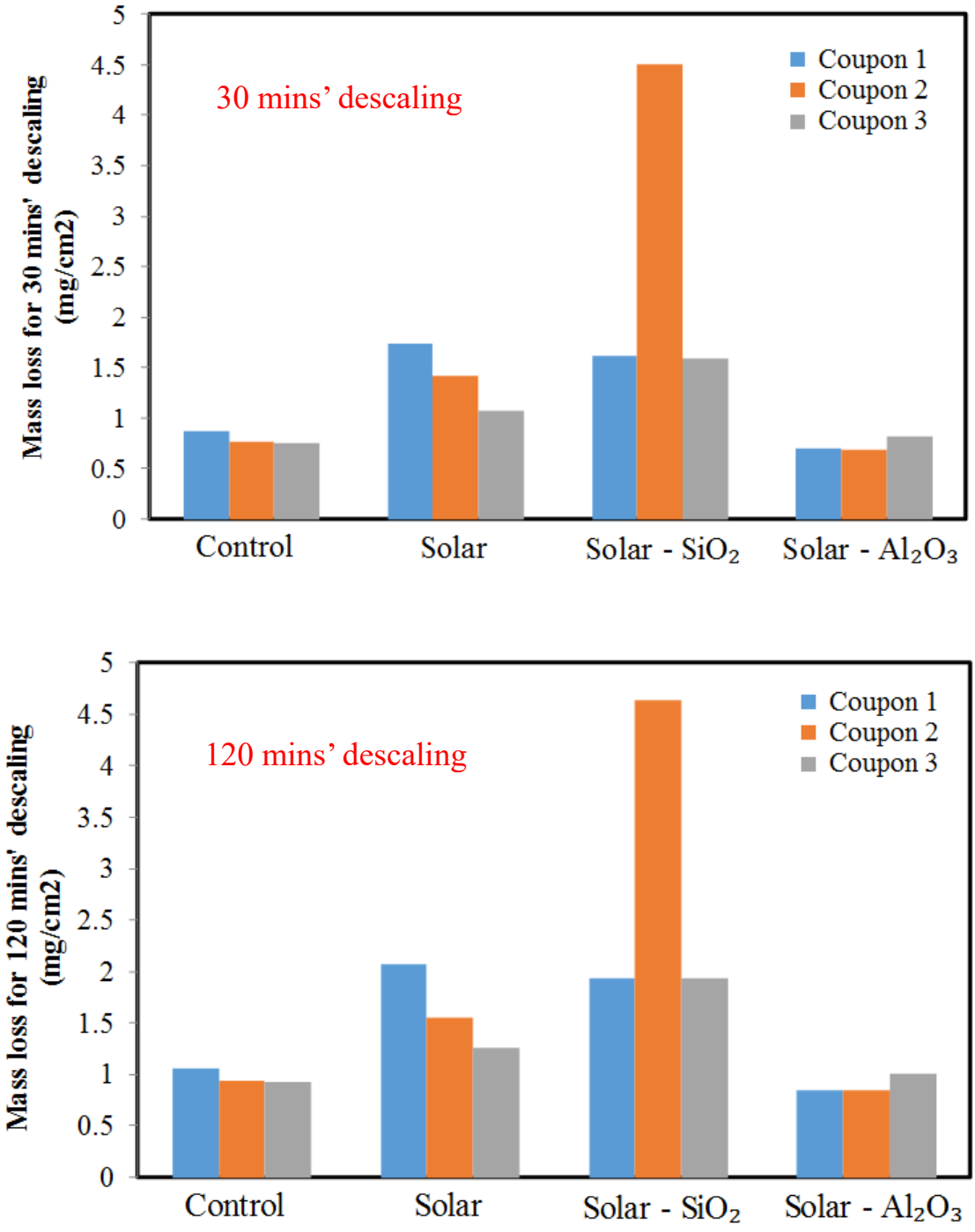

Figure 105. Mass loss of stainless steel coupons after descaling in HCl solution for: (TOP) 30 minutes; (BOTTOM) 120 minutes

6.1.1.2 Alternative descaling protocol

Figure 104 shows that the corroded SS 316 coupon regained the lustrous surface finish after descaling using HCl solution. Also, Figure 105 shows that the mass loss in the coupons exposed to air at high temperature (control experiment) increased when the descaling time for the HCl solution was increased from 30 minutes to 120 minutes. Hence, the HCl solution was also causing substantial corrosion of the test coupons and therefore an alternative descaling protocol was desired for improving the reliability of the test data. The corrosion experiments were repeated for the same conditions (as mentioned before) but a different descaling protocol was implemented using the recommendations from ASTM G01 [97]. These protocols include:

ASTM G01 C.7.1

- Mix 100 ml nitric acid with reagent water to make 1000 ml solution
- Immerse coupons in the nitric acid solution at 60ºC for 20 mins.

ASTM G01 C.7.2

- Mix 150 g diammonium citrate with reagent water to make 1000 ml solution
- Immerse coupons in the solution at 60ºC for 60 mins.

ASTM G01 C.7.4

- Mix 200 g sodium hydroxide, 30 g potassium permanganate with reagent water to make 1000 ml solution
- Boil the coupons in the solution at 60ºC for 5 mins.

Figure 106 shows images of coupons following corrosion test and after descaling by the three different protocols. Visual observation shows that the test coupons descaled using protocol C.7.1 and C.7.2 did not completely remove the byproducts of corrosion as

the surfaces of the coupons displayed a dark color (and the lustrous surface finish of the clean coupons was not recovered after descaling). Protocol C.7.4 appears to have removed the corrosion byproducts without corroding the metal surface as the surface of the test coupons are visually observed to have recovered their bright lustrous surface finish (except for a few dark traces).

Figure 106. Images of the corrosion test coupons showing the change in sample morphology on implementing the following descaling protocols [97]**: (LEFT) C.7.1; (MIDDLE) C.7.2; (RIGHT) C.7.4. Protocol C.7.4 appears to be the most effective descaling protocol in these experiments.**

The mass loss of the stainless steel coupons after descaling using protocol C.7.4 (which involved boiling in a solution consisting of a mixture of NaOH and $KMnO_4$ [97]) is plotted in Figure 107. Figure 107 shows that the average mass loss of coupons for control experiment (heated in air), pure solar salt, solar salt nanofluid (containing silica nanoparticles using two-step synthesis protocol) and solar salt nanofluid (containing alumina nanoparticles derived from aluminum nitrate additive using two step synthesis protocol) were 0.94 mg/cm^2, 1.32 mg/cm^2, 0.32 mg/cm^2 and 0.39 mg/cm^2 respectively. The results indicate that the presence of both SiO_2 and Al_2O_3 nanoparticles could protect

the metal from being corroded by molten salt as the mass loss was reduced by more than 50%.

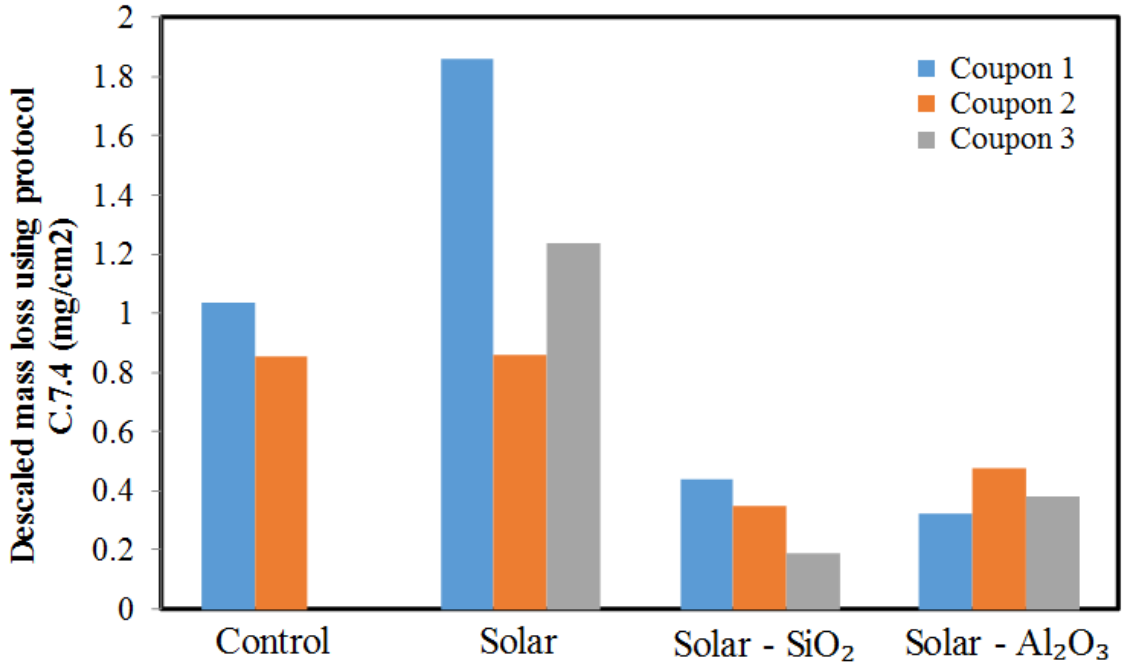

Figure 107. Mass loss of stainless steel (316) coupons after descaling using protocol C.7.4 [97] **Descaled involving boiling in a mixture of NaOH and $KMnO_4$ solution. The test coupons were heated at 565 °C for 120 hours in the presence of air (control experiment) or immersed in pure solar salt, solar salt nanofluid (with silica nanoparticles using two-step synthesis protocol), and solar salt nanofluid (with alumina nanoparticles from aluminum nitrate additive using one-step synthesis protocol).**

The mass loss values after descaling using the two different protocols (HCl solution and C.7.4 [97]) are plotted in Figure 108 for comparison. It is interesting to note from Figure 108 that the descaling protocol has marginal effect on the mass loss measurements for test coupons in the control experiments (heated in air) and for pure solar salt samples. However, the mass loss measurements for the stainless steel coupons

exposed to molten salt nanofluid samples were reduced significantly by changing the descaling method from HCl solution to the C.7.4 protocol [97].

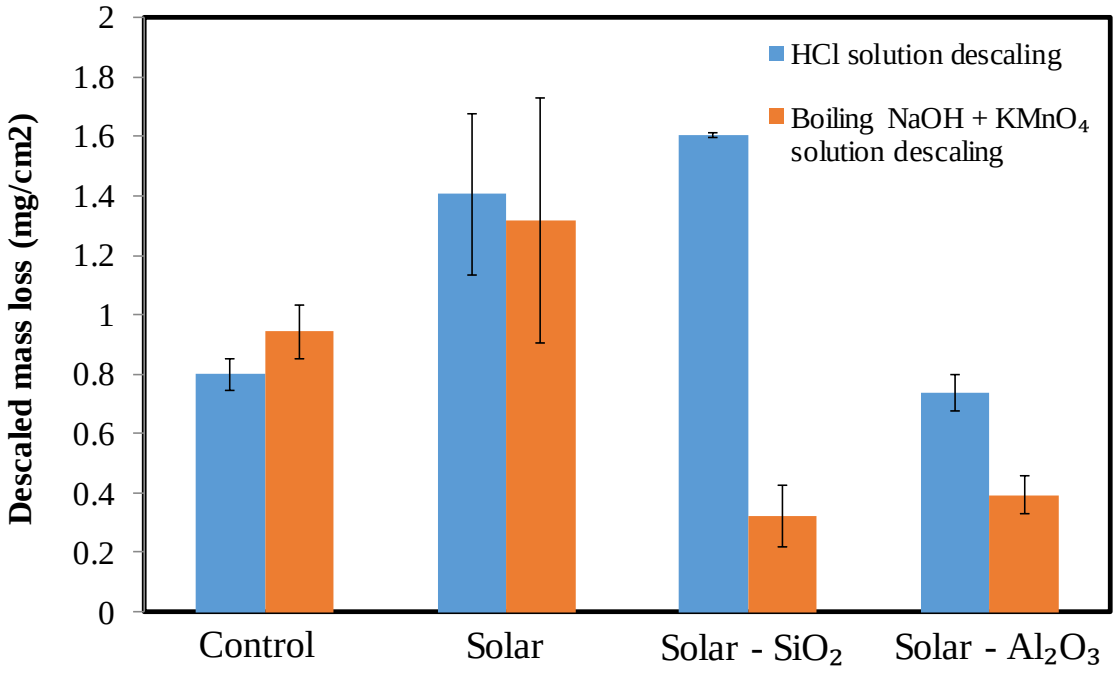

Figure 108. Comparison of mass loss in the stainless steel coupons from corrosion experiments using two different descaling protocols: HCl solution or boiling in a mixture of NaOH and $KMnO_4$ [97]. The test coupons were heated at 565 °C for 120 hours in air (control experiment) or immersed in pure solar salt, solar salt nanofluid (with silica nanoparticles using two-step synthesis protocol), and solar salt nanofluid (with alumina nanoparticles from aluminum nitrate additive using one-step synthesis protocol)

Considering that descaling of the coupons using HCl solution produced a bright lustrous surface finish – it can be inferred that the oxidation reaction between HCl and the metal surface is much more vigorous (than that between the metal and the solution used in C.7.4, i.e., mixture of $KMnO_4$ and NaOH). Since the mass loss values in these experiments were in the order of milligrams, even marginal amounts of mass loss that can

occur from the descaling solution corroding the bare metal would cause large uncertainties in the values of mass loss measured in these experiments and potential misinterpretation of the corrosion test results. Hence, the choice of the descaling protocol is an important parameter in these corrosion experiments.

6.1.2 Material characterization

Figure 109 shows the SEM images of stainless coupons after heating at 565 °C for 120 hours (i.e., before descaling). The images for the coupons immersed in solar salt nanofluid samples (with silica nanoparticles using two-step synthesis protocol) show silica nanoparticles precipitated on the surface and are scattered over the surface with a very sparse areal density of the precipitates. The precipitated silica nanoparticles served as a passivation layer and impedes the corrosion of the coupons. Similar features (of scattered nanoparticle precipitates) are observed for the images for the coupons immersed in solar salt nanofluid samples (with alumina nanoparticles using one-step synthesis protocol), where the areal density of the precipitates was lower than that of the silica nanoparticles.

The nanoparticles in both solar salt nanofluid samples potentially agglomerated and precipitated on the coupon surface, possibly at locations of surface defects (such as cavities and surface imperfections). The high surface energy of the nanoparticles can preferentially attract the ions in the molten salt (since it is an ionic liquid) and can create a localized galvanic cell since the nanoparticles acquire an effective electric potential with respect to both the metal surface and the solvent (molten salt). As a result the precipitated nanoparticles potentially serves as a sacrificial material for reaction with the ions in the

molten salt while passivating the stainless steel from corrosion. As a result, even if the precipitated nanoparticles do not provide uniform coating of the stainless steel coupons they are effective in reducing the corrosion within their "zone-of-influence" for every nanoparticle that is precipitated and scattered over the surface of the test coupons. Thus, the scattered precipitation of the nanoparticles from the nanofluids with heterogeneous surface coverage can effectively reduce corrosion in the stainless steel coupons used in this study. This phenomenon is also termed as the "nanoFin Effect (nFE)" where the precipitated nanoparticles act as fins for augmenting transport phenomena on the nano-scale [81] [82].

Figure 110 shows the SEM images of the same test coupons after descaling using protocol C.7.4. The images for coupons immersed in molten salt samples (with or without nanoparticles) show that even after descaling some scattered residues still remained on the surface (potentially from a few crystals of salt). This suggests that the descaling method effectively removed all corroded parts without attacking the metal itself. Hence the mass loss measured in these experiments accurately reflects the level of corrosion of the stainless-steel coupons immersed in different molten salt samples (with and without nanoparticles).

A complete set of high magnification SEM images and corresponding EDS spectrums can be found in Appendix F. However, these images did not provide much insights into the formation mechanism or structural characteristic of the corroded metal or protective layer.

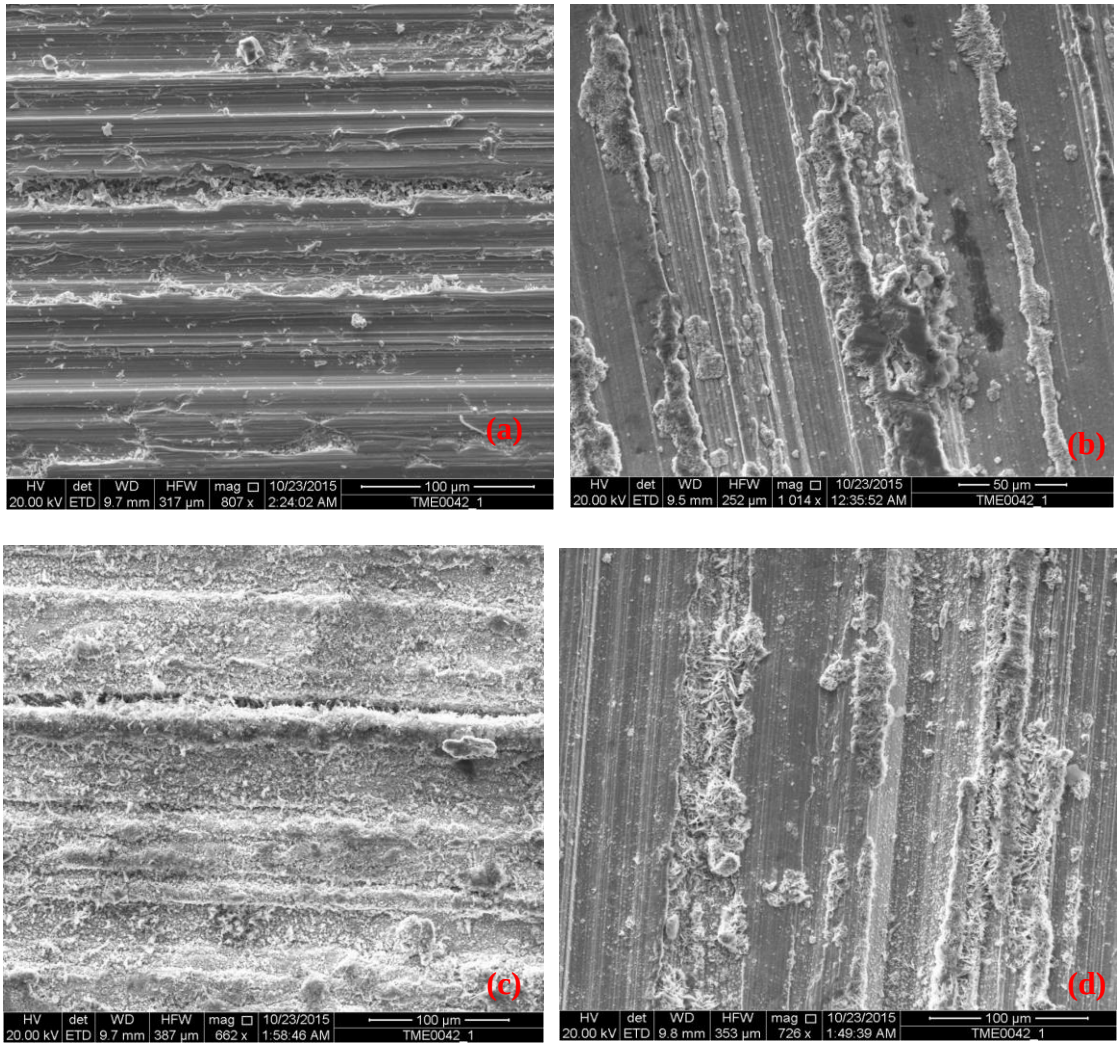

Figure 109. SEM images of stainless steel coupons before descaling and after heating at 565 °C for 120 hours: (a) in air (control experiment); or immersed in: (b) pure solar salt, (c) solar salt nanofluid (with silica nanoparticles using two-step synthesis protocol), and (d) solar salt nanofluid (with alumina nanoparticles from aluminum nitrate additive using one-step synthesis protocol)

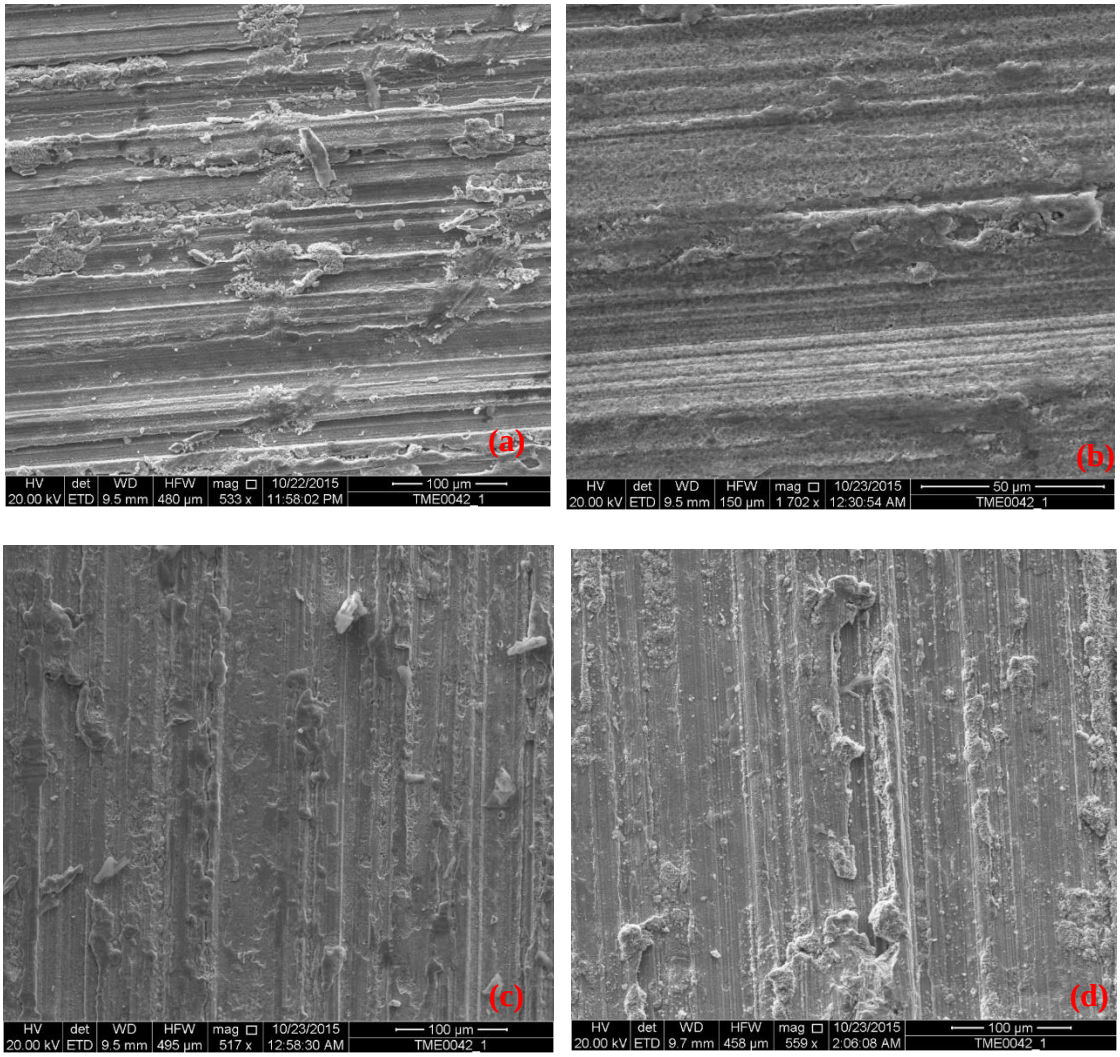

Figure 110. SEM images of stainless steel coupons following descaling using protocol C.7.4 [97] **and after heating at 565 °C for 120 hours: (a) in air (control experiment); or immersed in: (b) pure solar salt, (c) solar salt nanofluid (with silica nanoparticles using two-step synthesis protocol), and (d) solar salt nanofluid (with alumina nanoparticles from aluminum nitrate additive using one-step synthesis protocol)**

6.2 Thermal stability

The protocol for evaluating the thermal stability of the solar salt samples (with and without nanoparticles) is discussed in Chapter 2.4. The change in mass of the solar salt samples were measured after performing the thermal stability experiments which involved heating the samples in a furnace at 550 °C for 67.5 hours. The values of mass loss obtained from these measurements are listed in Table 36 and plotted in Figure 111. As discussed in Chapter 2.4, $M_0 - M_1$ indicates the total mass loss of the samples due to the trapped/dissolved gas. Also, $M_2 - M_3$ indicates the actual mass loss resulting from partial thermal decomposition (excluding trapped gas or from evaporation or ablation of the salt samples). These experiments were repeated three times for ensuring the repeatability of the measurements.

The results showed that the major mass loss of the molten salt nanofluid samples during the heating cycle was attributed to evaporative mass loss. The total mass loss of molten solar salt after heating for 67.5 hours at 550ºC due to evaporation is around 0.5% (and 0.05% due to thermo-chemical decomposition). In other words, the physical evaporative loss of molten solar salt samples was occurring at relatively moderate rate in these experiments - but the decomposition reaction occurred at significantly slower rate. The table shows that the molten salt nanofluid samples showed marginally higher values of average mass loss due to thermo-chemical decomposition reactions (than that of the pure solar salt samples). However, considering the uncertainty of the measurement results and the slow rate of decomposition process, such effects due to the presence of the

nanoparticles can be considered to be negligible and did not appear to reduce the chemical stability of molten solar salt significantly in this study.

Nanoparticles can serve as enhanced catalysts in various chemical reactions due to their high surface energy values and more coordination of unsaturated sites on the surface [125]. This can be a plausible reason for the marginally accelerated values of thermo-chemical decomposition reactions, as was observed from the measurements performed in this study.

6.3 Summary

The corrosivity and thermal stability of molten salt nanofluids were explored experimentally in this chapter. It was found that the presence of nanoparticle can reduce the corrosive mass loss of metal coupons by forming a protective layer on the sample surface, while they have negligible impact on the thermal stability of the base molten salt.

Table 36. Results from chemical stability tests (mass loss values) of solar salt samples (with or without nanoparticles) prepared using one-step synthesis protocol from additives

Samples	container mass [g]	M_0 [g]	M_1 [g]	M_2 [g]	M_3 [g]	M_0-M_1 [g]	M_0-M_1 [percent loss]	M_2-M_3 [g]	M_2-M_3 [percent loss]
Solar salt	33.012	59.946	59.849	49.272	49.266	0.097	0.4%	0.006	0.04%
Solar salt – Al_2O_3	33.302	60.023	59.801	49.176	49.164	0.222	0.8%	0.012	0.08%
Solar salt - MgO	32.716	56.802	56.74	46.208	46.201	0.062	0.3%	0.007	0.05%
Solar salt - ZnO	32.301	60.352	60.265	49.466	49.458	0.087	0.3%	0.008	0.05%
Solar salt	33.012	59.843	59.749	49.178	49.173	0.094	0.4%	0.005	0.03%
Solar salt – Al_2O_3	33.302	59.789	59.611	48.987	48.98	0.178	0.7%	0.007	0.04%
Solar salt - MgO	32.716	56.783	56.673	46.091	46.085	0.110	0.5%	0.006	0.04%
Solar salt - ZnO	32.301	60.102	59.972	49.328	49.322	0.130	0.5%	0.006	0.04%
Solar salt	33.012	59.754	59.682	49.103	49.097	0.072	0.3%	0.006	0.04%
Solar salt – Al_2O_3	33.302	59.609	59.46	48.831	48.821	0.149	0.6%	0.010	0.06%
Solar salt - Mgo	32.716	56.674	56.597	46.012	46.005	0.077	0.3%	0.007	0.05%
Solar salt - ZnO	32.301	59.971	59.853	49.204	49.198	0.118	0.4%	0.006	0.04%

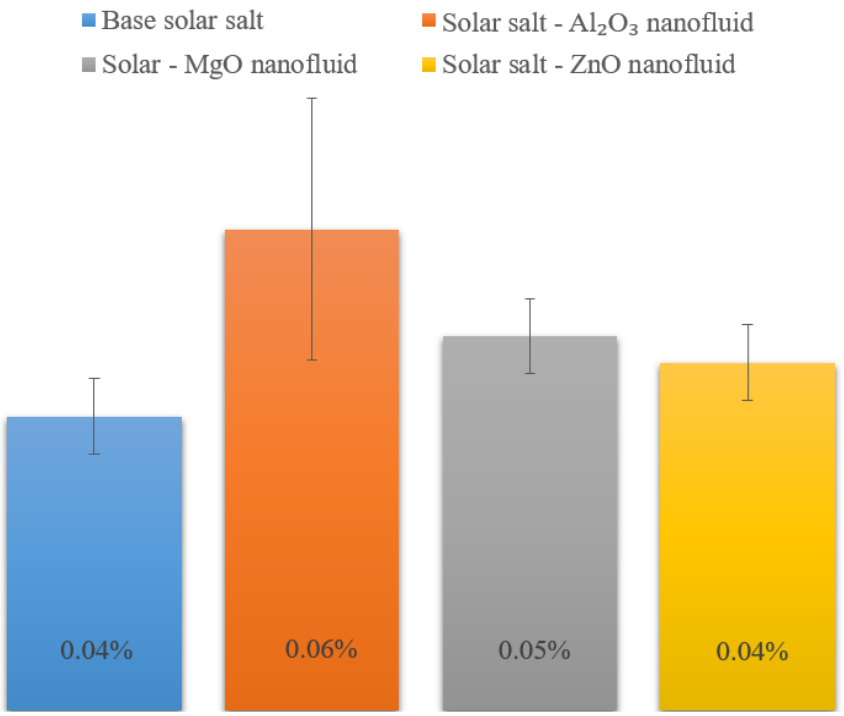

Figure 111. Plot of mass loss values from chemical stability tests of solar salt samples (with or without nanoparticles) prepared from additives using one-step synthesis protocol

7. NUMERICAL STUDY: CFD SIMULATION

Various studies in the literature [47, 65, 126, 127, 128] have reported that the enhanced thermo-physical properties of nanofluids can enable the augmentation of heat transfer in thermal management systems (i.e., as heat transfer fluid or "HTF"). Computational models developed to analyze the thermal-hydraulic performance of nanofluids have been implemented numerically using either a single-phase approach or a two-phase approach. Although two-phase approach is advantageous in capturing the particle-liquid interaction and modeling the complex mechanism induced by the dispersed nanoparticles, it is reasonable to approximate nanofluids as a single-phase flow system in certain cases (e.g., where the particle size and concentration are small enough such that they are easily fluidized and behave like continuous fluid [47]). Such approach is in general much simpler than the two-phase approach and hence requires less computational resources. Nevertheless, it has been shown in a few comparative studies [129, 130, 131] that the two-phase models provide more accurate predictions for the convective heat transfer performance (compared to that of the single-phase models). The enhanced accuracy afforded by the two-phase models is associated with the requirements for additional computational resources. However, there is a possibility that the effect of the particle-fluid interaction represented in the two-phase model could be re-produced in the single-phase model, by incorporating non-homogeneous fluid properties. The benefit of such approach is that it enables better accuracy of the predicted results (than the traditional single-phase model) and while requiring less computational resources (than the traditional two-phase models).

In this study, a single-phase homogeneous model was implemented initially to explore the effects of nanoparticle concentration on the hydrodynamic and thermal performance of chosen nanofluids under mixed laminar forced flow conditions in a horizontal tube at different flow rates. In the second part of this computational study, a two-phase model was used to demonstrate the heterogeneous nature of the flow morphology (i.e., anisotropic distribution of the nanoparticles in the flow cross section) which suggests that a non-homogeneous model (non-linear anisotropic model) for calculating nanofluid properties should be incorporated in the single-phase approach to accurately predict the thermal-hydraulic behavior of flow loops incoroporating nanofluids (e.g., for thermal management applications and for using nanofluids as HTF). The objective of this computational study was to enable the prediction of pressure drop and heat transfer values obtained using nanofluids in a flow loop under design, development, assembly and experimental testing as a part of this study. The thermo-physical properties of pure solar salt and solar salt nanofluids that were used in these numerical models, were based on reports in the literature for the experimental measurements as well as correlations for properties of nanofluids.

7.1 Single-phase homogeneous model

7.1.1 Model construction

The thermal-hydraulic performance was analyzed for solar salt nanofluid samples (with alumina nanoparticles) flowing in a long straight tube (internal diameter, D_{in} = 0.37 inch; external diameter, D_{out} = 0.5 inch, and length of test section, L = 24 inches). The

numerical model was developed assuming 2-D axisymmetric geometry and convective heat transfer boundary condition (heat loss by natural convection to ambient air at 25°C under quiescent conditions). The inlet flow temperature is set at 300°C. Figure 112 shows the schematic for the boundary conditions and the representative computational mesh configuration used in the numerical simulations, where structured mesh of 15×2800 (radial × axial) and 30×2800 (radial × axial) were employed in the liquid region and solid region, respectively.

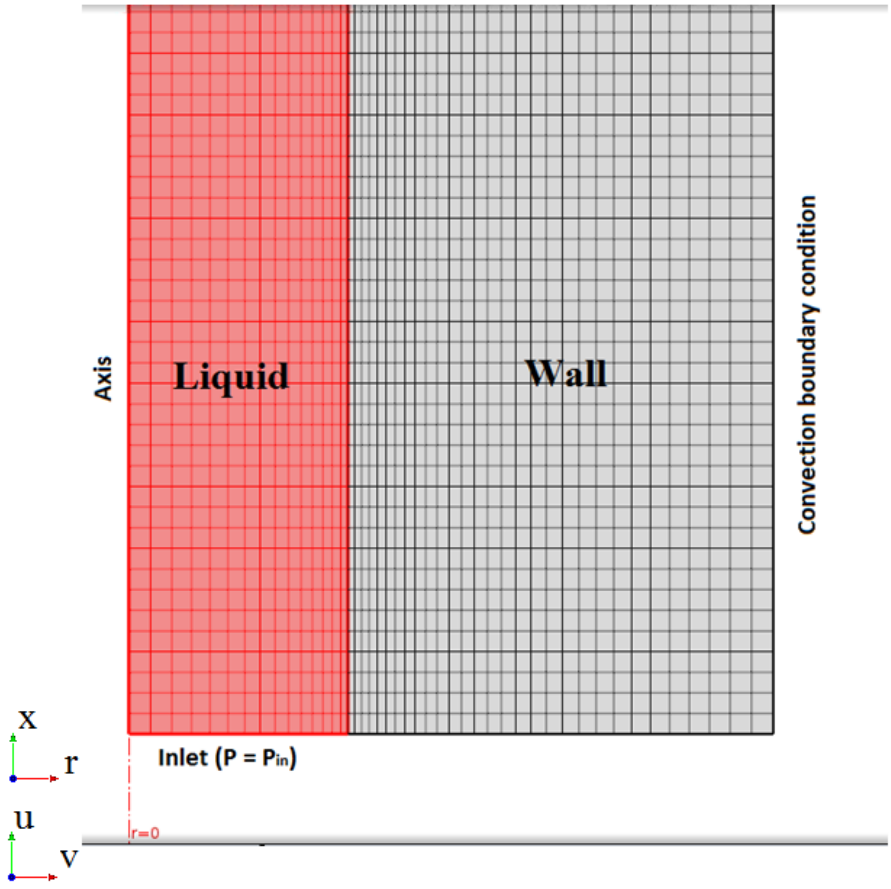

Figure 112. Schematic showing the boundary conditions and the representative computational mesh configuration used in the numerical simulations.

By treating the nanofluid as a homogeneous fluid (in which the nanoparticles are in thermal and hydrodynamic equilibrium with the surround fluid), the following governing equations are formulated for steady state homogeneous flow conditions:

Continuity equation:

$$\frac{\partial}{\partial x}u + \frac{1}{r}\frac{\partial}{\partial r}(rv) = 0 \tag{54}$$

where, $\boldsymbol{x}$ is the coordinate location in axial direction (flow direction) starting from the entrance to the test section, $\boldsymbol{r}$ is the location in radial direction, $\boldsymbol{u}$ is axial component of velocity and v is the radial component of velocity.

Momentum equation:

$$\rho\left[\frac{\partial}{\partial x}(uu) + \frac{1}{r}\frac{\partial}{\partial r}(ruv)\right] = -\frac{\partial P}{\partial x} + \frac{1}{r}\frac{\partial}{\partial r}\left(r\mu\frac{\partial u}{\partial r}\right) \tag{55}$$

$$\rho\left[\frac{\partial}{\partial x}(uv) + \frac{1}{r}\frac{\partial}{\partial r}(rvv)\right] = -\frac{1}{r}\frac{\partial P}{\partial r} + \frac{\partial}{\partial r}\left[\frac{\mu}{r}\frac{\partial(rv)}{\partial r}\right] \tag{56}$$

where, $\boldsymbol{\rho}$ is the density (assumed incompressible and isotropic), $\boldsymbol{\mu}$ is the viscosity, and P is the pressure.

Energy equation:

$$\rho\left[\frac{\partial}{\partial x}(uT) + \frac{1}{r}\frac{\partial}{\partial r}(rvT)\right] = \frac{\partial}{r\partial r}\left[r\frac{k_f}{C_{p,f}}\frac{\partial T}{\partial r}\right] \tag{57}$$

where, $\boldsymbol{T}$ is the temperature of the fluid, $\boldsymbol{k_f}$ is the effective thermal conductivity and $\boldsymbol{C_{p,f}}$ is the net effective specific heat capacity of the nanofluid.

The conductive heat transfer in the solid region (wall) was calculated using the following equation:

$$\frac{\partial}{\partial x}\left(k_s \frac{\partial T}{\partial x}\right) + \frac{1}{r}\frac{\partial}{\partial r}\left(k_s r \frac{\partial T}{\partial r}\right) = 0 \quad (58)$$

where, $\boldsymbol{k_s}$ is the thermal conductivity of the wall.

The nanofluid density was calculated by traditional mixing rule. The dynamic viscosity of nanofluid was calculated using the Renewed Ward Model [132] with an additional correction to the correlation using the effective volume ratio [133]. For specific heat capacity and thermal conductivity, Equation 18 and Equation 26 were used, respectively, to predict the effective mixture property as a function of the size of nanoparticles and concentration (i.e., mass fraction of the nanoparticles). These are shown in the Equation 59 and Equation 60. The material properties used in the simulation are listed in Table 37.

Density

$$\rho_{nf} = \varphi_n \rho_n + (1 - \varphi_n)\rho_f \quad (59)$$

where, $\boldsymbol{\varphi}$ is the volume fraction. The subscripts *n*, *f*, and *nf* represent the properties of the nanoparticles, pure solvent and net effective value (for the nanofluid sample), respectively.

Dynamic viscosity

$$\mu_{nf} = \mu_f(1 + 2.5\varphi_{\text{eff}} + (2.5\varphi_{\text{eff}})^2 + (2.5\varphi_{\text{eff}})^3 + (2.5\varphi_{\text{eff}})^4 + \cdots) \quad (60)$$

where, $\boldsymbol{\varphi_{\text{eff}}}$ is the effective volume ratio of the solvated nanoparticle in fluid, which can be expressed as

$$\varphi_{\text{eff}} = \varphi_n \left(1 + \frac{h}{r}\right)^3 \quad (61)$$

where $\boldsymbol{h}$ is the thickness of compressed layer and r is the radius of nanoparticle.

Table 37. Parameters used in nanofluid simulation with single-phase method

	Solar salt	SiO_2 nanoparticle (15 nm diameter)	Solar salt + 1% SiO_2 nanoparticle	Solar salt + 5% SiO_2 nanoparticle
Density (kg/m3)	2019.8	2400	2030	2071
Specific heat capacity (J/kg-K)	1550	700	1794	2768
Viscosity (kg/m-s)	0.004	N/A	0.00456	0.0103
conductivity (W/m-K)	0.45	1.7	0.476	0.590
Prandtl number	13.78	N/A	17.18	48.29

7.1.2 Simulation result

The simulations were performed using commercial software Comsol 4.2. The results were obtained for temperature, pressure, velocity, pressure drop and heat transfer as a function of the mass average values of the inlet velocity of the pure solar salt and solar

salt nanofluid samples. Figure 113 shows the typical example of velocity and temperature profile under one specific flow condition

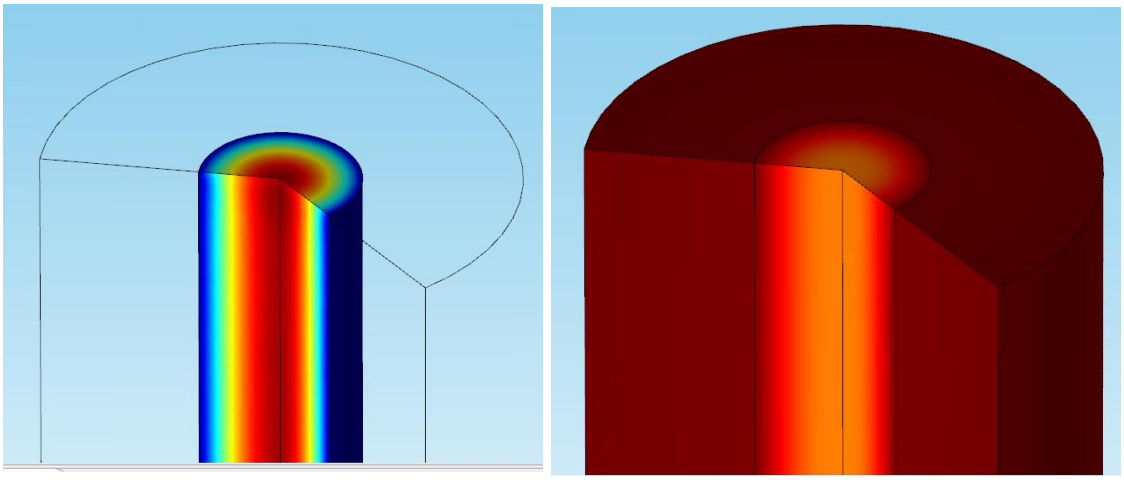

Figure 113. Typical velocity distribution (left) and temperature distribution (right) obtained from the simulations in the computational domain.

To estimate the heat transfer in the test section from the solved values of the velocity and temperature field, the following equations were used to calculate the average heat transfer coefficient for pure solar salt and solar salt nanofluid.

Mean velocity:

$$u_m = \frac{2}{r_o^2}\int_0^{r_0} ur\,dr = \frac{2}{r_o^2}\sum_{i=0}^{n}\frac{u_i}{2}(r_{i+1}^2 - r_i^2) \tag{62}$$

where, r_o is the radius of the flow channel and u_i is the local velocity in the simulation cell located at radius of r_i.

Mean temperature:

$$T_m = \frac{2}{u_m r_o^2}\int_0^{r_0} uTr\, dr = \frac{2}{u_m r_o^2}\sum_{i=0}^{n}\frac{u_i T_i}{2}(r_{i+1}^2 - r_i^2) \tag{63}$$

where, u_m is the mean velocity and T_i is the local temperature in the simulation cell located at radius of r_i.

Heat transfer coefficient:

$$h_x = \frac{q''}{(T_m - T_{wall})_x} \tag{64}$$

where, q'' is the boundary heat flux, T_m and T_{wall} are the bulk mean temperature of flowing fluid and surface temperature.

Nusselt number:

$$Nu_x = \frac{h_x D}{k}, \quad Nu_{avg} = \frac{\int_0^L Nu_x}{L} \tag{65}$$

Figure 114 and Table 38 shows the temperature drop and pressure drop in the test section obtained from these simulations (marked as dots) as well as from theoretical predictions (marked by curves and lines) as a function of flow rate for both pure solar salt and solar salt nanofluid (with alumina nanoparticles at a mass fraction of 1%). The simulations were performed assuming a boundary condition of natural convection heat loss to the ambient air with a heat transfer coefficient of 5 W/(m^2·K). The theoretical

prediction of pressure drop was calculated using Darcy–Weisbach equation in laminar flow region as:

$$\Delta P = \frac{64}{\mathrm{Re}} \cdot \frac{L}{D} \cdot \frac{\rho v^2}{2} \tag{66}$$

where, ***L*** is the length of the pipe, ***D*** is the inner diameter of the tube, ***ρ*** is the density of fluid and ***v*** is the bulk mean velocity of the fluid.

The theoretical temperature drop was calculated by the integration method as:

$$\begin{cases} \int_0^L h(T(x) - T_{air})\,\pi D_o \mathrm{dx} = \frac{\pi}{4} {D_i}^2 v \rho c_p \Delta T \\ T(x) = T_0 - x \cdot \frac{\Delta T}{L} \end{cases} \xrightarrow{\text{yields}} \Delta T = \frac{L(T_0 - T_{air})}{\frac{L}{2} + \frac{v {D_i}^2 \rho c_p}{4 h D_o}} \tag{67}$$

where, $\boldsymbol{T_0}$ is the inlet temperature, $\boldsymbol{T_{air}}$ is the ambient temperature, ***h*** is the external convective heat transfer coefficient, $\boldsymbol{D_i}$ and $\boldsymbol{D_o}$ are the inner and outer diameters of the tube modeled in the simulation.

It is observed that the variation of pressure head with increasing flow rate is significantly higher in nanofluids compared to that of the pure solar salt. Figure 115 shows that for the same flow rate, the enhancement in heat transfer by using nanofluid is only about 1% while the increment in pressure drop is 15~150%. Such scenario is due to the fact that the convection coefficient is so small that the overall heat transfer performance is dominated by the low values of heat transfer coefficient at the boundary (i.e., natural convection in air). Since the thermal resistance for heat transfer external to the computational domain (on the outer surface of the wall) is the dominant parameter for the overall heat transfer coefficient, the total value of heat transfer is relatively insensitive to

changes in the values of the internal convective heat transfer coefficient (on the inner surface of the pipe). However, when the value of the external heat transfer coefficient is changed to 1000 W/(m^2·K), the enhancement in total heat transfer was found to be in the range of 60%, while the while the pressure head is increased by 150% (Figure 116). Such performance characteristic suggests that it is more favorable to use the nanofluid as heat transfer fluid in scenarios where the external heat transfer rate is high (i.e., solar radiation, phase change, etc.) than when it is relatively low (i.e., natural convection heat loss to ambient air).

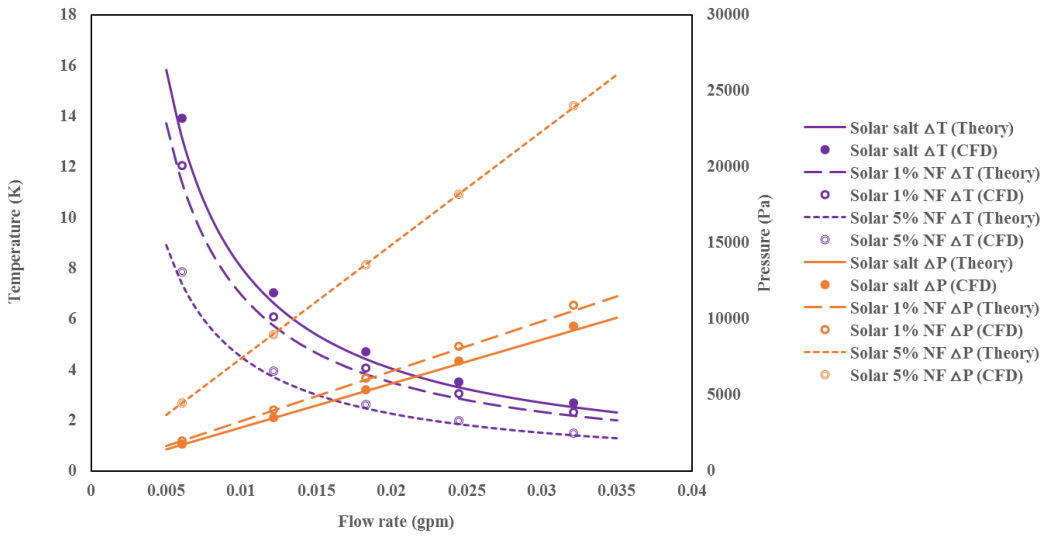

Figure 114. Plot of temperature and pressure drop as a function of flow rate for solar salt nanofluids, with external heat transfer coefficient of *h* = 5 W/(m^2·K)

Table 38. Nanofluid CFD simulation results from parametric studies

Flow inlet (input parameter)		Simulation result for pure solar salt		Simulation result for solar salt + 1.0% SiO_2		Simulation result for solar salt + 5.0% SiO_2	
v (m/s)	Flow rate (gpm)	Pressure (Pa)	ΔT (K)	Pressure (Pa)	ΔT (K)	Pressure (Pa)	ΔT (K)
0.105	0.00606	1741	13.9	1982	12.0	4451	7.9
0.210	0.0122	3524	7.0	4006	6.1	8958	3.9
0.315	0.0183	5350	4.7	6077	4.1	13528	2.6
0.422	0.0245	7221	3.5	8195	3.0	18166	2.0
0.554	0.0321	9529	2.7	10872	2.3	23989	1.5

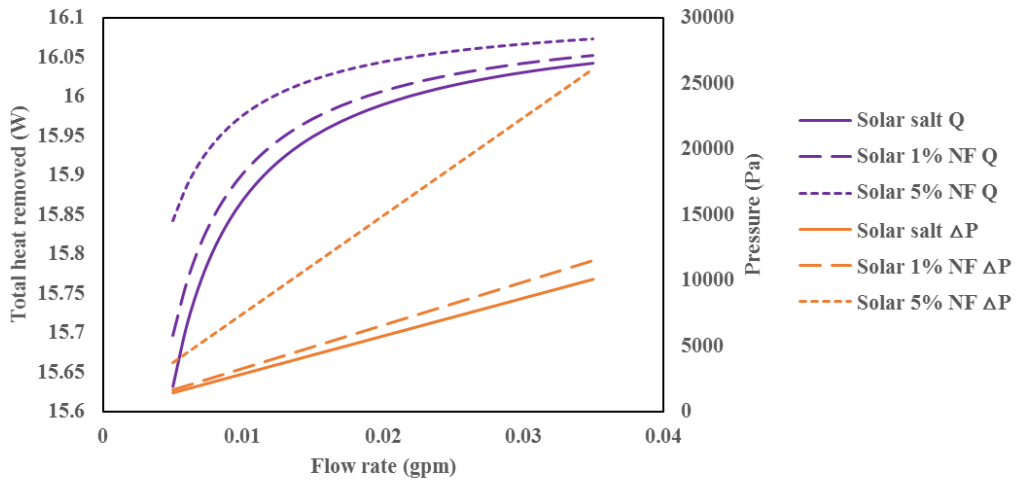

Figure 115. Plot of total heat transfer and pressure drop as a function of flow rate for solar salt nanofluids, with external heat transfer coefficient of h = 5 W/(m^2·K)

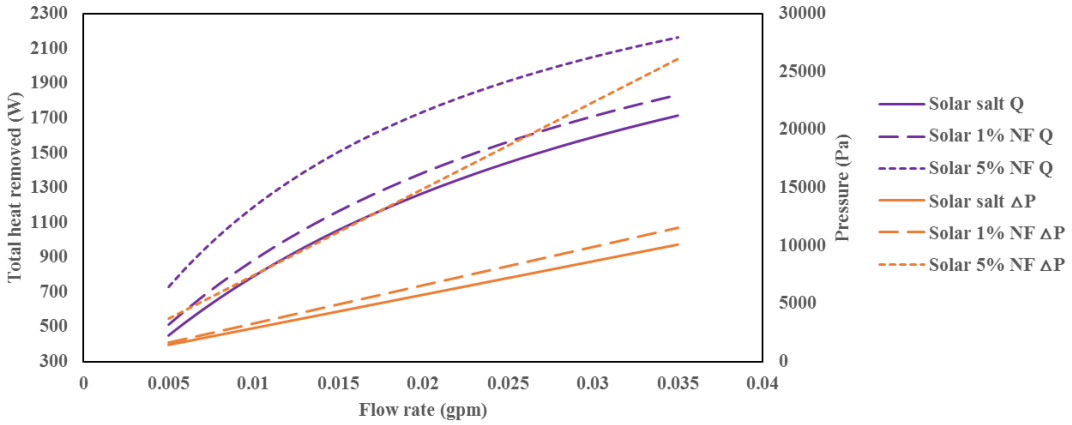

Figure 116. Plot of temperature and pressure drop as a function of flow rate for solar salt nanofluids, with external heat transfer coefficient of h = 10^3 W/(m^2·K)

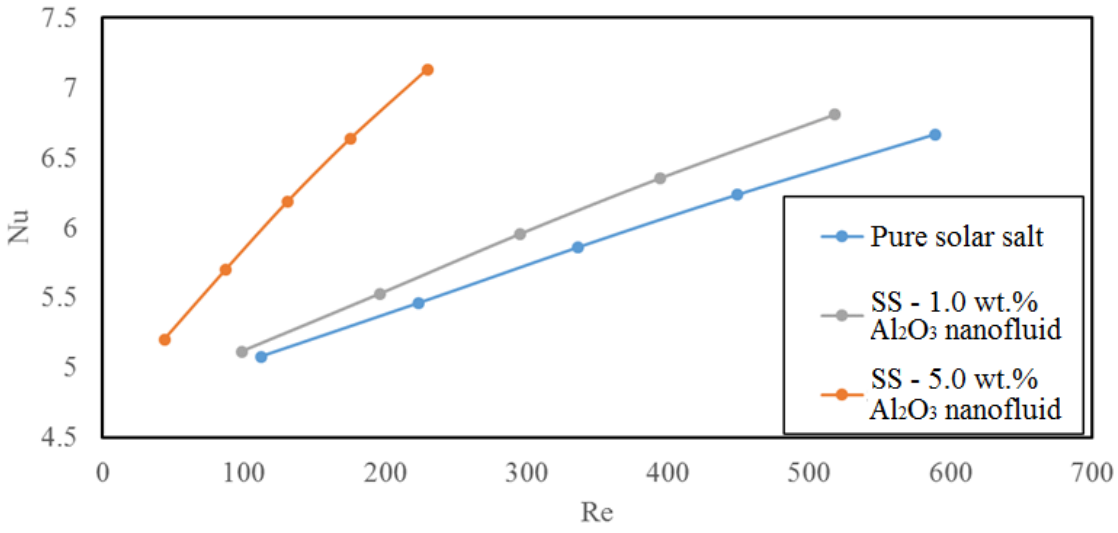

Figure 117. Nusselt number (Nu) plotted as a function of Reynolds number for pure solar salt and solar salt nanofluids with h = 1000 W/(m^2·K)

7.2 Inhomogeneity of nanofluid

7.2.1 Particle trajectory in mixed laminar flow

The hydrodynamic behavior of the nanoparticles flowing in a pipe can also be analyzed by incorporating a Lagrangian particle transport model [134]. In case of very dilute concentration of the nanoparticles, it is reasonable to assume that the flow of the solvent phase is not significantly affected by the dynamics of the nanoparticles. This allows for the solution of fluid and particle dynamics to be analyzed separately, which is known as the Eulerian-Lagrangian one-way coupling [134]. For solving the velocity and pressure field in the single-phase flow part (pure fluid), the same set of governing equations (54)~(57) and boundary conditions were used for the numerical solutions. For tracking the particle dynamics, the velocity and position field could then be solved with a set of ordinary differential equations following the classic numerical integration method (i.e., by combining velocity Verlet method [135] and Runge–Kutta–Fehlberg method [136]). The initial value problems are formulated as the follows:

$$\frac{\mathrm{d}\vec{X}}{\mathrm{d}t} = \vec{V} \tag{68}$$

$$\frac{\mathrm{d}\vec{V}}{\mathrm{d}t} = \vec{a} = \frac{\vec{F}}{m} \tag{69}$$

where, the driving force for nanoparticle motion is the drag force and virtual mass force. These are expressed as follows:

Drag force

$$F_b = \frac{1}{2} C_d \rho A_p \left(v_f - v_p\right)^2 \tag{70}$$

where, $\boldsymbol{\rho}$ is the density of the particle, $\boldsymbol{A_p}$ is the surface area of the particle, $\boldsymbol{v_f}$ and $\boldsymbol{v_p}$ are the local velocities of the bulk fluid and particle, $\boldsymbol{C_d}$ is the drag coefficient given by

$$C_d = \begin{cases} \frac{24}{Re_p}\left(1 + 0.15 Re_p^{0.687}\right) & Re_p \leq 10^3 \\ 0.44 & Re_p > 10^3 \end{cases} \tag{71}$$

Virtual mass force

$$F_m = \frac{\rho V_p}{2} \frac{\mathrm{d}\left(v_f - v_p\right)}{\mathrm{d}t} \tag{72}$$

In these simulations, Al_2O_3 nanoparticles with 100 nm diameter and mass fraction of 1% were injected at the inlet of the test section with uniform volumetric distribution and with the same velocity as the mass average velocity of the bulk fluid phase. The simulations were performed using STAR-CCM+ (version 11.04.010). The computational mesh configuration for the nanoparticle injection using multi-phase flow model are shown in Figure 118 and Table 39.

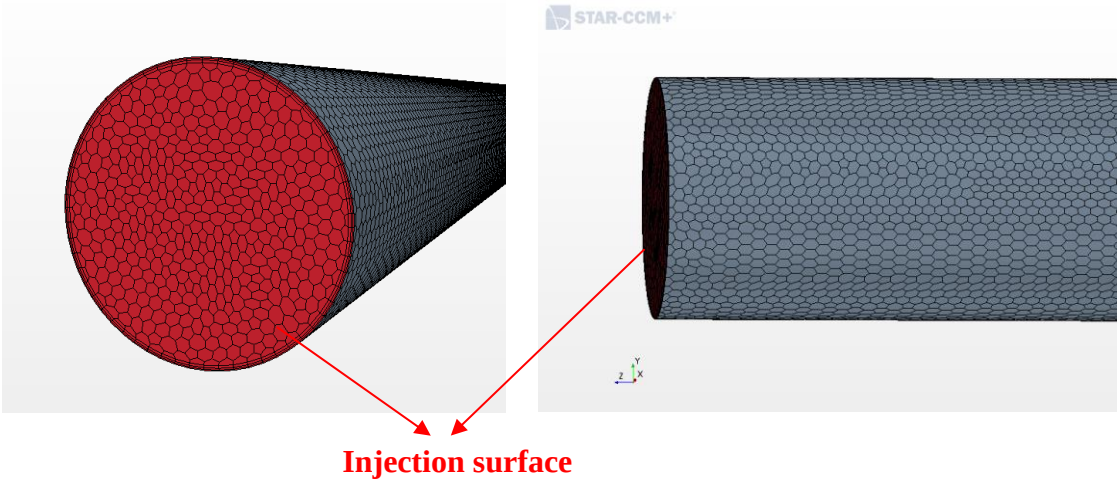

Figure 118. Computational mesh configuration involving nanoparticle injection at the inlet for multi-phase flow modeling and analyses

Table 39. Parameters used in nanoparticle injection at the inlet for multi-phase flow modeling and analyses

Parameter	Particle mass flow rate	Diameter	Particle injection velocity
Value	6.94×10^{-5} kg/s	100 nm	0.1 m/s

7.2.2 Particle distribution in laminar flow

Figure 119 shows the trajectory of the nanoparticles in the pipe for laminar flow at different time steps. The path line for the nanoparticles shows that the nanoparticles located in the vicinity of the center of the pipe tend to have lower values of local particle density (number of particles per unit volume) since the velocity of the fluid is higher at the center; while the nanoparticles located near the wall tend to have have higher values of local particle density since the flow near the boundary is significantly lower. The drastic difference in the value of the local particle density and the nanoparticles distribution in the

flowing system suggests that the material property of the nanofluids can vary anisotropically with significant variation in the thermos-physical property values from the center to the wall. Figure 120 shows the distribution of particles in the laminar pipe flow obtained from numerical simulations involving continuous injection of nanoparticles from the inlet. By zooming in the flow region near the wall and near the center-line in Figure 105, it can be seen that the local particle density in near-wall region is much higher than that of the region in the vicinity of the center of the pipe. Hence, local values of particle concentration vary significantly as a function of radial distance from the center in fully developed flow. Since the material properties of nanofluid is strongly sensitive to the nanoparticle concentration, the non-homogeneous and anisotropic distribution of nanoparticle concentration induced by the flow would cause substantial variation in the property of the nanofluid across the cross section of the pipe. Consequently, in order to faithfully portray the physics of the transport phenomena in flow loop experiments involving nanofluids - a non-homogeneous model should be implemented by coupling the local values of the material properties of the nanofluid to the local values of transport properties (such as velocity, mass fraction of nanoparticles, etc.) for the numerical simulations.

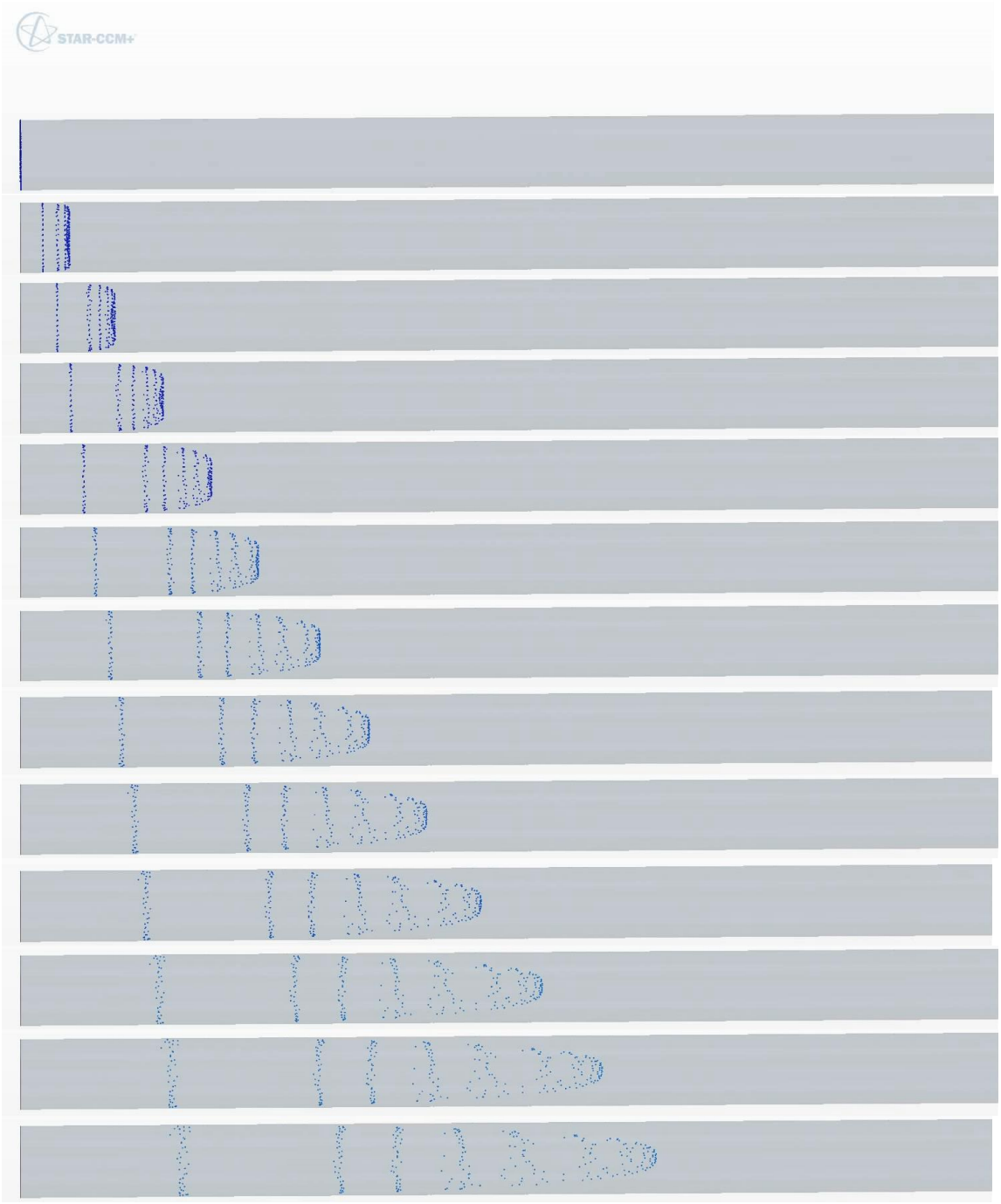

Figure 119. Numerical simulations showing the trajectory of nanoparticles for laminar flow in a pipe.

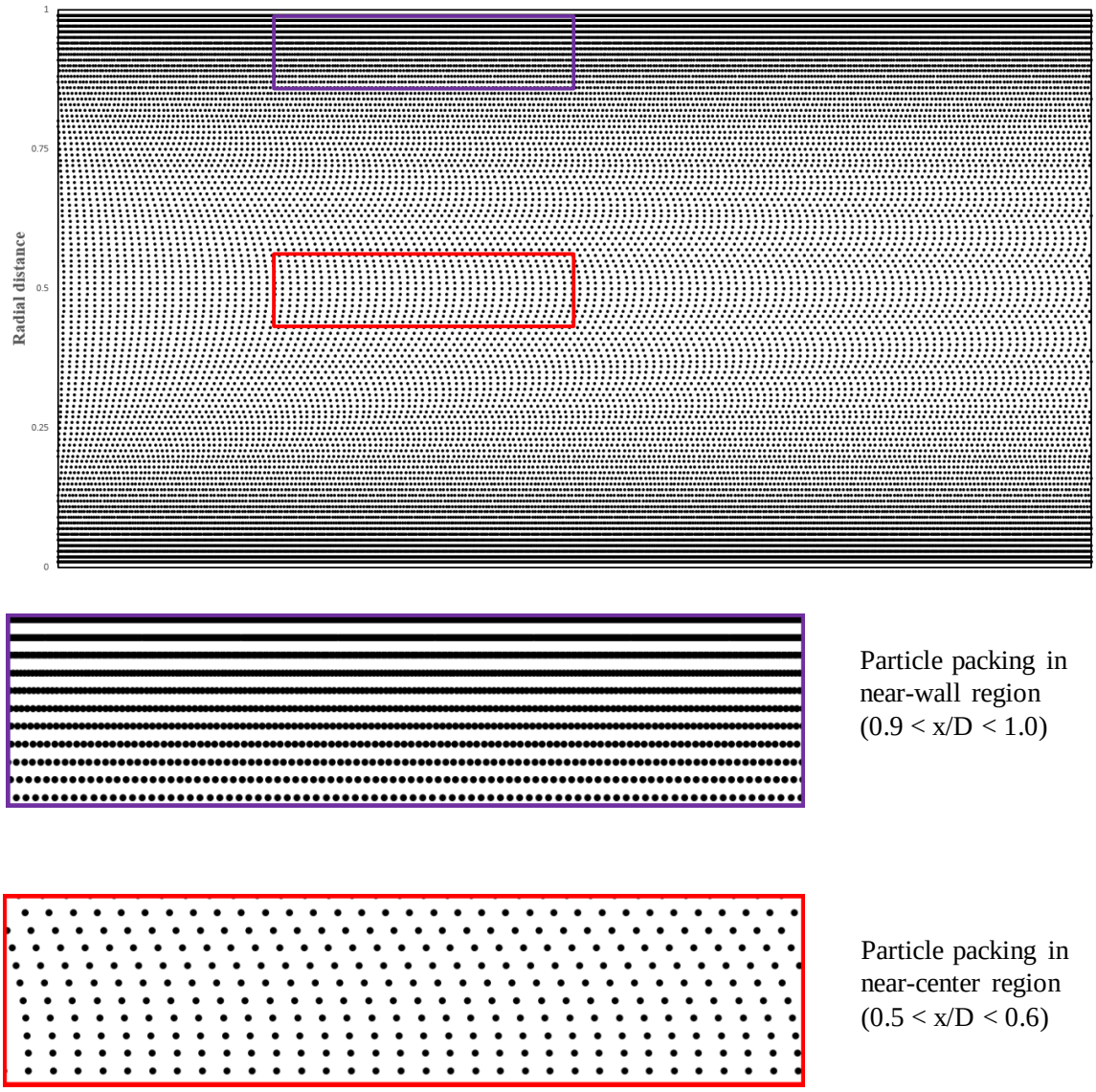

Figure 120. Numerical simulations showing the trajectory of nanoparticles an local values of particle density (number of particles per unit volume) for laminar flow in a pipe. (TOP) Global view of local particle density. (MIDDLE) Local particle density distribution in the vicinity of the wall. (BOTTOM) Local particle density distribution in the vicinity of the center.

7.2.3 Mathematical formulation for radial distribution of nanoparticles

The distribution of particle concentration along radial direction can be formulated if the velocity field of bulk flow is given. Considering a simple scenario of flow of nanofluids in a pipe at a mass fraction of 1.0% where the nanoparticles are injected at the inlet continuously with a uniform particle density, the local value of nanoparticle mass fraction can be derived under fully developed conditions. Assuming that mass fraction fo the nanoparticles is 1%, then the mass injection rate of nanoparticles per unit area (unit = kg $m^{-2}s^{-1}$) is given by

$$\dot{J}_p = \frac{0.01\dot{m}_f}{A} = \frac{0.01\rho_f A v_m}{A} = 0.01\rho_f v_m \tag{73}$$

where, $\dot{m}_f$, ρ_f, and v_m represent the mass flow rate, density and mean velocity of the solvent phase (base fluid). Now for sufficiently long pipe of length *L* starting from the flow entrance (such that fully developed flow conditions are achieved), the mass of nanoparticles confined in the concentric cylinder within radii of *r* and *r*+*dr* (with a toroid of area *dA*) is given by

$$m_p(r, L) = \dot{J}_p \cdot \mathrm{d}A \cdot \frac{L}{v(r)} \tag{74}$$

The mass of base fluid in this concentric cylinder region is given by

$$m_f(r, L) = \mathrm{d}V \cdot \rho_f = \mathrm{d}A \cdot L \cdot \rho_f \tag{75}$$

Hence the mass concentration of nanoparticles (M_p) within this differential toroidal region at radial location, *r*, is given by

$$M_p(r) = \frac{m_p(r, L)}{m_f(r, L)} = \frac{\dot{J}_p}{v(r)\rho_f} = \frac{0.01\rho_f v_m}{v(r)\rho_f} = 0.01\frac{v_m}{v(r)} \tag{76a}$$

Hence, for an average global mass fraction of the nanoparticles (x), the mass concentration of nanoparticles (M_p) within this differential toroidal region at radial location, r, is given by a more generalized formulation as:

$$M_p(r) = \frac{m_p(r,L)}{m_f(r,L)} = \frac{\dot{j}_p}{v(r)\rho_f} = \frac{0.01\rho_f v_m}{v(r)\rho_f} = x\frac{v_m}{v(r)} \tag{76b}$$

Equation 76 shows that the local values of particle density is inversely proportional to the local values of the velocity distribution in the flow field. For parabolic velocity profile in laminar pipe flow, the particle mass concentration in radial direction can be expressed as:

$$M_p(r) = \frac{2}{3}\frac{1}{1-\left(\frac{r}{R}\right)^2}\cdot M_{p,avg} \tag{77}$$

Figure 121 shows the plot of particle concentration as a function of radial distance from the center of the pipe, based on Equation 77. Towards the surface of the wall, the nanoparticle concentration approaches a large value (and the assumption used for developing this theoretical model based on very dilute concentration of the nanoparticles is not valid anymore near the wall due to the non-slip boundary condition), while the centerline concentration is ~67% of the average particle density. However, additional considerations need to be incorporated in this simplified model since the viscosity of the nanofluid increases with concentration (and often nanofluids display non-Newtonian rheology as the mass fraction of the nanoparticles exceed a threshold value) and the viscosity values can be anisotropic (i.e., the viscosity values can be a function of direction and location in the flow field). Hence, this implies that in reality the velocity profile and

concentration gradient of the nanoparticles would be significantly different from the parabolic profiles assumed in this theoretical model (that was derived based on the assumption of uniform and isotropic viscosity of the nanofluid). Hence, the appropriate model for predicting hydrodynamic and thermal behavior of nanofluid as well as the thermal-hydraulic performance of a chosen flow loop architecture should incorporate the anisotropic behavior of the material properties of the nanofluid (due to heterogeneous distribution of the nanoparticles in the flow field).

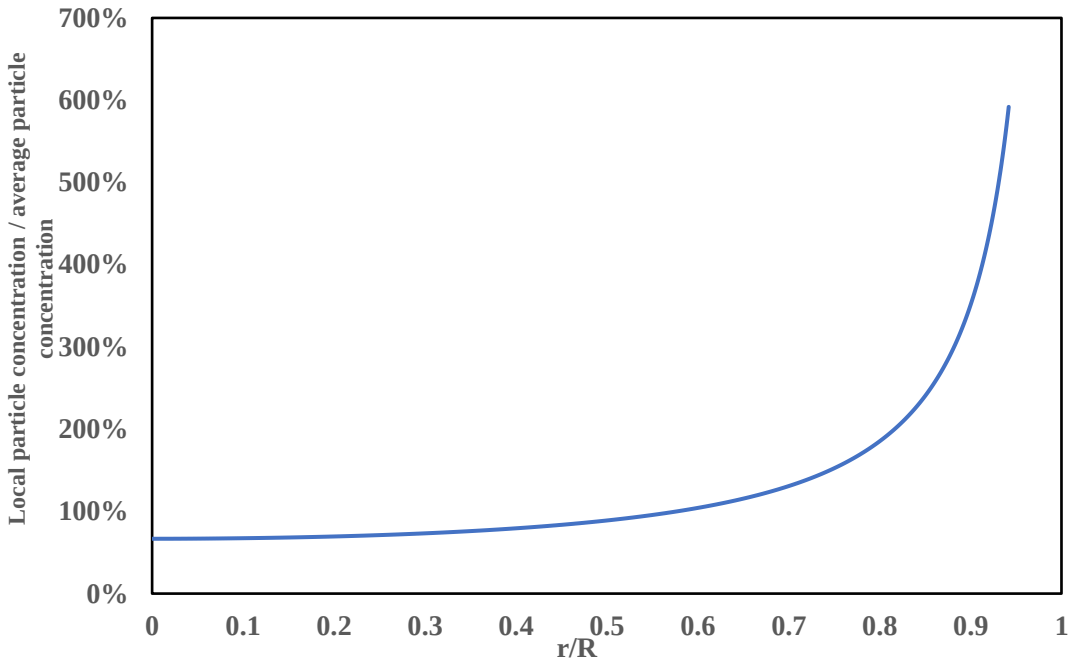

Figure 121. Plot of particle concentration ratio (local value to global value) as a function of radial distance from the center of the pipe, based on Equation 75

7.3 Summary

The heat transfer performance of molten salt nanofluids were investigated numerically using both single-phase and two-phase models. The result from single phase model suggested that molten salt nanofluids has superior convective heat transfer coefficient comparing to the pure molten salt with the drawback of higher friction loss. It is more advantageous to use molten salt nanofluids in heat transfer applications with high external heat flux input. The result from the two-phase model revealed that nanofluid is an inhomogeneous medium in flowing system. A proper and accurate model for nanofluid within the single-phase regime needs to take into consideration of the property variation with respect to geometric location in space.

8. NUMERICAL STUDY: PARTICLE GROWTH SIMULATION

The one-step synthesis protocol involving thermal decomposition of additives to yield nanoparticles in-situ is modeled in this study. This synthesis protocol does not yield monodispersed particles, but particles with certain size distributions. The size distribution of the nanoparticles can vary drastically depending on the additive (i.e., nanoparticle precursor) employed in the synthesis process. To better understand the mechanism of nanoparticle generation in molten salt and optimize the synthesis protocol for achieving a desired shape and size, the temporal evolution of the particle size distribution (PSD) was explored. This approach involved population balance simulation method that is based on the kinetics of the nucleation and growth of nanoparticles during different stages in the thermal-cycling synthesis process [137].

8.1 Mechanistic model of nanoparticle formation

Nanofluid synthesis using wet chemistry typically starts with the supersaturation of the particle ions in the base fluid. When mixed with additives, e.g., addition of NaOH into $Al(NO_3)_3$, or when there is decomposition of the dissolved components, the concentration of target ions quickly grows beyond the saturation level and bring a comparatively high degree of supersaturation. As a consequence, crystal nuclei are formed in the fluid. Considering the nucleation as the event where an ensemble of free ions in the fluid form a cluster leading to the formation of a small mono-crystal, the overall free energy change would comprise of two primary components: (1) the latent heat of solidification of liquid into solid; and (2) the excess surface energy resulting from the

formation of new surface. These competing terms determine the critical size of the initial nuclei from which further crystal growth and aggregation starts. Hence, this model predicts that if the cluster size is smaller than this critical size – the nucleated mono-crystal is not able to overcome the energy barrier and dissolves back into the liquid phase. The salient steps for the transport processes involved in the nucleation and growth of alumina nanoparticles from the aluminum nitrate additive are illustrated in the schematic of Figure 122.

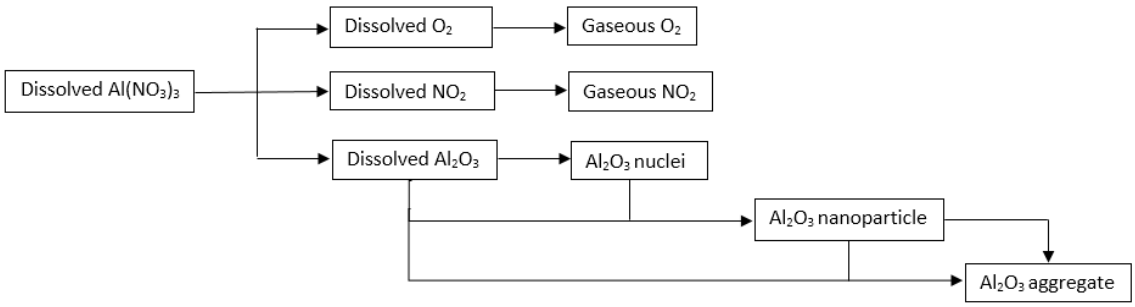

Figure 122. Kinetic process of Al_2O_3 nanoparticle generation from $Al(NO_3)_3$

In the following discussion, the chemical reactions and the reaction kinetics will be explored for each step identified in the schematic of Figure 122. Each step will be explored separately, which includes: thermal decomposition, supersaturation, nucleation, crystal growth and coagulation. Aluminum nitrate precursor will be used as an example for illustrating the process but the principle holds for other additives which serve as nanoparticle precursors.

8.1.1 Thermal decomposition

The thermal decomposition reaction of metal nitrate hydrate could be differentiated into two stages: (i) dehydration of the hydrated salt; and (ii) decomposition of the nitrate ions. This is illustrated in the reactions steps as follows:

$$2Al(NO_3)_3 \cdot 9H_2O \xrightarrow{\text{Heating}} 2Al(NO_3)_3 + 18H_2O \quad (78)$$

$$2Al(NO_3)_3 \xrightarrow{\text{Heating}} Al_2O_3 + 3NO_2 + 4.5O_2 \quad (79)$$

It should be noted that the formation of the Al_2O_3 molecules is only taking place in the final stages of the decomposition process. To properly analyze the formation rate of Al_2O_3 molecules in the synthesis reaction, the reaction kinetics can be represented by an n^{th} order equation:

$$\frac{d\alpha}{dt} = k_0(1-\alpha)^n \exp\left(-\frac{E}{RT}\right) \quad (80)$$

where, $\boldsymbol{\alpha}$ is the percentage of precursor reacted, $\boldsymbol{k_0}$ is the rate constant, $\boldsymbol{n}$ is the order of reaction, $\boldsymbol{E}$ is the activation energy, $\boldsymbol{R}$ is universal gas constant and $\boldsymbol{T}$ is the reaction temperature.

Equation 77 is used to characterize the decomposition step of the reaction. The decomposition kinetics of different metal nitrate hydrate precursors were measured experimentally by using thermogravimetric analysis (TGA) as shown in Figure 13. The decomposition curves were re-plotted with the de-hydrated nitrate salt as starting condition. Table 40 shows the parameters for decomposition kinetics of $Mg(NO_3)_2$ and $Al(NO_3)_3$ obtained by curve fitting of Equation 55 to the experimental data (Figure 13). In additions, Figure 123 and Figure 124 shows the comparison between experimental

measurements and the interpolation parameters obtained from curve fitting exercise employed in this study. The plots show that the curve fitting exercise matches the experimental data with negligible error.

Table 40. Interpolation parameters obtained from curve fitting exercise using Equation (55) for thermal decomposition of $Mg(NO_3)_2$ and $Al(NO_3)_3$.

Compound		Conversion range for regression fit (α)	k_0	n	$-E/R$
Initial	Final				
$MgNO_3$	MgO	0 - 0.15	0.043	2/3	-1500
		0.15 - 1.00	3.8×10^7	2/3	-15500
$Al(NO_3)_3$	Al_2O_3	0-0.61	0.052	5/8	-1
		0.61-1.00	0.016	5/8	-50

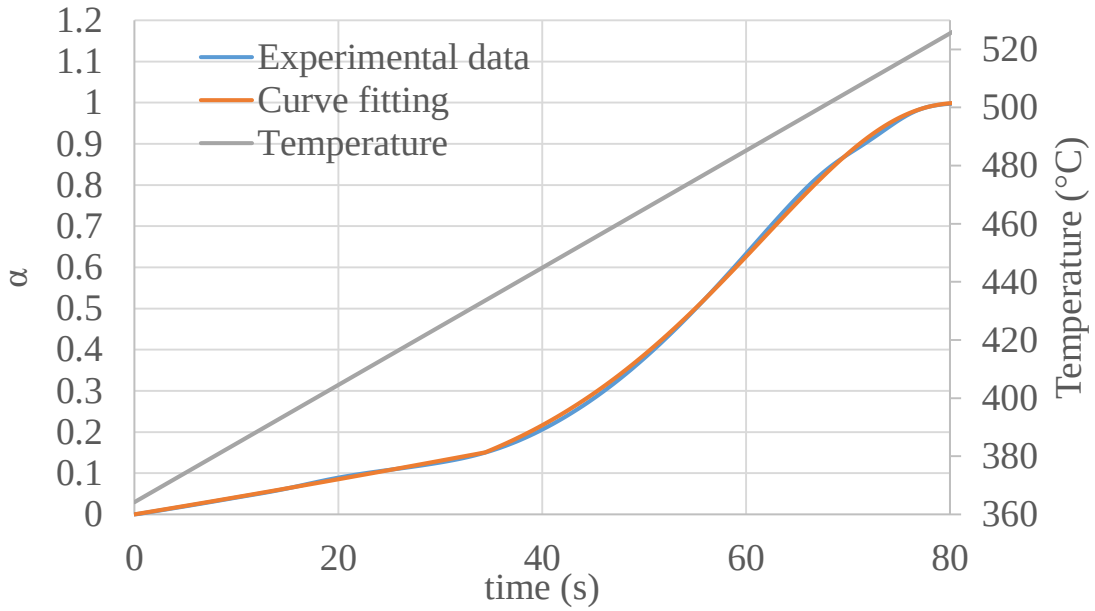

Figure 123. Comparison between experimental measurements and the interpolation parameters obtained from curve fitting exercise using Equation (80) for the thermal decomposition of $Mg(NO_3)_2$

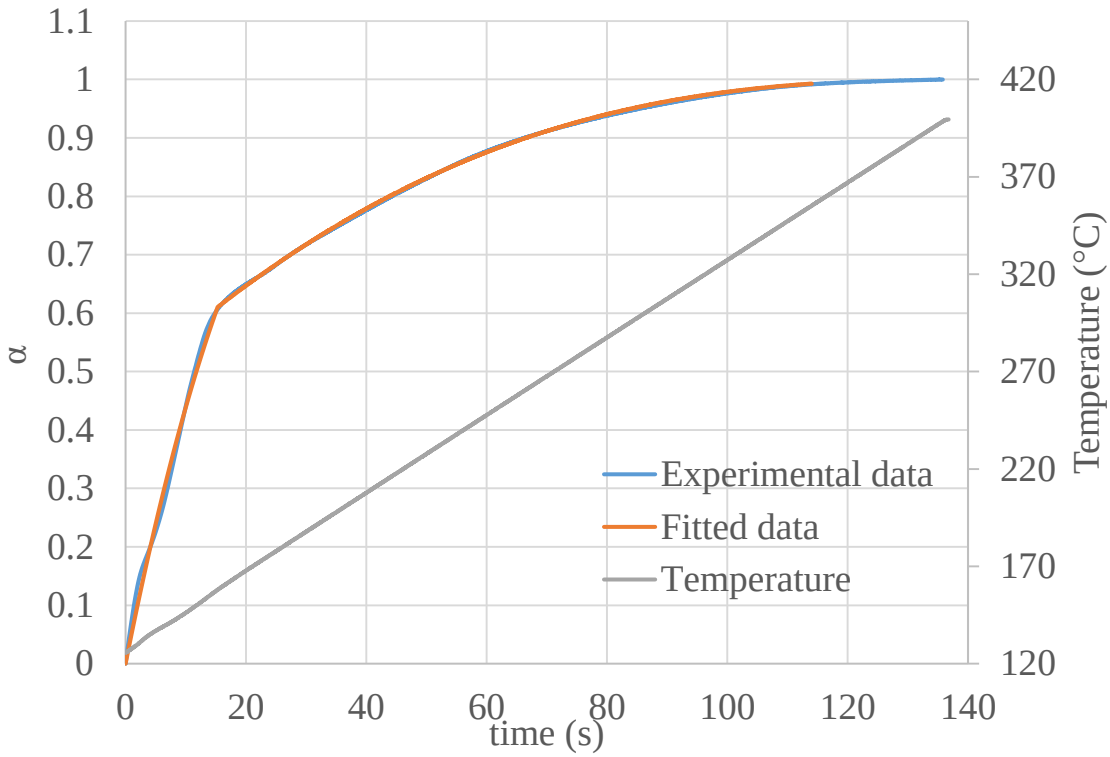

Figure 124. Comparison between experimental measurements and the interpolation parameters obtained from curve fitting exercise using Equation (80) for the thermal decomposition of $Al(NO_3)_3$

8.1.2 Nucleation

When the concentration of Al_2O_3 monomer exceeds the solubility limit in the liquid salt, the molecules will start to nucleate. This can modeled by accounting for the change in free energy of a single solid particle bounded by a solid/liquid interface at a constant temperature and pressure, as follows:

$$dG = \gamma dA + \mu dn \tag{81}$$

where, γ is the interfacial energy, A is interfacial area, μ is the bulk chemical potential and n is the number of moles of the substance. Assuming the particle is of spherical shape, the surface area, $A = 4\pi r^2$ and the volume, $V = (4/3)\pi r^3$, we have

$$\mathrm{dA} = 8\pi \mathrm{r dr} = \frac{2\mathrm{dV}}{\mathrm{r}} = \frac{2v_{\mathrm{m}}\mathrm{dn}}{\mathrm{r}} \tag{82}$$

where, v_{m} is the molar volume of the particle. Substituting Equation (82) into Equation (81) we get

$$\mathrm{dG} = \left(\frac{2\gamma v_{\mathrm{m}}}{r} + \mu\right)\mathrm{dn} \tag{83}$$

The chemical potential of a nanoparticle that nucleates is given by

$$\mu' = \frac{\partial \mathrm{G}}{\partial \mathrm{n}} = \frac{2\gamma v_{\mathrm{m}}}{r} + \mu \tag{84}$$

Hence, the change in chemical potential (due to nucleation of a single nanoparticle) is expressed as:

$$\mu' - \mu = \frac{2\gamma v_{\mathrm{m}}}{r} \tag{85}$$

While the chemical potential of the solvent and solute phases are expressed as:

$$\mu = \mu^{\circ} + k_B T \ln \mathrm{a} \tag{86}$$

$$\mu' = \mu^{\circ} + k_B T \ln \mathrm{a}' \tag{87}$$

where, *a* and *a'* are the aqueous phase activity of the solvent and solute phases. Hence these equations can be further simplified as follows:

$$\frac{2\gamma v_{\mathrm{m}}}{r} = \mu' - \mu = k_B T \ln\left(\frac{\mathrm{a}'}{\mathrm{a}}\right) = k_B T \ln\left(\frac{\mathrm{C}'}{\mathrm{C}}\right) \tag{88}$$

where, C' is the solute concentration associated with the nanoparticle which can be regarded as the supersaturation concentration at the surface of the nucleus, while C is the equilibrium saturation concentration of the solute in the bulk phase of the solvent. Hence,

the ratio of C'/C represents the supersaturation ratio of the solute on the surface of the nucleated nanoparticle to that in the bulk phase of the solution.

The nucleation event can be represented as a thermodynamic process in which some of the internal energy is liberated as latent heat during phase change (liquid phase is converted to solid phase) and some of the energy is utilized for creating a new surface (liquid-solid interface of the nucleated nanoparticle). Thus, the change in the total free energy change associated with nucleation event is represented as:

$$\Delta G_{\text{nucleation}} = \Delta G_{\text{volume}} + \Delta G_{\text{surface}} \tag{89}$$

where, $\Delta G_{\text{volume}} = 4/3 \cdot \pi r^3 \Delta G_{\text{v}}$ is a negative term and $\Delta G_{\text{surface}} = 4\pi r^2 \gamma$ is a positive term. Nucleation event occurs when the change in the internal energy (i.e., the Gibbs free energy) is minimized. This occurs when the derivative of the change in internal energy with respect to radius of the nucleated particle is zero. Hence, the derivation of the critical size of the nucleated nanoparticle is expressed as follows:

$$\frac{d\Delta G_{\text{nucleation}}}{dr} = 4\pi r^2 \Delta G_{\text{v}} + 8\pi r\gamma = 0 \tag{90}$$

which yields, the critical radius of the nucleated nanoparticle, r_{crit}, as:

$$r_{\text{crit}} = \frac{-2\gamma}{\Delta G_{\text{v}}} \tag{91}$$

By substituting Equation (91) into Equation (89) the critical value of the internal energy is obtained as:

$$\Delta G_{\text{crit}} = \frac{16\pi\gamma^3}{3(\Delta G_{\text{v}})^2} = 4\pi\gamma r_{\text{crit}}^2/3 \tag{92}$$

By substituting Equation (92) in Equation (88) the expression for the critical value of change in internal energy (ΔG_{crit}) is obtained as follows:

$$\Delta G_{crit} = \frac{16\pi\gamma^3 v_m^2}{3\left(k_B T \ln\left(\frac{C'}{C}\right)\right)^2} \tag{93}$$

Using Arrhenius type expression, the rate of nucleation ($f_{nucleation}$) is obtained as:

$$f_{nucleation} = V \cdot A \cdot \exp(-\Delta G_{crit}/k_B T) = V \cdot A \cdot \exp\left[-\frac{16\pi\gamma^3 v_m^2}{3{k_B}^3 T^3 \left(\ln\left(\frac{C'}{C}\right)\right)^2}\right] \tag{94}$$

The parameters needed for evaluating the kinetic of nucleation for MgO and Al_2O_3 using Equation (94) were culled from the literature and are listed in Table 41.

Table 41. Parameters for evaluating the kinetics of nucleation (Equation 94) [138] [139] [140]

Material	Parameters	Definition	Value	Unit
Common	k_B	Boltzmann constant	1.38×10^{-23}	J/K
MgO	γ	Interfacial free energy	0.52 [138]	J/m^2
	v_m	Molecular volume	1.869×10^{-29}	m^3/mole
	C	Solubility	3.54×10^{-7} [139]	mol/L
	A	Pre-exponential factor	1.0×10^{34} [140]	$m^{-3}s^{-1}$
Al_2O_3	γ	Interfacial free energy	0.5 [138]	J/m^2
	v_m	Molecular volume	4.352×10^{-29}	m^3/mole
	C	Solubility	3.54×10^{-7} [139]	mol/L
	A	Pre-exponential factor	1.0×10^{100} [140]	$m^{-3}s^{-1}$

8.1.3 Nanoparticle growth

The growth of nanoparticle after the nucleation stage in molten salt is modulated by two different transport processes: (i) diffusion of Al_2O_3 monomers from the bulk liquid to the surface of the nucleated nanoparticle; and (ii) adsorption of Al_2O_3 monomer on the nanoparticle surface. Since nanoparticles typically have a high density of surface defects the kinetics of the surface integration is very fast resulting in very fast reaction kinetics and very small-time constants for this transport process (compared to the kinetics of diffusion, which is typically associated with very slow reaction kinetics and very large time constants). Hence, it can be assumed that the adsorption reaction is an instantaneous process compared to the diffusion of Al_2O_3 monomer in the liquid. Since the adsorption reaction is a much faster process than the diffusion process, it is reasonable to assume a diffusion-controlled nanoparticle growth model in which the growth rate for the particle size can be characterized by the standard diffusion equation:

$$\frac{\mathrm{d}r_p}{\mathrm{d}t} = \frac{DvN_A}{r}(C_b - C_r) \tag{95}$$

where, D is the diffusion coefficient, v is the molecular volume of Al_2O_3, N_A is Avogadro's number, C_b is the bulk concentration of Al_2O_3 monomer in liquid salt and C_r is the concentration of Al_2O_3 monomer at particle surface. Since the surface adsorption reaction is instantaneous, the concentration of Al_2O_3 monomer at particle surface can be approximated to be the same value as the solubility of Al_2O_3 in the molten phase of pure solar salt. The parameters used in Equation 70 for calculating the diffusion controlled

growth of MgO and Al_2O_3 nanoparticles were culled from the literature and are listed in Table 42.

Material	Parameters	Definition	Value	Unit
Common	N_A	Avogadro's number	6.02×10^{23}	mol^{-1}
MgO	D	Diffusivity	1.56×10^{-9}	m^2/s
	v_m	Molecular volume	1.869×10^{-29}	m^3/mole
	C_r	Solubility	3.54×10^{-7} [139]	mol/L
Al_2O_3	D	Diffusivity	1.56×10^{-9}	J/m^2
	v_m	Molecular volume	4.352×10^{-29}	m^3/mole
	C_r	Solubility	3.54×10^{-7} [139]	mol/L

Table 42. Parameters for evaluating the growth rate of nucleated nanoparticles (Equation 93) [139]

8.1.4 Nanoparticle coagulation

In the agglomeration process, two small nanoparticles merge into a large particle by collision. The process of agglomeration (or coagulation) is usually associated with sintering and coalescence of the smaller particles occurs via Brownian motion of the solvent molecules and the intermolecular potential between the particles.

For each collision, two particles with volume v_i and v_j combine to form a new particle with volume $v_k = v_i + v_j$ (assuming incompressible materials). Denoting n_i as the number of particles with volume v_i, the evolution of particles due to agglomeration can be described by the Smoluchowski's equation [141]:

$$\frac{\mathrm{d}n_k}{\mathrm{d}t} = \frac{1}{2}\sum_{i+j=k}\beta(v_i, v_j)n_i n_j - n_k\sum_{i=1}^{\infty}\beta(v_i, v_k)n_i \tag{96}$$

where β is the Brownian collision frequency, and is expressed using the following equation:

$$\beta = \frac{2k_B T}{3\mu}\left(2 + \frac{r_i}{r_j} + \frac{r_j}{r_i}\right) \tag{97}$$

Hence, the agglomeration or coagulation frequency (f_{coa}) is expressed as:

$$f_{coa} = \frac{1}{V}\frac{k_B T}{3\mu}\left(2 + \frac{r_i}{r_j} + \frac{r_j}{r_i}\right)n_i n_j \tag{98}$$

Hence, Equation (98) can be used to estimate the growth rate of nanoparticles due to agglomeration (i.e., the number of coagulated nanoparticles formed per second).

8.2 Simulation methodology

The numerical simulations for predicting the nucleation and growth of nanoparticles from the liquid phase were performed by numerical integration and using very small time steps. The nanoparticle growth mechanism consists of four events: decomposition, nucleation, diffusion growth, and coagulation growth. All four events will occur simultaneously as soon as the reactions are initiated. Hence, a deterministic approach was used for monitoring the change in the particle size distribution, in which the number of particles that nucleated and agglomerated (or coagulated) were calculated for each time step using the expressions for nucleation rate and frequency of agglomeration (i.e., using Equations 89-96).

Two sets of simulations were performed where the simulations were started for an initial condition of 0.5 mole of $Mg(NO_3)_2{\cdot}6H_2O$ precursor in a1 liter container. A time

step of 10^{-4} s was used in the simulation after performing a thorough convergence test. The quantity (in moles) of precursor and monomer as well as the particle size distribution (the number of each particle for each size or diameter) were monitored, accounted for and updated after each iteration. The coagulation process is not considered in the first set of simulations but included in the second set of simulations. Initially the simulations are performed for a very short time interval to predict the rate of nucleation and growth of the nanoparticles. Figure 125 shows the flow-chart (numerical algorithm) that was employed for implementing the iteration procedure in each cycle for the second step in the simulations (i.e., for estimating the rate of agglomeration or coagulation).

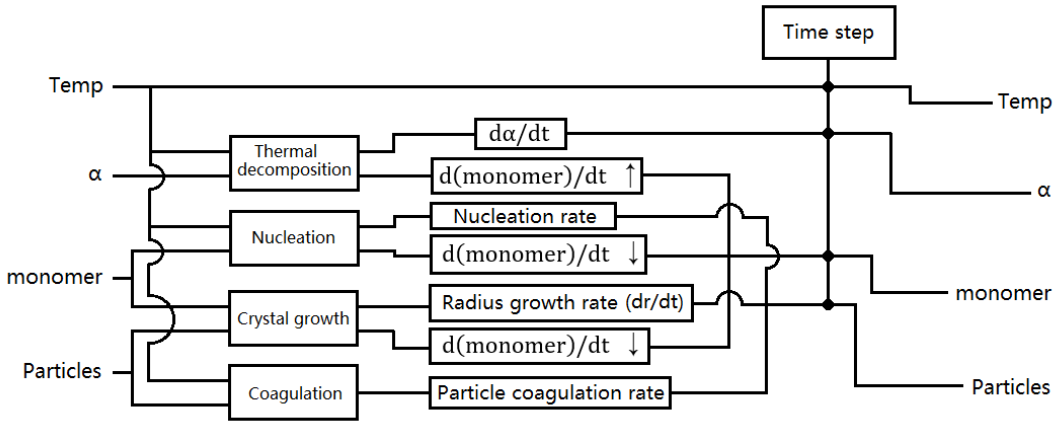

Figure 125. Flow-chart showing the numerical algorithm used for predicting the nucleation, growth and agglomeration of nanoparticles

To avoid the number of nanoparticles from reaching an intractably large value and to reduce the computational labor during the implementation of the numerical simulations, the value of the particle size and the associated number of nanoparticles are discretized with a resolution of 1.0×10^{-12} m after every 20000 iterations. In other words, particles with

size falling in the range of $n\times10^{-12}$ to $(n+1)\times10^{-12}$ were assigned the same diameter after every 20000 cycles. During the discretization process, the number of nanoparticles were monitored, accounted for and re-adjusted accordingly to ensure that the total volume and mass of the nanoparticles is conserved. Besides, few other approximation techniques were also used to reduce the computational labor for predicting the growth of the nanoparticles arising from agglomeration or coagulation. The numerical simulation of agglomeration process was computationally very expensive sine the coagulation process requires the calculation of reaction kinetics between any two pair of nanoparticles in the computational domain. This computational exercise can become intractable and inefficient when the number of nanoparticles nucleating in the system becomes too large.

8.2.1 Optimization of computational resources for agglomeration

To reduce the number, *m*, of nanoparticle couplings (combinations) needed for simulation of the agglomeration process, the assorted array of nanoparticles (p_1, p_2, p_3, …, p_m) of a given size or radius (r_1, r_2, r_3, …, r_m) and the associated number of nanoparticles (n_1, n_2, n_3, …, n_m) in the ensemble are re-classified into $\boldsymbol{k}$ new particle groups. The collections of nanoparticles are classified into groups that are 5% above and 5% below the nominal value of a given particle size (say, r_1). Hence, the number of nanoparticles are re-classified into the following size groups:

$$\left[\boldsymbol{r_1},\ \frac{\mathbf{1.05}}{\mathbf{0.95}}\boldsymbol{r_1}\right],\ \left[\frac{\mathbf{1.05}}{\mathbf{0.95}}\boldsymbol{r_1},\ \left(\frac{\mathbf{1.05}}{\mathbf{0.95}}\right)^{\mathbf{2}}\boldsymbol{r_1}\right],\ \left[\left(\frac{\mathbf{1.05}}{\mathbf{0.95}}\right)^{\mathbf{2}}\boldsymbol{r_1},\ \left(\frac{\mathbf{1.05}}{\mathbf{0.95}}\right)^{\mathbf{3}}\boldsymbol{r_1}\right],\ \boldsymbol{\ldots\ldots},\ \left[\left(\frac{\mathbf{1.05}}{\mathbf{0.95}}\right)^{\boldsymbol{k-1}}\boldsymbol{r_1},\ \left(\frac{\mathbf{1.05}}{\mathbf{0.95}}\right)^{\boldsymbol{k}}\boldsymbol{r_1}\right] \tag{99}$$

This exercise in reclassifying the nanoparticles by fixed values of size ranges enables a significant reduction in the computational labor – since the number of calculations needed are now reduced from ***m(m-1)/2*** $\frac{m(m-1)}{2}$ to $\frac{k(k-1)}{2}$ ***k(k-1)/2***. In the preliminary trials for implementing the numerical simulations, it was found that the typical value of *k* is usually less than 60 while the value of m could exceed 10^4 (this is not surprising, since at any instant in the numerical simulations - the maximum value of the radius of the nanoparticles is a hundred times larger than the minimum value). By implementing the re-classification (or re-discretization approach), the computational labor involving the number of mathematical calculations for numerically simulating the agglomeration process was reduced by a factor of 10^5.

For calculating the collision frequency during agglomeration, the error between the values calculated with and without re-classification (of the number density of the nanoparticles) was estimated using the Equation (77) and is plotted in Figure 126. The plot in Figure 126 shows that the maximum error is less than 10% when the ratio between r_1 and r_2 is maximized or minimized. This suggests that the error introduced by re-classification (sub-discretization) is moderate and is within acceptable range:

$$\boldsymbol{\varepsilon_{f_{coag}}} = \frac{\left(\mathbf{2} + \frac{\boldsymbol{r_1^{avg}}}{\boldsymbol{r_2^{avg}}} + \frac{\boldsymbol{r_2^{avg}}}{\boldsymbol{r_1^{avg}}}\right)}{\mathbf{2} + \frac{\boldsymbol{r_1}}{\boldsymbol{r_2}} + \frac{\boldsymbol{r_2}}{\boldsymbol{r_1}}} < \frac{\left(\mathbf{2} + \frac{\mathbf{0.95}\boldsymbol{r_1}}{\mathbf{1.05}\boldsymbol{r_2}} + \frac{\mathbf{1.05}\boldsymbol{r_2}}{\mathbf{0.95}\boldsymbol{r_1}}\right)}{\mathbf{2} + \frac{\boldsymbol{r_1}}{\boldsymbol{r_2}} + \frac{\boldsymbol{r_2}}{\boldsymbol{r_1}}} \in [\mathbf{90}\%, \mathbf{110}\%] \qquad (100)$$

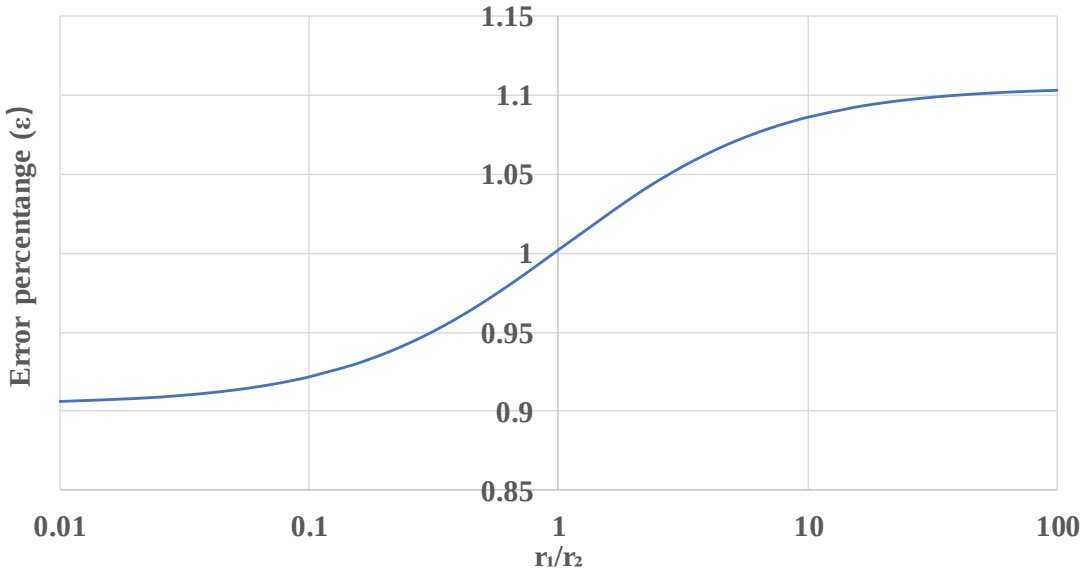

Figure 126. Error in calculating agglomeration frequency (due to reclassification of the size of the nanoparticles) as function of the ratio of maximum and minimum radius (r_1/r_2)

With the objective of accelerating the calculations for predicting the rate of agglomeration while ensuring the stability of the solutions for the governing equations – the time step was varied (and not fixed) as the coagulation of the nanoparticles were calculated in each time step. The values of the time step were selected based on the criteria that reduction in the number of nanoparticles due to agglomeration in numerical iteration was fixed to be less than 10%. This was implemented to enable better numerical accuracy and prevent numerical instability during the numerical simulations.

Hence, for a system initially starting with a total number of nanoparticles of value n_t, the reduction in the number of nanoparticles during agglomeration (due to coagulation) is approximated by the following expression:

$$\Delta \boldsymbol{n_t} = \frac{\boldsymbol{dn_t}}{\boldsymbol{dt}} \cdot \Delta \boldsymbol{t} \approx \frac{\boldsymbol{1}}{\boldsymbol{V}} \frac{\boldsymbol{k_B T}}{\boldsymbol{3\mu}} \cdot \boldsymbol{4n_t^2} \cdot \Delta \boldsymbol{t} \leq \boldsymbol{10\% n_t} \quad (101)$$

This can be simplified as follows:

$$\Delta \boldsymbol{t} \leq \frac{\boldsymbol{3\mu V}}{\boldsymbol{40 k_B T n_t}} \quad (102)$$

Hence, Equation (102) restricts the size of the time steps for ensuring numerical stability in the calculations performed in this study. Preliminary results from initial simulations performed in this study - revealed that the average time step used in calculating the agglomeration of nanoparticles is 0.03s (which is 30 times faster than the time steps used for calculating the nucleation and growth process for the nanoparticles). The numerical code (script) for simulating nanoparticle growth is provided for references in Appendix I.

8.3 Simulation results

Figure 127 shows the results obtained from the numerical simulations for the temporal evolution of the size distribution of MgO nanoparticles in the nanofluid sample using the one-step synthesis protocol from magnesium nitrate additive (i.e., without considering the coagulation process and agglomeration of the nanoparticles). The results show that by neglecting the kinetics of coagulation and agglomeration, the size distribution of the nanoparticles tend to be highly-monodispersed with very narrow range of values for the size of the nanoparticles that nucleate and grow at any instant of time. The average particle size increases as the reaction proceeds with time (as shown in Figure 128), but the size distribution of the particles become increasingly narrow. The final value for the average diameter of the nanoparticles saturates to 11 nm in less than 800 seconds.

Figure 129 shows the variation of supersaturation and nucleation rate during the particle formation process which is very typical of burst nucleation (BN) kinetics [142]. The supersaturation increases drastically in the first 2 seconds, during which large quantities of MgO monomers were released into the liquid via the thermal decomposition of the additive, magnesium nitrate (as a precursor of nanoparticles). At this stage, the monomer production rate is far exceeding the consumption rate, which in turn - promotes a high nucleation rate. With large numbers of nuclei generated within a short period, the monomer consumption rate increases rapidly due to the diffusion-controlled crystal growth kinetics. The continuous growth of the existing nanoparticles depletes the over-saturated monomers in the system which results in the rapid drop in the supersaturation and nucleation rate at longer time-scales (e.g., for time-scales exceeding 40 seconds).

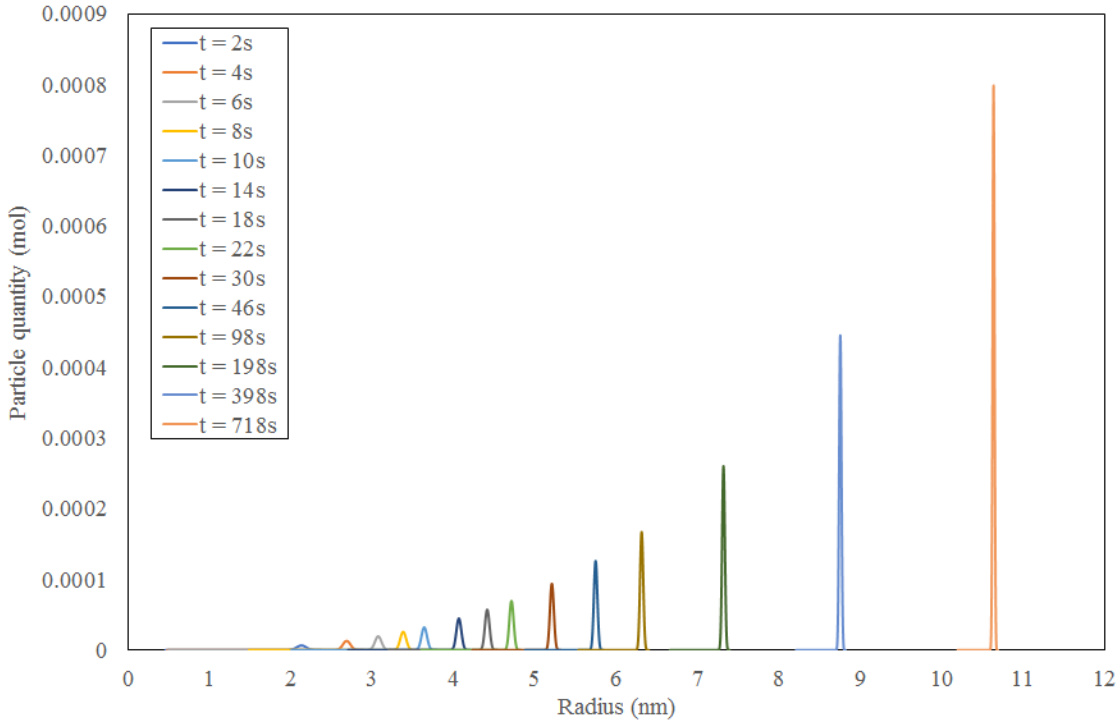

Figure 127. Temporal evolution of size distribution during nucleation and growth of nanoparticles (without coagulation and agglomeration)

After 5 seconds, the nucleation rate ceased (to almost zero), after which no new nuclei of nanoparticles were generated in the system. Consequently, the total number of nanoparticles remained constant during the remaining period for the numerical simulations. As a result, the acute variation in particle size distribution originating from the nucleation stage was gradually smoothened by the crystal growth process. Hence these simulations results can be categorized into two separate and distinct stages: (i) Burst nucleation stage for less than 5 seconds); and (ii) Stable crystal growth stage (from 5 ~ 720 seconds). This behavior favors the formation of monodispersed particles in the system with a narrow range and almost uniform distribution for nanoparticle size.

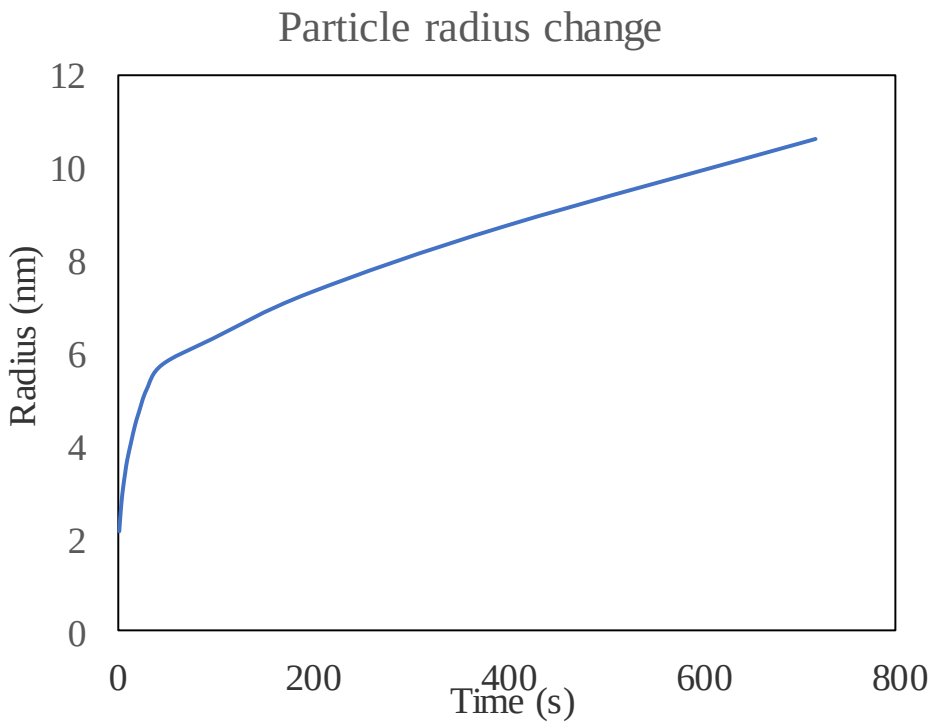

Figure 128. Temporal evolution of the value of average size of nanoparticles during nucleation and growth (without accounting for coagulation and agglomeration).

Figure 130 and Figure 131 show the particle size distribution changes drastically with time when numerical models are incorporated with the coagulation process (and nanoparticle agglomeration) in the numerical simulations. For shorter period of the simulation (e.g., at 0.2 and 0.4 second) Figure 130 shows the high concentration of small nanoparticles generated from the burst nucleation and the sizes are restricted to a very narrow range (less than 1 nm). These fine particles are quickly consumed by the high frequency of nanoparticle coagulation and agglomeration, which quickly shifts the peak values for nanoparticle diameter from 1 nm to 2.2 nm within 0.4 second. Once the average

number of nanoparticles drops below 10^{15} however, the coagulation frequency becomes significantly lower, with only a few large nanoparticles forming in the system.

The discontinuity in the peak values of nanoparticle diameter arises from the step-wise numerical integration used for computing the coagulation process. Nevertheless, the numerical results show that the size distribution has been altered significantly from the initial monodispersed distribution (at shorter periods of the simulation) to the polydispersed distribution when the coagulation mechanisms for nanoparticle agglomeration are incorporated in the numerical simulations. The polydispersity of nanoparticle size-distribution increases with time, as the gap between the minimum and maximum values of nanoparticle radius becomes larger as the decomposition reactions and transport processes proceed with time.

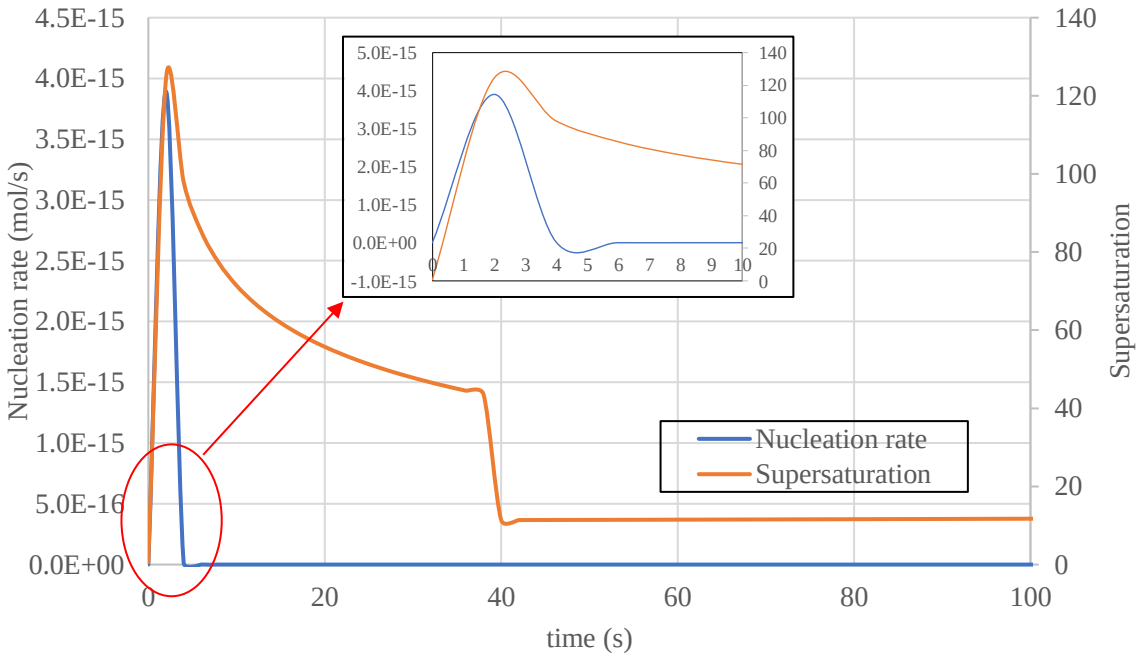

Figure 129. Plot for the temporal variation of supersaturation values and the rate of nucleation during the numerical simulations (i.e., without coagulation and agglomeration)

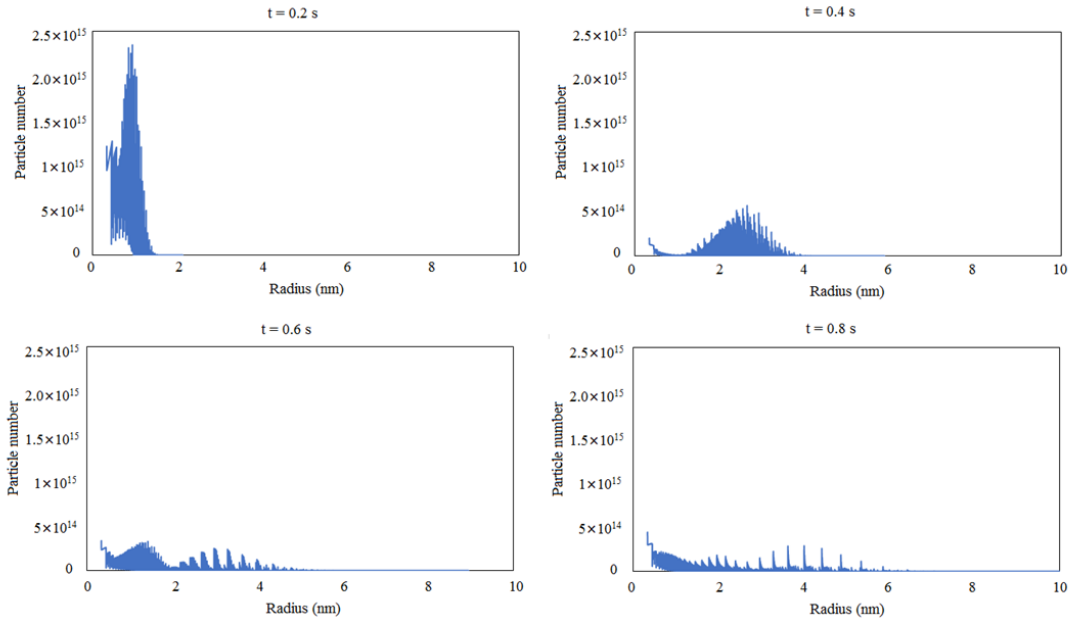

Figure 130. Change in the size distribution of nanoparticles within the first second (nanoparticle growth incudes particle coagulation and agglomeration)

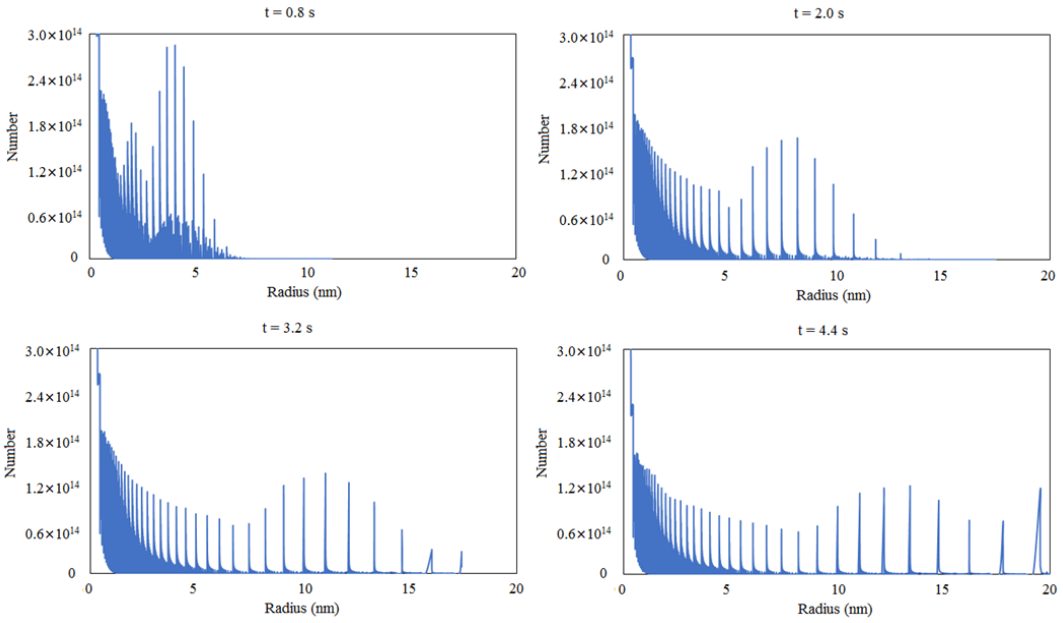

Figure 131. Change in the size distribution of nanoparticles within the first four seconds (nanoparticle growth includes particle coagulation and agglomeration)

Computational models were developed for predicting the temporal evolution of the size distribution of nanoparticles during one-step synthesis of nanofluids (from thermos-chemical decomposition reactions of additives which serve as precursors for nanoparticles). The computational models were developed by coupling the transport mechanisms involving reaction kinetics for thermal decomposition, nucleation, crystal growth and Brownian motion induced particle coagulation. The results from the numerical simulations show that initially burst nucleation of nanoparticles dominates the transport processes resulting in the formation of nanoparticles clusters of very small mono-dispersed sizes (fine nanoparticles) at very high concentrations. In later stages of the numerical simulation, the diffusion-controlled growth as well as coagulation of nanoparticles (and agglomeration) dominates the transport processes. This causes the size distribution to be polydispersed with larger nanoparticles that are substantially smaller in number.

Hence, it is crucial that the one-step synthesis protocols be implemented with the objective of minimizing the rate of particle coagulation in order to obtain nanofluids with uniform particle distribution as well as nanoparticles with significantly smaller size. Nanofluids containing smaller size nanoparticles can enable the formation of significant quantities of secondary nanostructures (i.e., percolation networks between adjacent nanoparticles that form from the “compressed phase” – which in turn nucleates from the solvent molecules adsorbed on the surface of the nanoparticles) and therefore enable enhancement in the thermo-physical properties of the molten salt samples.

9. CONCLUSION

9.1 Summary

Procurement of nanoparticles from commercial suppliers is an expensive proposition since nanoparticles can cost as much as $1000/ kg. Mixing solvents with nanoparticles (the conventional two-step synthesis protocol) is also an expensive and laborious task.

In contrast, cheap additives when heated at low temperatures - serve as precursors for nanoparticles that are synthesized in-situ (one-step synthesis protocol for nanoparticles and nanofluids). The additives can be derived from conventional materials such as soaps/ surfactants/ detergents and conventional salts (e.g., aluminum nitrate and magnesium nitrate - that cost less than $0.50/ kg when procured from commercial suppliers). The one-step synthesis protocol is amenable for rapid scale-up to industrial scale volume manufacturing of solar salt nanofluids. This enables a faster and cheaper manufacturing technique with narrower size distribution of the nanoparticles synthesized in-situ – thus enabling synthesis of nanofluids with better material properties (e.g., enhanced specific heat capacity and thermal conductivity as well as non-Newtonian rheology). The nanofluids obtained by the one-step synthesis protocol can increase the energy storage capacity (by 2×); power rating (by 1.5×); reduce corrosion/ fouling (by 2×); improve the operating life-time of power systems, thermal management platforms and heat exchangers (by 1.5×); cheaper raw material costs (by 1000×) as well as rapid scale-up and ease/ simplicity of manufacturing with reduced materials processing costs (2×); while improving lubrication (“smart grease” that is responsive to varying load conditions and

external stimuli). This manufacturing technique is also amenable for large-scale industrial deployment due to economies of scale (in contrast, the two-step synthesis protocol becomes more expensive at larger scales due to complications arising from environmental issues/ footprint and materials handling problems involving nanoparticles in large quantities). Since the one-step synthesis protocol used conventional and cheap materials (expensive and exotic nanoparticles are not required), therefore the environmental footprint and materials handling issues are obviated. In addition to generation of nanoparticles in-situ by heating from external thermal sources, by using stimuli responsive additives this technique is also amenable for alternate manufacturing techniques, such as nuclear radiation, electro-magnetic radiation (microwaves), ultra-sound, laser irradiation, electrical heating (immersion heaters), low temperature plasma sources, etc.

In this study, a novel technique was developed for one-step synthesis of molten salt nanofluids using salt additives (which serve as precursors for nanoparticles when heated). The solar salt nanofluid samples were observed to be very stable colloidal suspensions that remained unaffected several weeks after synthesis. Results from additional experiments performed using materials characterization techniques (such as scanning electron microscopy/ SEM and energy dispersive X-Ray Spectroscopy/ EDS), materials compatibility (corrosion) and chemical stability analyses show that nanoparticle precipitates can effectively reduce mass loss of stainless steel (SS316 samples) due to corrosion by 50% without significantly affecting the thermo-chemical stability of the molten salt. Thermo-physical properties of the solar salts, such as the specific heat capacity and thermal conductivity, were enhanced by 20~50% and 10~30%, respectively,

when mixed with nanoparticles (two-step synthesis protocol) or when mixed with additives that served as precursors for nanoparticles (one-step synthesis protocol).

The significant enhancement in the thermo-physical properties of nanofluids, such as specific heat capacity and thermal conductivity (compared to that of the pure molten salts) can enable their use as materials for thermal energy storage (TES) and as heat transfer fluids (HTF), respectively. Hence, the solar salt nanofluids developed in this study can enable the applications in large-scale industrial plants for generating Concentrated Solar Power (CSP). Alternate applications include TES for load balancing in conventional power generation (coal fired and gas fired power plants), nuclear power generation, geothermal power generation, etc. TES applications of these solar salt nanofluids (and allied molten salt nanofluids) include industrial process heating, desalination, etc. Other conventional and unconventional applications include molten salt batteries (for mart grids and grid-scale power distribution/ electrical energy storage), chemicals processing, metallurgical operations (refining of metals and alloys from ores), synthesis of ceramic micro/ nano-particles, life-sciences/ medical applications, enhanced oil recovery (EOR) from tar-sands as well as in conventional and unconventional oil fields (e.g., hydraulic fracturing for recovery of hydrocarbons trapped in shale rocks), etc.

This study also highlights the need for appropriate choice and control over the operating parameters for the one-step synthesis protocol as this is crucial for obtaining the desired secondary nanostructures that are formed by the solvent molecules – since these secondary nanostructures are induced during the formation of the nanoparticles in-situ. The formation of the secondary nanostructures is the dominant parameter for the

enhancement of the thermo-physical properties of the solar salt nanofluid samples. The thermo-physical properties (as well as the secondary nanostructures) were found to be sensitive to the selection of additive (precursor for nanoparticles), the concentration of the additive, synthesis temperature, synthesis time and, in certain cases, the use of dispersing agents (for preventing agglomeration of the nanoparticles formed in-situ). Inappropriate choice of the operating parameters in the one-step synthesis protocol can result in generation of micron-sized particles (probably due to rapid agglomeration and precipitation of the nanoparticles from the colloidal suspension, thus forming micro-particles), which in-turn, showed no enhancement in the thermophysical properties of the molten salt samples. The optimum synthesis condition, however, could produce highly stable nanofluid with interconnected networks (secondary nanostructures in solvent phase were observed to form percolation networks between adjacent nanoparticles in the samples). These experimental results, therefore, have significant implication for the development of Thermal Energy Storage (TES) materials in Concentrating Solar Power (CSP) plants and other industrial applications.

The hypothesis developed and proven in this study is that the dominant parameter controlling the enhancement in the specific heat capacity of the molten salt nanofluids is due to the formation of secondary nanostructures in the solvent phase of the samples that were experimentally characterized in this study. These network structures (percolation networks formed by the secondary nanostructures between adjacent nanoparticles) are inherently and extension of the compressed layer that are formed due to adsorption of the solvent molecules that adsorbed on the surface of the nanoparticles. Hence, the

combination of compressed phase and the secondary nanostructures (all composed of the solvent molecules at a different mass concentration than the bulk phase of the solvent) acts virtually as the third phase in the molten salt nanofluid system. The third phase has a different inter-molecular structure and therefore enhanced material properties compared to that of the bulk phase of the solvent.

Simple mathematical models developed in this study demonstrated that this third phase possesses higher effective specific heat capacity values (potentially due to reordering of the molecules on the surface of the nanoparticles). The third phase can thus have a semi-crystalline structure akin to that of the solid phase of the bulk solvent phase and this semi-solid third phase has a crystal structure that occurs in the vicinity of the melting point of the solvent material.

Using a simple mathematical model, it was shown that for a constant value and uniform size of the nanoparticles - the volume fraction of the third phase (i.e., these networks of secondary nanostructures forming the percolation network between adjacent nanoparticles) can first increase and then decline with increasing nanoparticle concentration. Such physical behavior implies an optimum value exists for nanoparticle concentration for maximizing the enhancement of the specific heat capacity of molten salt nanofluid samples.

A simple analytical model was also developed for predicting the total specific heat capacity of nanomaterials as a function of the mass concentration and diameter of nanoparticle which in turn affect the structure and morphology of the compressed layer (consisting of solvent molecules adsorbed on the surface of the nanoparticles). The

predictions from this analytical model for spherical nanoparticles showed that the enhancement of the specific heat capacity is strongly sensitive to the contribution from the compressed layer for nanoparticle diameters less than 10 nm (and ideally less than 6 nm). However, more comprehensive analysis is required for more in-depth study of the molecular structure and re-ordering of the solvent molecules that form the compressed layer. Additional insights into the structure and morphology of the compressed layer can help ascertain the true material property values of this third phase that is induced by the presence of the nanoparticles.

Computational Fluid Dynamics (CFD) models were used for performing thermal-hydraulic analyses of flow of nanofluids in a straight pipe of uniform cross-section. This exercise was performed with the objective of designing a flow loop test section for verifying the efficacy of solar salt nanofluids as heat transfer fluids (HTF). The predictions from the CFD simulations showed that the heat transfer coefficient of the ambient air (boundary condition) is a dominant parameter for modulating the total heat transfer from the test section. For higher values of the external heat transfer coefficient (boundary condition) the molten salt nanofluid can potentially enhance the total rate of heat transfer from the test section designed in this study. However, the higher pumping power (pump penalty) is a detriment due to the enhanced viscosity of the nanofluids. The results are derived using a homogeneous fluid model which underestimates the nature of the viscous forces arising from the anisotropic distribution of the nanoparticles near the wall of the pipe (compared to that of the central part of the pipe) during flow of nanofluid in the test section. Hence, an appropriate analysis for verifying the efficacy of molten salt nanofluids

as HTF would require the development of material property models (as a function of the anisotropic distribution of nanoparticles due to shear driven flows) for nanofluids subjected to forced convection.

As stated in the Introduction (Chapter 1), the practical applications of molten salt nanofluids (such as in CSP plants) is hindered by the prohibitive material cost arising from the use of costly raw materials (nanoparticles can cost as high as $1000/kg while the pure solar salt costs ~$0.40/kg). Although the enhanced specific heat capacity of molten salt nanofluids can greatly reduce the amount of materials used for TES, which further leads to reduction of the cost of power (electricity) produced – since the TES platform can contribute up to 40% of the total cost of power produced in a typical commercial CSP plant. However, the high cost of nanoparticles used in the two-step synthesis protocol is a big impediment for these industrial applications. In contrast, single-step synthesis protocol provides a cheap and novel approach that is simple, flexible, and amenable for scale-up to large volume industrial scale synthesis as well was ease of deployment of solar salt nanofluids. Table 43 shows the cost-comparison for raw materials used for the same molten salt nanofluid obtained by either two-step synthesis protocol or one-step synthesis protocol (based on contemporary market price of these raw materials procured from commercial sources). The values listed in Table 43 shows that the net cost of solar salt nanofluids is reduced by 5 times by the one-step synthesis protocol (compared to that of the conventional two-step synthesis protocol) and there is only a marginal increase in the cost when compared to that of the pure solar salt. In addition, Table 44 shows the cost of energy storage ($/kWh$_{thermal}$) of pure molten salt and molten salt nanofluid (produced by

both two-step and one-step method) based on the energy storage capacity and material costs. It was found that the energy cost is increased by 3~6 times when solar salt nanofluid produced by two-step synthesis protocol is used, while such cost is reduced by 20% when solar salt nanofluids produced by one-step synthesis protocol) is used.

Hence this study, combining both experimental measurements and computational modeling, has shown the efficacy and cost-effectiveness of the solar salt nanofluids synthesized using one-step synthesis protocol for augmenting the material properties (thermal conductivity and specific heat capacity), and enhancing the material compatibility with stainless steel (for corrosion), while the chemical stability of the solar salt samples is virtually unaffected. Computational models and analytical models further helped to elucidate the nature of the transport processes responsible for the observed anomalous enhancements in the material properties of the solar salt nanofluids as well as design and development of a molten salt flow loop apparatus for the testing the efficacy of the solar salt nanofluids for both thermal energy storage (TES) and as heat transfer fluids (HTF).

Table 43. Cost-comparison for raw materials used for manufacturing solar salt nanofluids (between the pure solar salt as well as nanofluids produced using the two-step synthesis protocol and one-step synthesis protocol)

	Salt (Market)				Nano-powder (US Nano Inc.)	
Material	$NaNO_3$	KNO_3	$Al(NO_3)_3{\cdot}9H_2O$	$Mg(NO_3)_2{\cdot}6H_2O$	Al_2O_3 nanoparticle	MgO nanoparticle
Cost (/kg)	$0.4	$0.4	$0.5	$0.3	185	212

			Two-Step Synthesis Protocol		One-Step Synthesis Protocol	
Molten salt nanofluid samples		**Cost of Pure Solar Salt**	**Nanoparticle mass needed**	**Nanoparticle cost (adding Al_2O_3)**	**Precursor mass needed**	**Precursor cost (adding $Al(NO_3)_3{\cdot}9H_2O$)**
1 kg molten salt +	**0.5% Al_2O_3**	**$0.4/kg**	**5g Al_2O_3**	**$0.90**	**36.8 g $Al(NO_3)_3{\cdot}9H_2O$**	**$0.018**
	1.0% Al_2O_3		**10g Al_2O_3**	**$1.80**	**73.60 g $Al(NO_3)_3{\cdot}9H_2O$**	**$0.037**
	1.5% Al_2O_3		**15g Al_2O_3**	**$2.70**	**110.30 g $Al(NO_3)_3{\cdot}9H_2O$**	**$0.055**
	1.0% MgO		**10g MgO**	**$2.12**	**63.6 g $Mg(NO_3)_2{\cdot}6H_2O$**	**$0.019**

			Two-Step Synthesis Protocol		One-Step Synthesis Protocol	
Molten salt nanofluid samples		**Cost of Pure Solar Salt**	**Total Cost [$/kg]**	**Cost Increase [%] over pure solar salt [%] over one-step synthesis protocol**	**Total Cost [$/kg]**	**Cost Increase [%] over pure solar salt**
1 kg molten salt +	**0.5% Al_2O_3**	**0.4**	**$1.30**	**225% 210%**	$0.42	5%
	1.0% Al_2O_3		**$2.20**	**450% 400%**	$0.44	10%
	1.5% Al_2O_3		**$3.10**	**675% 574%**	$0.46	15%
	1.0% MgO		**$2.52**	**630% 600%**	$0.42	5%

Table 44. Comparison of energy storage cost for raw materials used for manufacturing solar salt nanofluids (between the pure solar salt as well as nanofluids produced using the two-step synthesis protocol and one-step synthesis protocol). The storage capacity was calculated based on total sensible heat change between 300°C and 550°C

Salt system		Specific heat capacity (kJ/kg-K)	Density (kg/m^3)	Cost ($ / kg)	Energy storage capacity (kW·hr/kg)	Energy storage material cost ($/kW·hr)
Base salt	Solar salt ($NaNO_3$-KNO_3)	1.49	2020	0.40	0.103	3.9
Nanofluid (two-step)	Solar salt + 0.5% Al_2O_3	1.75	2025	1.30	0.122	10.7
	Solar salt + 1.0% Al_2O_3	2.07	2030	2.20	0.144	15.3
	Solar salt + 1.5% Al_2O_3	1.96	2035	3.10	0.136	22.8
	Solar salt + 1.0% MgO	1.95	2029	2.52	0.135	18.6
Nanofluid (one-step)	Solar salt + 0.5% Al_2O_3	1.75	2025	0.42	0.122	3.5
	Solar salt + 1.0% Al_2O_3	2.07	2030	0.44	0.144	3.1
	Solar salt + 1.5% Al_2O_3	1.96	2035	0.46	0.136	3.4
	Solar salt + 1.0% MgO	1.95	2029	0.42	0.135	3.1

9.2 Future direction

One of the goals of this study is to enable the industrial applications of molten salt nanofluids. Hence, a natural extension of this study would be to prove the feasibility of utilizing one-step synthesis protocol for in-situ synthesis of nanofluids from additives in commercial CSP plants. Such validation will require a wider exploration for developing a

library of additive materials as precursors for nanoparticles. This library will enable the appropriate choice of additives to be used as potential candidate for synthesizing nanoparticles in molten salt system, or even with different synthesis approaches. For example, use of microwave-assisted-reaction could provide an alternative technique for generating nanoparticle in-situ with much lower energy consumption (and hence a faster return on investment for recouping the energy back that was invested in producing the nanofluids). Furthermore, due to the time limitations in performing this study, the molten salt nanofluid has not been tested experimentally flow loop system (though it was designed, assembled and tested). The predictions from the CFD have shown the efficacy of the molten salt nanofluids for enhancing the rate of heat transfer in a flow loop. However, the thermal-hydraulic performance of the nanofluids is still an open question since the rheological behavior of the solar salt nanofluids are unknown, especialy with respect to preferential segregation of the nanoparticles in the flow field in response to shear driven flows (or pressure driven flows). Hence, experimental validation is needed for the numerical predictions obtained in this study involving the thermal conductivity values, specific heat capacity values, viscosity values (local and global) as well as the net rate of heat transfer and pressure drops for forced convection of molten salt nanofluids at elevated temperatures in a flow loop. The numerical models need to be formulated in a more sophisticated fashion by coupling the local values of the mass fraction of the nanoparticles to the thermo-fluidic property values which in-turn will affect the profiles for velocity and temperature in the flow field (and as a result the local values of the mass fraction of the nanoparticles will also change in the flow field). Finally, the characterization of corrosivity

and thermal stability of molten salt nanofluid needs to be performed for much longer time scale and using other materials (such as cast iron, hastalloy, stainless steel of differnet compositions, etc.) in order to evaluate their applicability in practical applications, such as CSP plants. The reduced rates f corrosion afforded by the solar salt nanofluids can perhaps enable the use of other cheaper alloys which are currently unsuitable in molten salt environments.

From the fundamental scientific perspective, there are still many unknowns that need to be resolved in order to elucidate the transport mechanisms that are responsible for the anomalous enhancement of specific heat capacity and thermal conductivity of molten salt nanofluid samples. One critical issue is the knowledge of how the ions are arranged/packed in the secondary nanostructures (compressed phase as well as the percolation network), their nucleation, growth and assembly. The structure-property relationships for these secondary nanostructures need to be modeled and validated experimentally. Studies in the literature have alluded to the "ordering behavior" of room temperature ionic liquids in the vicinity of a charged surface. However, similar studies involving both experimental and numerical approaches, for high temperature molten salt (> 500°C) is still desired. Sophisticated instrumentation that operate at these high temperatures need to be developed in order to develop enhanced cognition of the transport processes involved in the molten salt nanofluid samples.

REFERENCES

[1] "Key World Energy Statistics," The International Energy Agency, 2015.

[2] T. R. Karl, "Global climate change impacts in the United States," Cambridge University Press, 2009.

[3] T. Qi, X. Zhang and V. J. Karplus, "The energy and CO2 emissions impact of renewable energy developement in China," *Energy Policy,* vol. 68, pp. 60-69, 2014.

[4] M. Höök, R. Hirsch and K. Aleklett, "Giant oil field decline rates and their influence on world oil production," *Energy Policy,* vol. 37, no. 6, pp. 2262-2272, 2009.

[5] S. Sorrell, J. Speirs, R. Bentley, R. Miller and E. Thompson, "Shaping the global oil peak: A review of the evidence on field sizes, reserve growth, decline rates and depletion rates," *Energy,* vol. 37, no. 1, pp. 709-724, 2012.

[6] A. Sayigh, "Preface," in *Comprehensive Renewable Energy*, Elsevier Ltd., 2012, pp. xx-xxii.

[7] W. F. Deal, "Wind Power: An Emerging Energy Resource," *Technology and Engineering Teacher,* vol. 70, no. 1, pp. 9-15, 2010.

[8] D. Y. Leung and Y. Yang, "Wind energy development and its environmental impact: A review," *Renewable and Sustainable Energy Reviews,* vol. 16, no. 1, pp. 1031-1039, 2012.

[9] D. M. Rosenberg, R. A. Bodaly and P. J. Usher, "Environmental and social impacts of large scale hydroelectric development: who is listening?," *Global Environmental Change,* vol. 5, no. 2, pp. 127-148, 1995.

[10] O. Z. Sharaf and M. F. Orhan, "An overview of fuel cell technology: Fundamentals and applications," *Renewable and Sustainable Energy Reviews,* vol. 32, pp. 810-853, 2014.

[11] S. V. Vassilev, D. Baxter, L. K. Anderson and C. G. Vassileva, "An overview of the composition and application of biomass ash. Part 2. Potential utilisation, technological and ecological advantages and challenges," *Fuel,* vol. 105, pp. 19-39, 2013.

[12] J. H. Seinfeld and S. N. Pandis, "2.7.7 Biomass Burning," in *Atmospheric Chemistry and Physics: From Air Pollution to Climate Change, 3rd Edition*, John Wiley & Sons., 2016, p. 53.

[13] H. N. Pollack, S. J. Hurter and J. R. Johnson, "Heat flow from the Earth's interior: analysis of the global data set," *Reviews of Geophysics,* vol. 31, no. 3, pp. 267-280, 1993.

[14] I. B. Fridleifsson, R. Bertani, E. Huenges, J. W. Lund, A. Ragnarsson and L. Rybach, "The possible role and contribution of geothermal energy to the mitigation

of climate change.," in *IPCC scoping meeting on renewable energy sources proceedings*, Luebeck, Germany, 2008.

[15] C. Richter, S. Teske and R. Short, "Global Concentrating Solar Power Outlook 09," in *Greenpeace International Solar Paces and ESTELAA*, Amsterdam, Netherlands, 2009.

[16] J. Tsao, N. Lewis and G. Crabtree, *Solar FAQs*, US department of Energy, 2006.

[17] Y. Chu, "Review and comparison of different solar energy technologies," Global Energy Network Institute (GENI), San Diego, CA, 2011.

[18] W. Shockley and H. J. Queisser, "Detailed Balance Limit of Efficiency of p-n Junction Solar Cells," *Journal of applied physics*, vol. 32, no. 3, pp. 510-519, 1961.

[19] V. Tiangco and E. Sison-Lebrilla, "Solar thermal parabolic trough electric power plants for electric utilitie in California," California Energy Commision. Public Interest Energy Research Program, California, 2005.

[20] J. E. Pacheco, S. K. Showalter and W. J. Kolb, "Development of a Molten-Salt Thermocline Thermal Storage System for Parabolic Trough Plants," *Journal of Solar Energy Engineering*, vol. 124, no. 2, pp. 153-159, 2002.

[21] A. Gil, M. Medrano, I. Martorell, A. La´zaro, P. Dolado, B. Zalba and L. F. Cabeza, "State of the art on high temperature thermal energy storage for power generation. Part 1—Concepts, materials and modellization," *Renewable & Sustainable Energy Review*, vol. 14, no. 1, pp. 31-55, 2010.

[22] C. Y. Zhao, W. Lu and T. Y, "Heat transfer enhancement for thermal energy storage using metal foams embedded within phase change materials (PCMs)," *Solar Energy*, vol. 84, no. 8, pp. 1402-1412, 2010.

[23] "Survey of thermal storage for parabolic trough power plants," NREL, 2000.

[24] M. Zhang and R. G. Reddy, "Evaluation of Ionic Liquids as Heat Transfer Materials in Thermal Storage Systems," in *Energy: Energy Materials*, Materials Park, 2007.

[25] D. Kearney, U. Herrmann, P. Nava, B. Kelly, R. Mahoney, P. J, R. Cable, N. Portrovitza, D. Blake and H. Price, "Assessment of a Molten Salt Heat Transfer Fluid in a Parablic Trough Solar Field," *Journal of Solar Energy Engineering*, vol. 125, no. 2, pp. 170-176, 2003.

[26] L. S. Fichter, "Binary Eutectic Phase Diagram," 29 9 2000. [Online]. Available: http://csmres.jmu.edu/geollab/Fichter/IgnRx/BinryEu.html. [Accessed 1 5 2015].

[27] G. J. Janz, C. B. Allen, N. P. Bansal, R. M. Murphy and R. P. T. Tomkins, " Physical properties data compilations relevant to energy storage. II. Molten salts: data on single and multi-component salt systems," Rensselaer Polytechnic Inst., Troy, NY, 1979.

[28] G. J. Janz and R. P. T. Tomkins, "Physical properties data compilations relevant to energy storage. IV. Molton salts: data on additional single and multi-component salt systems.," National Standad Reference Data System, 1981.

[29] R. W. Carling, C. M. Kramer, R. W. Bradshaw, D. A. Nissen, S. H. Goods and R. W. Mar, "Molten nitrate salt technology development status report," Sandial National Labs, Albuquerque, NM, 1981.

[30] K. Coscia, S. Neti, A. Oztekin, S. Nelle, S. Mohapatra and T. Elliott, "THE THERMOPHYSICAL PROPERTIES OF THE NaNO3-KNO3, LiNO3-NaNO3, AND LiNO3-KNO3 SYSTEMS," in *Proceedings of the ASME 2011 International Mechanical Engineering Congress & Exposition* , Denver, 2011.

[31] R. W. Bradshaw and N. P. Siegel, "Molten nitrate salt development for thermal energy storage in parabolic trough solar power systems," in *ASME 2009 3rd International Conference on Energy Sustainability collocated with the Heat Transfer and InterPACK09 Conferences*, Jacksonville, Florida, 2009.

[32] R. G. Reddy, "Novel Molten Salts Thermal Energy Storage for Concentrated Solar Power Generation," The University of Alabama, Tuscaloosa, 2013.

[33] E. S. Freeman, "The kinetics of the thermal decomposition of sodium nitrate and of the reaction between sodium nitrite and oxygen," *The Journal of Physical Chemistry,* vol. 60, no. 11, pp. 1487-1493, 1956.

[34] G. D. Sirotkin, "Equilibrium in melts of the nitrates and nitrites of sodium potassium," *Russian Journal of Inorganic Chemistry*, vol. 4, no. 11, pp. 1180-1184, 1959.

[35] B. D. Bond and P. W. Jacobs, "The Thermal Decomposition of Sodium Nitrate," *Journal of the Chemical Society A: Inorganic, Physical, TheoreticaL*, pp. 1265-1268, 1966.

[36] S. Yuvaraj, F.-Y. Lin, T.-H. Chang and C.-T. Yeh, "Thermal decomposition of metal nitrates in air and hydrogen environments," *The Journal of Physical Chemistry B,* vol. 107, no. 4, pp. 1044-1047, 2003.

[37] C. A. Sequeira, "Fundamentals of Molten Salt Corrosion," in *High temperature corrosion in Molten salts*, Zürich, Switzerland, Trans Tech Publications Ltc, 2003, pp. 3-4.

[38] I. B. Singh, "The influence of moisture on the oxidation rate of iron in NaNO 3 and KNO 3 melts," *Corrosion science,* vol. 37, no. 12, pp. 1981-1989, 1995.

[39] W. H. Smyrl, "Corrosion in molten salts used for solar thermal storage applications," *NASA STI/Recon Technical Report N,* vol. 79, p. 32683, 1978.

[40] I. B. Singh and U. Sen, "Influence of temperature and sulphate ion on corrosion of mild steel in molten NaNO3," *British Corrosion Journal*, vol. 27, pp. 299-304, 1992.

[41] A. G. E. Hosary, A. Baraka and A. I. Abdel-Rohman, "Effects of Halides on the Corrosion of Mild Steel in Molten NaNO3-KNO3 Eutectic," *British Corrosion Journal*, vol. 11, no. 4, pp. 228-230, 1976.

[42] A. G. E. Hosary, A. Baraka and A. I. Abdel-Rohman, "Corrosion of Mild Steel in Molten Sodium Nitrate–Potassium Nitrate Eutectic," *British Corrosion Journal*, vol. 11, no. 1, pp. 44-46, 1976.

[43] D. Banerjee and N. Singh, Nanofins: Science and Applications, Springer, 2014.

[44] C. N. R. Rao, A. Müller and A. K. Cheetham, The chemistry of nanomaterials: synthesis, properties and applications, Darmstadt, Hesse: John Wiley & Sons, 2006.

[45] H. Masuda, A. Ebata, K. Teramae and N. Hishinuma, "Alteration of Thermal Conductivity and Viscosity of Liquid by Dispersing Ultra-Fine Particles. Dispersion of Al2O3, SiO2 and TiO2 Ultra-Fine Particles," *Netsu Bussei,* vol. 7, no. 4, pp. 227-233, 1993.

[46] J. A. Eastman, U. S. Choi, S. Li, L. J. Thompson and S. Lee, "Enhanced Thermal Conductivity through the Development of Nanofluid," *Nanophase and Nanocomposite Materials II,* vol. 457, pp. 3-11, 2-5 December 1996.

[47] Y. Xuan and Q. Li, "Heat transfer enhancement of nanofluids," *International Journal of Heat and Fluid Flow,* vol. 21, no. 1, pp. 58-64, 2000.

[48] H. Xie, J. Wang, T. Xi, Y. Liu, F. Ai and Q. Wu, "Thermal conductivity enhancement of suspensions containing nanosized alumina particles," *Journal of Applied Physics,* vol. 91, no. 7, pp. 4568-4572, 2002.

[49] M. j. Assael, I. Metaxa, K. E. Kakosimos and D. Constantinou, "Thermal Conductivity of Nanofluids – Experimental and Theoretical," *International Journal of Thermophysics,* vol. 27, no. 4, pp. 999-1017, 2006.

[50] Z. H. Han, B. Yang, S. H. Kim and M. R. Zachariah, "Application of hybrid sphere/carbon nanotube particles in nanofluids," *Nanotechnology,* vol. 18, no. 10, 2007.

[51] S. Shaikh, K. Lafdi and R. Ponnappan, "Thermal conductivity improvement in carbon nanoparticle doped PAO oil:An experimental study," *Journal of Applied Physics,* vol. 101, no. 6, p. 064302, 2007.

[52] Y. Yang, E. A. Grulke, Z. Zhang and G. Wu, "Thermal and rheological properties of carbon nanotube-in-oil dispersions," *Journal of Applied Physics,* vol. 99, no. 11, p. 114307, 2006.

[53] Y. J. Kim, H. Ma and Q. Yu, "Plasma nanocoated carbon nanotubes for heat transfer nanofluids," *Nanotechnology,* vol. 21, no. 29, p. 295703, 2010.

[54] N. Jha and S. Ramaprabhu, "Thermal conductivity studies of metal dispersed multiwalled carbon nanotubes in water and ethylene glycol based nanofluids," *Journal of Applied Physics,* vol. 106, no. 8, p. 084317, 2009.

[55] M. Beck, Y. Yuan, P. Warrier and A. Teja, "The effect of particle size on the thermal conductivity of alumina nanofluids," *Journal of Nanoparticle Research,* vol. 11, no. 5, pp. 1129-1136, 2009.

[56] N. Shalkevich, W. Escher, T. Burgi, B. Michel, L. Si-Ahmed and D. Poulikakos, "On the Thermal Conductivity of Gold Nanoparticle Colloids," *Langmuir,* vol. 26, no. 2, pp. 663-670, 2009.

[57] P. D. Shima and J. Philip, "Tuning of Thermal Conductivity and Rheology of Nanofluids Using an External Stimulus," *The Journal of Physical Chemistry c* , vol. 115, no. 41, pp. 20097-20104, 2011.

[58] Y. He, Y. Jin, H. Chen, Y. Ding, D. Cang and H. Lu, "Heat transfer and flow behaviour of aqueous suspensions of TiO2 nanoparticles (nanofluids) flowing upward through a vertical pipe," *International Journal of Heat and Mass Transfer,* vol. 50, no. 11-12, pp. 2272-2281, 2007.

[59] T.-P. Teng, Y.-H. Hung, T.-C. Teng, H.-E. Mo and H.-G. Hsu, "The effect of alumina/water nanofluid particle size on thermal conductivity," *Applied Thermal Engineering,* vol. 30, no. 14-15, pp. 2213-2218, 2010.

[60] S. H. Kim, S. R. Choi and D. Kim, "Thermal Conductivity of Metal-Oxide Nanofluids: Particle Size Dependence and Effect of Laser Irradiatio," *Journal of Heat Transfer,* vol. 129, no. 3, pp. 298-307, 2006.

[61] J. K. Horrocks and E. McLaughlin, "Non-Steady-State Measurements of the Thermal Conductivities of Liquid Polyphenyls," in *Horrocks, J. K., and E. McLaughlin. "Non-steady-state measurements of the thermal conductivities of liquid polyphenyls." In Proceedings of the Royal Society of London A: Mathematical, Physical and Engineering Sciences,* London, 1963.

[62] S. Lee, S. Choi, S. Li and J. Eastman, "Measuring thermal conductivity of fluids containing oxide nanoparticles," *ASME J Heat Transf,* vol. 121, no. 2, pp. 280-288, 1999.

[63] X. Wang, X. Xu and S. U. S. Choi, "Thermal conductivity of nanoparticle–fluid mixture.," *Journal of thermophysics and heat transfer,* vol. 13, no. 4, pp. 474-480, 1999.

[64] H. Kurt and M. Kayfeci, "Prediction of thermal conductivity of ethylene glycol–water solutions by using artificial neural networks," *Applied energy,* vol. 86, no. 10, pp. 2244-2248, 2009.

[65] I. C. Nelson and D. Banerjee, "Flow Loop Experiments Using Polyalphaolefin Nanofluids," *Journal of Thermophysics and Heat Transfer,* vol. 23, no. 4, pp. 752-761, 2009.

[66] A. B. Kaul, Microelectronics to nanoelectronics : materials, devices & manufacturability, Boca Raton: CRC Pess, Taylor & Francis Group, 2013, p. 324.

[67] M. Chieruzzi, G. F. Cerritelli, A. Miliozzi and J. M. Kenny, "Effect of nanoparticles on heat capacity of nanofluids based on molten salts as PCM for thermal energy storage," *Nanoscale Research Letters,* vol. 8, no. 1, p. 448, 2013.

[68] D. Shin and D. Banerjee, "Specific heat of nanofluids synthesized by dispersing alumina nanoparticles in alkali salt eutectic," *International Journal of Heat and Mass Transfer,* vol. 74, pp. 210-214, 2014.

[69] P. Andreu-Cabedo, R. Mondragon, L. Hermandez, R. Martinez-Cuenca, L. Cabedo and J. E. Julia, "Increment of specific heat capacity of solar salt with SiO2 nanoparticles," *Nanoscale Research Letters,* vol. 9, p. 582, 2014.

[70] M. Schuller, Q. Shao and T. Lalk, "Experimental investigation of the specific heat of a nitrate–alumina nanofluid for solar thermal energy storage systems," *International Journal of Thermal Science,* vol. 91, pp. 142-145, 2015.

[71] S.-Q. Zhou and R. Ni, "Measurement of the specific heat capacity of water-based Al2O3 nanofluid," *Applied Physics Letters,* vol. 92, no. 9, p. 093123, 2008.

[72] R. S. Vajjha and D. K. Das, "Specific Heat Measurement of Three Nanofluids and Development of New Correlations," *Journal of Heat Transfer,* vol. 131, no. 7, p. 071601, 2008.

[73] L.-P. Zhou, B.-X. Wang, X.-F. Peng, X.-Z. Du and Y.-P. Yang, "On the specific heat capacity of CuO nanofluid," *Advances in mechanical engineering,* p. 172085, 2010.

[74] B. C. Pak and Y. I. Cho, "Hydrodynamic and heat transfer study of dispersed fluids with submicron metallic oxide particles," *Experimental Heat Transfer an International Journal ,* vol. 11, no. 2, pp. 151-170, 1998.

[75] E. D. Robertis, E. H. Cosme, R. S. Neves, A. Y. Kuznetsov, A. P. Campos, S. M. Landi and C. A. Achete, "Application of the modulated temperature differential scanning calorimetry technique for the determination of the specific heat of copper nanofluids," *Applied Thermal Engineering,* vol. 41, pp. 10-17, 2012.

[76] Y. Xuan and W. Roetzel, "Conceptions for heat transfer correlation of nanofluids," *International Journal of heat and Mass transfer,* vol. 19, no. 3701-3707, p. 43, 2000.

[77] D. Castro, C. Nieto, S. S. Murshed, M. J. V. Lourenço, F. J. V. Santos, M. L. M. Lopes and J. M. P. França, "Enhanced thermal conductivity and specific heat capacity of carbon nanotubes ionanofluids," *International Journal of Thermal Sciences,* vol. 62, pp. 34-39, 2012.

[78] D. Shin and D. Banerjee, "Enhanced specific heat of silica nanofluid," *Journal of heat transfer,* vol. 133, no. 2, p. 024501, 2011.

[79] Y. He, Y. Jin, C. Haisheng, Y. Ding, D. Cang and H. Lu, "Heat transfer and flow behaviour of aqueous suspensions of TiO2 nanoparticles (nanofluids) flowing upward through a vertical pipe," *International Journal of Heat and Mass Transfer,* vol. 50, no. 11-12, pp. 2272-2281, 2007.

[80] J. Yu, S.-W. Kang, S. Jeon and D. Banerjee, "Heat Transfer Measurements for Flow of Nanofluids in Microchannels using Temperature Nano-sensors," *Frontiers in Heat and Mass Transfer,* 2012.

[81] N. Singh and D. Banerjee, Nanofins: Science and Applications, SpringerBriefs in Thermal Engineering and Applied Science, 2013.

[82] H. Yang, "Experimental and Numerical Investigation of Pool Boiling Heat Transfer on Engineered Nano-Finned Surfaces," PhD dissertation, Texas A&M University, 2014.

[83] M. Gupta, N. Arora, R. Kumar, S. Kumar and N. Dilbaghi, "A comprehensive review of experimental investigations of forced convective heat transfer

characteristics for various nanofluids," *International Journal of Mechanical and Materials Engineering,* vol. 9, no. 11, 2014.

[84] D. Shin, "Molten Salt Nanomaterials for Thermal Energy Storage and Concentrated Solar Power Applications," PhD thesis, Texas A&M University, College Station, TX, 2011.

[85] B. Jo, "Numerical and Experimental Investigation of Organic Nanomaterials for Thermal Energy Storage and for Concentrating Solar Power Applications," PhD thesis, Texas A&M University, College Station, TX, 2012.

[86] S. Jung, "Numerical and Experimental Investigation of Inorganic Nanomaterials for Thermal Energy Storage (TES) and Concentrated Solar Power (CSP) Applications," PhD thesis, Texas A&M University, College Station, TX, 2012.

[87] L. C. Chen and C. C. Ho, "Submerged arc spray synthesis of TiO2 nanoparticles with desired form sphericity using process characterization and optimization," *Journal of Nanoscience and Nanotechnology,* vol. 8, no. 2, pp. 518-526, 2008.

[88] H. J. Kim, I. C. Bang and J. Onoe, "Characteristic stability of bare Au-water nanofluids fabricated by pulsed laser ablation in liquids," *Optics and Lasers in Engineering,* vol. 47, no. 5, pp. 532-538, 2009.

[89] A. Ghadimi, R. Saidur and H. S. Metselaar, "A review of nanofluid stability properties and characterization in stationary conditions," *International Journal of Heat and Mass Transfer,* vol. 54, no. 17-18, pp. 4051-4068, 2011.

[90] G. Paul, T. Pal and I. Manna, "Thermo-physical property measurement of nano-gold dispersed water based nanofluids prepared by chemical precipitation technique," *Journal of Colloid and Interface Science,* vol. 349, no. 1, pp. 434-437, 2010.

[91] A. S. Lanje, S. J. Sharma, R. B. Pode and R. S. Ningthoujam, "Synthesis and optical characterization of copper oxide nanoparticles," *Advances in Applied Science Research,* vol. 1, no. 2, pp. 36-50, 2010.

[92] M. L. Ramires, C. N. d. Castro, Y. Nagasaka, A. Nagashima, M. J. Assael and W. A. Wakeham, "Standard reference data for the thermal conductivity of water," *Journal of Physical and Chemical Reference Data,* vol. 24, no. 3, pp. 1377-1381, 1995.

[93] P. Gimenez and S. Fereres, "Effect of heating rates and composition on the thermal decomposition of nitrate based molten salts," *Energy Procedia,* vol. 69, pp. 654-662, 2015.

[94] A. P. Iyer, "The effect of silica nanoaprticles on corrosion of steel by molten carbonate eutectics," Doctoral dissertation, College Station, 2011.

[95] R. W. Bradshaw and S. H. Goods, "Corrosion of stainless steels and carbon steel by molten mixtures of commercial nitrate salts," *Journal of Materials Engineering and Performance,* vol. 13, no. 1, pp. 78-87, 2004.

[96] L. F. Cabeza, J. Illa, J. Roca, H. Mehling, S. Hiebler and F. Ziegler, "Immersion corrosion tests on metal-salt hydrate pairs used for latent heat storage in the 32 to

36°C temperature range," *Materials and Corrosion,* vol. 52, no. 2, pp. 140-146, 2001.

[97] A. C. G.-1. o. C. o. Metals, "Standard practice for preparing, cleaning, and evaluating corrosion test specimens," ASTM International, 2011.

[98] M. S. Sohal, P. Sabharwall, P. Calderoni, A. K. Wertsching, B. S. Grover and P. Sharpe, "Conceptual Design of Forced Convection Molten Salt Heat Transfer Testing Loop," Idaho National Laboratory, Idaho, 2010.

[99] Y. Iwadate, I. Okada and K. Kawamura, "Density and heat capacity of molten sodium nitrite-potassium nitrate mixtures," *Journal of Chemical and Engineering Data ,* vol. 27, no. 3, pp. 288-290, 1982.

[100] D. Shin, H. Tiznobaik and D. Banerjee, "Specific heat mechanism of molten salt nanofluids," *Applied Physics Letters,* vol. 104, no. 12, p. 121914, 2014.

[101] H. Tiznobaik, D. Banerjee and D. Shin, "Effect of formation of “long range” secondary dendritic nanostructures in molten salt nanofluids on the values of specific heat capacity," *International Journal of Heat and Mass Transfer,* vol. 91, pp. 342-346, 2015.

[102] J. Seo and D. Shin, "Size effect of nanoparticle on specific heat in a ternary nitrate (LiNO 3–NaNO 3–KNO 3) salt eutectic for thermal energy storage," *Applied Thermal Engineering,* vol. 102, pp. 144-148, 2016.

[103] N. R. Karthikeyan, J. Philip and B. Raj, "Effect of clustering on the thermal conductivity of nanofluids," *Materials Chemistry and Physics,* vol. 109, no. 1, pp. 50-55, 2008.

[104] J. Xu and B. Yu, "A new model for heat conduction of nanofluids based on fractal distributions of nanoparticles," *Journal of Physics D: Applied Physics,* vol. 39, no. 20, p. 4486, 2006.

[105] R. Prasher, P. Bhattacharya and P. E. Phelan, "Thermal Conductivity of Nanoscale Colloidal Solutions (Nanofluids)," *Physical review letters,* vol. 94, no. 2, p. 025901, 2005.

[106] K. K. Nanda, A. Maisels, F. E. Kruis, H. Fissan and S. Stappert, "Higher surface energy of free nanoparticles," *Physical review letters,* vol. 91, no. 10, p. 106102, 2003.

[107] Y. Yao, Y. Wei and S. Chen, "Size effect of the surface energy density of nanoparticles," *Surface Science,* vol. Size effect of the surface energy density of nanoparticles, no. 636, pp. 19-24, 2015.

[108] J. E. Lennard-Jones, "Cohesion," *Proceedings of the Physical Society,* vol. 43, no. 5, p. 461, 1931.

[109] S. Kameoka, Y. Ukisu and T. Miyadera, "Selective catalytic reduction of NOx with CH3OH, C2H5OH and C3H6 in the presence of O2 over Ag/Al2O3 catalyst: Role of surface nitrate species," *Physical Chemistry Chemical Physics,* vol. 2, no. 3, pp. 367-372, 2000.

[110] K. I. Hadjiivanov, "Identification of neutral and charged N x O y surface species by IR spectroscopy," *Catalysis Reviews,* vol. 42, no. 1-2, pp. 71-144, 2000.

[111] X. Zhang, H. He, H. Gao and Y. Yu, "Experimental and theoretical studies of surface nitrate species on Ag/Al2O3 using DRIFTS and DFT," *Spectrochimica Acta Part A: Molecular and Biomolecular Spectroscopy,* vol. 71, no. 4, pp. 1446-1451, 2008.

[112] R. Atkin, N. Borisenko, M. Drüschler, F. Endres, R. Hayes, B. Huber and B. Roling, "Structure and dynamics of the interfacial layer between ionic liquids and electrode materials," *Journal of Molecular Liquids,* vol. 192, pp. 44-54, 2014.

[113] X. Gong, A. Kozbial, F. Rose and L. Li, "Effect of π–π+ Stacking on the Layering of Ionic Liquids Confined to an Amorphous Carbon Surface," *ACS applied materials & interfaces,* vol. 7, no. 13, pp. 7078-7081, 2015.

[114] R. Hayes, G. G. Warr and R. Atkin, "Structure and Nanostructure in Ionic Liquids," *Chemical reviews,* vol. 115, no. 13, pp. 6357-6426, 2015.

[115] L. A. Jurado, H. Kim, A. Arcifa, A. Rossi, C. Leal, N. D. Spencer and R. M. Espinosa-Marzal, "Irreversible structural change of a dry ionic liquid under nanoconfinement," *Physical Chemistry Chemical Physics,* vol. 17, no. 20, pp. 13613-13624, 2015.

[116] R. S. Anaredy and S. K. Shaw, "Long-Range Ordering of Ionic Liquid Fluid Films," *Langmuir,* vol. 32, no. 20, pp. 5147-5154, 2016.

[117] V. M. Kuznetsov and V. I. Khromov, "Fractal Representation of the Debye Theory for Studying the Heat Capacity of Macro- and Nanostructures," *Technical Physics,* vol. 53, no. 11, pp. 1401-1406, 2008.

[118] C. Pang, J. W. Lee and Y. T. Kang, "Enhanced thermal conductivity of nanofluids by nanoconvection and percolation network," *Heat and Mass Transfer,* vol. 52, no. 3, pp. 511-520, 2016.

[119] J. C. Maxwell, A treatise on electricity and magnetism, Britain: Clarendon press, 1881.

[120] R. L. Hamilton and O. K. Crosser, "Thermal conductivity of heterogeneous two-component systems," *Industrial & Engineering chemistry fundamentals,* vol. 1, no. 3, pp. 187-191, 1962.

[121] T. B. Lewis and L. E. Nielsen, "Dynamic mechanical properties of particulate-filled composites," *Journal of Applied Polymer Science,* vol. 14, no. 6, pp. 1449-1471, 1970.

[122] S. Park, G. R. Choi, J. H. Kim, J. C. Lee and S.-J. Kim, "Dispersion effect of sodium hexametaphosphate on the photocatalytic efficiency of a solution-combusted ZnO nanopowder," *Journal of the Korean Physical Society,* vol. 61, no. 9, pp. 1400-1403, 2012.

[123] J. C. Mierzwa, V. Arieta, M. Verlage, J. Carvalho and C. D. Vecitis, "Effect of clay nanoparticles on the structure and performance of polyethersulfone ultrafiltration membranes," *Desalination,* vol. 314, no. 2, pp. 147-158, 2013.

[124] A. P. Iyer, "The Effect of Silica Nanoparticles on Corrosion of Steel by Molten Carbonate Eutectics," PhD dissertation, College Station, 2011.

[125] M. Mohapatra and S. Anand, "Synthesis and applications of nano-structured iron oxides/hydroxides–a review," *International Journal of Engineering,* vol. 2, no. 8, 2010.

[126] D. Wen and Y. Ding, "Experimental investigation into convective heat transfer of nanofluids at the entrance region under laminar flow conditions," *International Journal of Heat and Mass Transfer,* vol. 47, no. 24, pp. 5181-5188, 2004.

[127] Z. S. Heris, S. G. Etemad and N. M. Estahany, "Experimental investigation of oxide nanofluids laminar flow convective heat transfer," *International Communications in Heat and Mass Transfer,* vol. 33, no. 4, pp. 529-535, 2006.

[128] E. Ebrahimnia-Bajestan, M. . C. Moghadam, H. Niazmand, W. Daungthongsuk and S. Wongwises, "Experimental and numerical investigation of nanofluids heat transfer characteristics for application in solar heat exchangers," *International Journal of Heat and Mass Transfer,* vol. 92, pp. 1041-1052, 2016.

[129] M. Akbari, N. Galanis and A. Behzadmehr, "Comparative analysis of single and two-phase models for CFD studies of nanofluid heat transfer," *International Journal of Thermal Sciences,* vol. 50, no. 8, pp. 1343-1354, 2011.

[130] R. Lotfi, Y. Saboohi and A. M. Rashidi, "Numerical study of forced convective heat transfer of nanofluids: comparison of different approaches," *International Communications in Heat and Mass Transfer,* vol. 37, no. 1, pp. 74-78, 2010.

[131] M. H. Fard, M. N. Esfahany and M. R. Talaie, "Numerical study of convective heat transfer of nanofluids in a circular tube two-phase model versus single-phase model," *International Communications in Heat and Mass Transfer,* vol. 37, no. 1, pp. 91-97, 2010.

[132] J. Avsec and M. Oblak, "The calculation of thermal conductivity, viscosity and thermodynamic properties for nanofluids on the basis of statistical nanomechanics," *International Journal of Heat and Mass Transfer,* vol. 50, no. 21-22, pp. 4331-4341, 2007.

[133] R. Pal, "Modeling the Viscosity of Concentrated Nanoemulsions and Nanosuspensions," *Fluids,* vol. 1, no. 2, p. 11, 2016.

[134] F. Greifzu, C. Kratzsch, T. Forgber, F. Lindner and R. Schwarze, "Assessment of particle-tracking models for dispersed particle-laden flows implemented in OpenFOAM and ANSYS FLUENT," *Engineering Applications of Computational Fluid Mechanics,* vol. 10, no. 1, pp. 30-43, 2016.

[135] L. Verlet, "Computer" experiments" on classical fluids. I. Thermodynamical properties of Lennard-Jones molecules," *Physical review,* vol. 159, no. 1, p. 98, 1967.

[136] E. Fehlberg, "Low-order classical Runge-Kutta formulas with stepsize control and their application to some heat transfer problems," NASA Technical Report, 1969.

[137] T.-D. Nguyen, "From formation mechanisms to synthetic methods towards shape-controlled oxide nanoparticles," *Nanoscale,* vol. 5, no. 20, pp. 9455-9482, 2013.

[138] W. Xu, A. P. Horsfield, D. Wearing and P. D. Lee, "First-principles calculation of Mg/MgO interfacial free energies," *Journal of Alloys and Compounds,* vol. 650, pp. 228-238, 2015.

[139] M. Fredericks and R. B. Temple, "Solubility of metallic oxides and the free energy of solvation of oxide ion in molten alkali metal nitrates," *Inorganic Chemistry,* vol. 11, no. 5, pp. 968-970, 1972.

[140] A. Layek, G. Mishra, A. Sharma, M. Spasova, S. Dhar, A. Chowdhury and R. Bandyopadhyaya, "A Generalized Three-Stage Mechanism of ZnO Nanoparticle Formation in Homogeneous Liquid Medium," *The Journal of Physical Chemistry C,* vol. 116, no. 46, pp. 24757-24769, 2012.

[141] M. V. Smoluchowski, "Drei vortrage uber diffusion. Brownsche bewegung und koagulation von kolloidteilchen," *Z. Phys,* vol. 17, pp. 557-585, 1916.

[142] V. K. LaMer and R. H. Dinegar, "Theory, production and mechanism of formation of monodispersed hydrosols," *Journal of the American Chemical Society,* vol. 72, no. 11, pp. 4847-4854, 1950.

[143] I. Alloy Engineering Company, "Thermowell Material Service Guide," [Online]. Available: http://www.thermowells.com/secured%20pdf/Alloy%20Brief%20-%20Materials%20Service%20Guide.pdf. [Accessed 1 2 2015].

[144] O. Company, "Ultra-High Temperature Heating Tapes," [Online]. Available: http://www.omega.com/pptst/STH_SST_SWH.html. [Accessed 2015 1 5].

[145] S. A. Whitmore, W. T. Lindsey, R. E. Curry and G. B. Gilyard, "Experimental Characterization of the Effects of Pneumatic Tubing on Unsteady Pressure Measurements," NASA , 1990.

[146] I. Bajsić, J. Kutin and T. Žagar, "Response time of a pressure measurement system with a connecting tube," *Instrumentation Science and Technology,* vol. 35, no. 4, pp. 399-409, 2007.

APPENDIX A

Design and construction of flow loop system

Tubing, fitting and valve

There are several options for choosing materials that are suitable for constructing a flow loop apparatus with high operating temperatures that are compatible with molten salts. A detailed guide on material selection can be found from the brochure "Thermowell Materials Service Guide" [143]. The flow loop is designed to be constructed with 316 SS seamless tubing (1'' outer diameter or "OD", 0.12'' tubing thickness) which has an excellent corrosion resistance in oxidizing and reducing environments up to 900 °C. Two different test sections were designed in this study (composed of 316 Stainless Steel seamless tubing):

Design 1: Consisting of a test section with 0.5'' OD (outer diameter), 0.065'' tubing thickness.

Design 2: Consisting of a test section with 0.25'' OD, 0.0825'' tubing thickness.

The test section is joined with the remaining components of the flow loop using SS316 compression fittings adaptors (i.e., 90-degree/45-degree elbows, tee and reducers). These compression fittings are recommended for connecting tubes with relatively small diameters (1 inch) when the assembly is tightened and cleaned thoroughly. The use of compression fittings is easy and straightforward which does not require any additional machining or processing. However, it should be noted that under high temperature operating conditions, the thermal expansion may lead to formation of crevice near the

edges of the compression fittings which can cause leaking of molten salts. Hence high temperature sealant is required for appropriate sealing of the junctions in the flow loop.

According to the design shown in Figure A.1, the differential pressure transducer and the two mainstream thermocouples are used for measuring the properties of the bulk fluids during flow conditions at the inlet and outlet ports of the test sections. Hence, two four-way cross unions were used at these two locations for accommodating all the measurement ports of these devices. Figure below shows the cross union where the thermocouple is inserted through a small hole in a 0.5'' OD rod and the compression fitting at each of the two ends of the cross union. The insertion length of the thermocouple was adjusted such that the end of the measuring tip is located in the middle of the flowing fluid.

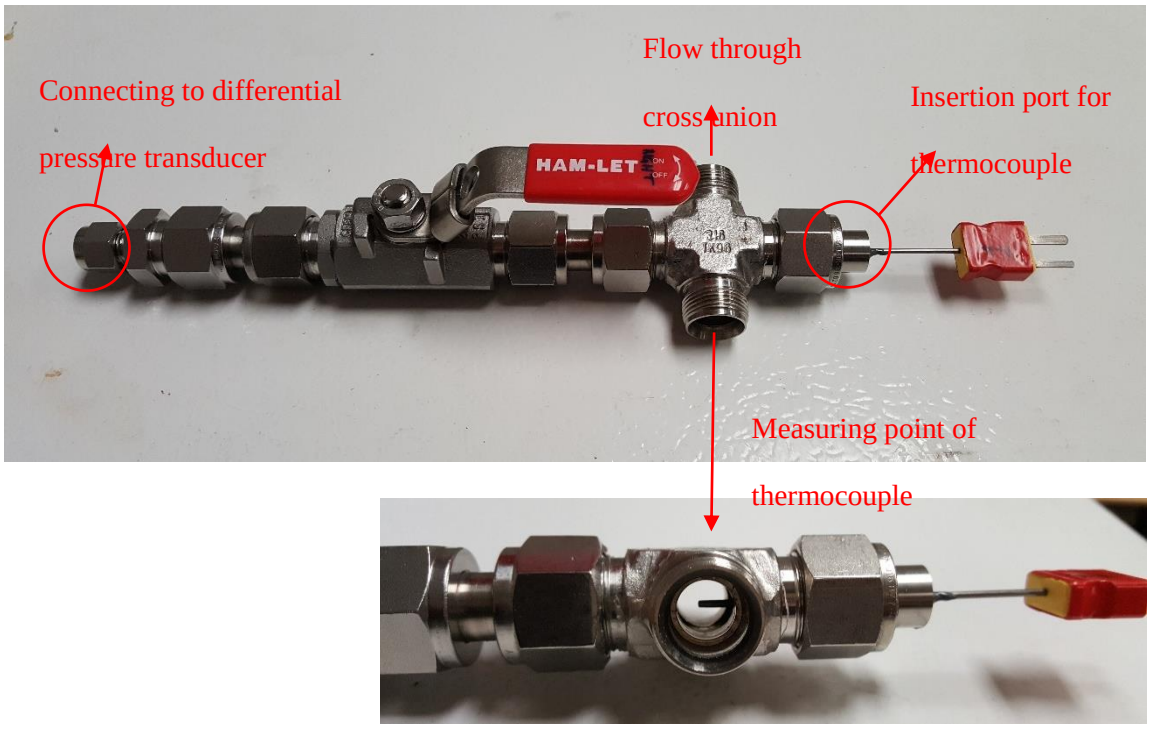

Figure A 1. Cross union setup for accommodating measuring devices

Valves typically use PTFE as sealing material and hence are incompatible with high temperature working environment (>200°C). In order to control the flow of molten salt at operating temperatures as high as 550°C, a service needle valve SS-12NBS16 from Swagelok was used in the system (which is rated for an operating temperature of 648°C).

Pump and tank

Due to the high operating temperatures and small flow rates, there are only a few options for commercial pump that are compatible with the specifications of the flow loop apparatus needed for this study. A commercial-scale high temperature pump integrated with a heating tank (with operating temperatures up to 700°C) was procured from Wenesco Inc. The pump is rated for an insertion depth of 12 inches and minimum flow rate of 0.1 gal/min. A variable-frequency drive (VFD) is connected to the pump which provides more flexibility for flow control and the volumetric flow rate of the molten salt samples.

Heating Elements (Heat Trace)

The main heating element is embedded in the heating tank which is pre-installed with the high temperature pump by the supplier (Wennesco Inc.). The heating port provides 6800 W heat input and works up to 600°C which is sufficient for meeting the specifications of the current study. In order to prevent possible thermal shock and unexpected freezing of molten salts, the whole tubing system is wrapped with "Ultra-High Temperature Heating Tapes" [144] from Omega Inc. which were used to preheat the

system before initiating the experiments and to keep salts molten in the tubing (i.e., to prevent them from freezing). Such heating tapes are rated to work at high temperature conditions up to 760°C and are rated to provide heat flux of 12 kW/m^2.

Pressure measurement

The maximum operating temperature of typical commercial pressure transducers do not exceed 500°C (since extreme temperature fluctuations could seriously degrade the transducer's output signal). In this test, the Siemens Ds III differential 7MF4433 model pressure transmitter is being explored for measuring the pressure drop across the test section. This differential pressure transmitter employs NaK as the intermediate fluid to enable a maximum operating temperature of 585°C and an accuracy of ±0.029 psi (for 5.75 psi range). A schematic of the pressure transmitter assembly is illustrated below.

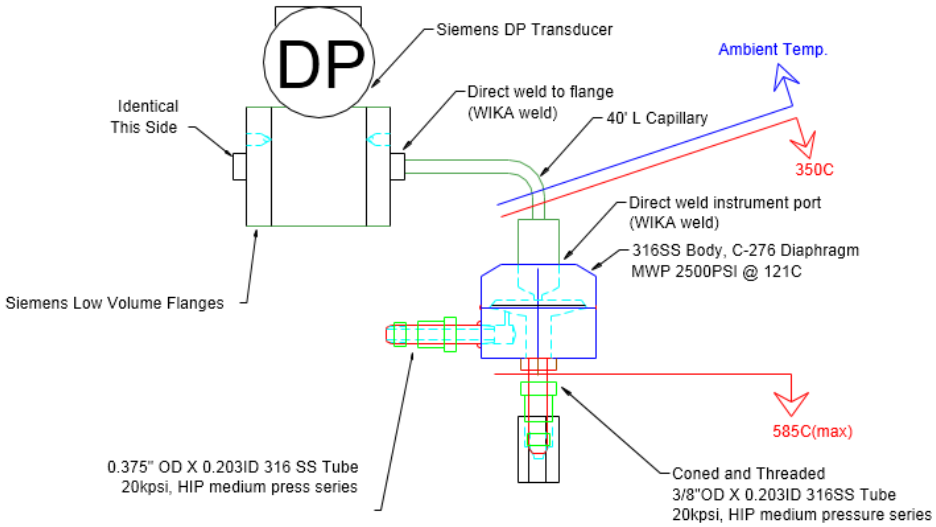

Figure A 2. Schematic diagram of the differential pressure transducer[8]

[8] Schematic diagram provided by project collaborator Alstom Inc.

The connecting tube between the measuring port and pressure sensor is also of important concern as the dynamic characteristics of the fluid oscillator may significantly influence the magnitudes of the measurement uncertainty for the pressure drop data. Studies have shown that the natural frequencies of the measurement apparatus (for the pressure response) are highest for short lengths and larger internal diameter tubes. This implies that the damping in the measurement apparatus increases with the increasing length and decreasing diameter [145, 146]. This behavior was experimentally verified in experiments involving the flow of water as the test liquid in the flow loop (as shown in the figure below). The pressure signal fluctuates severely between 0 and 24 mA when 0.25'' ID (internal diameter) tubing was used to join pressure transducer with the test section. Such fluctuations were dramatically minimized when the inner diameter of the connection tube was reduced to 0.14 inch and more consistent measurement of pressure drop data across the test section was then obtained. Thus, the differential pressure transducer was eventually connected to the test section by two pieces of tubing with 0.14'' ID and 44'' length.

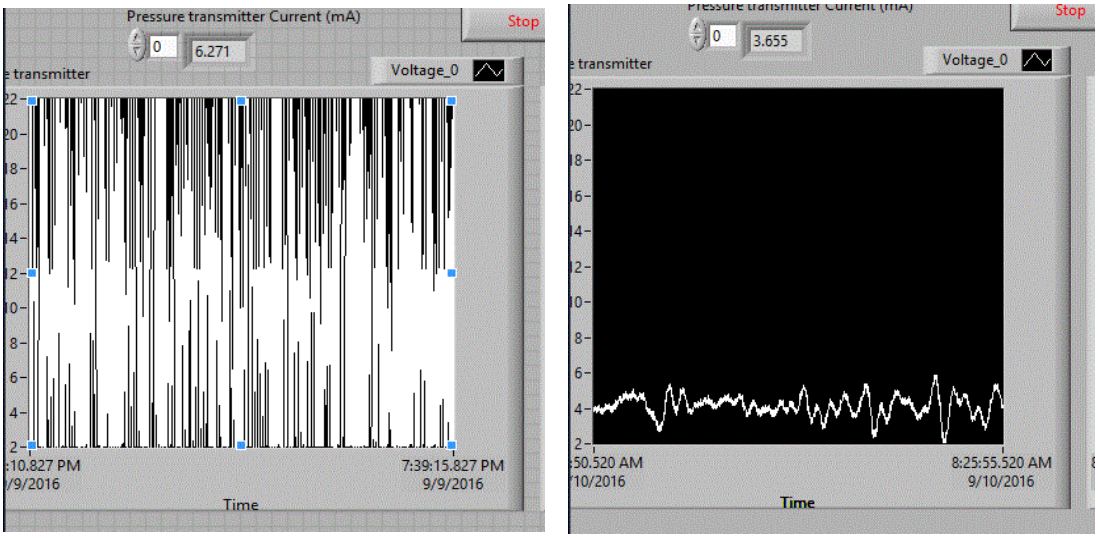

Figure A 3. Comparison of pressure transducer signals with: (LEFT) 0.25'' ID connection tube; (RIGHT) 0.14'' ID connection tube

Flow rate measurement

So far, no commercial flow meter was found to match the requirements and operating conditions for this proposed study. Most mechanical flow meters are limited to operating temperature of 500°C due to limitations of sealing. Ultrasonic flow meters are good candidates but the measurement accuracy is incompatible with the requirement of the proposed study. Eventually, a small container will be installed inside the heating tank just beneath the test loop return port for collecting molten salts after steady state conditions are achieved in the experiments. By measuring the mass of salt collected by the container in a specific period of time, the flow rate can be estimated.

Solid Model

The assembly diagram of the designed flow loop apparatus was performed using SolidWorks and is shown in Figure A4. All fittings are comprised of standard stainless-steel 316 components procured from Swagelok. Two tubes were bent at 45° using a conventional tube bender. The flow loop apparatus was designed and assembled as shown in the photograph in Figure A5.

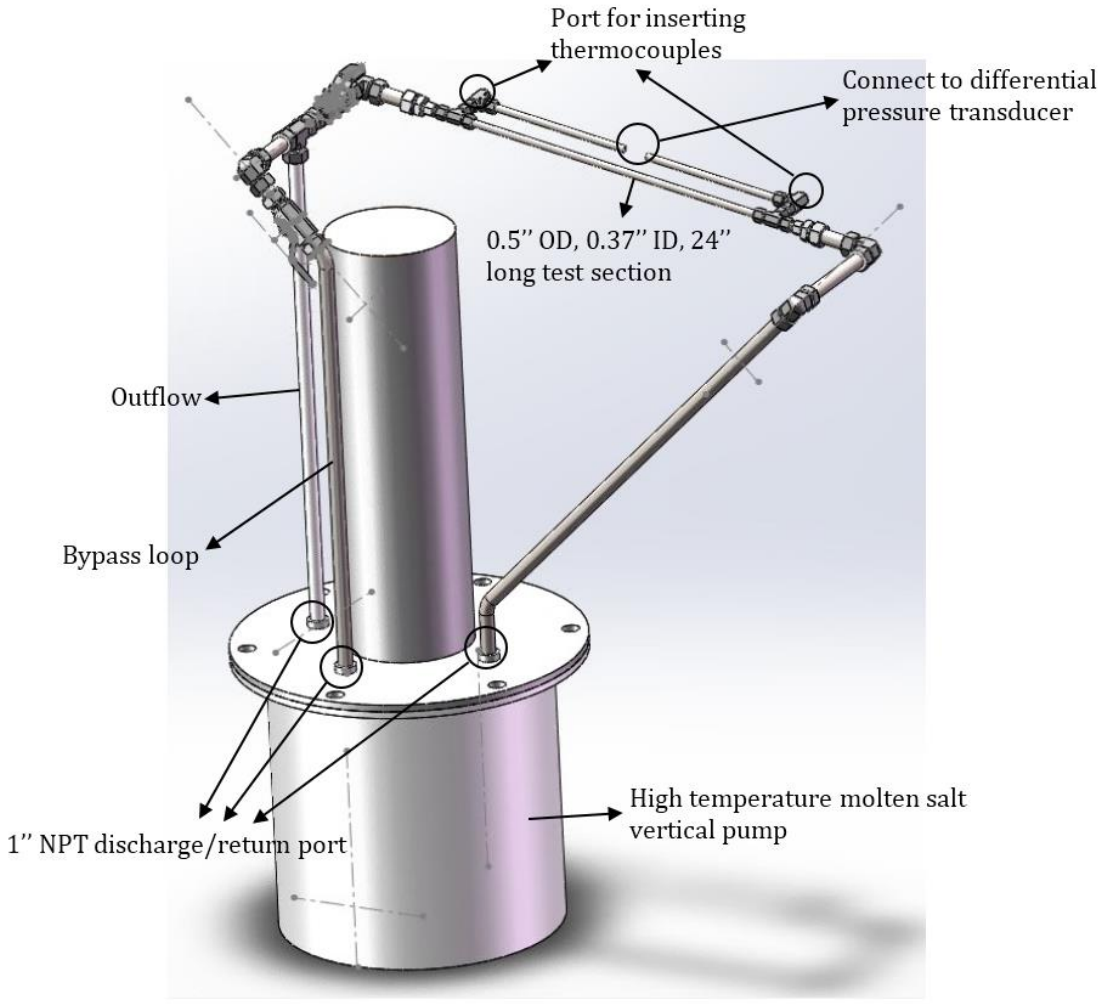

Figure A 4. Solid model of the flow loop apparatus.

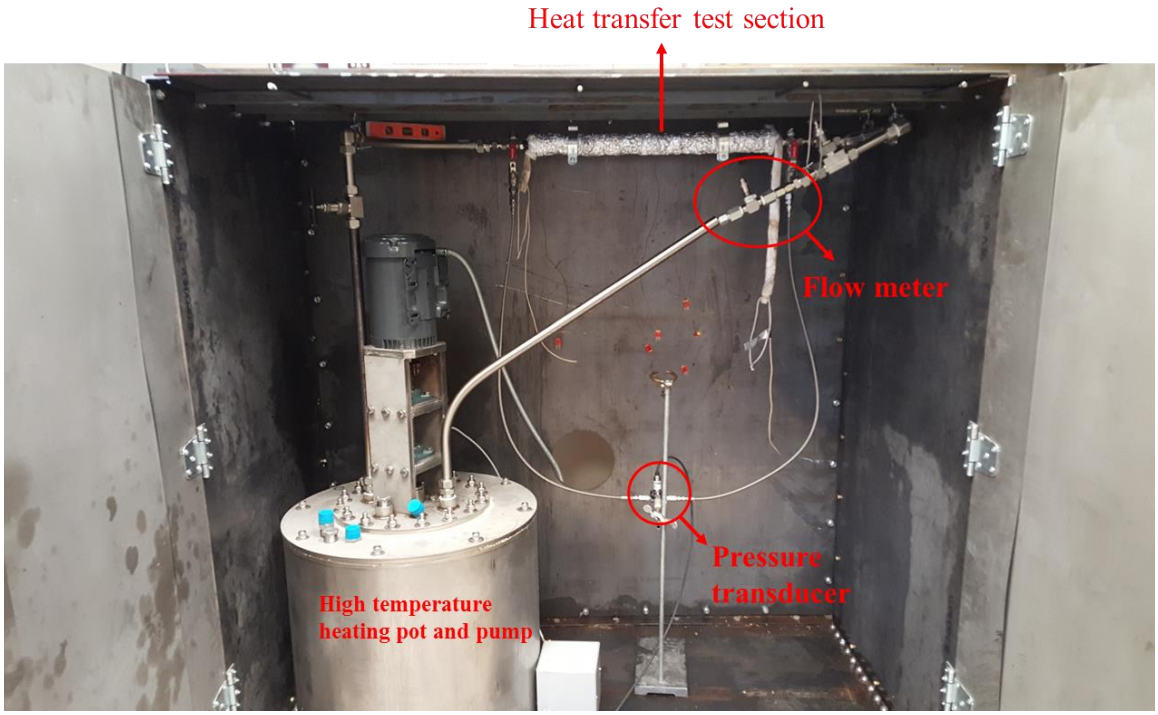

Figure A 5. Actual flow loop system

APPENDIX B

Repeated T-History tests of solar salt nanofluids containing 1.0% mass fraction of SiO_2 nanoparticle

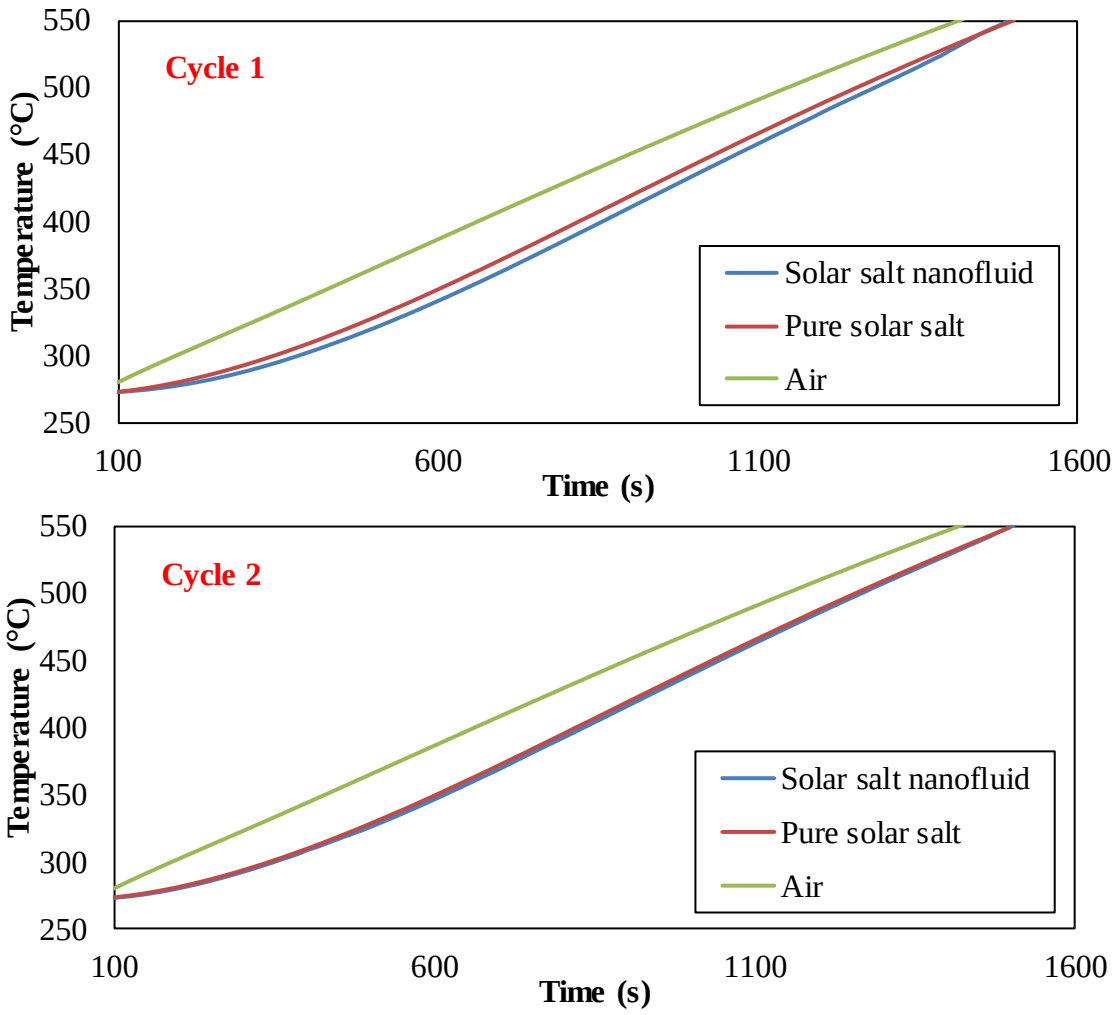

(To be continued on next page)

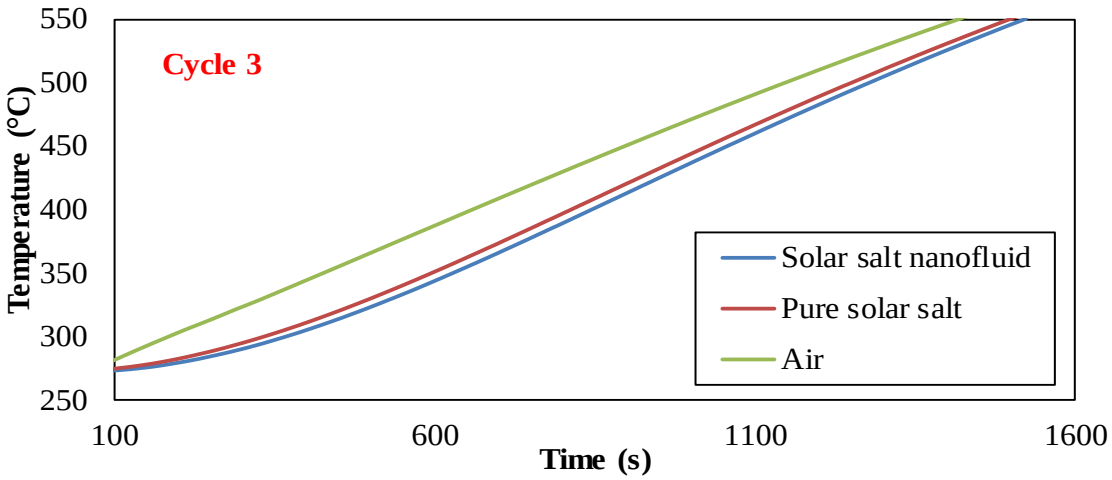

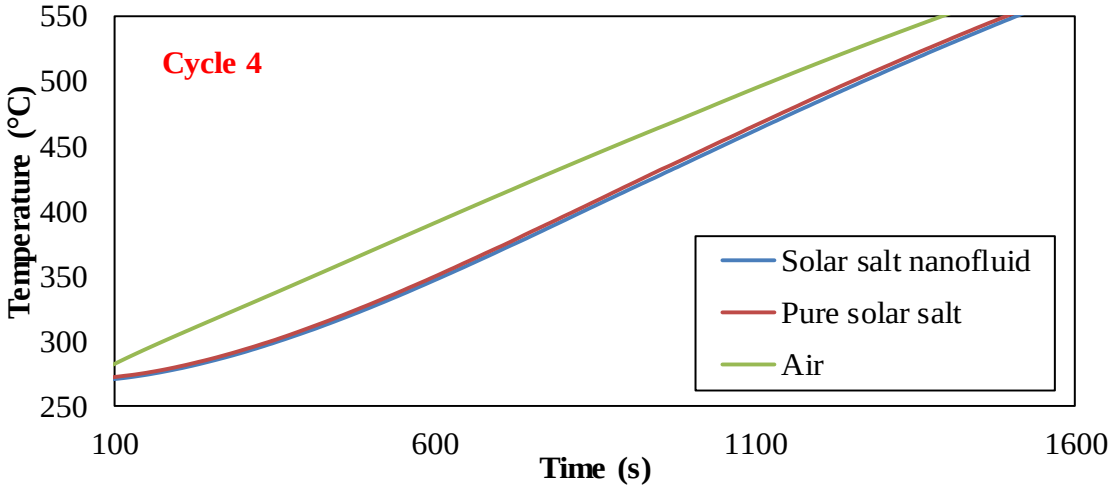

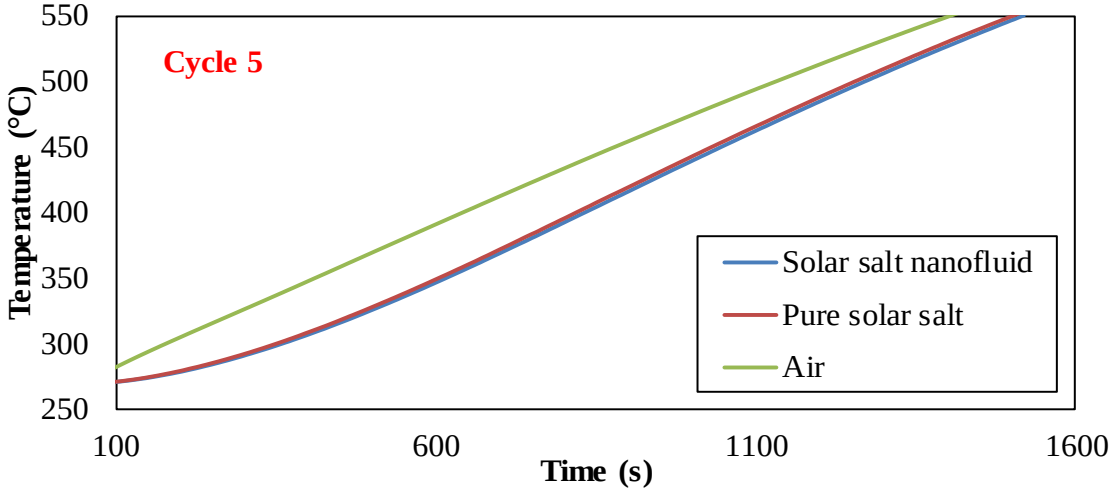

(To be continued on next page)

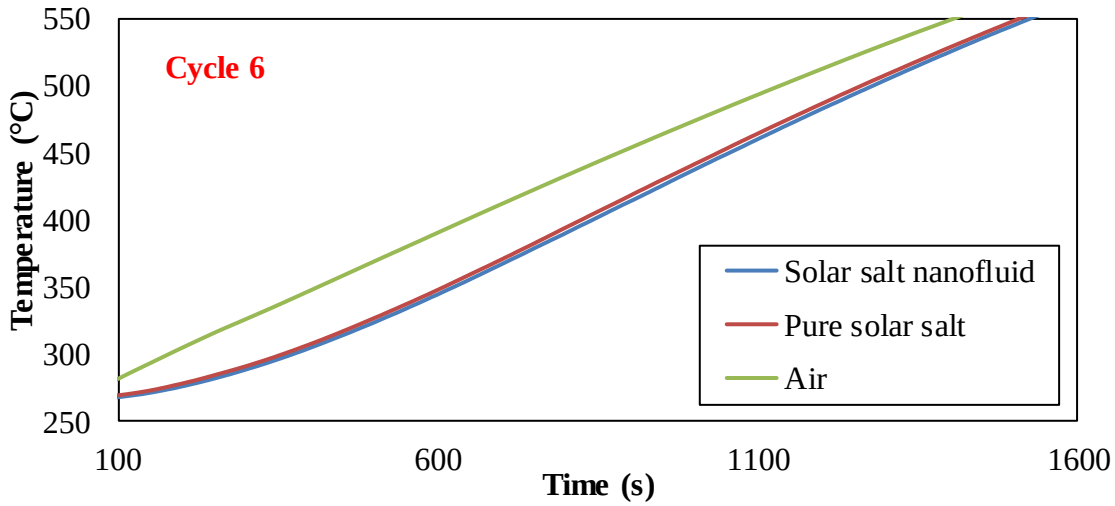

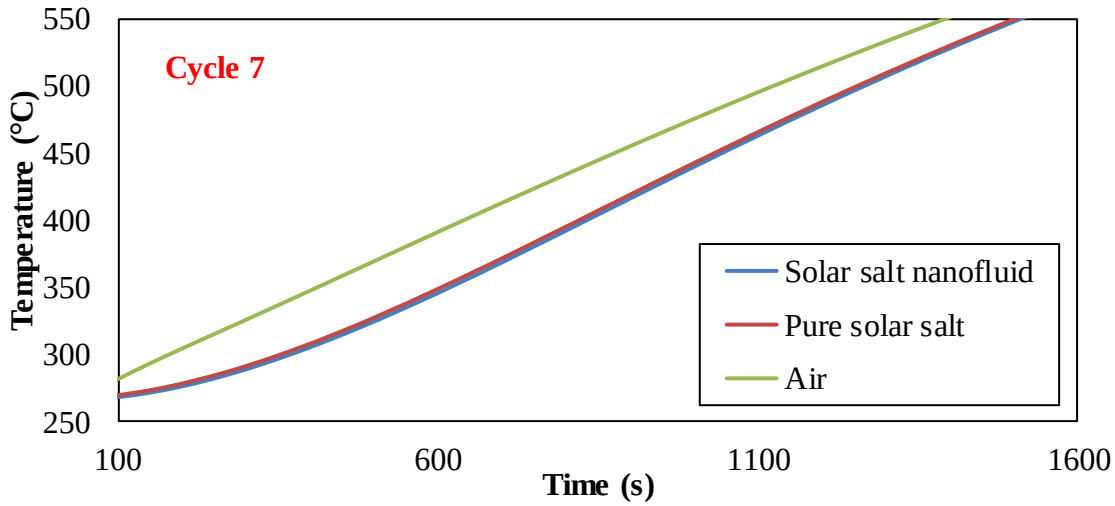

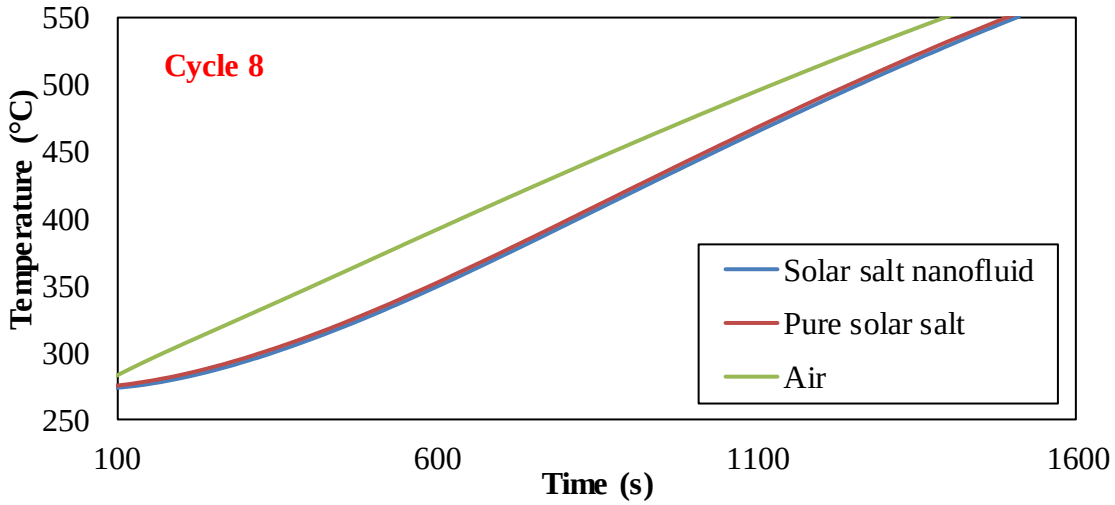

(To be continued on next page)

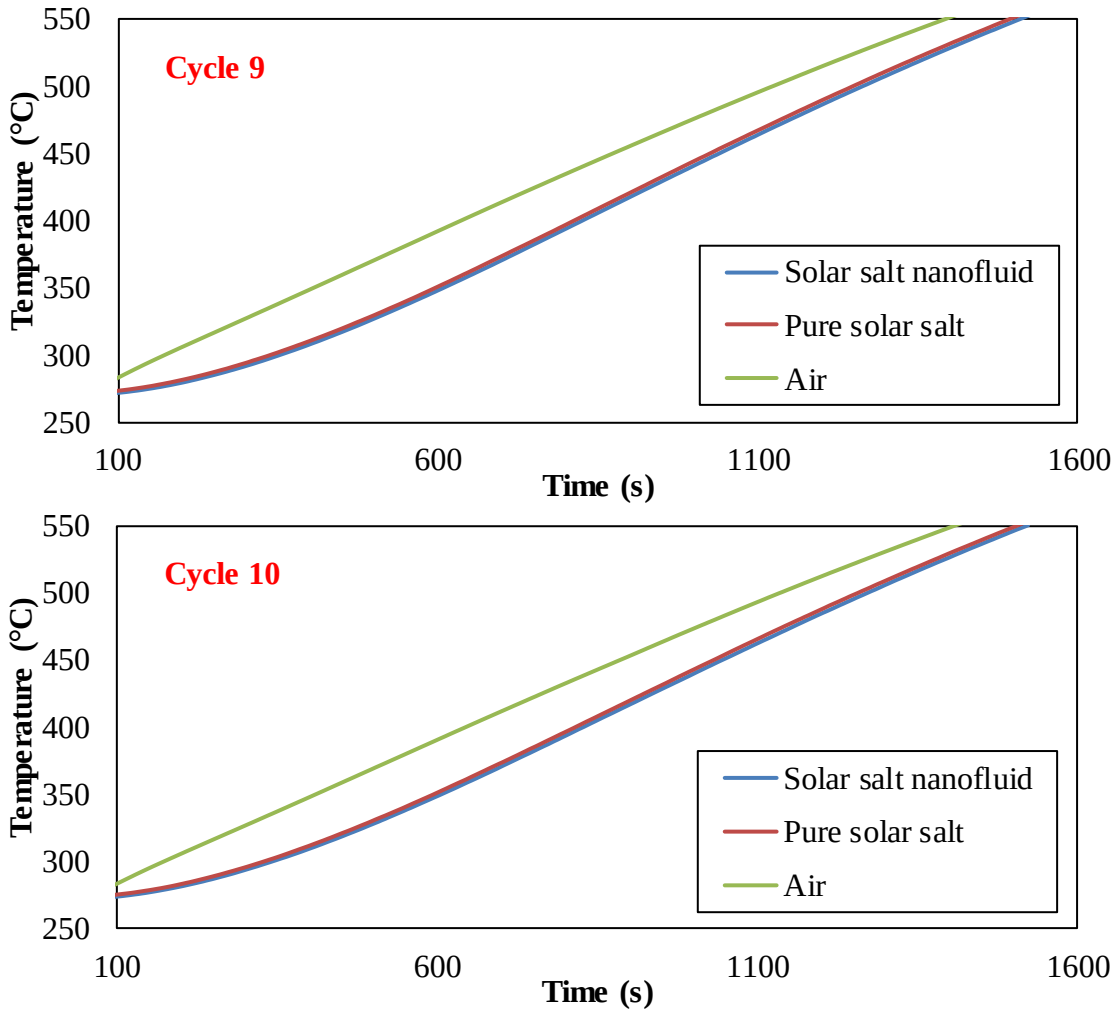

Figure B 1. Plot of temperature response obtained from repeated T-History experiments for thermocouples places in air (in the furnace), pure solar salt samples and solar salt nanofluids containing SiO_2 nanoparticles (with initial nominal diameter of 5 ~ 15 nm) at a mass concentration of 1.0%

APPENDIX C

Repeated T-History tests of solar salt nanofluid samples obtained by adding $Al(NO_3)_3 \cdot 9H_2O$ precursor for yielding Al_2O_3 nanoparticles

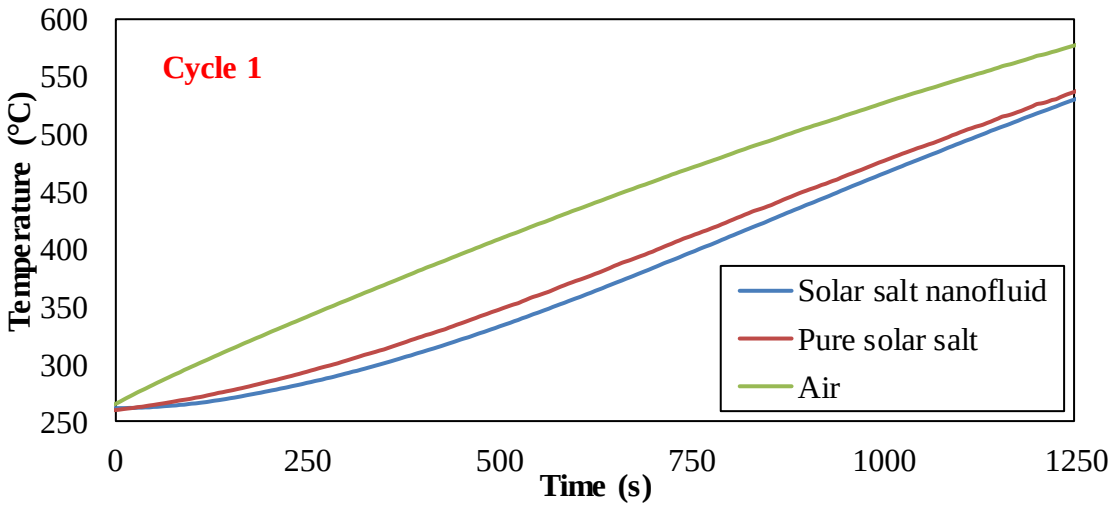

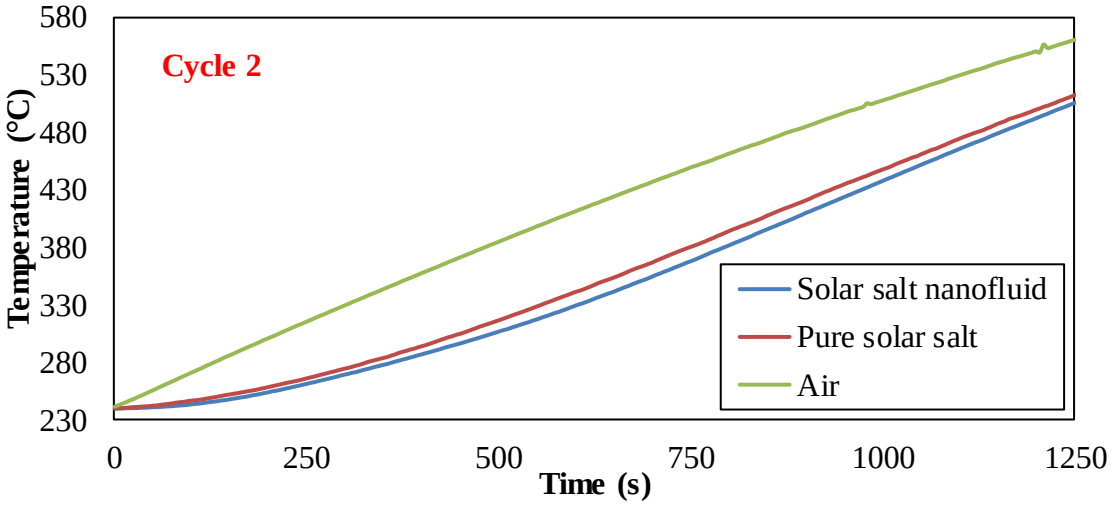

(To be continued on next page)

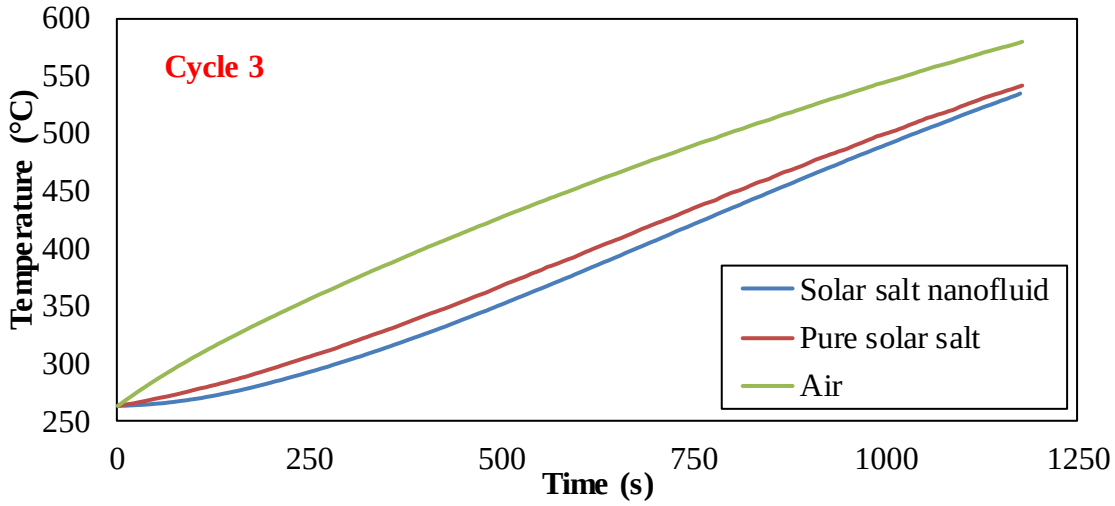

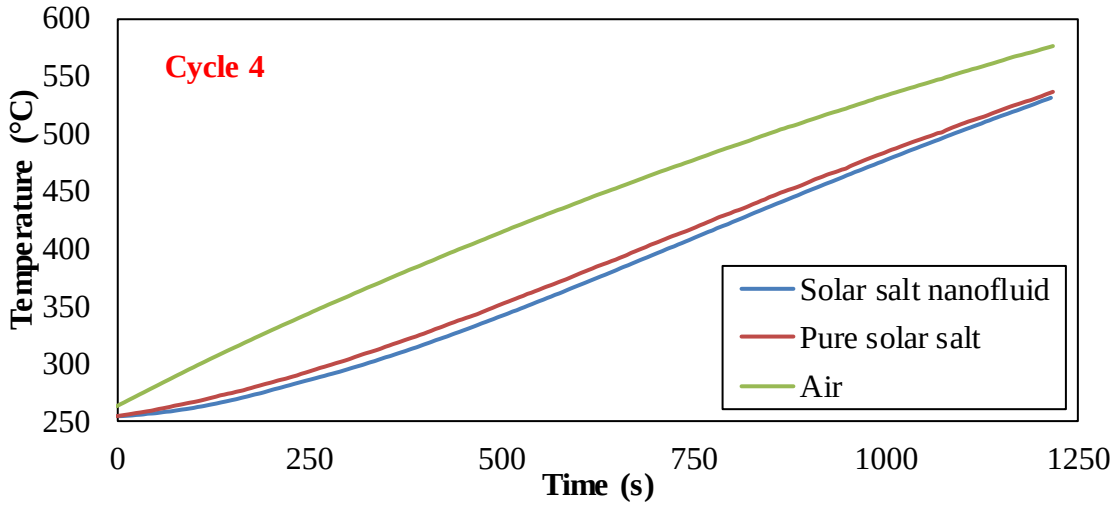

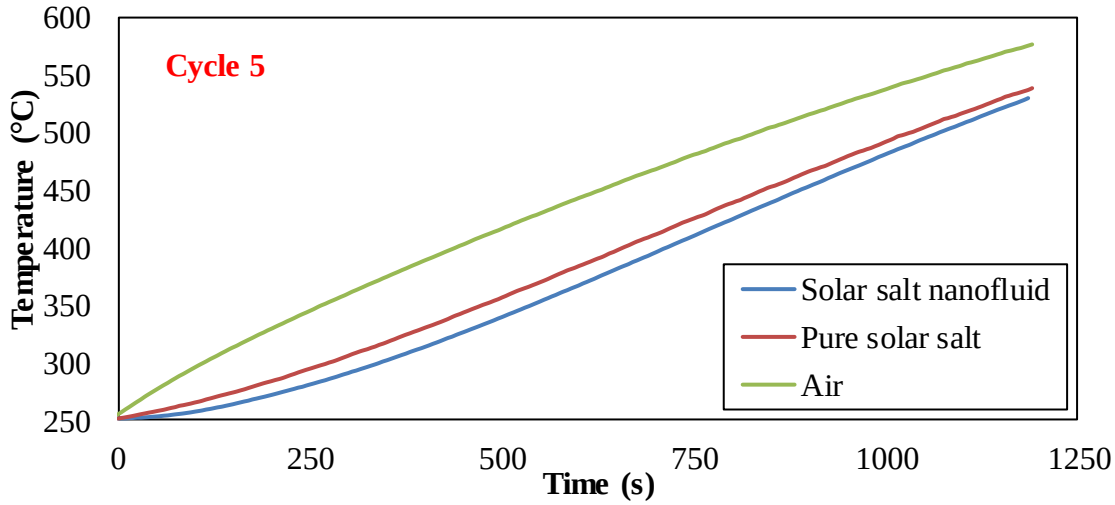

(To be continued on next page)

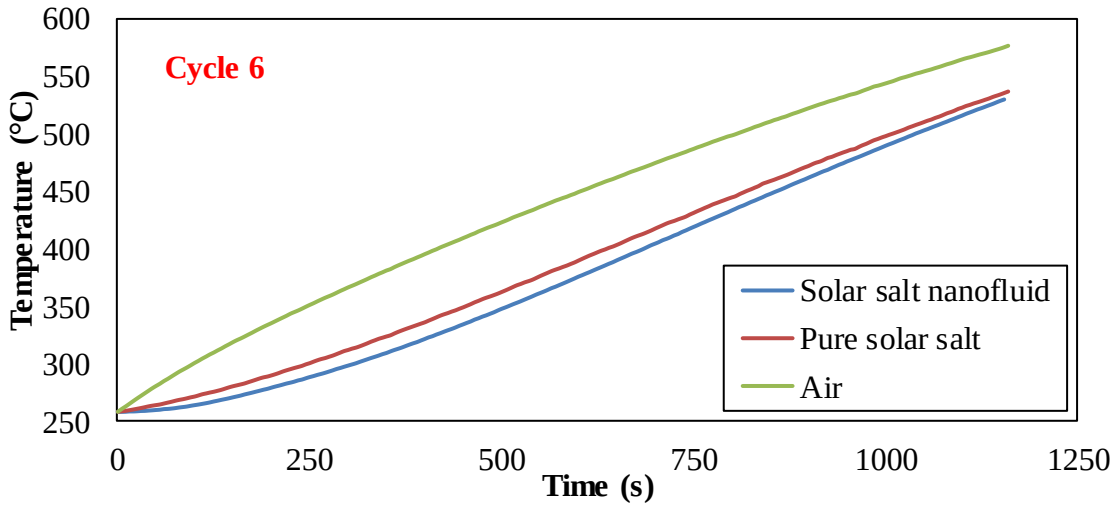

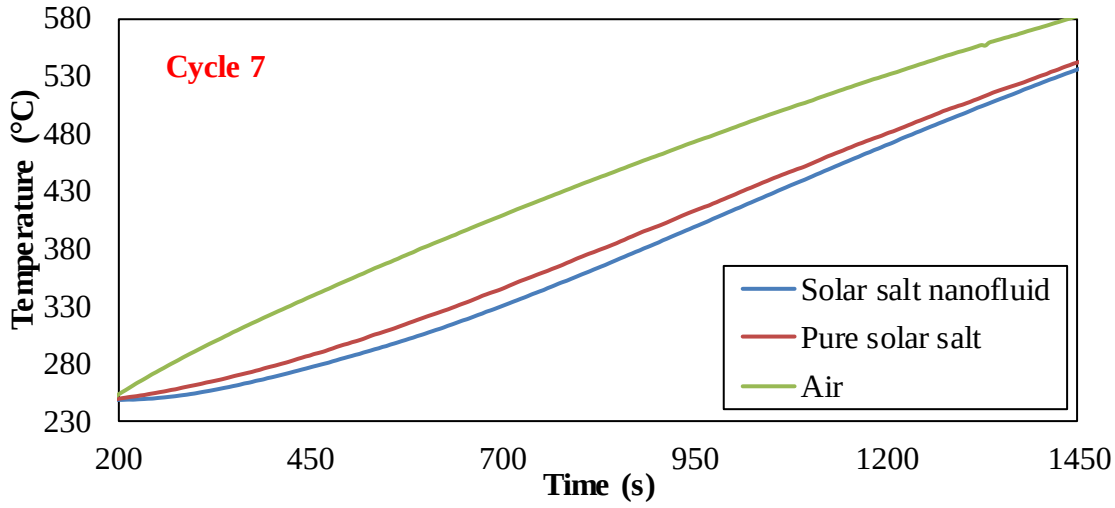

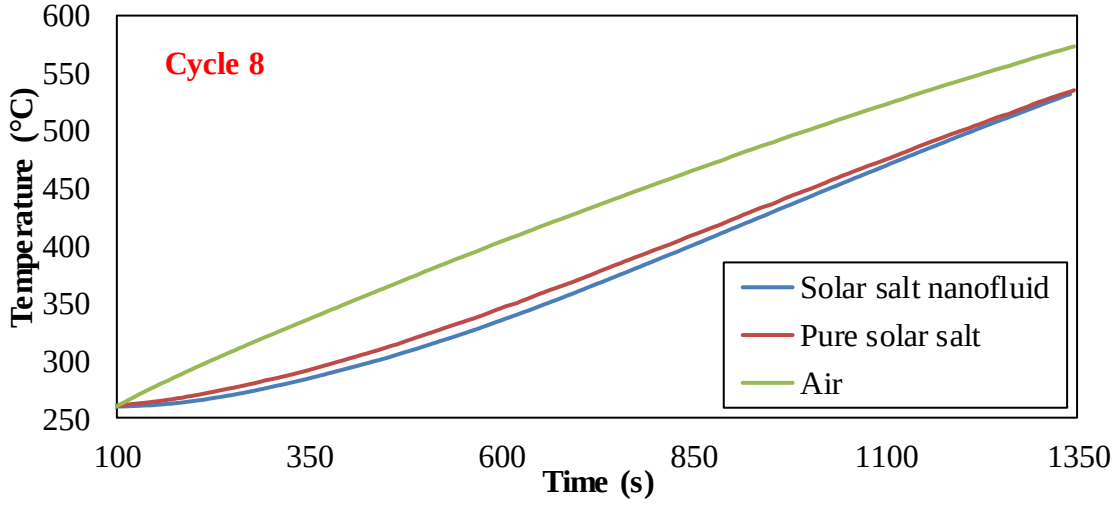

(To be continued on next page)

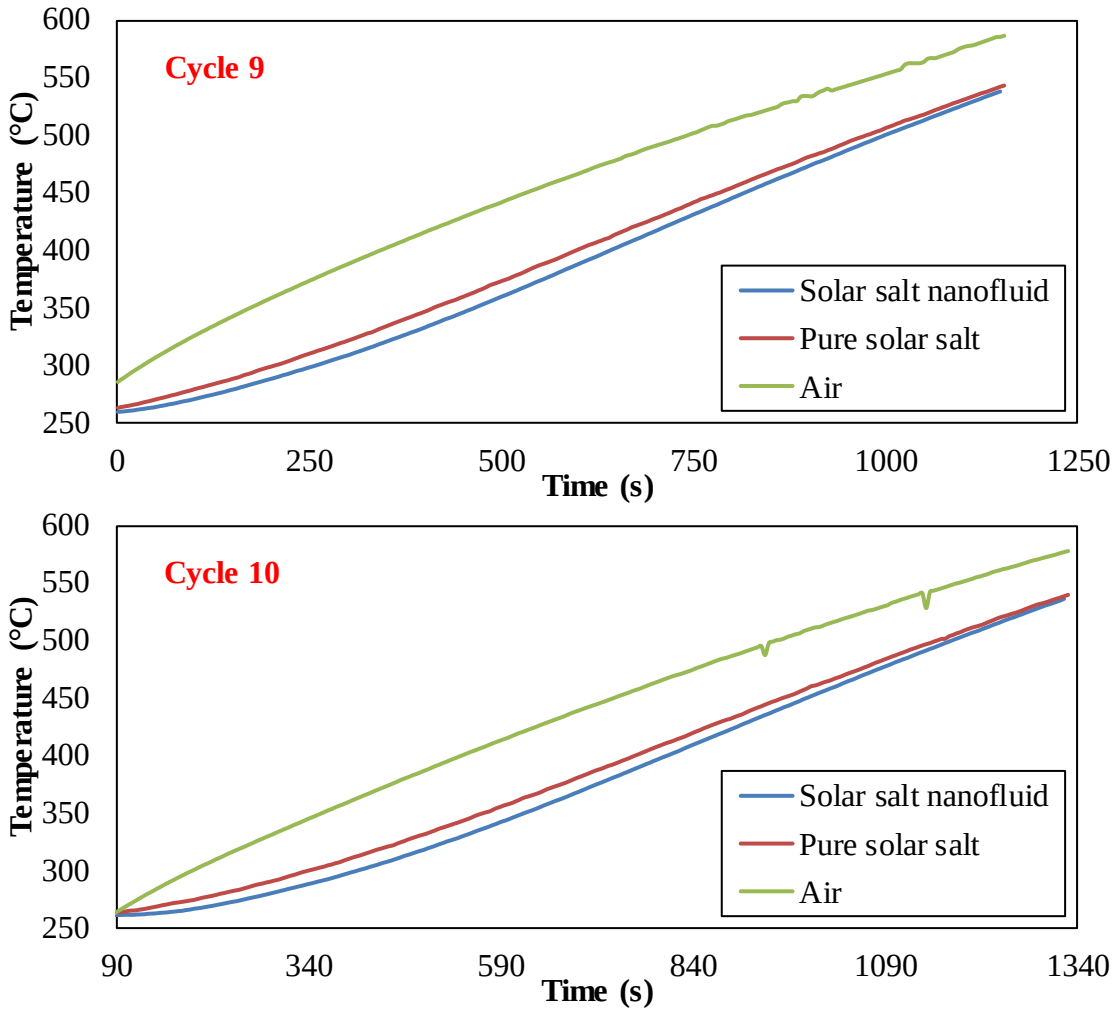

Figure C 1. Plot of temperature response obtained from T-History experiments for thermocouples places in air (in the furnace), pure solar salt samples and solar salt nanofluid samples (prepared using one-step synthesis protocol). The molten salt nanofluid samples were obtained by adding $Al(NO_3)_3 \cdot 9H_2O$ at 3.5% mass fraction (as nanoparticle precursors for yielding nanofluids) to pure solar salt for a target mass fraction of 0.5% for the resulting Al_2O_3 nanoparticles obtained by thermal decomposition (one-step synthesis protocol)

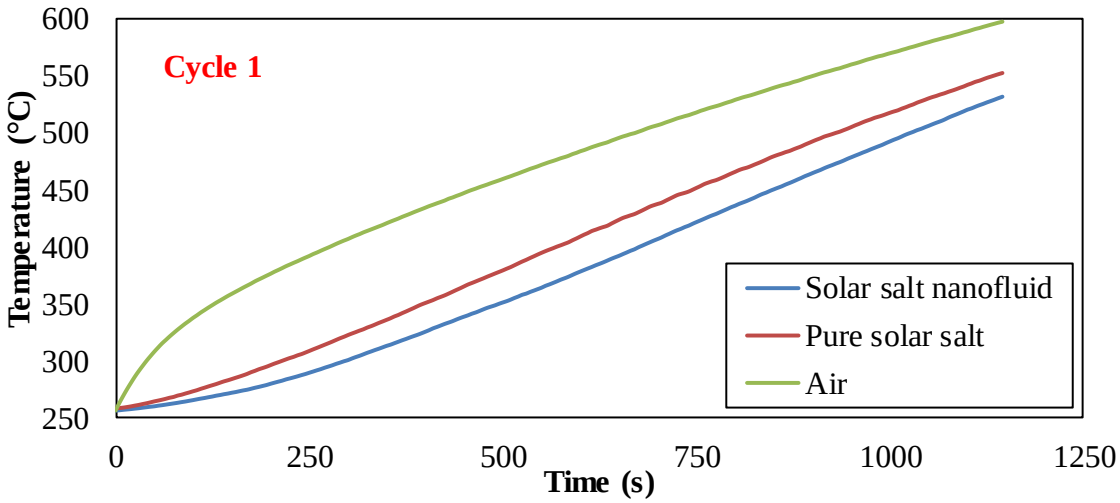

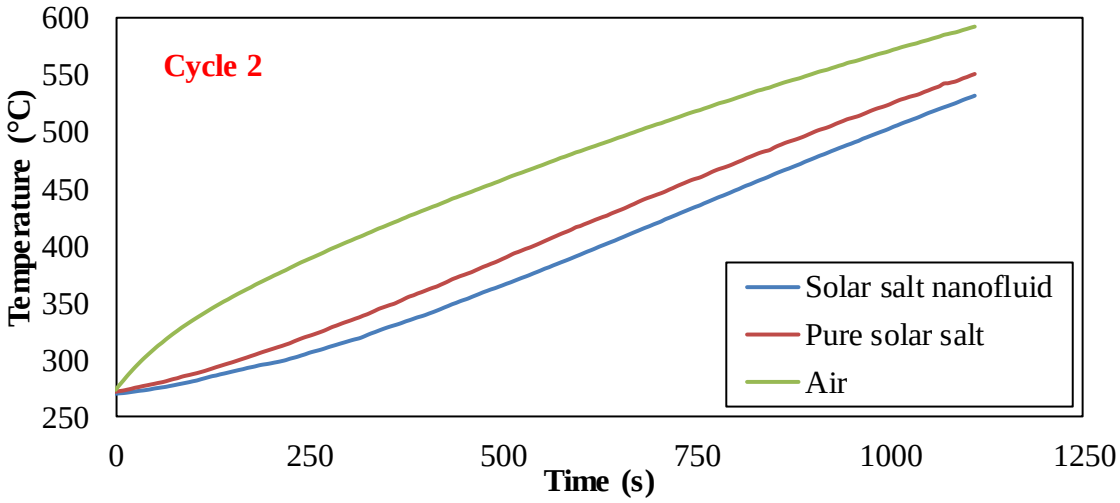

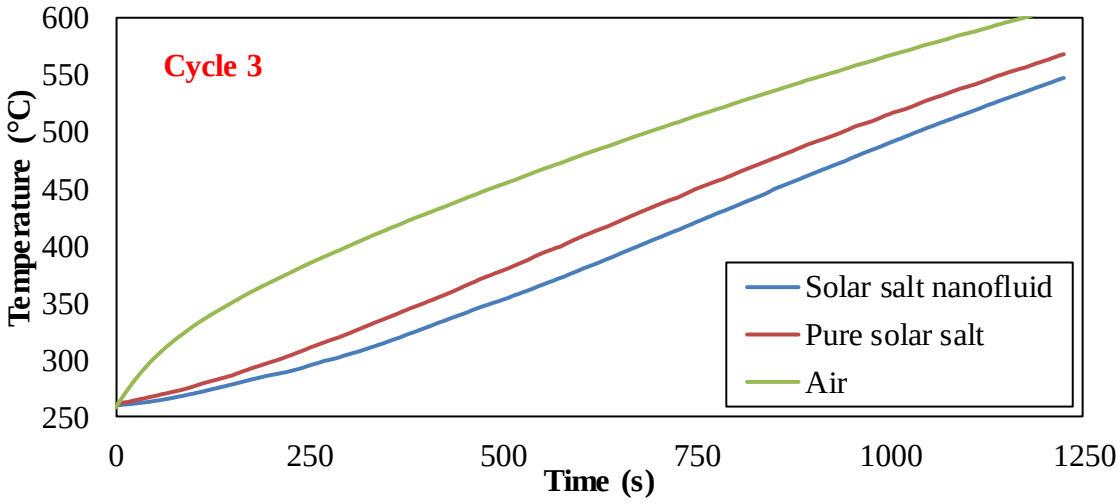

(To be continued on next page)

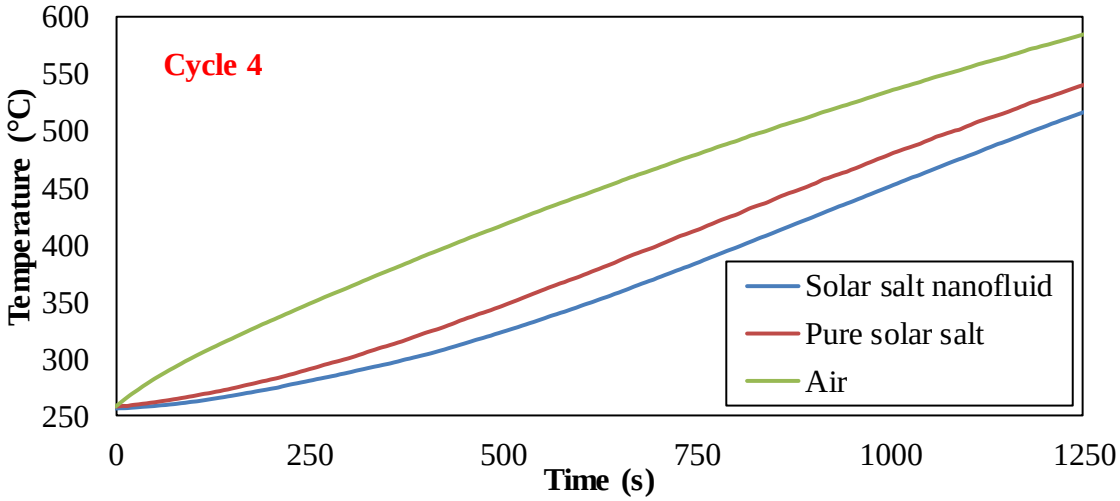

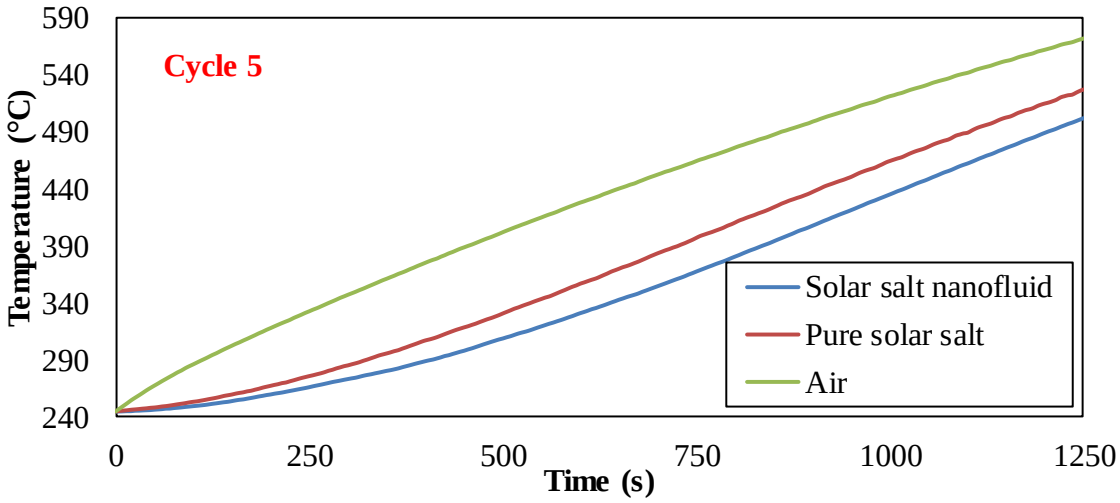

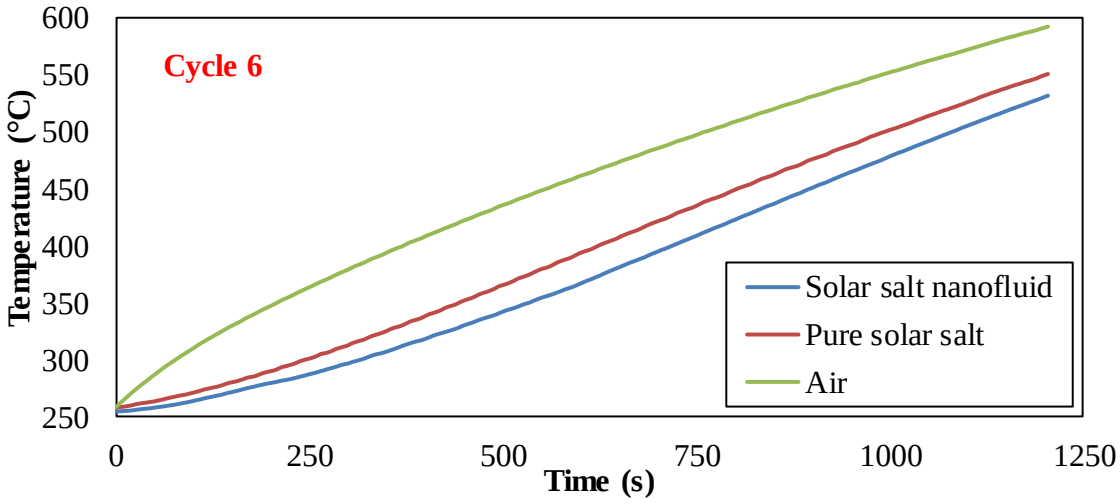

(To be continued on next page)

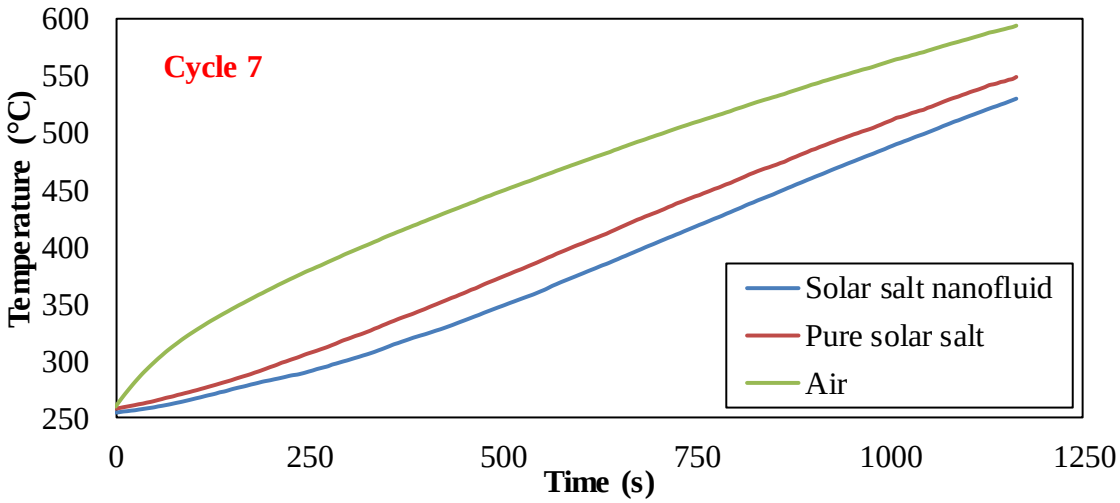

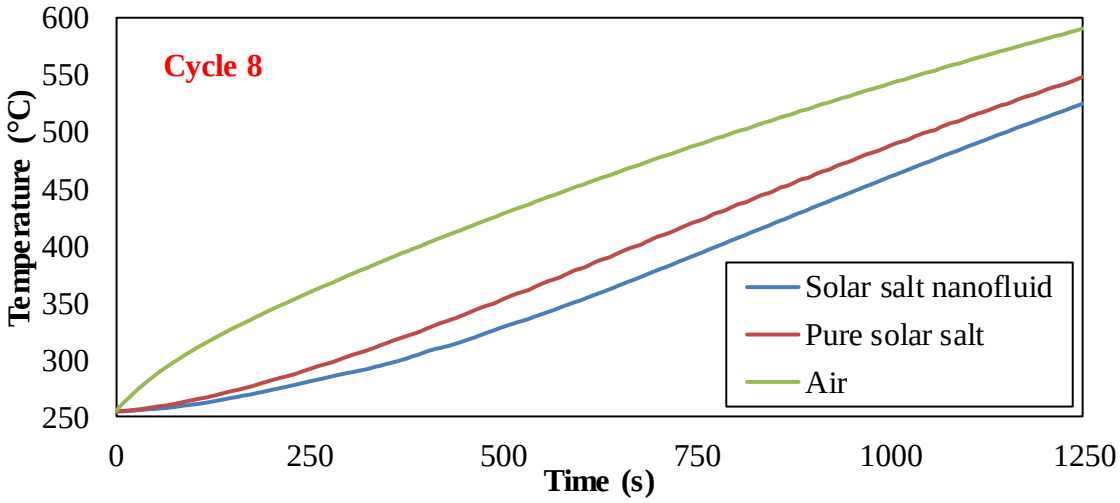

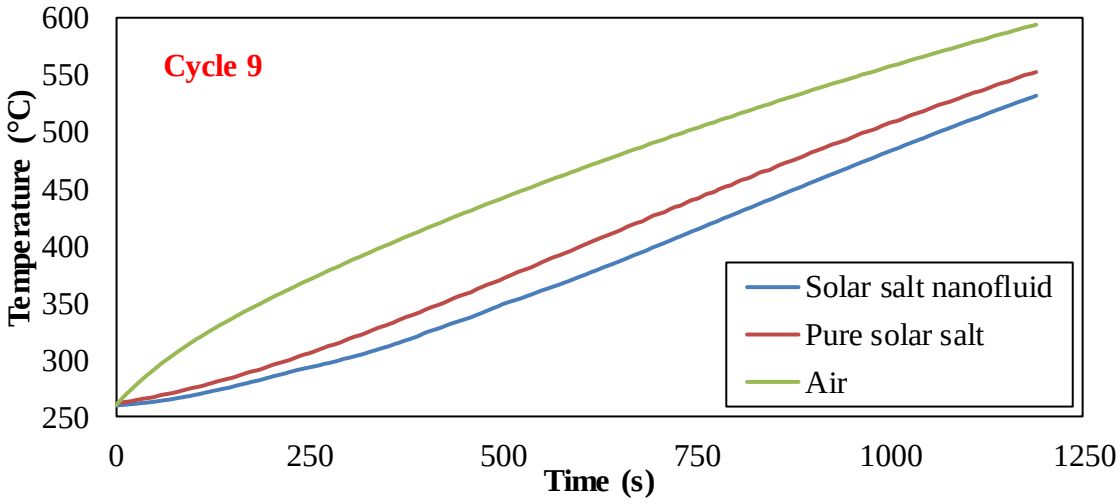

(To be continued on next page)

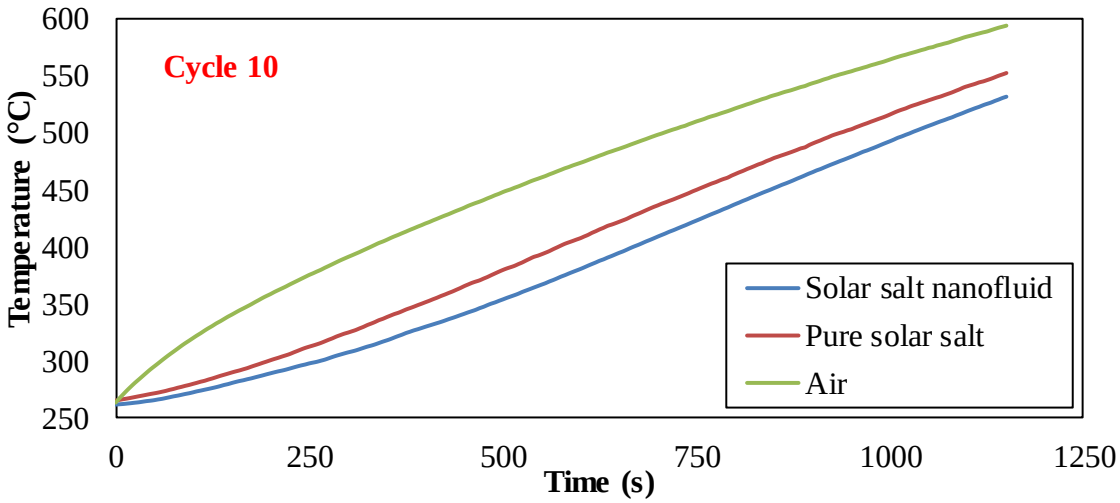

Figure C 2. Plot of temperature response obtained from T-History experiments for thermocouples places in air (in the furnace), pure solar salt samples and solar salt nanofluid samples (prepared using one-step synthesis protocol). The molten salt nanofluid samples were obtained by adding $Al(NO_3)_3 \cdot 9H_2O$ at 6.9% mass fraction (as nanoparticle precursors for yielding nanofluids) to pure solar salt for a target mass fraction of 1% for the resulting Al_2O_3 nanoparticles obtained by thermal decomposition (one-step synthesis protocol)

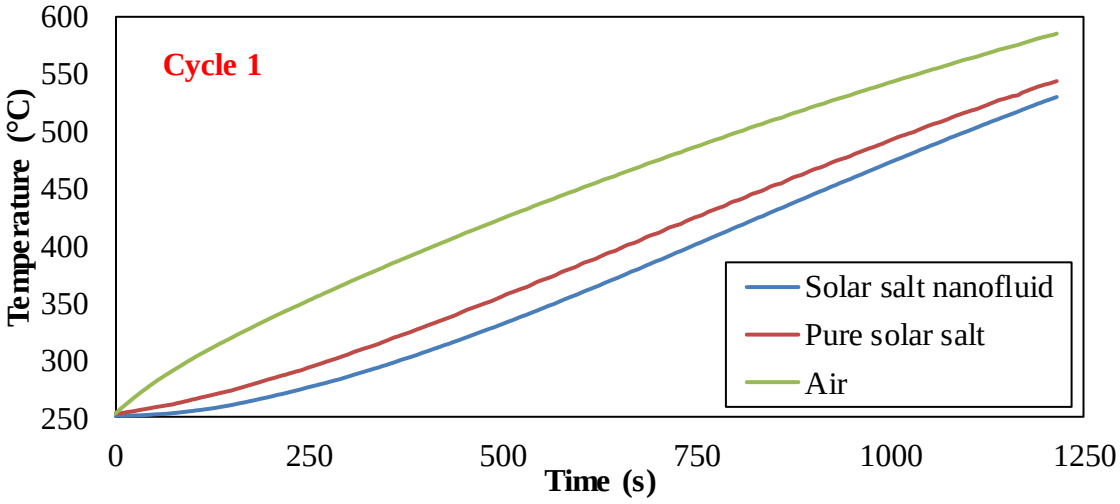

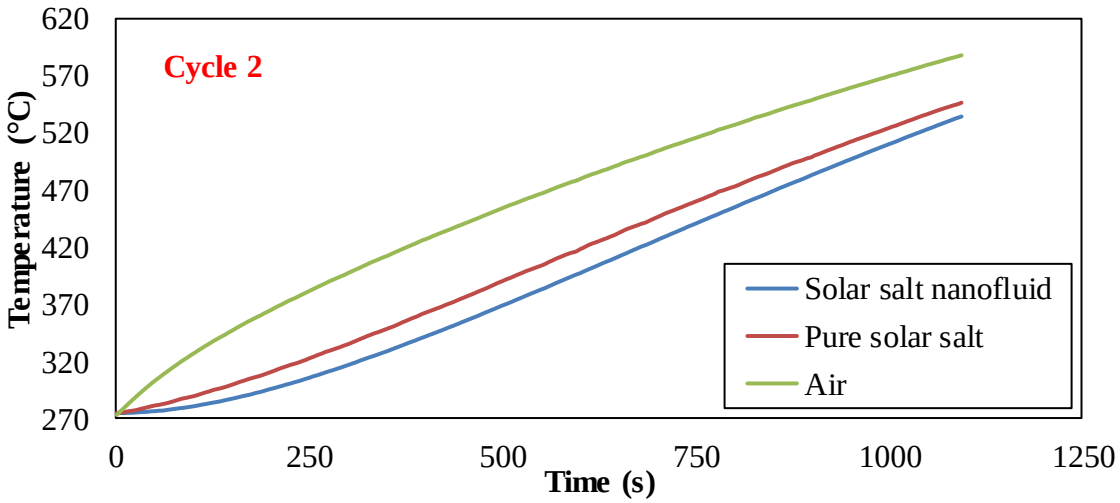

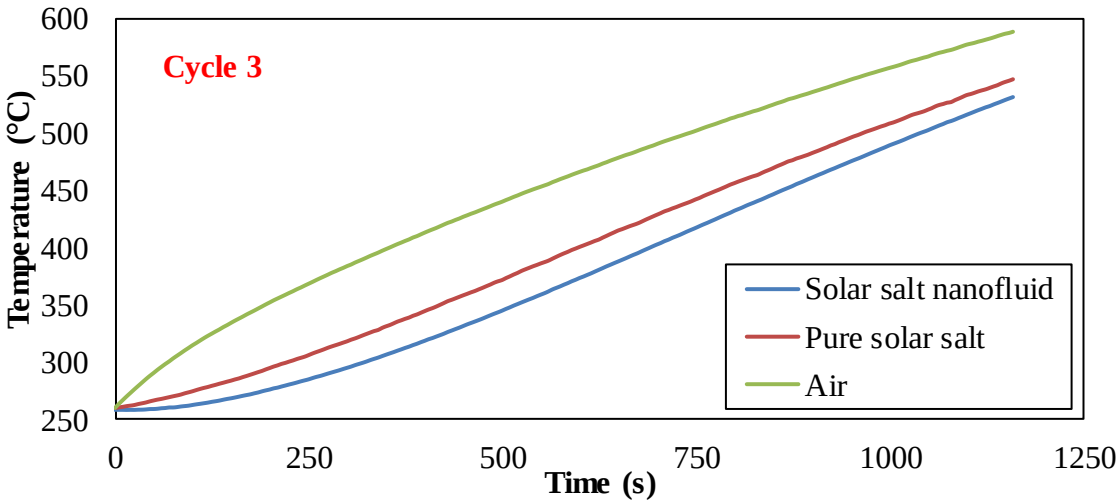

(To be continued on next page)

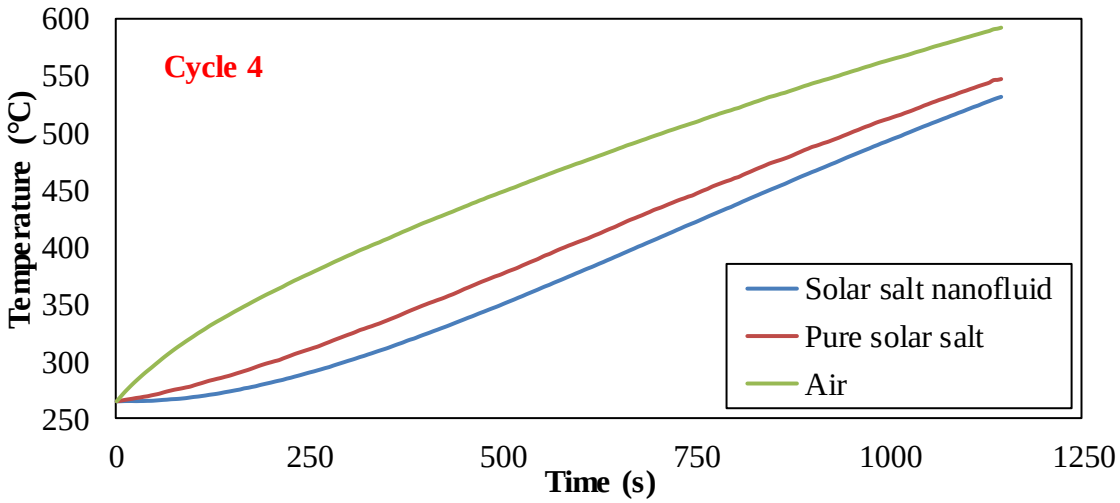

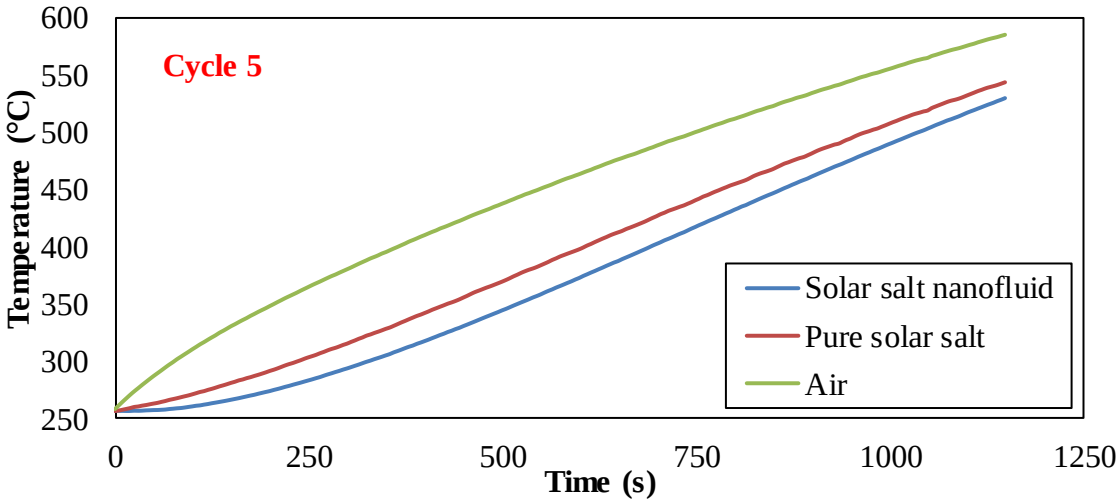

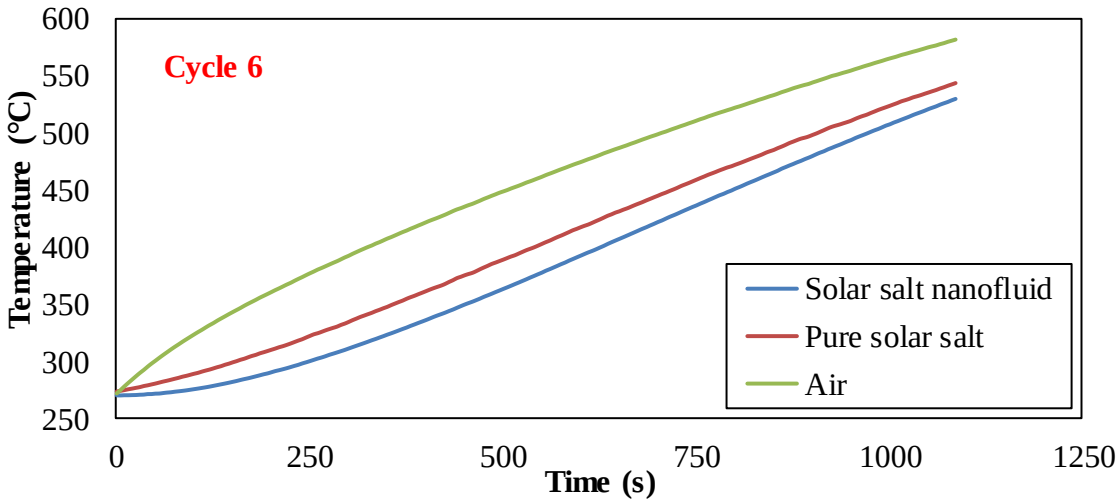

(To be continued on next page)

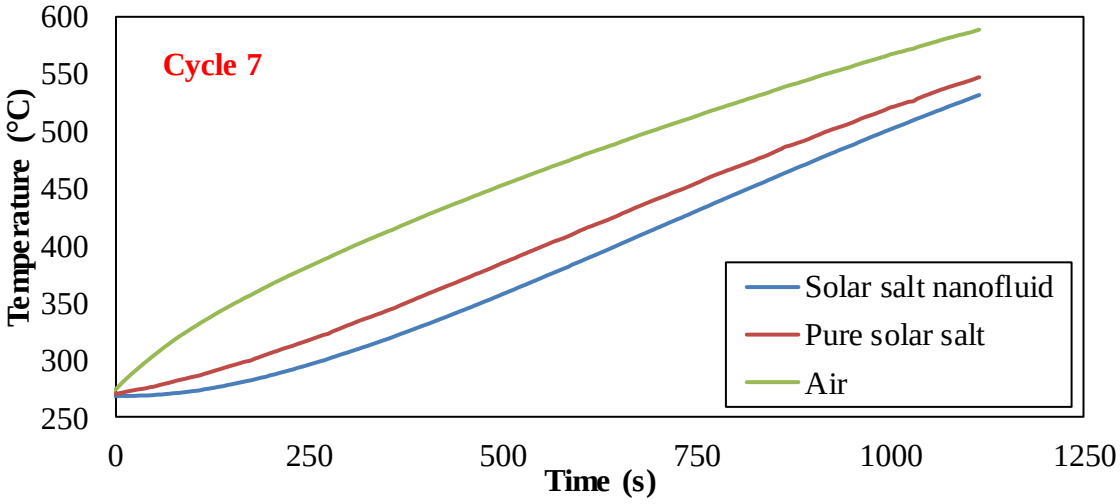

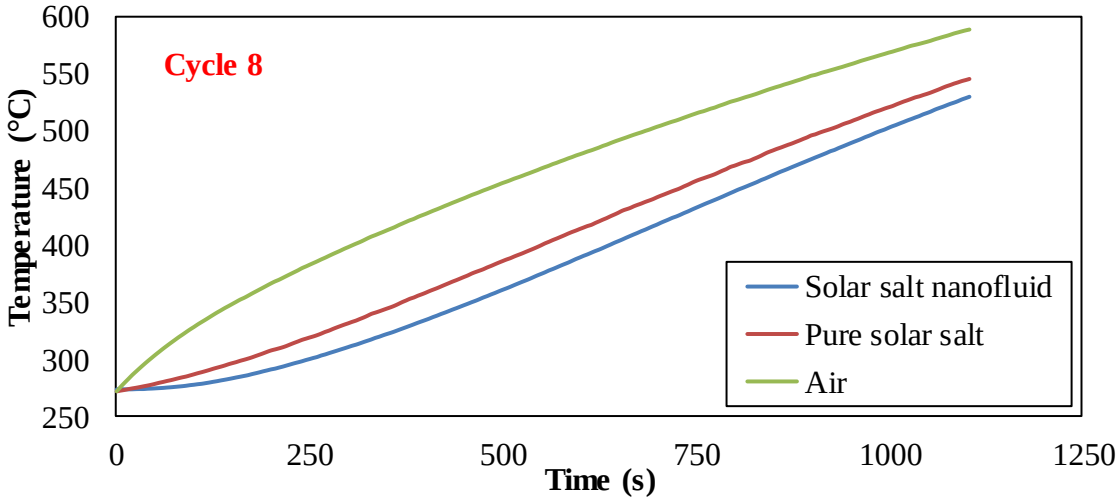

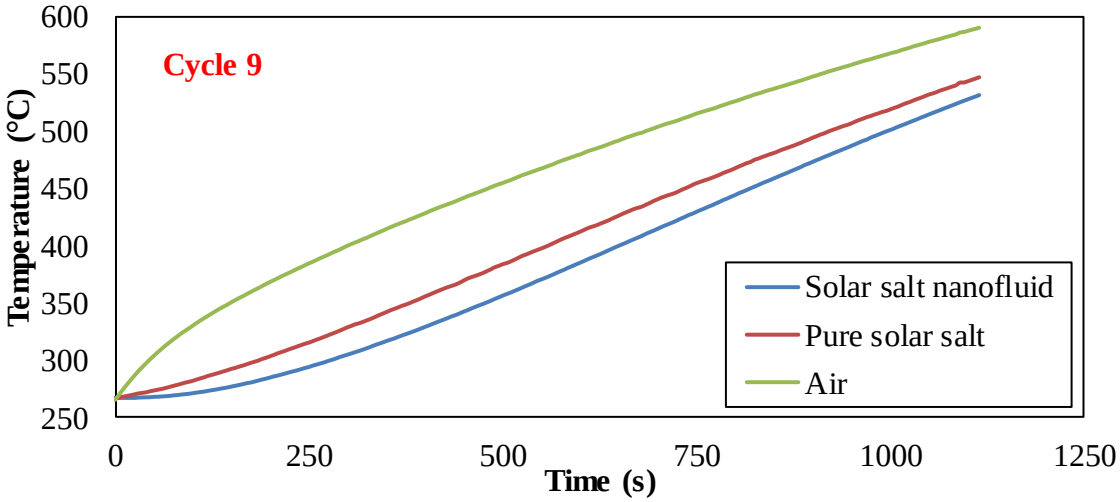

(To be continued on next page)

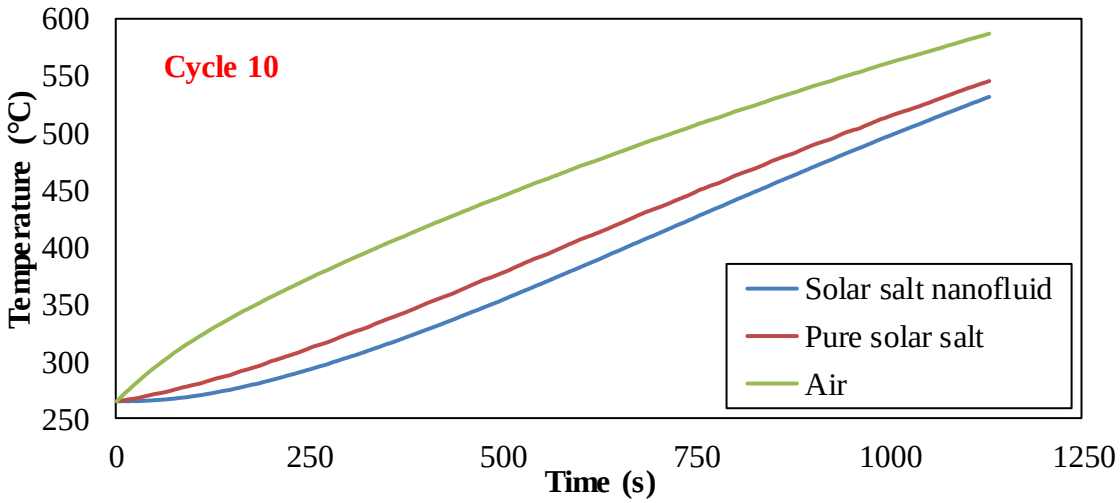

Figure C 3. Plot of temperature response obtained from T-History experiments for thermocouples places in air (in the furnace), pure solar salt samples and solar salt nanofluid samples (prepared using one-step synthesis protocol). The molten salt nanofluid samples were obtained by adding $Al(NO_3)_3{\cdot}9H_2O$ at 10.1% mass fraction (as nanoparticle precursors for yielding nanofluids) to pure solar salt for a target mass fraction of 1.5% for the resulting Al_2O_3 nanoparticles obtained by thermal decomposition (one-step synthesis protocol)

APPENDIX D

Parametric study of solar salt nanofluids obtained using one-step synthesis protocol for $Mg(NO_3)_3{\cdot}6H_2O$ additive as precursor for MgO nanoparticles

Solar Salt mixed with $Mg(NO_3)_3{\cdot}6H_2O$ at mass fraction of 6% (synthesized at 550°C for 10 hours)

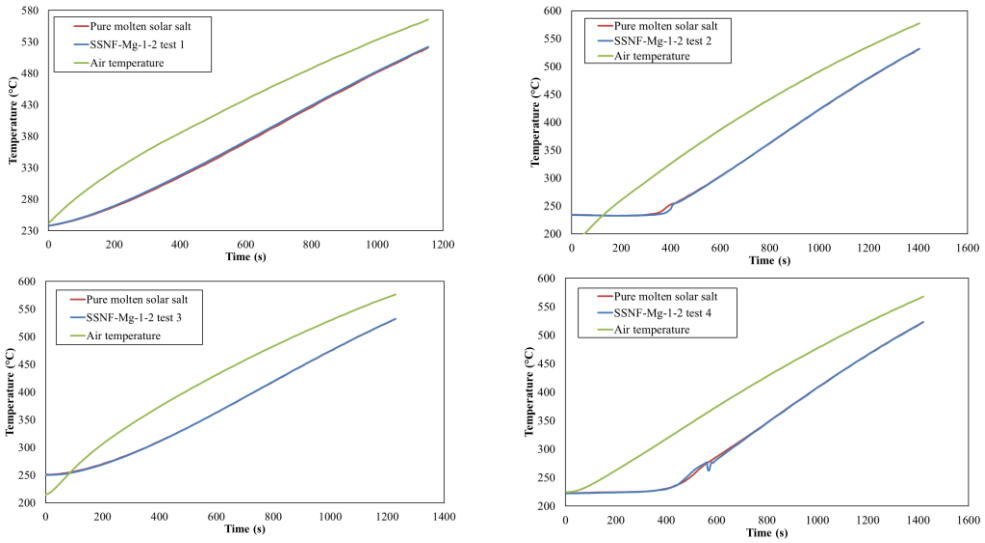

Figure D 1. Temperature ramping curves for T-History experiments repeated four times

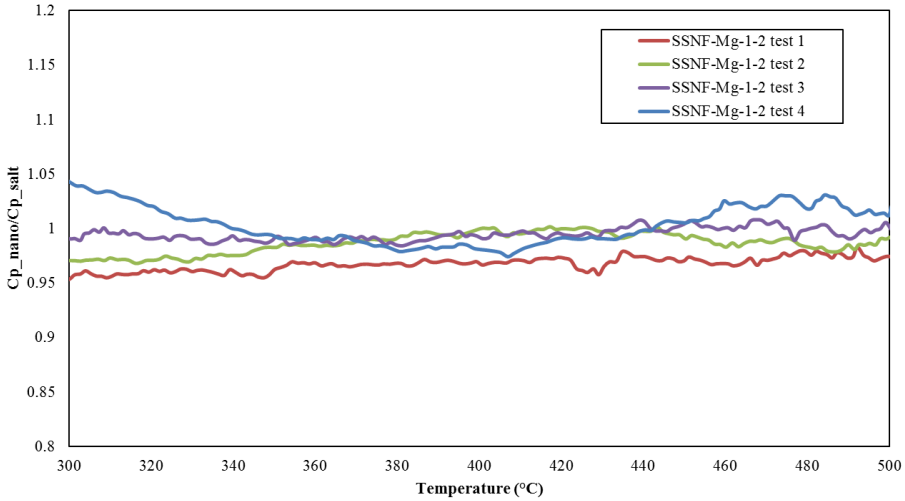

Figure D 2. Specific heat capacity ratio in repeated tests

Solar Salt mixed with $Mg(NO_3)_3 \cdot 6H_2O$ at mass fraction of 6% (synthesized at 600°C for 10 hours)

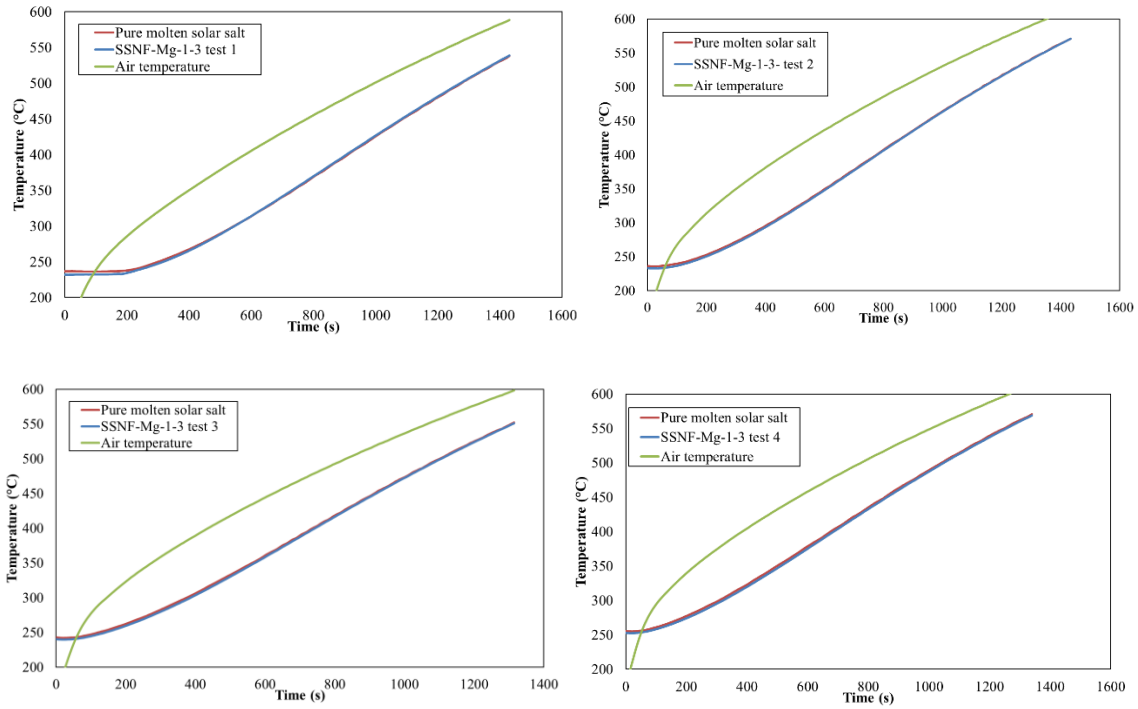

Figure D 3. Temperature ramping curves for T-History experiments repeated four times

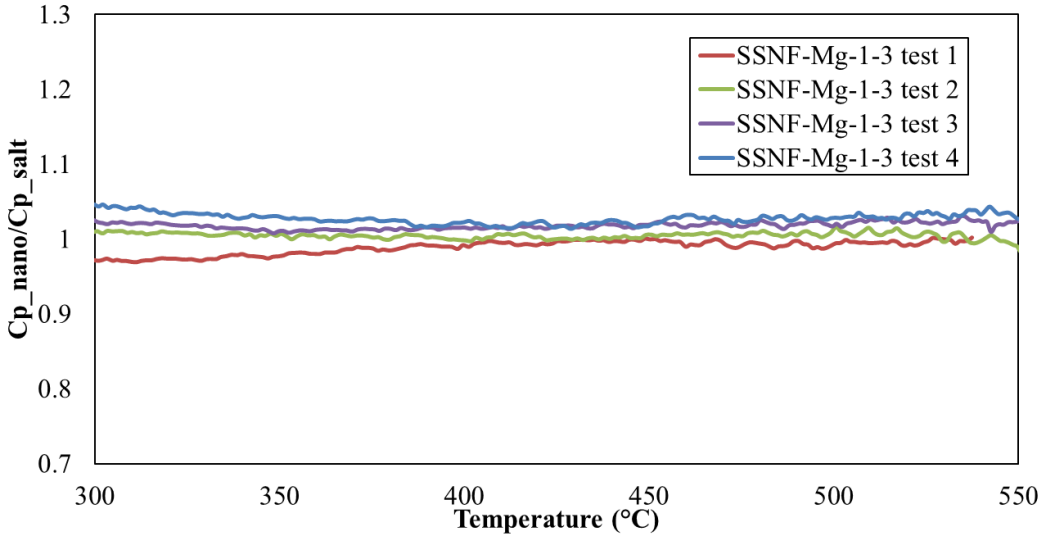

Figure D 4. Specific heat capacity ratio in repeated tests

Solar Salt mixed with $Mg(NO_3)_3 \cdot 6H_2O$ at mass fraction of 6% (synthesized at 650°C for 1, 2, 3 and 4 hours; synthesized at 700°C for 1 and 2 hours)

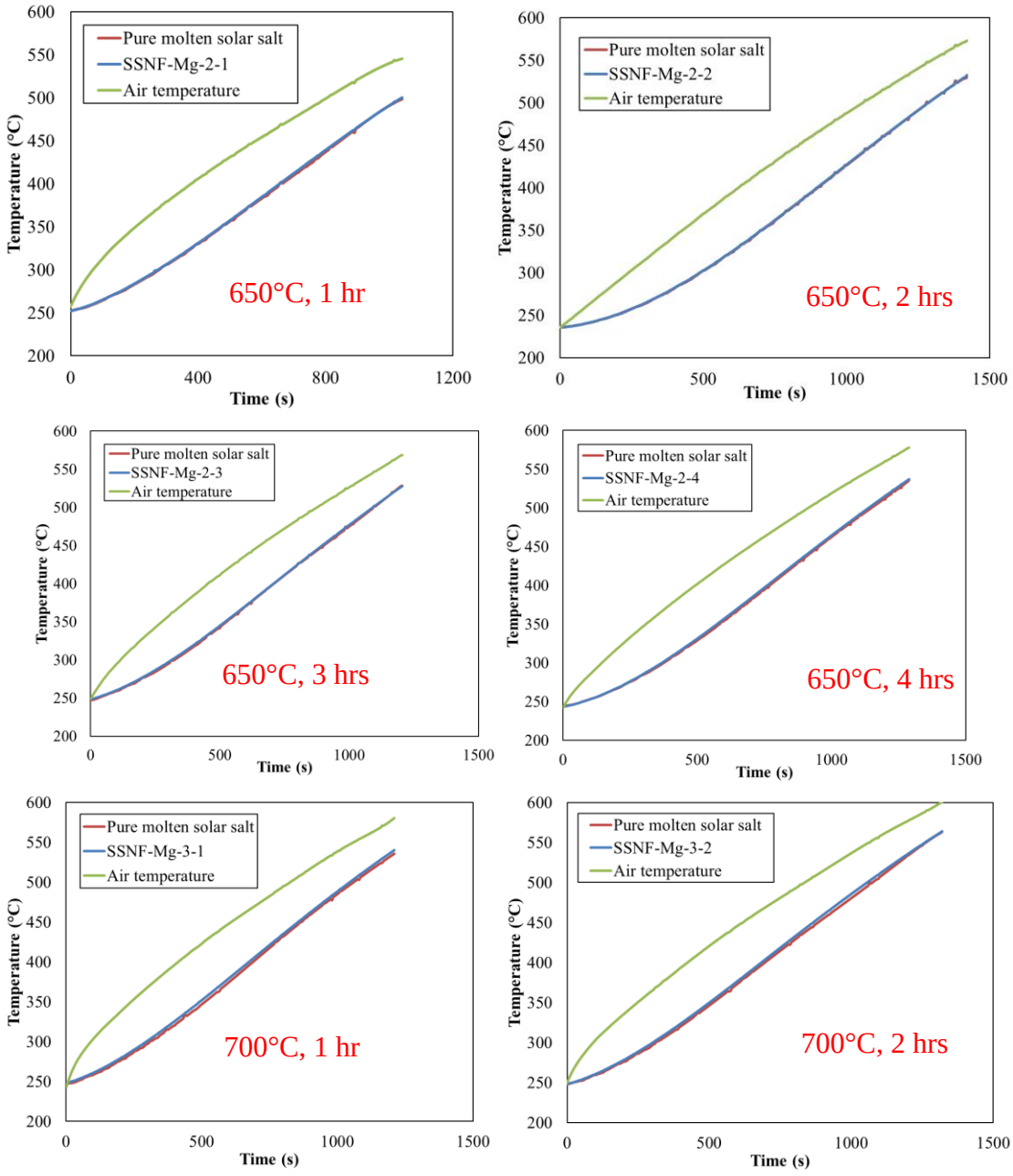

Figure D 5. Temperature ramping curves for T-History experiments

Solar Salt mixed with $Mg(NO_3)_3 \cdot 6H_2O$ at mass fraction of 6% (synthesized at 650°C for 1, 2, 3 and 4 hours; synthesized at 700°C for 1 and 2 hours)

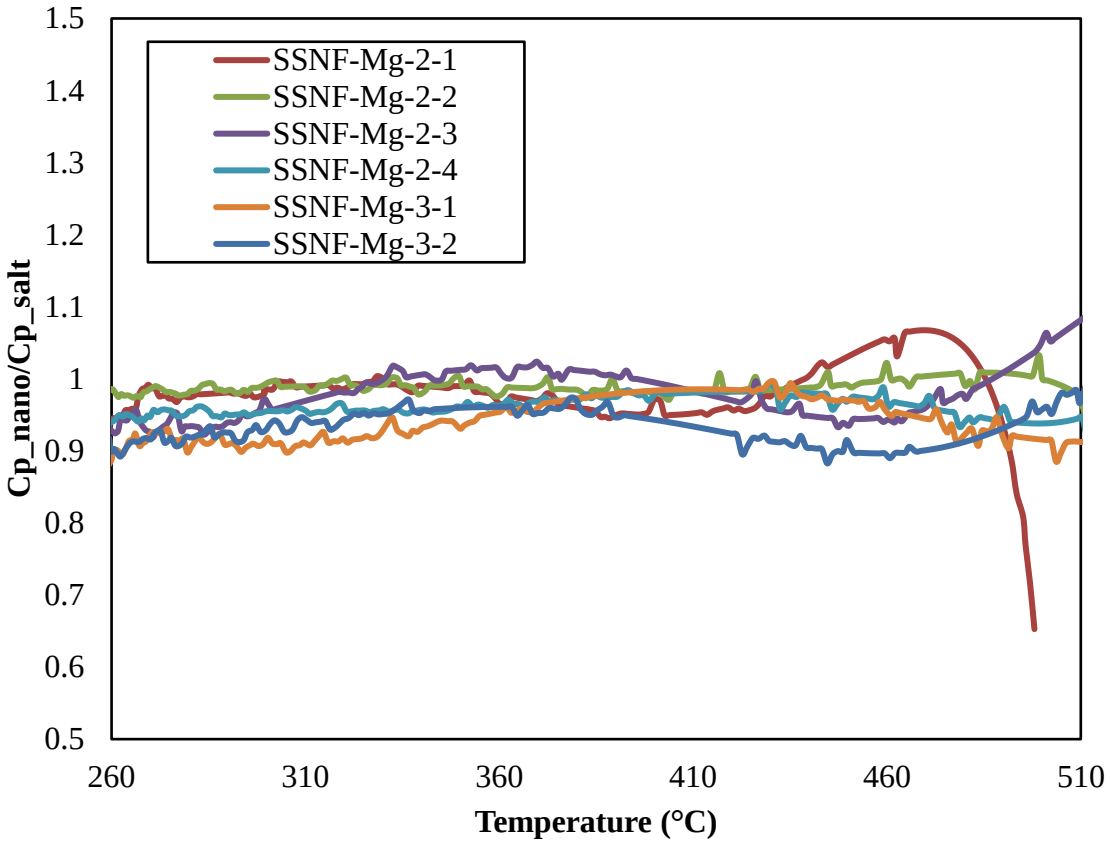

Figure D 6. Specific heat capacity ratio in repeated tests

* ***SSNF-Mg-2-1***: solar salt + 6.0 wt.% $Mg(NO_3)_3 \cdot 6H_2O$ (targeting 1.0 wt.% MgO nanoparticle), synthesized at 650ºC for 1 hr
* ***SSNF-Mg-2-2***: solar salt + 6.0 wt.% $Mg(NO_3)_3 \cdot 6H_2O$ (targeting 1.0 wt.% MgO nanoparticle), synthesized at 650ºC for 2 hrs
* ***SSNF-Mg-2-3***: solar salt + 6.0 wt.% $Mg(NO_3)_3 \cdot 6H_2O$ (targeting 1.0 wt.% MgO nanoparticle), synthesized at 650ºC for 3 hrs
* ***SSNF-Mg-2-4***: solar salt + 6.0 wt.% $Mg(NO_3)_3 \cdot 6H_2O$ (targeting 1.0 wt.% MgO nanoparticle), synthesized at 650ºC for 4 hrs
* ***SSNF-Mg-3-1***: solar salt + 6.0 wt.% $Mg(NO_3)_3 \cdot 6H_2O$ (targeting 1.0 wt.% MgO nanoparticle), synthesized at 700ºC for 1 hrs
* ***SSNF-Mg-3-2***: solar salt + 6.0 wt.% $Mg(NO_3)_3 \cdot 6H_2O$ (targeting 1.0 wt.% MgO nanoparticle), synthesized at 700ºC for 2 hrs

APPENDIX E

Thermal conductivity measurement of solar salt colloidal samples synthesized using $Mg(NO_3)_3{\cdot}6H_2O$ / $Zn(NO_3)_2{\cdot}6H_2O$ additive as precursor for MgO / ZnO particles[9]

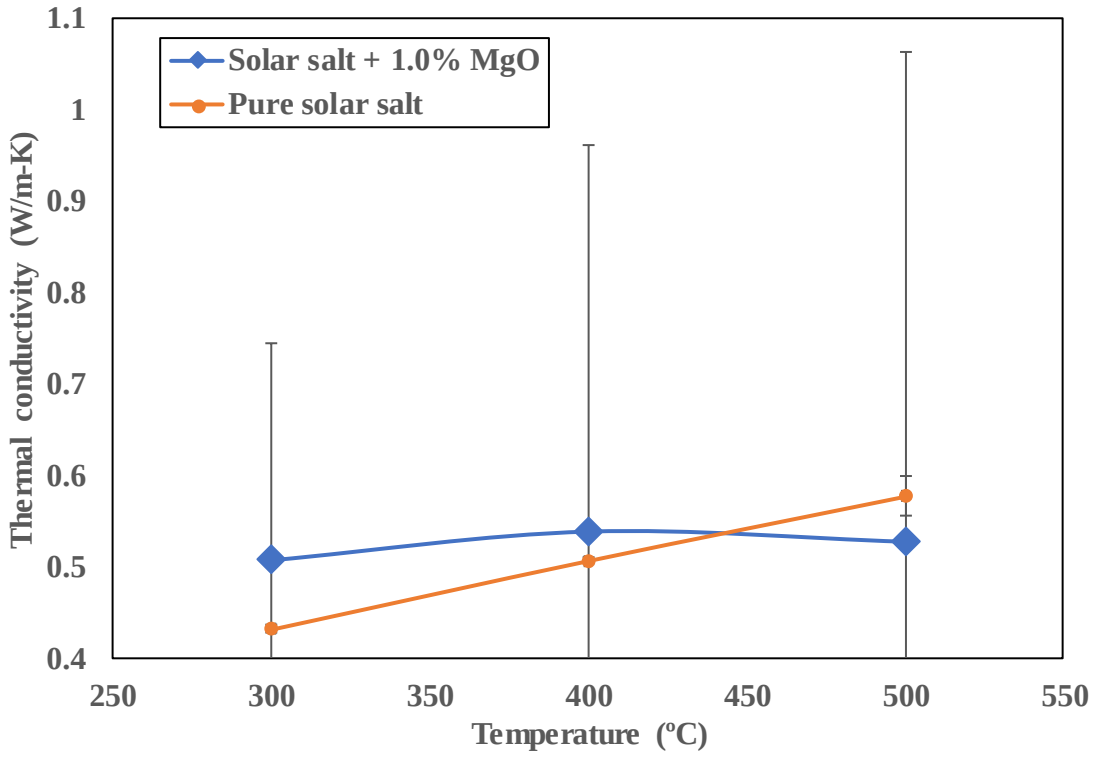

Figure E 1. Plot of thermal conductivity as a function of temperature for pure solar salt samples and molten salt colloid samples (prepared using one-step synthesis protocol). The molten salt colloid samples were obtained by adding $Mg(NO_3)_2{\cdot}6H_2O$ at 6.0 % mass fraction (as particle precursor) to pure solar salt for a target mass fraction of 1% for the resulting MgO particles obtained by thermal decomposition (one-step synthesis protocol)

[9] These measurements are inaccurate due to thermocouple failing in the testing procedure.

Table E 1. Thermal conductivity as a function of temperature for pure solar salt samples and molten salt colloid samples (prepared using one-step synthesis protocol). The molten salt colloid samples were obtained by adding $Mg(NO_3)_2 \cdot 6H_2O$ at 6.0 % mass fraction (as particle precursor) to pure solar salt for a target mass fraction of 1% for the resulting MgO particles obtained by thermal decomposition (one-step synthesis protocol)

Temperature (°C)	Solar salt + 1.0% MgO		Pure solar salt		Enhancement (%)
	k [W/(m·K)]	Standard deviation	*k* [W/(m·K)]	Standard deviation	
300	0.507	47%	0.431	0.9%	17.5%
400	0.538	79%	0.507	0.8%	6.2%
500	0.527	102%	0.577	3.6%	-8.7%
Average	0.524	80%	0.505	11.8%	3.8%

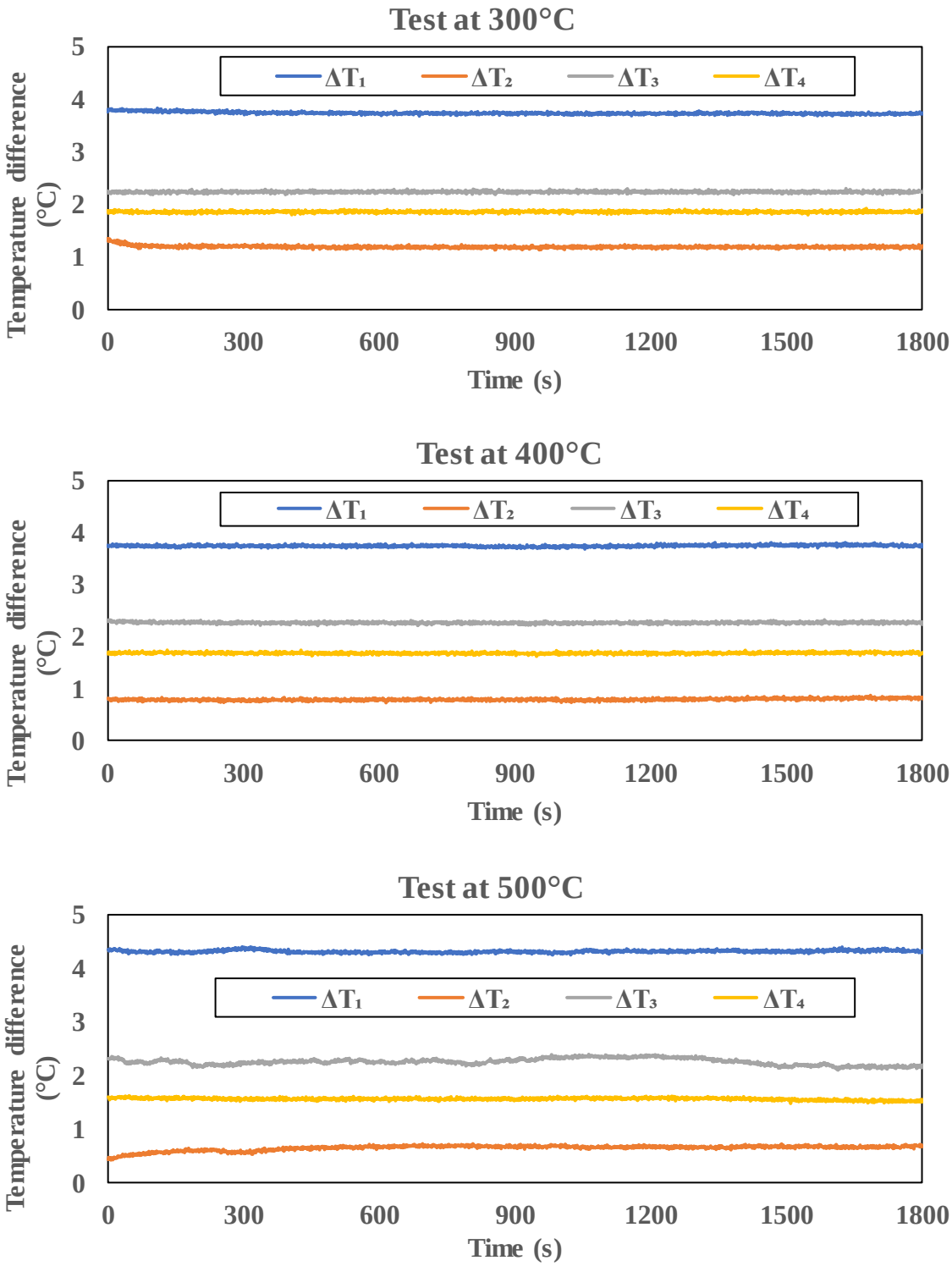

Figure E 2. Measurements of temperature drop in thermal conductivity tests of solar salt colloid sample with MgO particle

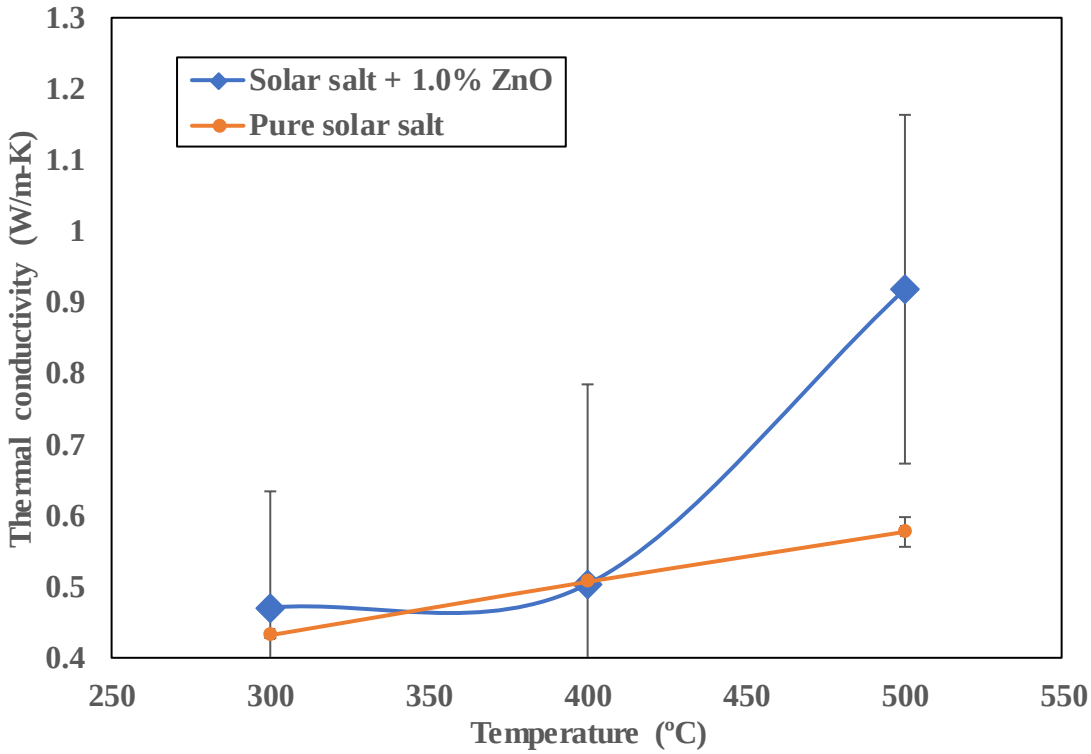

Figure E 3. Plot of thermal conductivity as a function of temperature for pure solar salt samples and molten salt colloid samples (prepared using one-step synthesis protocol). The molten salt colloid samples were obtained by adding $Zn(NO_3)_2 \cdot 6H_2O$ at 3.6 % mass fraction (as particle precursor) to pure solar salt for a target mass fraction of 1% for the resulting ZnO particles obtained by thermal decomposition (one-step synthesis protocol)

Table E 2. Thermal conductivity as a function of temperature for pure solar salt samples and molten salt colloid samples (prepared using one-step synthesis protocol). The molten salt colloid samples were obtained by adding $Zn(NO_3)_2 \cdot 6H_2O$ at 3.6 % mass fraction (as particle precursor) to pure solar salt for a target mass fraction of 1% for the resulting ZnO particles obtained by thermal decomposition (one-step synthesis protocol)

Temperature	Solar salt + 1.0% ZnO		Pure solar salt		Enhancement
(ºC)	*k* [W/(m·K)]	Standard deviation	*k* [W/(m·K)]	Standard deviation	(%)
300	0.469	35%	0.431	0.9%	8.7%
400	0.502	56%	0.507	0.8%	-0.9%
500	0.918	27%	0.577	3.6%	59.1%
Average	0.630	50%	0.505	11.8%	24.7%

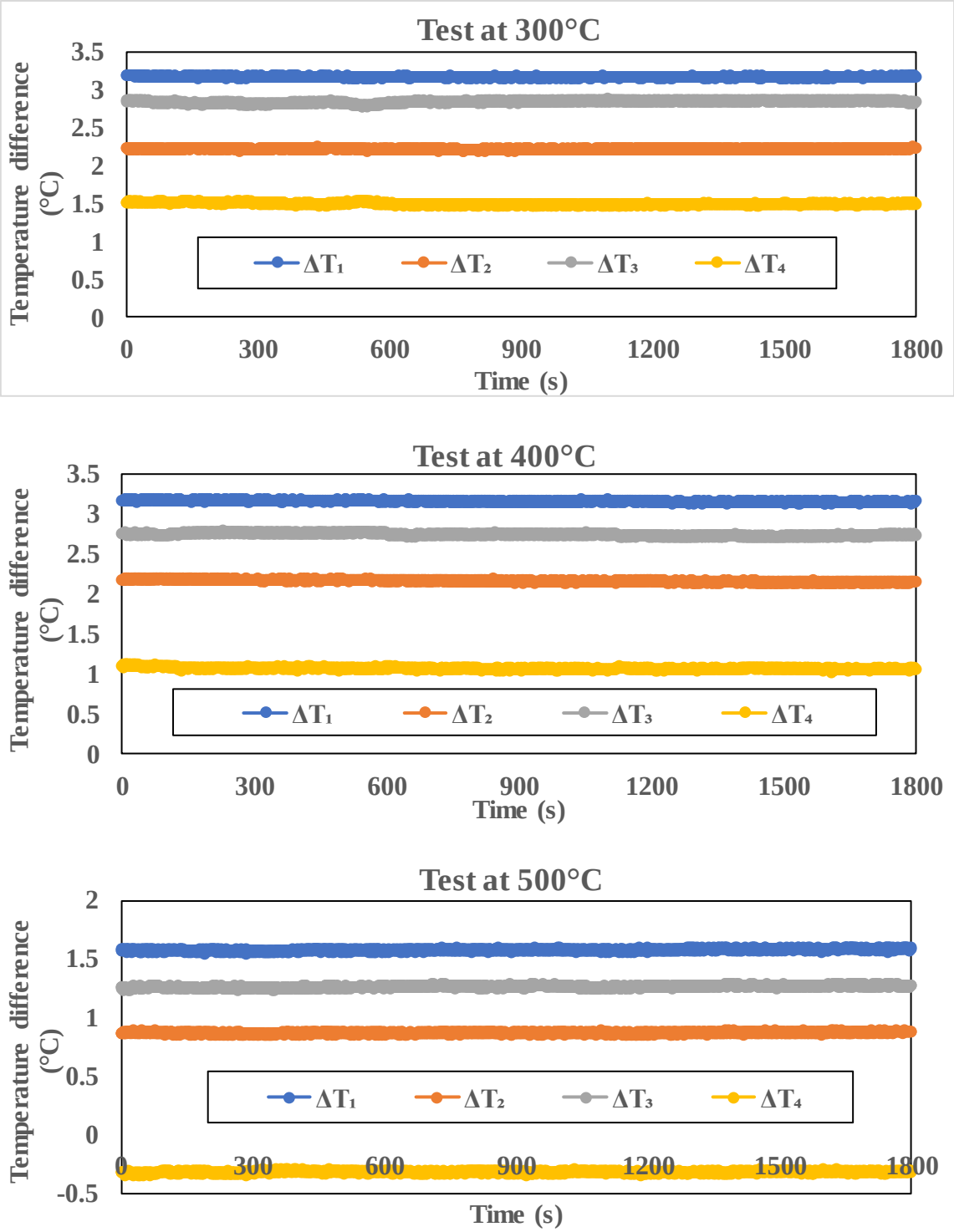

Figure E 4. Measurements of temperature drop in thermal conductivity tests of solar salt colloid sample with ZnO particle

APPENDIX F

SEM CHARACTERIZATION OF CORROSION COUPONS

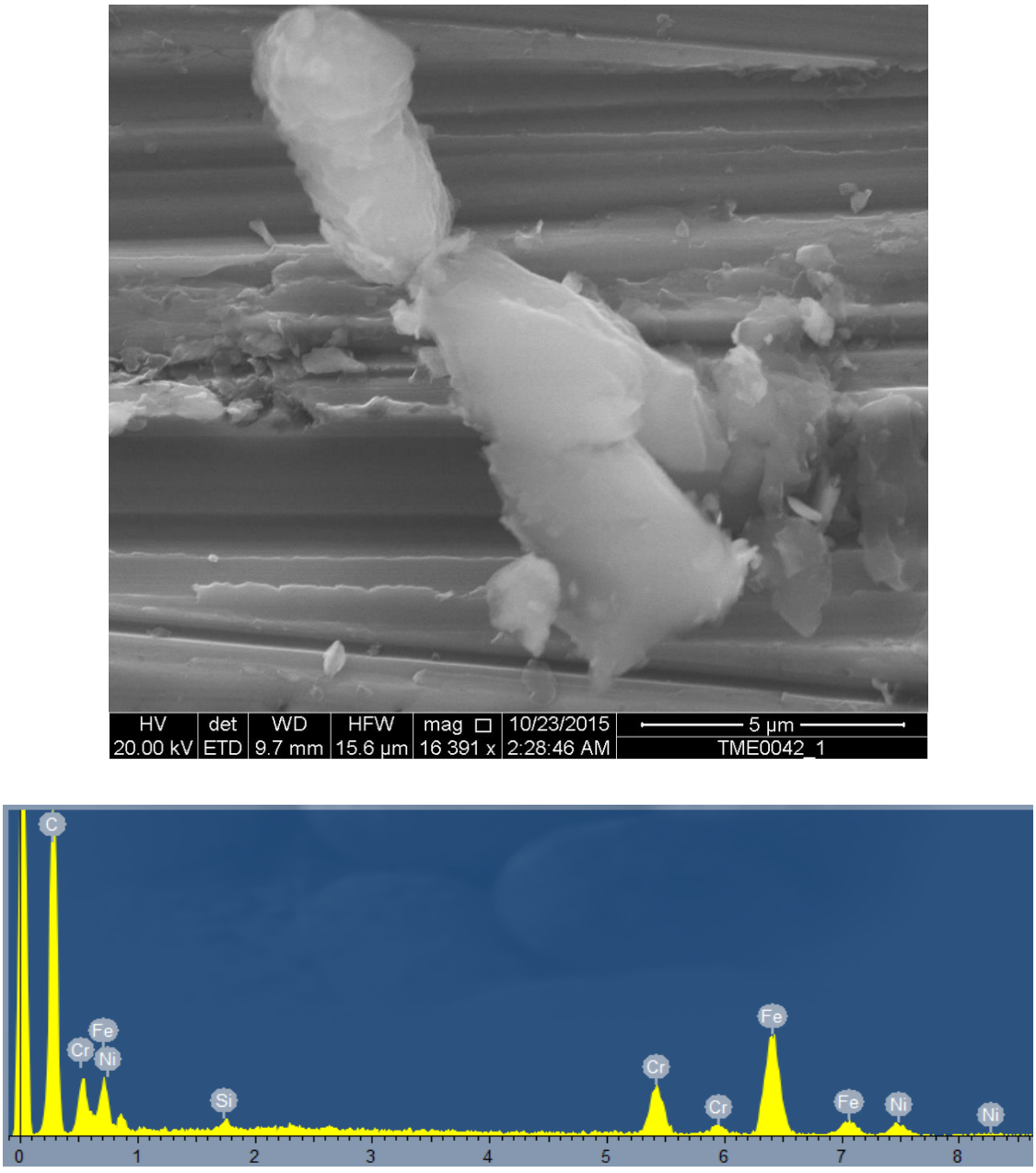

Figure F 1. SEM image of blank stainless steel coupon (in air) before descaling and after heating at 565 °C for 120 hours with EDS spectrum of the surface area

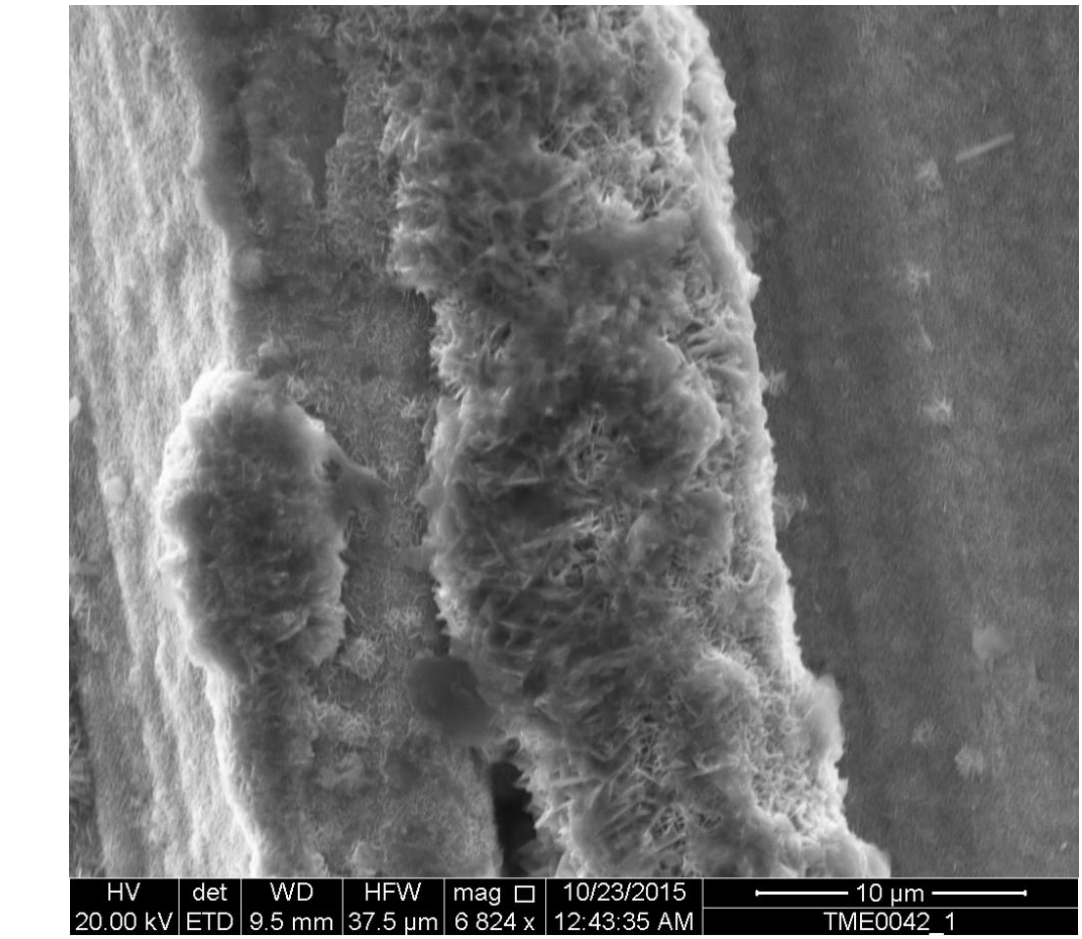

Figure F 2. SEM image of corrosion stainless steel coupon (in pure molten solar salt) before descaling and after heating at 565 °C for 120 hours with EDS spectrum of the surface area

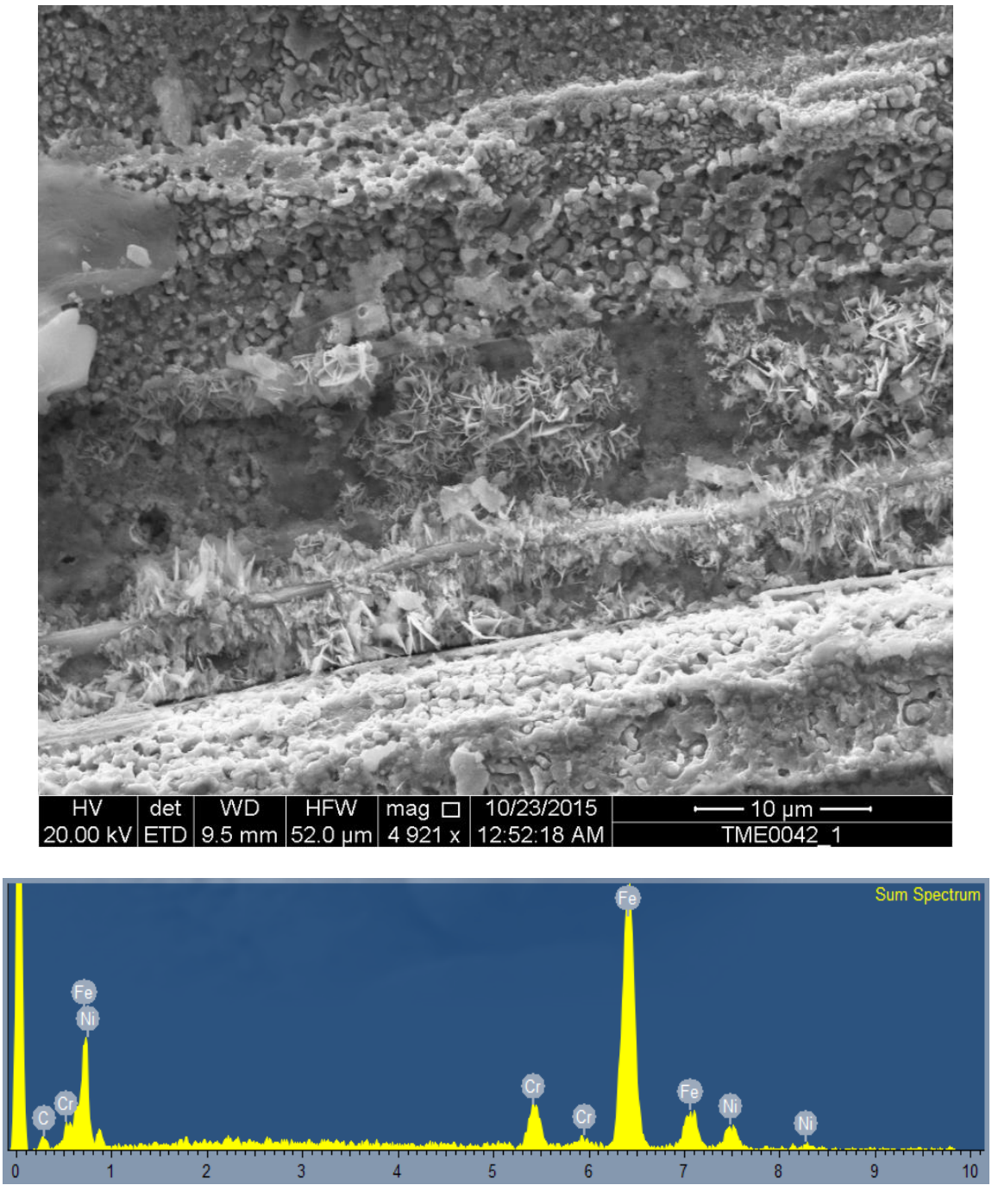

Figure F 3. SEM image of corrosion stainless steel coupon (in pure molten solar salt) following descaling using protocol C.7.4 after heating at 565 °C for 120 hours with EDS spectrum of the surface area

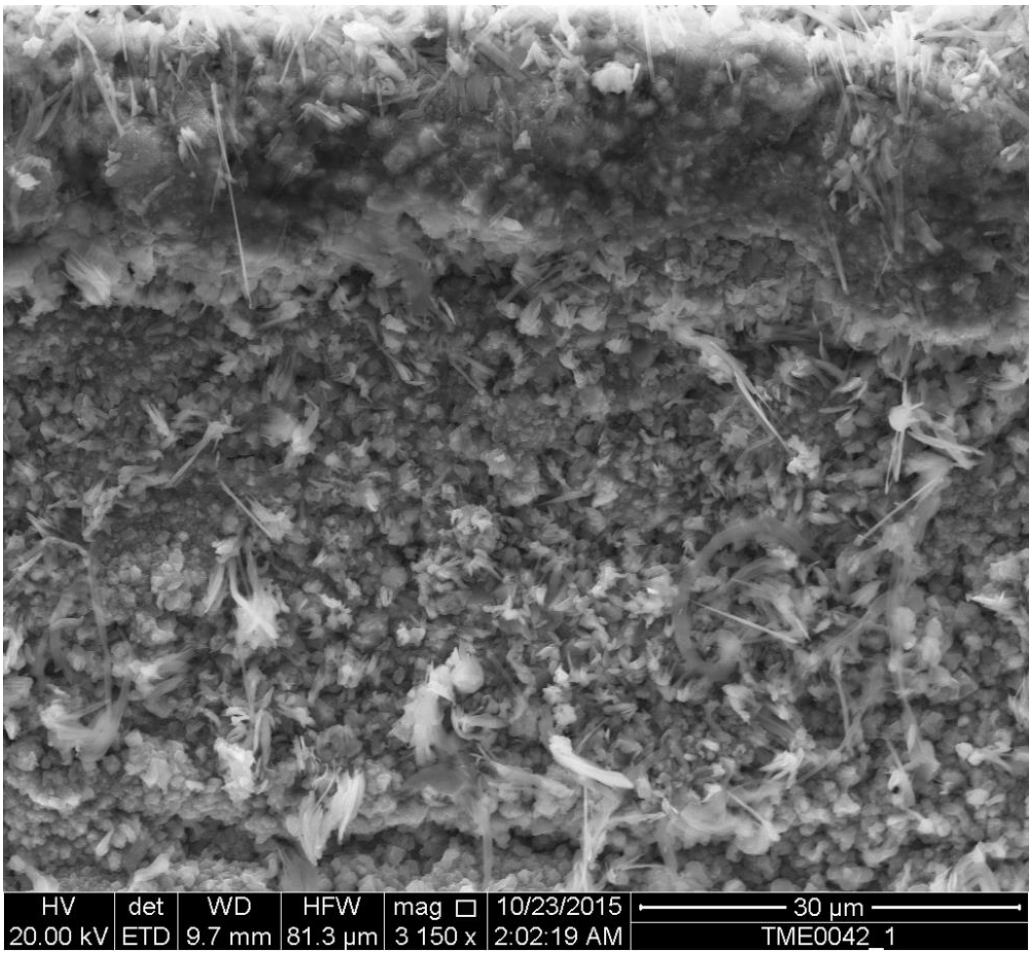

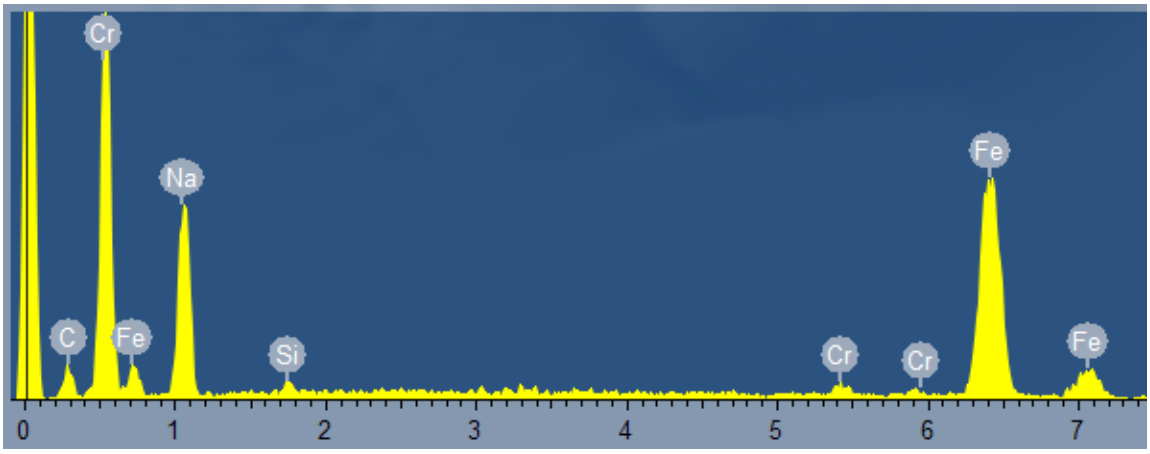

Figure F 4. SEM image of corrosion stainless steel coupon (in solar salt nanofluid doped with 1.0% mass fraction of SiO_2 nanoparticle) before descaling and after heating at 565 °C for 120 hours with EDS spectrum of the surface area

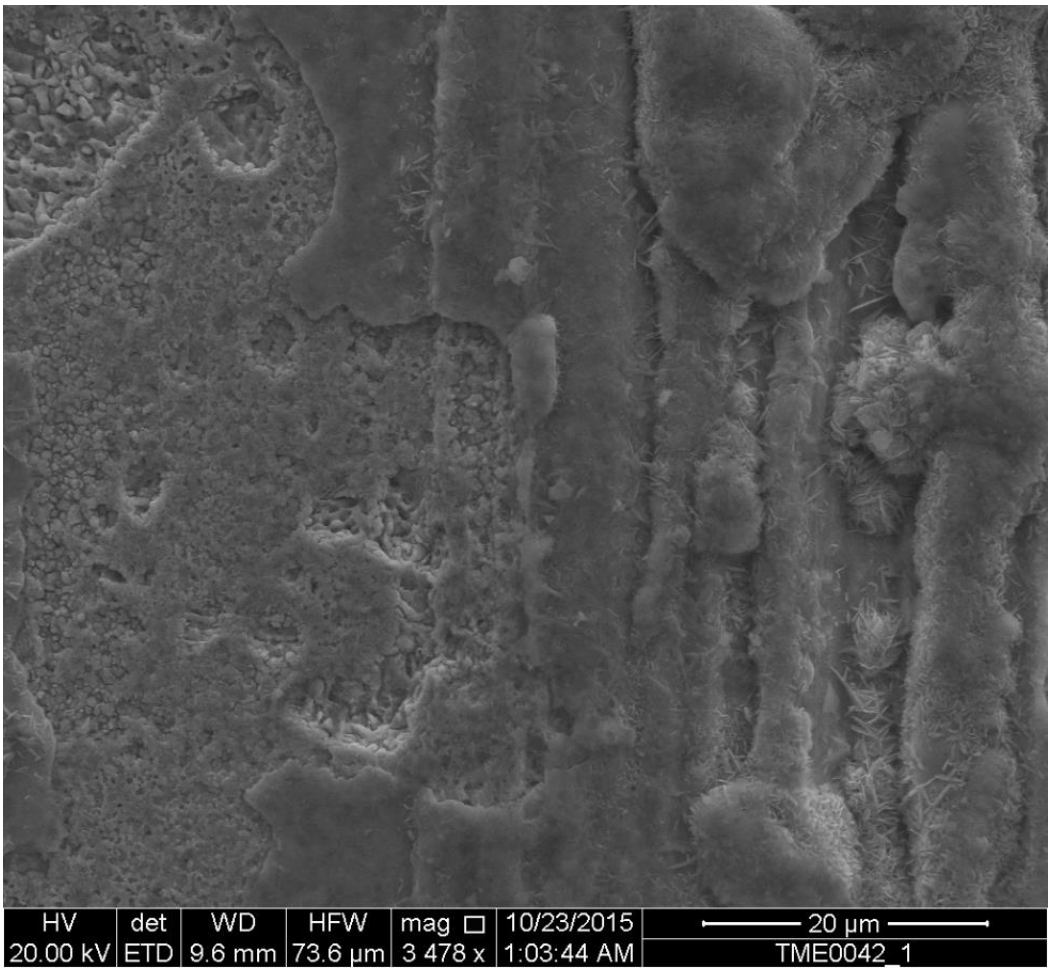

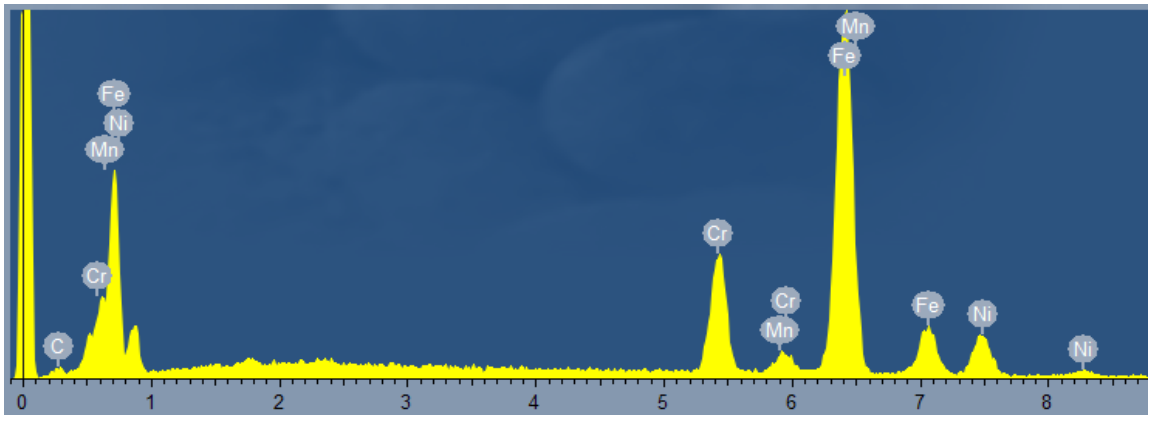

Figure F 5. SEM image of corrosion stainless steel coupon (in solar salt nanofluid doped with 1.0% mass fraction of SiO_2 nanoparticle) following descaling using protocol C.7.4 after heating at 565 °C for 120 hours with EDS spectrum of the surface area

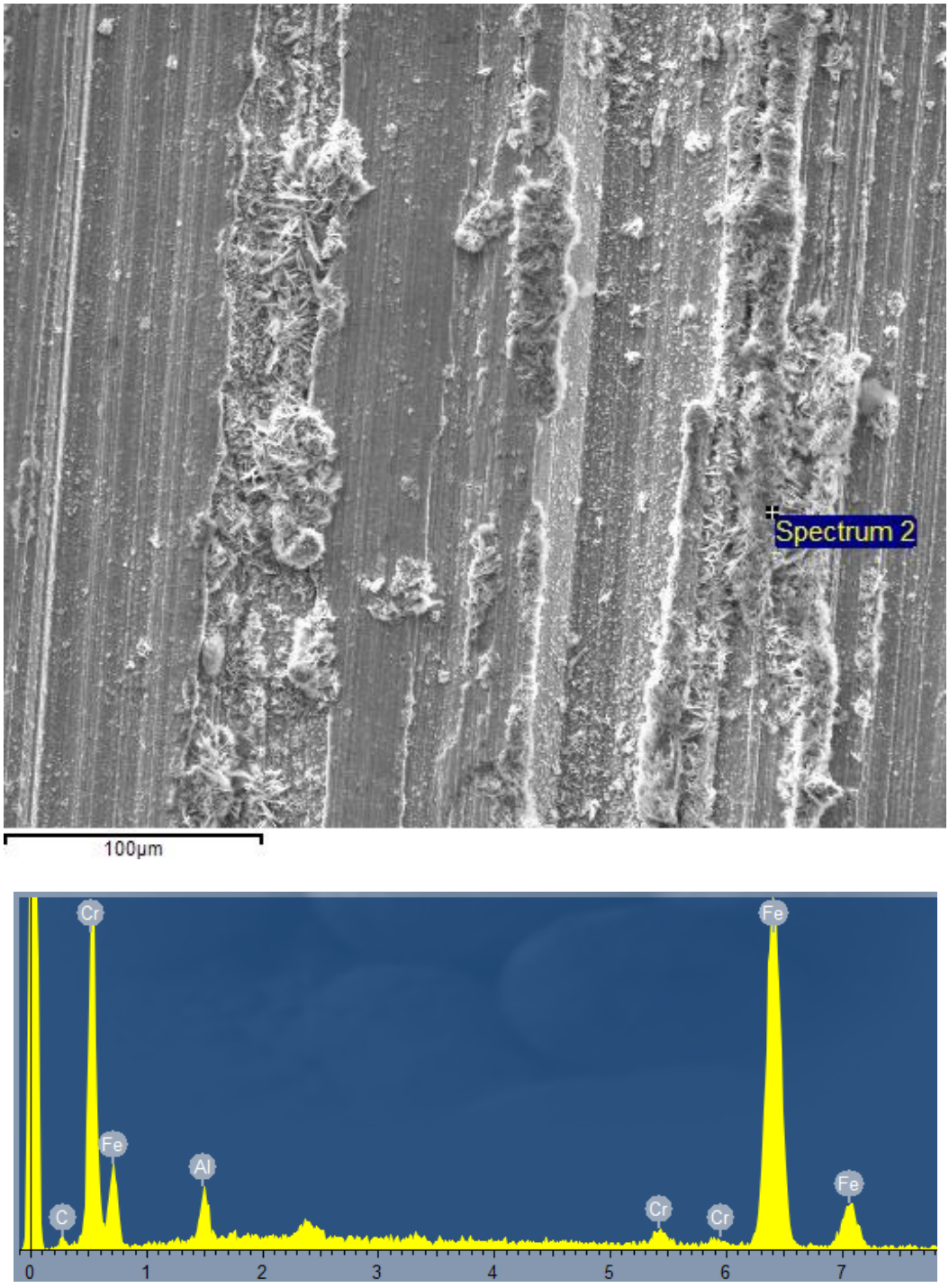

Figure F 6. SEM image of corrosion stainless steel coupon (in solar salt nanofluid synthesized using 6.9% mass fraction of $Al(NO_3)_3 \cdot 9H_2O$ for yielding 1.0% mass fraction of Al_2O_3 nanoparticle) before descaling and after heating at 565 °C for 120 hours with EDS spectrum of the surface area

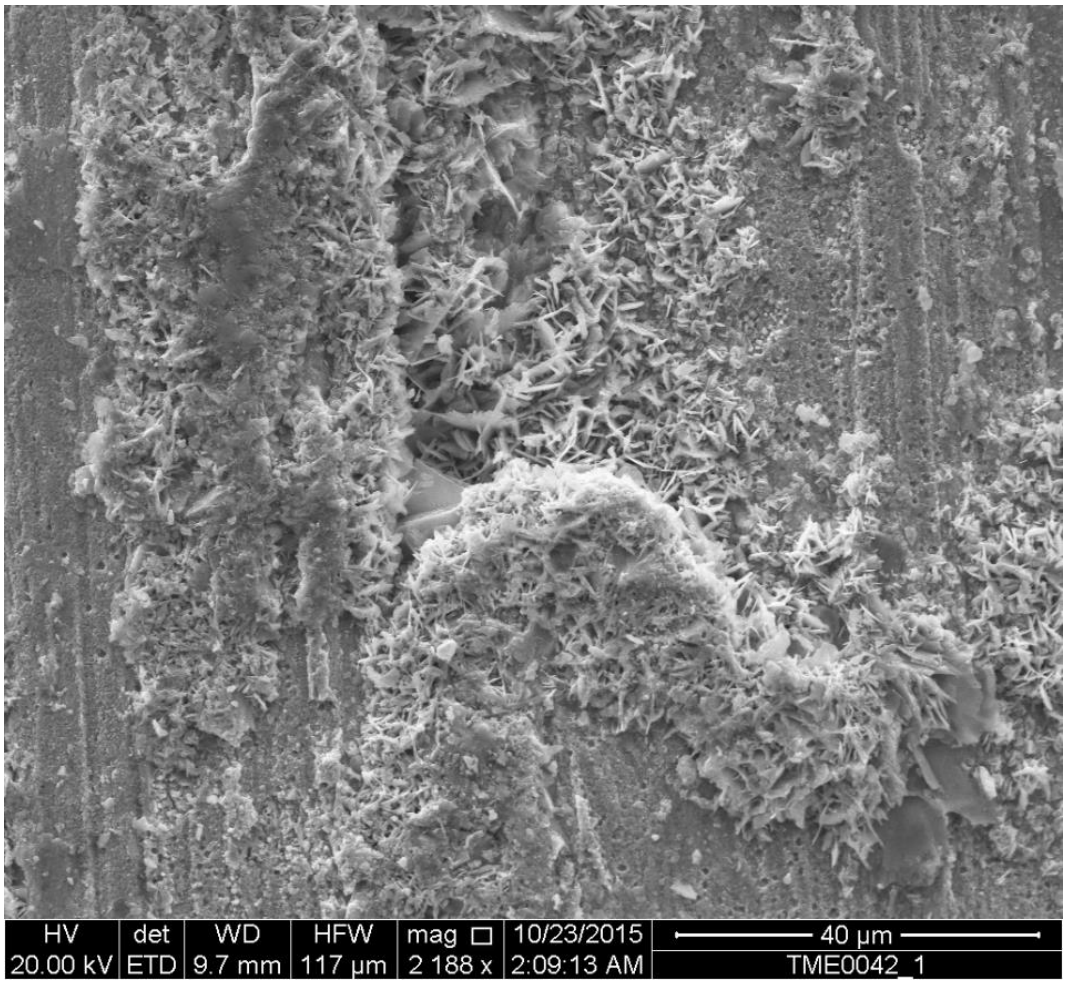

Figure F 7. SEM image of corrosion stainless steel coupon (in solar salt nanofluid synthesized using 6.9% mass fraction of $Al(NO_3)_3 \cdot 9H_2O$ for yielding 1.0% mass fraction of Al_2O_3 nanoparticle) following descaling using protocol C.7.4 after heating at 565 °C for 120 hours with EDS spectrum of the surface area

APPENDIX G

ESTIMATION OF COMPRESSED LAYER THICKNESS USING MOLECULAR DYNAMICS (MD) SIMULATIONS

MD simulation setup

Molecular dynamic simulations were performed to estimate the thickness of compressed layer formed due to adsorption of the solvent molecules on the surface of nanoparticles. In the MD simulation, the position and velocities of each individual atoms and molecules are numerically calculated by solving the Newton's equation of motion. The forces between particles and the potential energy of the overall system is determined by using interatomic potentials or molecular force fields. The overall potential energy in the system includes bonded terms for inter-atomic interactions linked by covalent bonds and nonbonded terms for inter-molecular forces.

$$E_{\text{total}} = E_{\text{bonded}} + E_{\text{nonbonded}} \tag{C1}$$

The bonded interactions usually include stretching, bending and torsional terms, which are expressed as follows:

$$E_{\text{bonded}} = \underbrace{k_s(r - r_0)^2}_{\text{Stretching term}} + \underbrace{k_b(\theta - \theta_0)^2}_{\text{Bending term}} + \underbrace{k_t\{1 + d\cos(n\varphi)\}}_{\text{Torsional term}} \tag{C2}$$

In this study, standard Lennard-Jones potential along with Coulomb force interactions were employed for modeling the non-bonded interactions:

$$E_{\text{nonbonded}} = C\frac{q_i q_j}{r^2} + 4\epsilon\left[\left(\frac{\sigma}{r}\right)^{12} - \left(\frac{\sigma}{r}\right)^{6}\right] \tag{C3}$$

All relevant parameters can be found in a variety of literatures reports [81]. In this test, the molecular dynamics simulation software package “Large-scale Atomic/Molecular Massively Parallel Simulator (LAMMPS)” distributed by Sandia National Laboratories was used to perform the simulation and explore the density distribution of salt molecules on the surface of nanoparticles.

Simulation procedure

The first step of the simulation is the construction of the simulation domain. Commercial tool (Material Studio 5.0) was used to construct the simulation box (49.19 Å × 49.19 Å × 49.19 Å) in which a single nanoparticle (either single-walled carbon nanotube or a spherical metal oxide nanoparticle) was immersed into a mixture of target molten salts (either binary or ternary salt eutectic). Based on the actual molar ratio of different nitrate salts in the eutectic, the number of molecules for each salt is fixed (when the numerical model is implemented in Material Studio and LAMMPS).

The second step of the simulation procedure is to minimize the total potential energy of the system. The temperature of the system is decreased to 0 K followed by NVE integration step. In the NVE integration process, the system is allowed to relax with N (number of atoms), V (volume of system) and E (total energy of system) fixed. Molecules in non-physical configurations are removed (e.g., overlapping molecules) in the NVE integration (micro-canonical ensemble). This prevents computational instability that can be induced by high force or velocities of atoms if they are in non-physical configuration.

The last step is to raise the raise the system temperature to the target value using NPT integration (isobaric-isothermal ensemble). In the present study 800 K was used as the system temperature since the operating temperature of solar salt (binary nitrate salt) in a typical CSP plant is around 565°C. In the NPT integration process, the number of atoms and total pressure is fixed while the system is allowed to exchange energy with an exterior heat sink that was fixed at a constant temperature. After the system reaches equilibrium and steady state conditions are achieved (after sufficiently large number of time steps), the coordinate of each individual atom is updated and the atomic density distribution is calculated. These calculations provide additional insights into the nanostructures (compressed layer) that are induced to form on the nanoparticle surface.

MD simulation result

The figure below shows the spatial distribution of the molecules of the solar salt in the vicinity of a SiO_2 nanoparticle and Al_2O_3 nanoparticle, in which the mass concentration of SiO_2 and Al_2O_3 in the nanofluid system are 4.4% and 1.8% respectively.

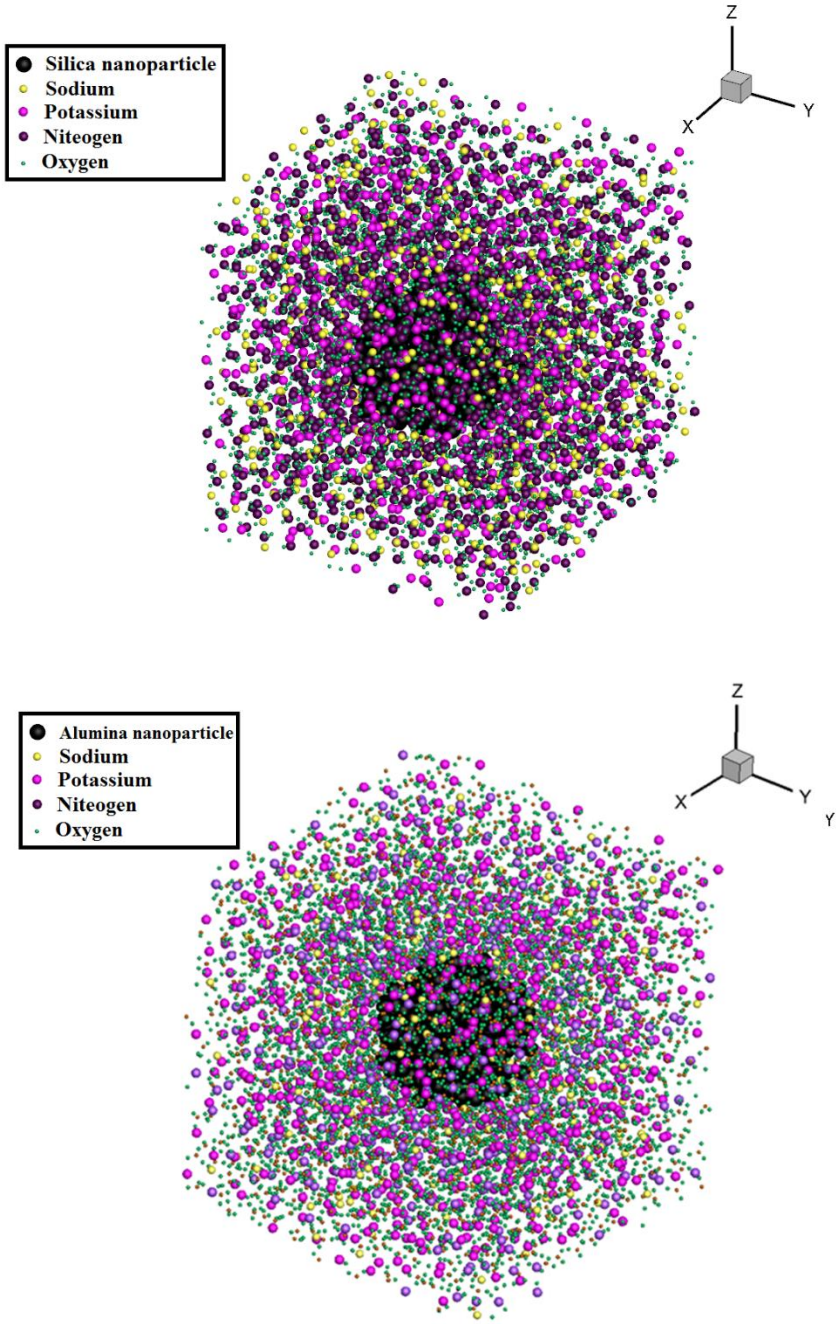

Figure G 1. Atomic distribution of the solar salt-SiO_2 nanofluid system (TOP) and solar salt-Al_2O_3 nanofluid system (BOTTOM)

Based on the results from the MD simulations, the plot of density of solar salt molecules as a function of distance from the surface of the nanoparticle is plotted in Figure G2 for silica and alumina nanoparticle. The plot shows that within 5 Å of the nanoparticle surface the density values peak and then asymptotically decreases to the free stream value of density. This shows that a higher density phase or "compressed phase" is induced by the presence of the nanoparticle due to surface adsorption of the molecules of the solar salt. Hence, this phenomenon implies that the higher density of the compressed phase is also associated with enhanced values of other thermo-physical properties, such as, thermal conductivity and specific heat capacity (as well as different rheological properties).

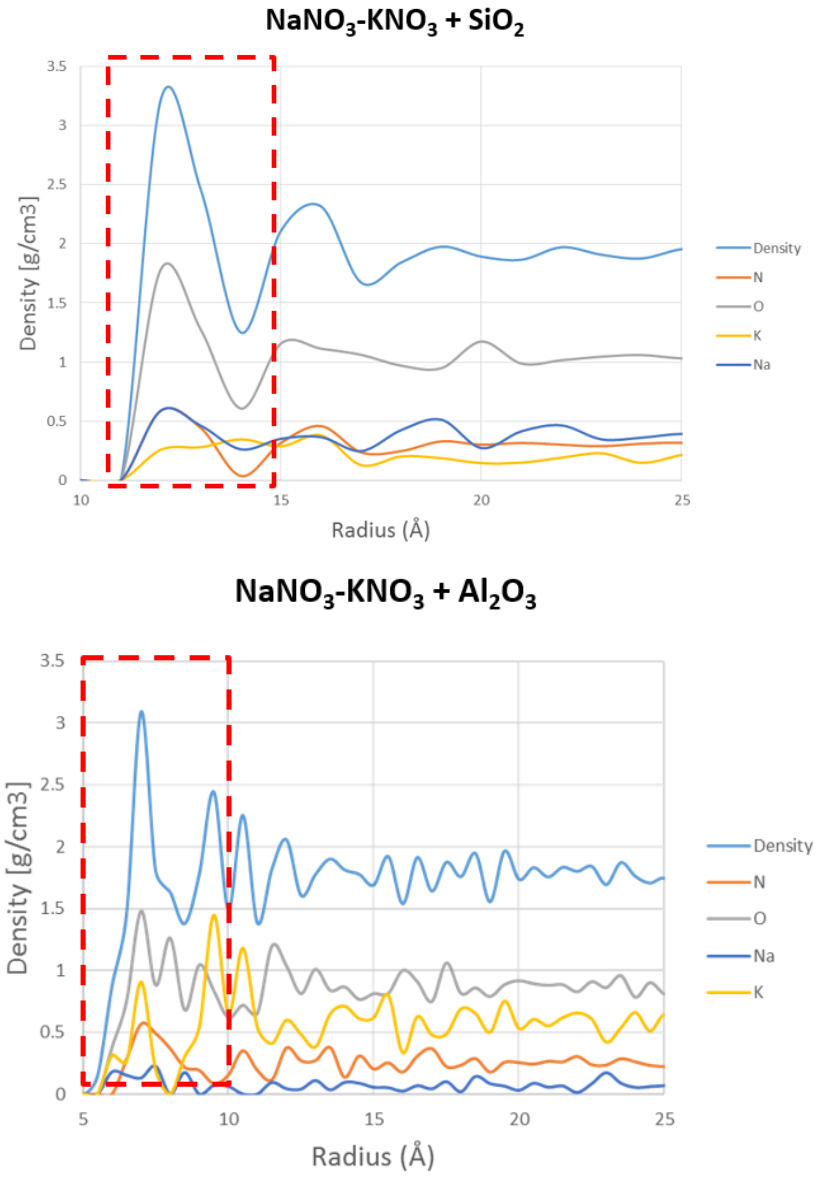

Figure G 2. Plot of density as a function distance from the surface of the nanoparticle surface. (TOP) Silica nanoparticle. (BOTTOM) Alumina nanoparticle.

APPENDIX H

OSCILATION PARTICLE MOTION

```
1.  import math
2.
3.  def main():
4.      global A_NaNa, A_NaK, A_NaNO3, A_KK, A_KNO3, A_NO3NO3, B_NaNa, B_NaK, B_NaN
    O3, B_KK, B_KNO3, B_NO3NO3
5.  # unit for timestep is ps
6.      dt = 0.00002
7.  # Leonard-Jones potential parameters
8.  # e unit in kcal/mol
9.      e_OO = 0.155
10.     e_NN = 0.2
11.     e_NaNa = 0.086
12.
13. # r unit in Angstrom
14.     r_OO = 3.154
15.     r_NN = 3.9
16.     r_NaNa = 2.73
17.
18.     e_ON = math.sqrt(e_OO*e_NN)
19.     e_ONa = math.sqrt(e_OO*e_NaNa)
20.     e_NNa = math.sqrt(e_NN*e_NaNa)
21.     r_ON = 1/(1/r_OO+1/r_NN)
22.     r_ONa = 1/(1/r_OO+1/r_NaNa)
23.     r_NNa = 1/(1/r_NN+1/r_NaNa)
24.
25.
26. # A unit in kcal*A^12/mol, B unit in kcal*A^6/mol
27.
28.     A_NaNO3 = 4*e_NNa*(r_NNa**12)+12*e_ONa*(r_ONa**12)
29.     B_NaNO3 = 4*e_NNa*(r_NNa**6)+12*e_ONa*(r_ONa**6)
30.
31. # Initial conditions
32.     a = 1.2
33.     x_Na = 0
34.     m_tot = 23 /(6.022e26)
35.     T = 600
36. # Velocity unit in A/ps
37.     v_Na = math.sqrt(3*(1.38e-20)*T/m_tot) / 100
38.     print("v_Na",v_Na,"Initialization!")
39. # Velocity_Verlet
40.     particle_position = open("position",'w')
41.     for i in range(5000):
42.         KE = 0.5* 23 /(6.022e26) * ((v_Na * 100)**2)
43.         PE1 = (4*e_NNa*((r_NNa/(a-x_Na))**12-(r_NNa/(a-
    x_Na))**6) + 12*e_ONa*((r_ONa/(a-x_Na))**12-(r_ONa/(a-
    x_Na))**6) + 4*e_NNa*((r_NNa/(a+x_Na))**12-
    (r_NNa/(a+x_Na))**6) + 12*e_ONa*((r_ONa/(a+x_Na))**12-
    (r_ONa/(a+x_Na))**6))* 4184 /(6.022e26)
44.         PE2 = (8.99e9/((a-x_Na)*(1e-10))+8.99e9/((a+x_Na)*(1e-10)))*(1.602176e-
    19**2)
45.         particle_position.write(str(i*dt)+'\t'+str(x_Na)+'\t'+str(v_Na)+'\t'+st
    r(KE)+'\t'+str(PE1)+'\t'+str(PE2)+'\n')
```

```
# Calculate new position after dt and intermediate velocity after dt/2
        a_Na_left = ((12*A_NaNO3*((a+x_Na)**(-13))-6*B_NaNO3*((a+x_Na)**(-7)))*418.4-138517/((a+x_Na)**2))/23
        a_Na_right = -((12*A_NaNO3*((a-x_Na)**(-13))-6*B_NaNO3*((a-x_Na)**(-7)))*418.4-138517/((a-x_Na)**2))/23
        a_Na = a_Na_left + a_Na_right
        new_x = x_Na + v_Na*dt + a_Na*(dt**2)/2
        new_v = v_Na + a_Na*dt/2
# Calculate new velocity after dt
        x_Na = new_x
        v_Na = new_v
        a_Na_left = ((12*A_NaNO3*((a+x_Na)**(-13))-6*B_NaNO3*((a+x_Na)**(-7)))*418.4-138517/((a+x_Na)**2))/23
        a_Na_right = -((12*A_NaNO3*((a-x_Na)**(-13))-6*B_NaNO3*((a-x_Na)**(-7)))*418.4-138517/((a-x_Na)**2))/23
        a_Na = a_Na_left + a_Na_right
        new_v = v_Na + a_Na*dt/2
        v_Na = new_v
main()

```

APPENDIX I

PARTICLE GROWTH SIMULATION

```
import math

def ln(n):
    return math.log(n,math.exp(1))

def eliminate_zeros(Particles):
    n = len(Particles)
    New_PSD = []
    in_combination = False
    for i in range(n):
        r = Particles[i][0]
        n = Particles[i][1]
        if in_combination == True:
            r_t = r_t + (r**3) * n
            n_t = n_t + n
            if n_t > 1:
                New_PSD.append([(r_t/n_t)**(1/3),n_t])
                in_combination = False
        else:
            if n > 1:
                New_PSD.append([r,n])
            else:
                r_t = (r**3) * n
                n_t = n
                in_combination = True
    return New_PSD

def Sequence(Particles):
    Ordered_particles = []
    n = len(Particles)
    for i in range(n):
        if i == 0:
            Ordered_particles.append(Particles[i])
        else:
            if Particles[i][0] <= Ordered_particles[0][0]:
                Ordered_particles.insert(0,Particles[i])
            elif Particles[i][0] > Ordered_particles[-1][0]:
                Ordered_particles.append(Particles[i])
            else:
                for j in range(len(Ordered_particles)-1):
                    if Ordered_particles[j][0] < Particles[i][0] <= Ordered_particles[j+1
][0]:
                        Ordered_particles.insert(j+1,Particles[i])
                        break
    return(Ordered_particles)

# For numerical integration of coagulation process, each iteration should result in less
than 10% change of total quantity of particle quantity
def calc_time_step(Particles, kb, temp, mu):
    n = 0
    for i in range(len(Particles)):
        n = n + Particles[i][1]
```

```
    coeff = kb * (temp+273.15) / 3 / mu * 4 * n / 0.001
    time_step = 0.1 / coeff
    return time_step

# To reduce the computational cost, the particle size distribution will be discretized with +/- 5% range from the minimum size value
def coagulation(Particles, kb, temp, mu, time_step):
    Particles.sort()
    Particles = eliminate_zeros(Particles)
    p_num = len(Particles)
    p_min = Particles[0][0]
    p_max = Particles[-1][0]

    coag_size_dis = [p_min]
    while coag_size_dis[-1] * 1.05 / 0.95 <= p_max: # Creating discretized size chart
        coag_size_dis.append(coag_size_dis[-1] * 1.05 / 0.95)
    coag_size_dis.append(coag_size_dis[-1] * 1.05 / 0.95)
    del coag_size_dis[0]

    coag_num = len(coag_size_dis)
    Particles_seg = []
    Coag_particles = []
    for i in range(coag_num):
        Particles_seg.append([])

    for i in range(p_num):
        r = Particles[i][0]
        n = Particles[i][1]
        for j in range(coag_num):
            if r < coag_size_dis[j]:
                Particles_seg[j].append([r,n])
                break

    for i in range(coag_num):
        v_t = 0
        n_t = 0
        for j in range(len(Particles_seg[i])):
            r = Particles_seg[i][j][0]
            n = Particles_seg[i][j][1]
            v_t = v_t + r**3 * n
            n_t = n_t + n
        if n_t == 0:
            Coag_particles.append([coag_size_dis[i],0])
        else:
            Coag_particles.append([(v_t/n_t)**(1/3),n_t])

# Eample of p_list:
# Given particle radius = [1,2,3,4,5,6,7,8,9,10] and cut point of [1, 2.5, 5.5, 8.5], coag_num = 4, p_list becomes [2, 5, 8], Coag_particles = [[1.5, n1], [4.2, n2], [7.3, n3], [9.5, n4]]
    coag_p_num = len(Coag_particles)

    p_modify = []
    p_new = []
    for i in range(coag_p_num):
        p_modify.append(0)

    for i in range(coag_p_num):
```

```
        r1 = Coag_particles[i][0]
        n1 = Coag_particles[i][1]
        for j in range(i,coag_p_num):
            r2 = Coag_particles[j][0]
            n2 = Coag_particles[j][1]
            n_coagu = kb * (temp+273.15) / 3 / mu * (2+r1/r2+r2/r1) * n1 * n2 / 0.001 * t
    ime_step
            if i != j:
                n_coagu = n_coagu * 2
            if n_coagu < 1:
                continue
            else:
                p_modify[i] = p_modify[i] + n_coagu
                p_modify[j] = p_modify[j] + n_coagu
                r3 = (r1**3+r2**3)**(1/3)
                p_new.append([r3,n_coagu])

# Adjust p_modify to the original particle size list (before discretization!)
    p_index = 0
    for i in range(coag_num):
        r_t = Coag_particles[i][1]
        change_t = p_modify[i]
        if r_t == 0:
            continue
        else:
            for j in range(len(Particles_seg[i])):
                change = Particles_seg[i][j][1] / r_t * change_t
                Particles[p_index][1] = Particles[p_index][1] - change
                p_index = p_index + 1

# Converging to one single coagulated particles size
    #if p_new != []:
    #    p_new = discrete(p_new, 1e-10)
    new_p = Particles + p_new
    new_p.sort()
    new_p = eliminate_zeros(new_p)
    return new_p

def discrete(Particles, reso):
    p_num = len(Particles)
    p_d = []
    p_n = []
    PSD = []
    for i in range(p_num):
        d = Particles[i][0]
        n = Particles[i][1]
        d_new = int(d/reso)
        n_new = n * (d**3) / ((d_new*reso)**3)
        p_d.append(d_new)
        p_n.append(n_new)
    for i in range(1,p_num):
        d = p_d[i]
        n = p_n[i]
        if PSD == [] or d > PSD[-1][0]:
            PSD.append([d,n])
        else:
            for j in range(len(PSD)):
                if d <= PSD[j][0]:
```

```
                    if d == PSD[j][0]:
                        PSD[j][1] = PSD[j][1] + n
                    else:
                        PSD.insert(j,[d,n])
                    break
    for i in range(len(PSD)):
        PSD[i][0] = PSD[i][0] * reso
    return PSD

def main():

# constant values
# molecular volume (m3)
    v_mole = 1.869e-29
# molecular volume (m3/mol)
    v_m = 1.1257e-5
# Boltzmann constant (J/K)
    kb = 1.381e-23
# Interfacial free energy (J/m2)
    gamma = 0.52
# Solubility (mol/L)
    solub = 3.537e-7
# Pre-exponential factor for nucleation
    A_nuc = 1e34
# Diffusivity (m2/s)
    Diff = 1.56e-9
# Avogadro's number (mol-1)
    Na = 6.02e23
# Viscosity (Pa.s)
    mu = 0.004
# Defaule liquid volume (L), dont change this constant!!!
    V = 1

# Setup for initial conditions for numerical integration, MN stands for mol quantity of M
g(NO3)2
    time_step = 0.0001
    time = 0
    temp = 360
    MN = 0.5
    alpha = 0
# This rate stands for both Mg(NO3)2 consumption rate as well as MgO monomer generation r
ate (mol/s)
    dMN_dt = 0.043 * math.exp(-1500/(temp+273.15)) * 0.5
    MN_monomer = 0
# MgO monomer consumption rate (mol/s)
    dMN_monomer_cons = 0

### No more nucleation happening!!!
    MN_np_radius = 0

# Discrete particle size distribution (size, particle number)

    Particles = []

# Starts interation
    i = 0
    p = 1
    fname = 'Growth_property_track.txt'
```

```
    gpt = open(fname,'w')
    to_write = "iteration" + '\t' + "time" + '\t' + "temp" + '\t' + "MN" + '\t' + "dMN/dt" + '\t' + "dMN_monomer_cons" + '\t' + "Supersaturation" + '\n'
    gpt.write(to_write)
    while True:
        if MN - dMN_dt * time_step < 0:
            break
        time = time + time_step
        temp = temp + 5/60 * time_step
        MN = MN - dMN_dt * time_step
        MN_monomer = MN_monomer + dMN_dt * time_step - dMN_monomer_cons
        MN_np_growth_cons = 0
# Decomposition
        alpha = 1 - MN/0.5
        if alpha < 0.15:
            dMN_dt = 0.043 * ((1-alpha)**(2/3)) * math.exp(-1500/(temp+273.15)) * 0.5
        else:
            dMN_dt = (3.8e7) * ((1-alpha)**(2/3)) * math.exp(-15500/(temp+273.15)) * 0.5

# Coagulation growth (the coagulation will run at varied time_step!)
# To reduce the computational cost, the particle size distribution will be discretized with +/- 5%
        z = 0

        if i == int(i/100)*100 and Particles != []:
            t_interval = time_step*100 # changing time-step!!!
            t_cumu = 0
            while True:
                tstep = calc_time_step(Particles, kb, temp, mu)
                if t_cumu + tstep < t_interval:
                    Particles = coagulation(Particles, kb, temp, mu, tstep)
                    t_cumu = t_cumu + tstep
                    if i == 17500:
                        temp_file = open("temp_file.txt","w")
                        for j in range(len(Particles)):

                            to_write = str(Particles[j][0])+ '\t'+ str(Particles[j][1]) + '\n'
                            temp_file.write(to_write)
                        temp_file.close()
                    Particles.sort()
                else:
                    tstep = t_interval - t_cumu
                    Particles = coagulation(Particles, kb, temp, mu, tstep)
                    Particles.sort()
                break

# Nucleation
        if MN_monomer < solub:
            MN_np_radius = 0
            MN_np_rate = 0
        else:
            MN_np_radius = 2*gamma*v_mole/kb/(temp+273.15)/ln(MN_monomer/solub)
            MN_np_rate = 0.001 * A_nuc * math.exp(-16 * math.pi * gamma**3 * v_mole**2 / (3 * (kb*(temp+273.15))**3 * (ln(MN_monomer/solub))**2))

```

```
# Radius growth
        if i > 0 and Particles != []:
            for j in range(len(Particles)):
                if Particles[j][1] == 0:
                    continue
                else:
                    r_old = Particles[j][0]
                    r_new = Diff*v_mole*Na/r_old*(MN_monomer-solub)*time_step + r_old
                    MN_np_growth_cons = MN_np_growth_cons + 4/3*math.pi*(r_new**3 - r_old**3)/v_m * Particles[j][1]
                    Particles[j][0] = r_new

# Updating newly-nucleated particles
        if MN_np_rate * time_step > 1:
            Particles.append([MN_np_radius, MN_np_rate * time_step])
            MN_np_nucleate_cons = 4/3 * math.pi * MN_np_radius**3 / v_m * MN_np_rate * time_step
        else:
            MN_np_nucleate_cons = 0

        dMN_monomer_cons = MN_np_nucleate_cons + MN_np_growth_cons

# Discretize particle size distribution
        #if Particles != [] and i == int(i/20)*20:
        #    Particles = discrete(Particles, 1e-12)

        #if Particles != [] and i == int(i/2000)*2000:
            #Particles = discrete(Particles, 1e-11)

# Output_files
        if i == int(i/2000)*2000:
            print(i,temp,len(Particles),MN_monomer/solub)
        if i == int(i/2000)*2000:
            to_write = str(i) + '\t' + str(time)+ '\t' + str(temp) + '\t' + str(MN) + '\t' + str(dMN_dt) + '\t' + str(dMN_monomer_cons) + '\t' + str(MN_monomer/solub) +'\n'
            gpt.write(to_write)
            print(i,temp,MN, MN_monomer, MN_np_radius,dMN_monomer_cons)
            filename = 'temp_' + str(p) + '_' + str(i)
            np = open(filename,"w")
            for j in range(len(Particles)):
                to_write = str(Particles[j][0])+ '\t'+ str(Particles[j][1]) +'\n'
                np.write(to_write)
            np.close()
            p = p + 1
        i = i + 1

        #if Particles != [] and i == int(i/20000)*20000:
            #Particles = discrete(Particles, 1e-10)
            #Particles = Sequence(Particles)
            #Particles = eliminate_zeros(Particles)

        if temp > 420:
            gpt.close()
            break
main()
```